Université du Québec
Institut National de la Recherche Scientifique
Centre Énergie Matériaux Télécommunications

# Élaboration et caractérisations de nanostructures à base de $MoS_2$ et leurs applications pour le captage de l'énergie solaire et la photocatalyse

Par

**Driss MOULOUA**

Thèse présentée pour l'obtention du grade
de Philosophiae Doctor (Ph.D)
en Sciences de l'énergie et des Matériaux

**Jury d'évaluation**

| | |
|---|---|
| Président du jury et<br>Examinateur interne | Dr. François Piquemal<br>LNE, Paris, France |
| Examinateur externe | Dr. Xavier Wallart<br>CNRS-IEMN, Lille, France |
| Examinateur externe | Dr. Dominique Mangelinck<br>CNRS-IM2NP, Marseille, France |
| Examinateur interne | Dr. Franck Dahlem<br>Université de Grenoble, France |
| Examinateur interne | Prof. Sébastien Saitzek<br>Université d'Atrois, France |
| Directeur de recherche | Prof. My Ali El Khakani<br>INRS-EMT, Varennes, QC, Canada |
| Codirecteur de recherche | Prof. Mustapha Jouiad<br>UPJV-LPMC, Amiens, France |
| Codirecteur de recherche | Prof. Mimoun El Marssi<br>UPJV-LPMC, Amiens, France |

*À tous les enseignants qui ont éclairé mon chemin académique de leur sagesse et de leur dévouement, je dédie cette thèse. Leur enseignement exceptionnel a été la boussole qui a guidé mes pas vers ce parcours doctoral, et je suis profondément reconnaissant de leur impact inestimable sur mon développement académique. Merci pour votre inspiration et votre soutien constant.*

# RÉSUMÉ

Au cours de la dernière décennie, les matériaux bidimensionnels tels que le disulfure de molybdène (2D-$MoS_2$) ont clairement démontré un réel potentiel pour les dispositifs photoniques et optoélectroniques futurs en raison de leurs excellentes propriétés électriques et optiques.

Suite à l'essor de cette classe de matériaux, le présent travail de thèse vise à étudier les effets de deux approches de synthèse, à savoir le dépôt chimique en phase vapeur (CVD) et le dépôt par ablation laser pulsé (PLD), sur les propriétés optoélectroniques des nanostructures de $MoS_2$. Nous démontrons que le processus CVD est le plus approprié pour produire une variété de morphologies de $MoS_2$ incluant des microplaques de 1-30 µm de taille jusqu'à des nanofils hautement cristallins de ~100 nm de diamètre en contrôlant la position du substrat dans l'enceinte CVD. Par ailleurs, la position du substrat s'est avérée un paramètre important pour l'ingénierie de la bande interdite du MoS2, ce qui a conduit à une amélioration tangible de la photoréponse de ~ 20000 % et une détectivité de $2.6 \times 10^9$ Jones tout en réduisant le temps de réponse des photodétecteurs développés à base de nanostructures de $MoS_2$. Sur la base de ces résultats, la CVD a été ajustée pour fabriquer une hétérostructure de microfibres/microfleurs de $MoS_2/MoO_2$ qui a été intégrée dans un dispositif de photodétection. Le dispositif a montré une photoréponse intéressante à large bande attribuée aux effets synergiques du $MoS_2$ et du $MoO_2$.

D'autre part, le processus PLD a permis la fabrication de films de $MoS_2$ sur de grande surface, avec un degré de cristallinité élevée et un contrôle de l'épaisseur. Nos résultats soulignent le rôle critique joué par la température de dépôt sur le contrôle de l'orientation des couches de $MoS_2$. Le dispositif photoconducteur basé sur ces films a présenté une relation constante plus linéaire avec le degré d'alignement vertical des structures de $MoS_2$, atteignant une photoréponse et une détectivité de 1500% et $9.2 \times 10^9$ Jones, respectivement.

Les très bonnes performances de photodétection obtenues sont attribuées au très faible courant d'obscurité obtenu dans les nanostructures de $MoS_2$ CVD et au rendement élevé du photocourant pour les échantillons PLD.

Profitant de la très bonne photoconversion de ces nanostructures de $MoS_2$, une structure hybride 1T-$MoS_2$/2H-$MoS_2$ a été développée en utilisant la fabrication CVD en une étape, utilisée par la suite pour les tests de photodégradation du bleu de méthylène. Cette hétérostructure hybride a montré une efficacité de photodégradation de plus de 80% du bleu de méthylène à une constante de photodégradation très élevé obtenues sous les excitations UV et visibles.

Cette thèse propose différents scénarios pour permettre et promouvoir les capacités du $MoS_2$ dans le captage de lumière à large bande tout en réalisant une photoconversion élevée en termes de porteurs de charge qui peuvent être exploités dans deux applications majeures telles que la photodétection et la photodégradation.

**Mots-clés**: $MoS_2$, dépôt chimique a phase vapeur, dépôt par ablation laser, photodétection, photocatalyse

# ABSTRACT

In the last decade, two dimensional materials such molybdenum disulfide (2D-$MoS_2$) have clearly proven a real potential for the next generation of photonic and optoelectronic devices owing to their excellent electrical and optical properties.

Following the surge of this class of materials, the current thesis work aims at investigating the effects of two synthesis approaches namely chemical vapor deposition (CVD) and pulsed laser deposition (PLD) on the optoelectronic properties of $MoS_2$ nanostructures. We demonstrate that the CVD process is most appropriate to yield a variety of $MoS_2$ morphologies including microplates 1-30 µm in size to highly crystalline nanowires of ~100 nm in diameter by monitoring the CVD process through the control of the substrate position. Moreover, the control of the substrate position is found to be beneficial in engineering the $MoS_2$ band gap leading to tangible enhancement of the photoresponse of ~ 20000 % and a detectivity of $2.6 \times 10^9$ Jones while reducing the response time of the developed photodetectors based $MoS_2$ nanostructures. Based on these findings, the CVD was further tuned to fabricate $MoS_2/MoO_2$ microfiber/microflower heterostructure that was integrated into photodetection device. The device has shown an interesting broadband photoresponse ascribed to the synergic effects of both $MoS_2$ and $MoO_2$.

On the other hand, the PLD process has allowed the fabrication of large scale $MoS_2$ films, with high crystallinity and thickness control. Our finding emphasizes the critical role played by the deposition temperature in controlling the orientation of $MoS_2$ layers. The photoconductive device based on these films has exhibited a constant-plus-linear relationship with the degree of vertical alignment of the $MoS_2$ structures, achieving a photoresponse and a detectivity of 1500% and $9.2 \times 10^9$ Jones, respectively.

The very good photodetection performances obtained are attributed to the very low dark current obtained in CVD $MoS_2$ nanostructures and to the high photocurrent yield for the PLD samples.

Taking benefit of the very good photoconversion of $MoS_2$ nanostructures, a hybrid 1T-$MoS_2$/2H-$MoS_2$ heterostructure was developed using one step CVD fabrication, used for methylene blue photodegradation. This hybrid heterostructure has shown more than 80% photodegradation of methylene blue at a high rate-constant in both UV and visible excitations.

The thesis provides various scenarios to enable and promote the $MoS_2$ capabilities in broadband light harvesting while achieving high photoconversion in term of valuable charge carriers that can be exploited in two major applications such as the photodetection and the photodegradation.

**Keywords:** $MoS_2$, chemical vapor deposition, pulsed laser deposition, photodetection, photocatalysis

# ACKNOWLEDGMENT

I begin by expressing my sincere gratitude to God, Allah, the Almighty, whose guidance and blessings have illuminated my path throughout this transformative journey of knowledge and discovery.

A profound transformation has marked my entire life, as I extend special thanks to my research supervisor, Professor My Ali El Khakani from the Institut National de la Recherche Scientifique in Quebec. Under your guidance and mentorship, my intellectual journey has been remarkably enriched, and I am profoundly grateful for the depth of insights and expertise you have shared. Your invaluable contributions have not only shaped my research endeavors but have also left a lasting impact on my personal and academic growth.

To my esteemed thesis supervisors, Professor Mustapha Jouiad and Professor Mimoun El Marssi from Picardie Jules Verne University, your unwavering mentorship, expertise, and encouragement have been pivotal in shaping this research. I am truly fortunate to have had the privilege of working under your guidance.

I express my heartfelt appreciation to Mr. François Piquemal, Senior Research Director at LNE, Paris, for graciously accepting the role of chairing my thesis jury and to be an examiner of this thesis. Your support and presence in this endeavor are deeply valued.

My gratitude extends to Mr. Xavier Wallart, Research Director CNRS, IEMN, Lille, for agreeing to serve as a rapporteur for this work and for contributing valuable insights as a jury member.

I am also thankful to Mr. Dominique Mangelinck, CNRS Research Director, IM2NP, Marseille, for accepting the role of rapporteur for my thesis. Your expertise and feedback are invaluable to me.

Mr. Franck Dahlem, lecturer at the University of Grenoble Alpes, deserves appreciation for agreeing to be an examiner of this thesis and dedicating time and expertise to its evaluation.

I extend my thanks to Mr. Sébastien Saitzek, Professor at the University of Artois, for graciously agreeing to be an examiner of this thesis.

Heartfelt appreciation goes to my parents and my brother. You are the source of my happiness, and making you proud is the greatest feeling I can have. I love you all dearly.

To my soulmate, Ghizlane, discussing with you is the best hobby I have ever discovered. I love you.

To all friends, family, and colleagues who supported me throughout this journey, your encouragement and understanding were indispensable. I am deeply grateful for your unwavering support.

Lastly, I extend my thanks to all those whose names may not be mentioned here but who have contributed, in one way or another, to the successful completion of this thesis.

This work would not have been possible without the collective support and collaboration of each one of you. Thank you for being a vital part of this significant chapter in my academic journey.

# TABLE OF CONTENTS

**List of Tables** ........ ix
**List of Figures** ........ x
**Introduction** ........ 1
**Chapter 1 : State of the art of $MoS_2$ based nanostructures** ........ 5
1.1 $MoS_2$ crystal structure ........ 5
1.2 Properties of $MoS_2$ ........ 6
1.3 Fabrication of $MoS_2$ ........ 8
1.4 Application of $MoS_2$ ........ 9
**Chapter 2 : $MoS_2$ based nanostructures for optoelectronic applications** ........ 11
2.1 Principle of photodetection ........ 11
2.2 $MoS_2$ based photodetectors ........ 15
2.3 Optoelectronic properties of $MoS_2$ fabricated by CVD ........ 16
2.4 Optoelectronic properties of $MoS_2$ fabricated by PLD ........ 20
2.5 CVD-$MoS_2$ versus PLD-$MoS_2$ based photodetectors ........ 24
**Chapter 3 : Hybrid 1T/2H-$MoS_2$ for photocatalysis** ........ 26
**Chapter 4 : Résumé de la thèse en Français** ........ 29
4.1. Introduction générale ........ 29
4.2. Nanostructures à base de $MoS_2$ - État de l'art ........ 32
4.3. Photodétecteurs à base des nanostructures de $MoS_2$ ........ 38
4.4. Structure 1T/2H-$MoS_2$ pour la photocatalyse ........ 54
4.5. Conclusion et perspectives ........ 57
**Conclusion and outlouks** ........ 61
**Bibliographie** ........ 65
**Appendix : Characterisation techniques** ........ 71
X-ray diffraction ........ 71
Raman spectroscopy ........ 72
UV-Vis-near IR spectrometer ........ 73
X-ray photoelectron spectroscopy (XPS) ........ 73

Scanning electron microscopy (SEM) .......... 74

Energy dispersive x-ray spectroscopy (EDS) .......... 75

Transmission electron microscopy .......... 75

**Chapter 6: Articles .......... 77**

Article 1: D. Mouloua, A. Kotbi, G. Deokar, K. Kaja, M. EL Marssi, M. A. El Khakani, M. Jouiad, Materials-MDPI. 2021, 14, 3283 .......... 77

Article 2: D. Mouloua, N. S. Rajput, J.-F. Blach, M. Lejeune, M. El Marssi, M. A. El Khakani, M. Jouiad, Mater. Sci. Eng. B 2022, 286, 116035. .......... 78

Article 3: D. Mouloua, N. S. Rajput, S. Saitzek, K. Kaja, K. Hoummada, M. El Marssi, M. A. El Khakani, M. Jouiad, Sci. Rep. 2022, 12, 1. .......... 79

Article 4: D. Mouloua, J. Leblanc-Lavoie, L. Pichon, N.S. Rajput, M. El Marssi, M. Jouiad, and M. A. El Khakani, Submitted to Advanced Optical Materials .......... 80

Article 5: D. Mouloua, M. Lejeune, N. S. Rajput, K. Kaja, M. El Marssi, M. A. El Khakani, M. Jouiad, Ultrason. Sonochem. 2023, 95, 106381 .......... 81

Article 6: D. Mouloua, M. El Marssi, M. A. El Khakani, M. Jouiad, in IEEE EUROCON 2023 - 20th Int. Conf. Smart Technol., 2023, pp. 138–141. .......... 82

# LIST OF TABLES

**Table 2.1: Type of the photodetection mechanism and their characteristics. ....................13**

**Table 2.2: Physical parameters used to probe the optoelectronic performances of a photodetector. ........................................................................................................15**

**Table 2.3: Advantages and limitations of CVD and PLD process toward the fabrication of high performing $MoS_2$ based photodetectors. .....................................................................25**

# LIST OF FIGURES

**Figure 0.1: Evolution of the number of publications on $MoS_2$ in the last ten years ............2**

**Figure 1.1: Polymorphic crystalline structures of $MoS_2$ viewed from different projections 5**

**Figure 1.2: 2D-$MoS_2$ bandgap modulation with the number of layers. Note the bandgap transition from indirect for the multilayer $MoS_2$ to direct for the monolayer $MoS_2$[11]. .......6**

**Figure 1.3: PL spectra of $MoS_2$ as a function of the layer's thickness[12]. ..........................7**

**Figure 1.4: Raman Shift recorded for bulk and few layers $MoS_2$[16]. Note the Raman shift change with increasing layers' number. ....................................................................................7**

**Figure 1.5: Variation of the refractive index and the extinction coefficient of bulk and $MoS_2$ ML in the visible. [18] ..............................................................................................................8**

**Figure 1.6: Common reported $MoS_2$ applications ................................................................9**

**Figure 2.1: Actual applications of photodetectors................................................................11**

**Figure 2.2: Responsivity of Si and InGaAs as a function of wavelengths...........................12**

**Figure 2.3: Different mechanisms of photodetection ..........................................................12**

**Figure 2.4: Schematic of a charge carriers' generation in (a) the absence of illumination (dark current), (b) the presence of light excitation, and (c) resulting J-V curves in dark and under illumination. ...........................................................................................................14**

**Figure 2.5: 2D materials for photodetection applications spanning over wide range of the light spectrum. From left to right, the crystal structure of h-BN, $MoS_2$, black phosphorus (BP), and graphene as well as their respective electronic band's structure[31]. ...............16**

**Figure 2.6: Set up of $MoS_2$ fabrication at different positions inside the CVD system. .......17**

**Figure 2.7: Secondary electron image of $MoS_2$ nanowires.................................................17**

**Figure 2.8: (a) Schematic of a photodetector device, (b) responsivity and detectivity obtained as a function of the substrate position inside the CVD furnace...........................18**

**Figure 2.9: (Top left) SEM image of $MoS_2$/$MoO_2$ heterostructure, (bottom left) overlapping of EDS maps and SEM image, and EDS mapping considering Si, O, Mo and S as markers (scale bar =100 µm). ...........................................................................................................19**

**Figure 2.10: SEM images showing early stages of $MoS_2$/$MoO_2$ microfiber/microflower nucleation (left is the red box zoom out). ..................................................................20**

**Figure 2.11: Schematic of the PLD system used for the fabrication of $MoS_2$ thin films.....21**

**Figure 2.12: Tilted SEM images of as-grown $MoS_2$ deposited by PLD processed at RT (thickness 100 nm) and 700°C (thickness 60 nm). ...............................................................21**

**Figure 2.13: (a) Raman spectra of $MoS_2$ films as a function of $T_d$, (b) schematic of in-plane E12g and out of plane $A_{1g}$ vibration modes of $MoS_2$, (c) [$A_{1g}$]/[$E^1{}_{2g}$] intensity ratio variation as a function of $T_d$. ...........................................................................................................22**

**Figure 2.14: HRTEM image of $MoS_2$ films fabricated at (a) RT and (b-c) 500°C...................23**

**Figure 2.15: (a) Typical $MoS_2$ based photodetector fabricated by PLD at 500°C, (b) halogen lamp spectrum used for the excitation, (c) J-V curve recorded in dark and under illumination. ...........................................................................................................23**

**Figure 2.16: Linear dependence of the optical bandgap of the $MoS_2$ films upon the $[A_{1g}]/[E^1_{2g}]$ ratio. ......24**

**Figure 3.1: (a) HRTEM image and (b) Raman spectroscopy of 1T-$MoS_2$/2H-$MoS_2$ heterostructure......27**

**Figure 3.2: Proposed 1T-$MoS_2$ /2H-$MoS_2$ activity during the photodegradation of MB. .....28**

**Figure 4.1: Principle of XRD mechanism. ......71**

**Figure 4.2: Scattering effects involved in Raman spectroscopy ......72**

**Figure 4.3: Mechanism of XPS analysis......74**

**Figure 4.3: Mechanism of SEM analysis......75**

# INTRODUCTION

The recent decades have witnessed an unprecedented spur in worldwide energy consumption due to a frenetic growth in technology and a continuous increase in the global population. Fossil fuels such as oil, coal, and natural gas were used for years as essential resources to cope with the ever-growing demand for energy. Unfortunately, this practice has led to a dramatic surge in $CO_2$ emissions, which inflected serious pollution risks daunting the future of our planet. To deal with this global environmental threat, governments have resorted to innovative solutions by adopting several strategies based on the use of non-polluting energy resources or/and mitigating the $CO_2$ footprints. For instance, the mass use of renewable energies and the removal of pollutant effluents before their emission into the environment are the two major adopted strategies worldwide.

Green technologies based on solar energy harvesting and photocatalysis are among the most popular methods utilized to limit $CO_2$ emissions. Historically, silicon has been dominantly used as semiconducting material, driving the development of these technologies. Nonetheless, other semiconductors based on III-V materials have been also proposed as a new generation of materials for green energy applications in many areas including photovoltaics, electrocatalysis, and photocatalysis. Despite the great advances made in these directions, the upscaling process of these technologies remains highly costly. A major scientific breakthrough made with the first isolation of graphene in 2004 has changed the rules of the game by introducing a new class of two-dimensional (2D) semiconducting materials with compositional, structural, or interfacial properties. Graphene was the first 2D material with superlative properties. It was found to be harder than steel, exhibiting a very large surface area, and showing high electrical and thermal conductivity better than copper. Furthermore, it is transparent and flexible. The isolation of graphene has prompted scientists to increase their awareness of this class of materials. Since then, a wide range of 2D materials has emerged with various physical properties including insulators, semiconductors, conductors, and superconductors such as boron nitride (hBN), transition-metal dichalcogenides (TMDs), black phosphorene, MXenes, and other Van der Waals heterostructures. In particular, the TMDs family has known a growing interest owing to the ability to modulate their bandgap depending on the number of layers. In particular, molybdenum disulfide ($MoS_2$) is one of the most studied materials in the TMDs family owing to its abundance in nature. $MoS_2$ is also characterized by strong light-matter interaction, high optical absorption of visible light, and high carriers' mobility (200 $cm^2V^{-1}s^{-1}$). All these properties made $MoS_2$ a good candidate for many photocatalytic applications, explaining the continuous rise in the number of publications on $MoS_2$ during the last decade (Figure 0.1).

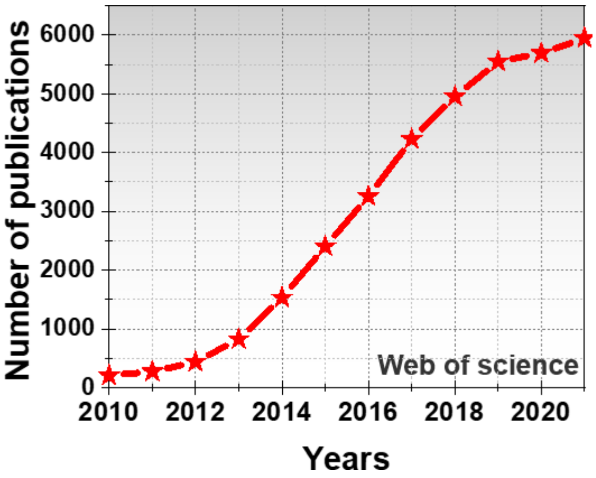

**Figure 0.1: Evolution of the number of publications on $MoS_2$ in the last ten years**

The work in this thesis focuses on the investigation of $MoS_2$ in its pure form and/or associated with other compounds such as $MoO_3$ or $MoO_2$ to enhance its optoelectronic and photocatalytic properties. To achieve this goal, $MoS_2$ films were synthesized via two processing routes, namely chemical vapor deposition (CVD) and pulsed laser deposition (PLD). By investigating the evolving microstructures of $MoS_2$ obtained by these methods, we identified and examined the parameters/mechanisms governing the growth of high-performing $MoS_2$ films with enhanced optoelectronic and photocatalytic properties. The main objectives of the thesis are:

(i) Synthesizing and controlling $MoS_2$ films by CVD and PLD techniques and systematically characterizing the resulting microstructures and morphologies, and performing photoelectrical measurements.

(ii) Identifying and comprehending the correlation between the obtained microstructures and the optoelectronic properties.

(iii) Integrating $MoS_2$ films into photodetection devices, and optimizing their performance.

(iv) Testing $MoS_2$ films in the photodegradation of pollutants such as methyl blue.

(v) Decorating $MoS_2$ films with Ag nanoparticles (NPs) to exploit Ag plasmonic effects for an improved photo conversion.

The chapters of this manuscript are presented in the form of articles, that can be read and explored independently. Each chapter consists of a brief summary highlighting the context and motivation of the study, the methodology, and the key findings, followed by the full version of the article in question.

Chapter 1 introduces the fundamental aspects of $MoS_2$ nanostructures. For instance, the most known $MoS_2$ crystalline structures, the $MoS_2$ relevant processing techniques including their advantages and drawbacks, the $MoS_2$ physical properties, and the $MoS_2$ potential targeted applications. Specifically, the use of $MoS_2$ in optoelectronic devices and in photocatalytic applications is presented.

Chapter 2 is divided into two main sections. The first part is dedicated to the fabrication and control of $MoS_2$ nanostructures exhibiting different microstructures and morphologies using the CVD technique. Based on the physical properties, a microstructure is selected and used for the development of $MoS_2$-based photodetectors. The second part concerns the use of the PLD technique to control the thickness and the crystal quality of high-yield $MoS_2$ thin films (2 inches' square substrate). The optimized structure is evaluated in terms of optoelectronic performances.

The general discussion confronts the outcomes of both CVD and PLD techniques while pointing out the major added values of each processing method toward the development of high-performing photodetectors. The key parameters controlling the yield of each technique will be discussed and recommendations will be drawn.

Chapter 3 is dedicated to the development of hybrid $MoS_2$ thin films used as efficient photo-catalyst. The aim of this chapter is to demonstrate the relevance of the CVD deposition in the fabrication of hybrid microstructure of $MoS_2$, namely of 1T-$MoS_2$/2H-$MoS_2$ heterostructures with high photocatalytic capabilities towards the degradation of methyl blue pollutant.

The conclusion provides a general overview of our findings and methodologies while putting forward the significance of our investigations in the development of new $MoS_2$ nanomaterials via two fabrication methods and their integration into optoelectronic devices used as photocatalysts.

A dedicated outlook on the research avenues that could emerge from this work will be given specifically for the development of photodetectors exhibiting a fast response time.

In particular, we found an interesting perspective that gave rise to a proceeding concerning the association of plasmonic materials with CVD-grown $MoS_2$.

# CHAPTER 1 : STATE OF THE ART OF $MOS_2$ BASED NANOSTRUCTURES

## 1.1 $MoS_2$ crystal structure

Molybdenum disulfide ($MoS_2$) is among the transition-metal dichalcogenides (TMDs) family with the standard formula $MX_2$, where M indicates a transition metal (Mo, W, etc.) and X denotes a chalcogen (S, Se, etc). The bulk $MoS_2$ crystal is a layered material formed by a stack of 0.65 nm thick two-dimensional (2D) layers [1]. Being weakly linked by Van Der Waals forces, these layers can be easily exfoliated using the known mechanical exfoliation method similar to common 2D materials. In the $MoS_2$ structure, $Mo^{+4}$ and $S^{-2}$ ions are arranged in a sandwich stack linked by covalent bonds in a sequence of S-Mo-S. $MoS_2$ exhibit three polymorphic crystalline structures namely: 2H (hexagonal), 3R (rhombohedral), and 1T (tetragonal) that belong, respectively to point groups $D_{6h}$, $C_{3v}$, and $D_{6d}$ as illustrated in figure 1.1. It is worth noting that the 2H-$MoS_2$ structure is considered the thermodynamically stable phase. 2H-$MoS_2$ and 3R-$MoS_2$ structures exhibit a semiconducting behavior[2–4]. Meanwhile, the metastable 1T-$MoS_2$ [5] phase behaves as a metal. Hence, several studies have been dedicated to investigating the phase transition and modulation between 1T-$MoS_2$ and 2H-$MoS_2$ [5–10].

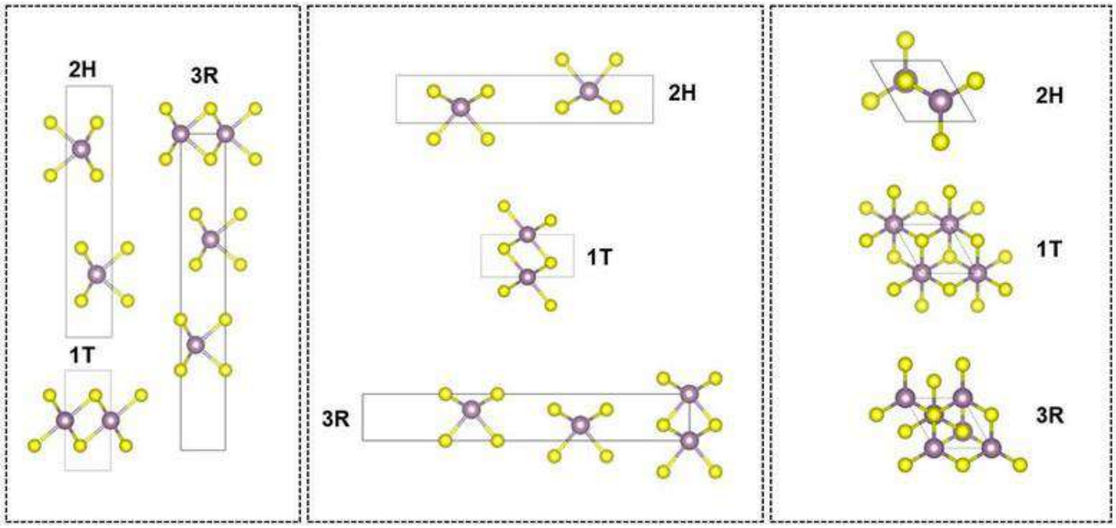

**Figure 1.1: Polymorphic crystalline structures of $MoS_2$ viewed from different projections**

## 1.2 Properties of $MoS_2$

Similar to most TMDs materials, the key advantage of using 2D-$MoS_2$ is the possibility of controlling its bandgap[11]. Unlike the zero-bandgap graphene, the bandgap of $MoS_2$ can be tuned by controlling the number of layers as shown in figure 1.2.

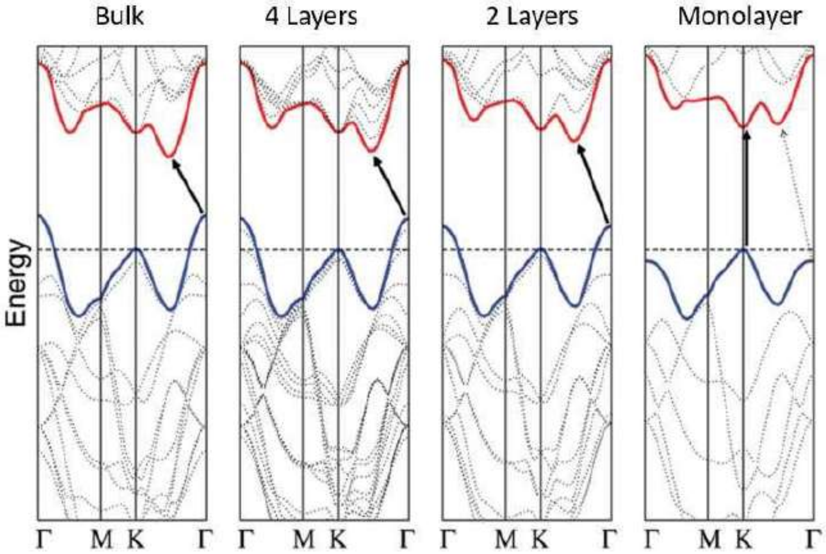

**Figure 1.2: 2D-$MoS_2$ bandgap modulation with the number of layers. Note the bandgap transition from indirect for the multilayer $MoS_2$ to direct for the monolayer $MoS_2$**[11]**.**

In general, the bulk $MoS_2$ (>10 layers) exhibits an indirect bandgap of ~ 1.23 eV, hence it does not systematically show a photoluminescence (PL) response. By contrast, the $MoS_2$ monolayer (ML), has a direct bandgap of 1.88 eV, showing a systematic PL response as illustrated in figure 1.3[12]. Furthermore, the PL spectra of ML-$MoS_2$ show two excitonic peaks that are attributed to the valence band splitting at the K-point (first Brillouin zone) due to the spin-orbit coupling, allowing for two optically active transitions. The first one is observed around ~ 675 nm (exciton: A), while the second one appears at around ~ 625 nm (exciton: B)[4,13,14].

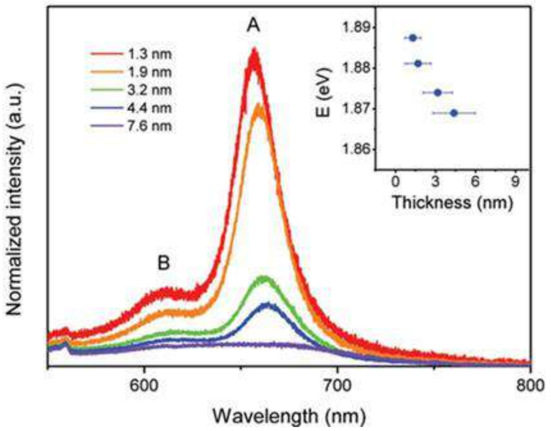

**Figure 1.3: PL spectra of $MoS_2$ as a function of the layer's thickness**[12]**.**

Raman spectroscopy is commonly used as an effective tool to identify the number of layers of 2D-$MoS_2$. The number of layers is obtained by calculating the frequency-shift difference ($\Delta\omega$) between the two characteristic vibrational modes of $MoS_2$[15,16], namely the in-plane $E^1_{2g}$ mode usually appearing in the 383–385 $cm^{-1}$ range, and the out-of-plane mode $A_{1g}$ appearing in the 402–408 $cm^{-1}$ range as shown in figure 1.4.

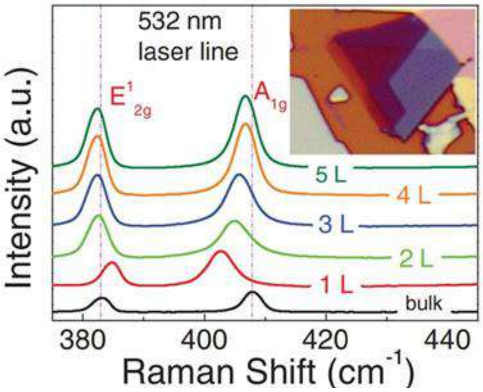

**Figure 1.4: Raman Shift recorded for bulk and few layers $MoS_2$**[16]**. Note the Raman shift change with increasing layers' number.**

For $MoS_2$ ML, $\Delta\omega$ is usually less than 20 $cm^{-1}$, which increases with the increasing $MoS_2$ layers. Furthermore, Raman spectroscopy is also a reliable tool to identify other polymeric forms of $MoS_2$, such as 1T-$MoS_2$ by tracking its characteristic vibrational modes $E_{1g}$, $J_1$, $J_2$, and $J_3$ located at 283, 152, 213, and 330 $cm^{-1}$, respectively[17]. Therefore, Raman spectroscopy is considered a suitable technique for evaluating the phase transitions and the phases ratio of 1T-$MoS_2$/2H- $MoS_2$ [10]. Beyond the bandgap modulation, the number of layers affects the $MoS_2$ optical constants[18] as shown in figure 1.5. The refractive index and the extinction coefficient variations appear different in shape and in value in the full visible range for bulk and ML $MoS_2$.

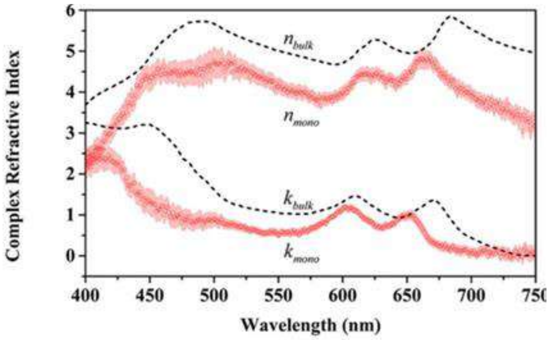

**Figure 1.5: Variation of the refractive index and the extinction coefficient of bulk and $MoS_2$ ML in the visible. [18]**

## 1.3 Fabrication of $MoS_2$

A wide range of fabrication methods was used to produce crystalline $MoS_2$. Mechanical exfoliation, similar to other 2D materials, was among the first synthesis method used to isolate $MoS_2$ samples to be tested for the photoelectric properties[19]. However, this technique does not offer precise control of the thickness and uniformity of the exfoliated flakes[20]. Alternatively, several groups have used chemical exfoliation based on Li-intercalation to generate $MoS_2$ on a centimeter scale[2,21]. This method enables the preparation of $MoS_2$ with high homogeneity but the layers are often altered by the Li-intercalation[12]. Besides, the chemical vapor deposition (CVD) approach has appeared to be one of the most popular processing methods to produce $MoS_2$, at a reasonable cost, with a wide range of morphologies such as planar triangles[22] and vertical nanosheets (NSs)[23]. These morphologies are seen to be useful in enhancing optoelectronic and photocatalytic properties. Nevertheless, the issue of CVD resides sometime in the purity of the films that may occur due to the incomplete reaction of precursors and secondary chemical reactions that are difficult to control[24]. In contrast, physical vapor deposition (PVD) approaches have shown great potential in terms of generating continuous, stoichiometric, and large-area due to their ability to transfer stoichiometry from the target to the substrate[25]. The PVD has shown strong repeatability and material property control[26]. PLD process for example has shown great potential for the fabrication of $MoS_2$ with a good crystalline quality and high thickness control[27]. Meanwhile, the PLD's relatively high cost is still the main drawback of this process[28].

## 1.4 Application of $MoS_2$

$MoS_2$ was first used as a solid lubricant in the form of nanoparticles of a few nanometers in diameter due to its good lubricating properties and thermal stability up to 350°C in an aggressive environment[29]. However, the 2D-materials revolution beyond graphene has prompted the emergence of $MoS_2$ in many applications. For example, due to its high optical absorbance and low dark current, $MoS_2$ was seen as a good candidate to be used as a photodetector[30]. Additionally, the ability to fabricate various heterostructures-based $MoS_2$ was extremely useful for the development of new photodetectors with a broadband response from UV to near IR range[31].

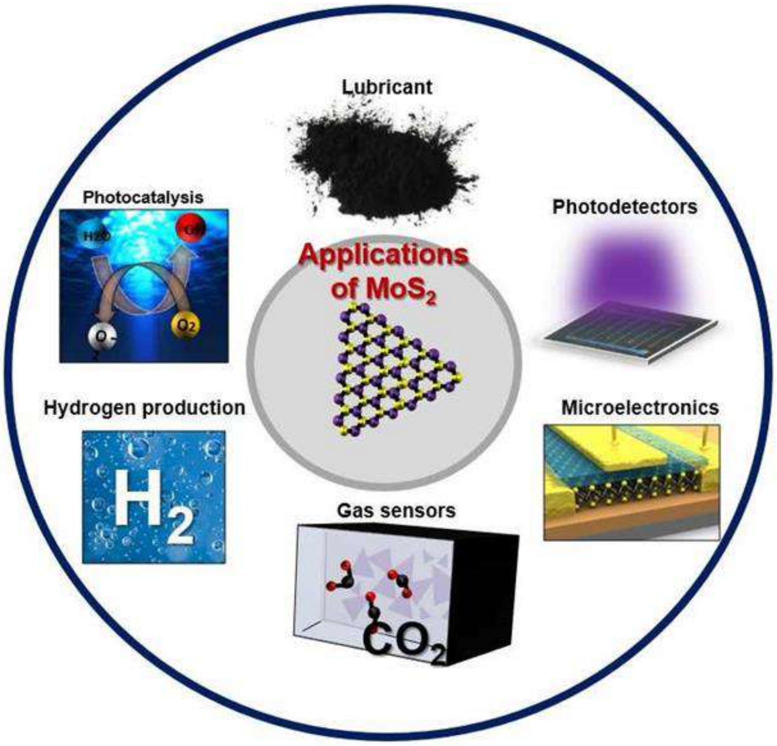

Figure 1.6: Common reported $MoS_2$ applications

Besides, many strategies have been adopted to boost its performance via enhancing its optical absorption and charge transfer using metal nanoparticles[32], doping[33], and its use in conjunction with other Van Der Waals heterostructures[34]. Moreover, $MoS_2$ is considered a good candidate for microelectronics due to its high carrier mobility, leading to high current on/off ratios[35,36], and a very interesting material for gas sensing due to its high surface area[37]. In addition, $MoS_2$-based photocatalyst has become very exciting solution for the hydrogen production and photocatalytic applications owing to its suitable band gap for visible-light harvesting. Several investigations have been reported on the use of $MoS_2$ in many applications such as water splitting [38], photodegradation[39], and dye solar cells[40], etc. as summarized in figure 1.6. Article 1 constitutes the background of the thesis. It provides a detailed overview of the fabrication, characterization, and most relevant recent applications of $MoS_2$.

# CHAPTER 2 : MOS$_2$ BASED NANOSTRUCTURES FOR OPTOELECTRONIC APPLICATIONS

## 2.1 Principle of photodetection

Photodetectors are critical components of optoelectronic devices that use semiconductor materials to convert absorbed light into electrical signals. Generally, photodetector materials are selected based on the range of light absorption required for the targeted application. Hence, the photodetector operates in a specific wavelength range. However, photodetectors-based heterostructures can be designed for broadband photodetection. Figure 2.1 shows the most popular applications based on photodetectors.

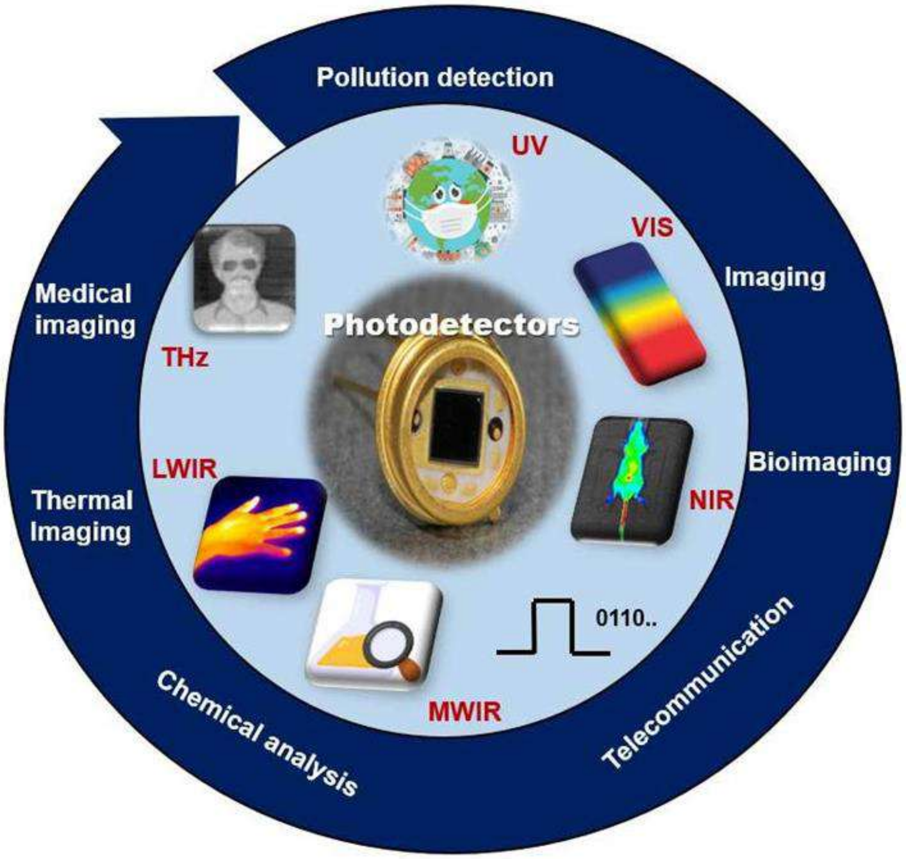

**Figure 2.1: Actual applications of photodetectors**

Figure 2.2 depicts the responsivity of a commercialized photodetector device based on Si and InGaAs, showing its dependency on the bandgap of the material-based photodetector thereby influencing its application range. This explains the wide acceptance of using Si for photovoltaic applications as opposed to InGaAs, which are popularly used in communication applications.

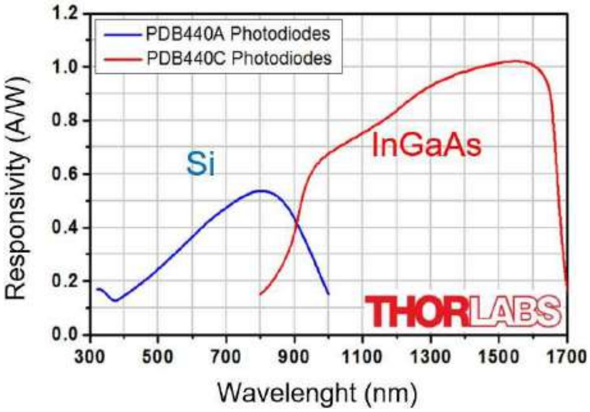

**Figure 2.2: Responsivity of Si and InGaAs as a function of wavelengths**

The process of light harvesting and photoconversion in photodetectors is based on two major known mechanisms. Namely, a thermal energy conversion process based on the photo-thermoelectric effect, and conversion based on the optical excitation generating an electric field, which includes photovoltaics, photoconducting, and photogating effects as illustrated in figure 2.3.

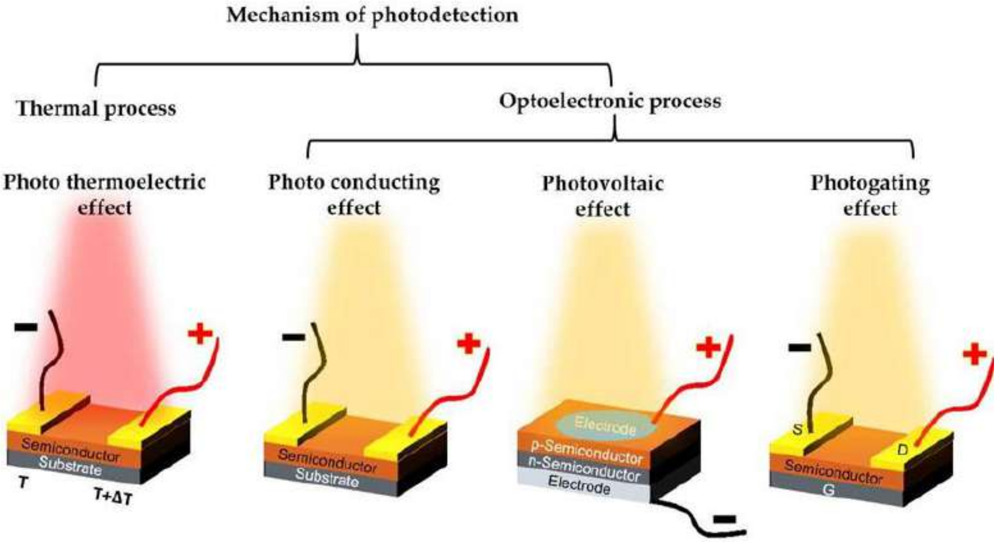

**Figure 2.3: Different mechanisms of photodetection**

Usually, technological choices are mainly dictated by the desired application. On the one hand, photoconductor-based devices are the most commonly used ones owing to their facile fabrication. This technology requires high crystalline semiconductor films possessing high optical absorption and a good susceptibility to electron-hole pairs formation. Nonetheless, the high dark current and the need for an external bias remain the significant drawbacks of this technology. Photovoltaic-based devices, on the other hand, are the most efficient due to the low dark current obtained at zero bias due to the internal built-in electric field by the p-n junction. Table 2.1 summarizes the aforementioned photoconversion effects showing their advantages and their limitations.

**Table 2.1: Type of the photodetection mechanism and their characteristics.**

| Mechanism | Characteristics | Advantages | Limitations |
|---|---|---|---|
| Photo thermo-electric effect | Temperature difference induces the Seebeck effect resulting on photogenerated carriers | No external bias | Detection in a specific range |
| Photoconductive effect | Photogenerated carriers are triggered by an externally applied field changing the device's conductivity. | Simple; flexible devices | Require an external bias; high dark current |
| Photovoltaics effect | Photogenerated carriers are generated by a built-in electric field due to the p-n junction. | No external bias; Low dark current | Tedious fabrication; costly |
| Photogating effect | Trapped carriers in localized states act as an additional local gate, modulating channel conductance. | Broadband, and fast response; Low dark current | Tedious fabrication; costly; Require an external Bias |

Figure 2.4 illustrates the mechanism of the photoconduction involved in a semiconductor when it generates excess free charge carriers by absorbing photons. The energies of photons are generally greater than the band gap, resulting in an increase in electrical conductivity. Figure 2.4a depicts the basic design of a photoconductor, which consists of a semiconductor with two metal contacts. The dark current is measured in the absence of excitation. When the device is exposed

to photons with energies greater than its band gap, the photogenerated excitons (electron-hole pairs) are created and their separation and mobility are ensured by an applied bias, as shown in Figure 2.4b. The difference between the light and dark currents allows for determining the photocurrent value and thus the optoelectronic performances of the device (e.g., Fig 2.4c).

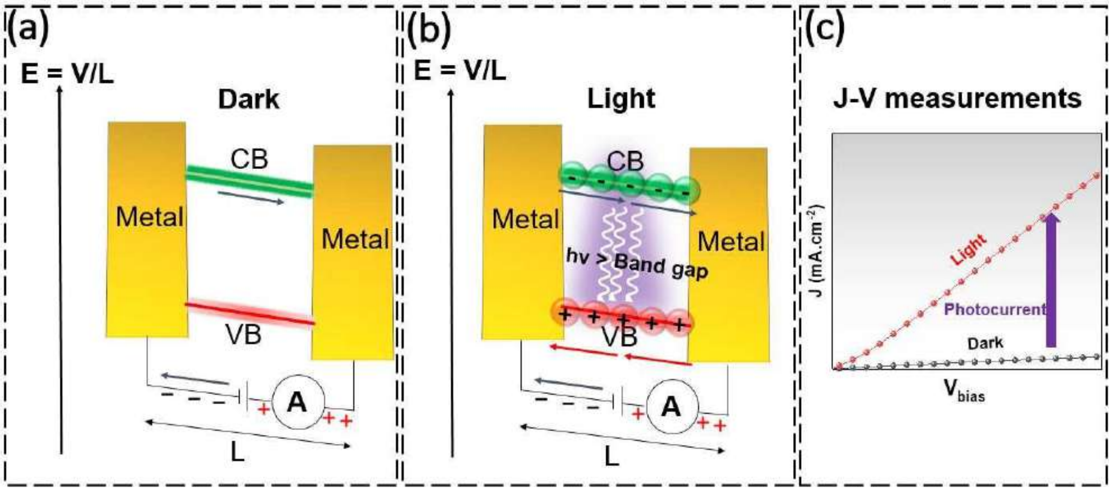

**Figure 2.4: Schematic of a charge carriers' generation in (a) the absence of illumination (dark current), (b) the presence of light excitation, and (c) resulting J-V curves in dark and under illumination.**

The performance of a photodetector consists of assessing its dark current ($I_d$) measured in the absence of any external illumination for a given duration until stability is reached. The significance of the Id stems from the basic operation of a photodetector consisting of evaluating its photoresponse, which is defined as the ratio between the photo-generated carriers induced by the light excitation indicated by a photocurrent ($I_{Ph}$) and the intrinsic carriers displayed by Id. These measured currents are further utilized to calculate the responsivity (R) and the specific detectivity (D*). R indicates the photodetector's sensitivity towards the generation of $I_{Ph}$ for a given incident power and D provides an overall evaluation of the device's performance. The response time (τ) is another parameter used to evaluate how fast a photoresponse is obtained and the quantum efficiency (EQE) translates the ratio between the generated carriers and the incident photons (e.g.,Table. 2.2).

**Table 2.2: Physical parameters used to probe the optoelectronic performances of a photodetector.**

| Parameter | Formula | Unit | Description |
|---|---|---|---|
| **Dark current** | $I_d$ | A | Current measured without illumination |
| **Photocurrent** | $I_{Ph}= I - I_d$ | A | The current difference between the light on and the light off |
| **Photoresponse** | $100xI_{Ph}/ I_d$ | % | The ratio of the photocurrent to the dark current |
| **Responsivity** | $R= I_{Ph}/P$ | A/W | The ratio of the photocurrent with respect to the excitation power |
| **Detectivity** | $D^*= R/(2e\lambda I_d)^{0.5}$ | Jones | The capacity of a photodetector to capture the weakest signals |
| **EQE** | $100hc\, I_{Ph} / e\lambda P$ | % | The ratio of the number of charge carriers collected by the photodetector to the number of photons of a given power. |
| **Response time** | $\tau_r$ and $\tau_d$ | s | Elapsed time to rise the photocurrent from 10 to 90% or to decay current from 90% to 10% |

## 2.2 MoS₂ based photodetectors

To evaluate its optoelectronic properties, pure $MoS_2$ was integrated, alone or combined with other compounds, into photodetector devices followed by photoelectrical measurements. A plethora of strategies has been reported in the literature to improve the photodetection efficiency of $MoS_2$-based devices. Most strategies relied on boosting the optical absorption and carrier mobility of $MoS_2$ including its use in hybrid heterostructures[34,41], or with plasmonic nanostructures[42,43]. The enhancement of the optoelectronic properties of MoS2 was also reported to be achieved by chemical doping[33] and surface functionalization[31]. In this sense, we have employed two different fabrication approaches CVD and PLD to yield to various $MoS_2$ nanostructures in terms of microstructure, morphology, size and shape to be linked to the optoelectronic performances. The CVD approach was chosen because of its ability to generate high crystalline $MoS_2$ with different morphologies[44–46], while the PLD process was employed to fabricate high-quality $MoS_2$ thin films with thickness control[47]. Owing to their very low thickness (atom-thick materials), a very low dark current is expected in 2D materials, which would dramatically improve their photoresponse. Based on their respective band gap values, these materials hold great potential for the next photodetectors generation, as presented in Figure 2.5. In particular, $MoS_2$ has generally been employed for UV and visible photodetection. Meanwhile, many $MoS_2$-based heterostructures have been reported to extend its performance into a broadband photodetection range.

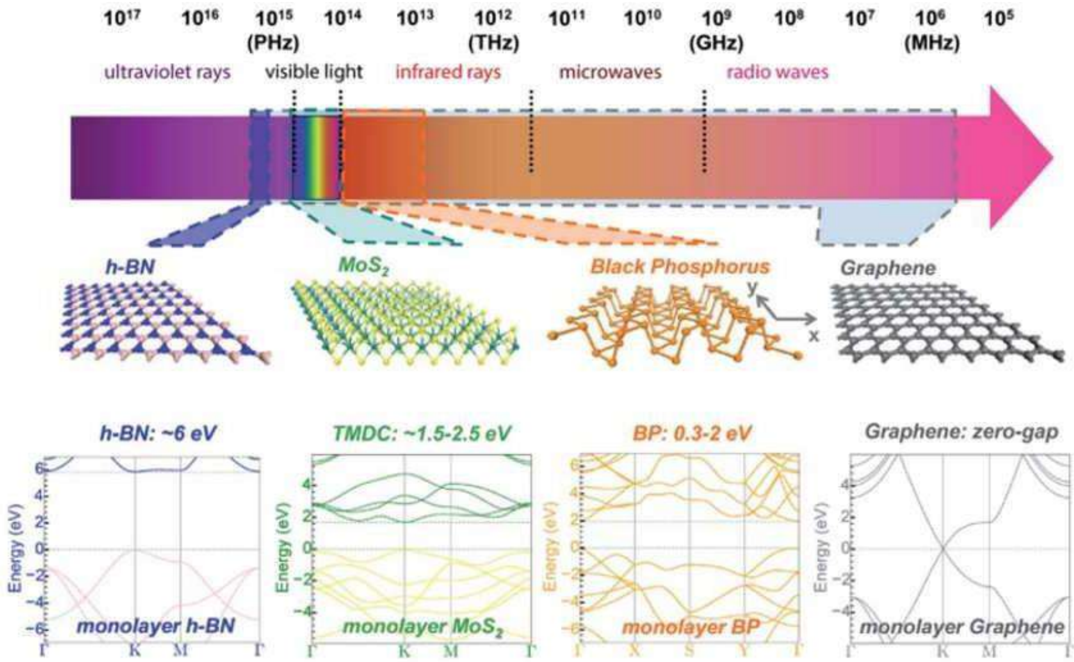

**Figure 2.5: 2D materials for photodetection applications spanning over wide range of the light spectrum. From left to right, the crystal structure of h-BN, $MoS_2$, black phosphorus (BP), and graphene as well as their respective electronic band's structure**[31]**.**

## 2.3 Optoelectronic properties of $MoS_2$ fabricated by CVD

### 2.3.1 Effect of the substrate position

The morphology of the material used in a photodetector has proven to significantly affect the enhancement of its performance. Many efforts have been devoted to fabricate $MoS_2$ with various shapes such as planar flakes[48], vertical NSs[37], microfibers[46], and nanowires[45]. For instance, CVD-fabricated vertical $MoS_2$ NSs exhibited a light emission behavior similar to that of mechanically exfoliated ML $MoS_2$ over a large area (2 $cm^2$)[23]. The vertical alignment of $MoS_2$ provides an ideal edge-terminated structure, exposing a large number of active sites leading to a similar behavior to ML $MoS_2$. Considering these interesting reported data, we have developed a strategy to control and monitor the growth conditions using the CVD system by identifying the key parameters influencing the fabrication process. For this, the collecting substrate was placed in different positions inside the tube furnace of the CVD system (e.g., Fig 2.6) to examine the effect of the substrate position on the growth of MoS2 structures and on their morphologies.

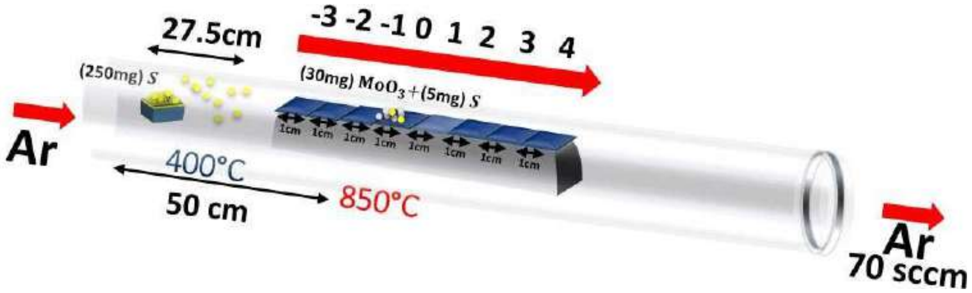

**Figure 2.6: Set up of $MoS_2$ fabrication at different positions inside the CVD system.**

As a result, $MoS_2$ and $MoS_2/MoO_2$ heterostructures with various morphologies were obtained simultaneously depending on the position of the collecting substrate. In particular, the $MoS_2/MoO_2$ heterostructure made of highly crystalline nanowires (NWRs) with a 100 nm diameter (e.g., Fig 2.7) has shown high photodetection performance.

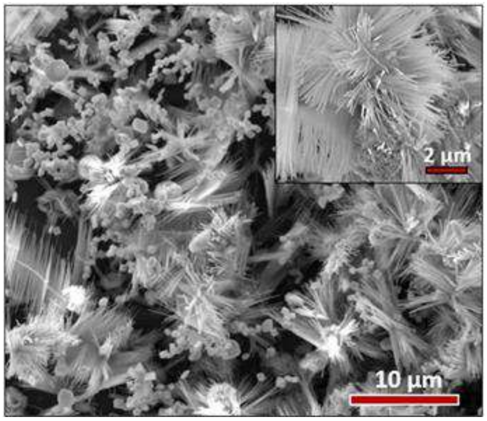

**Figure 2.7: Secondary electron image of $MoS_2$ nanowires.**

Figure 2.8a shows a schematic of the fabricated device. A few nanometers thick Au electrodes were deposited using a metal sputter coating system to lower the contact barrier and improve the charges transport with $MoS_2$. Indeed, when exposed to the illumination of a halogen lamp, $MoS_2/MoO_2$ NWRs have shown the highest photoresponse compared to other microstructures, reaching up to $10^4$ %, a high R of 1.13 mA/W, and a D* of 2.6 $10^9$ Jones at an operating voltage as low as 1V (e.g., Fig. 2.8b).

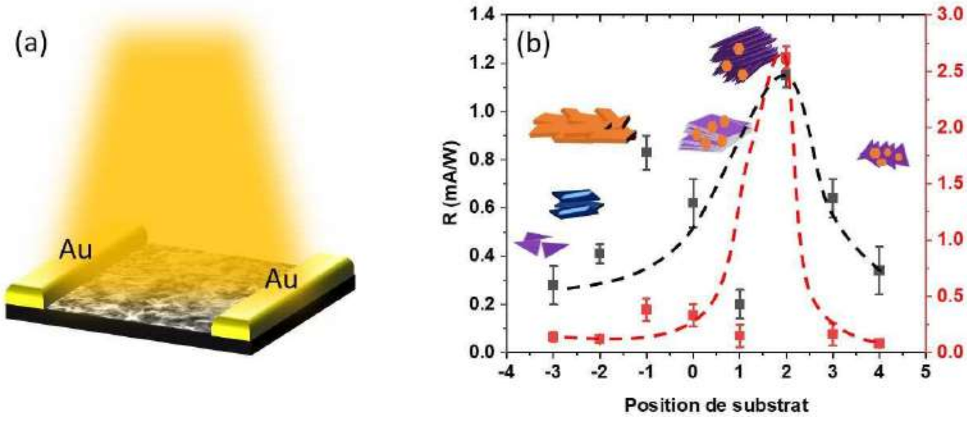

**Figure 2.8: (a) Schematic of a photodetector device, (b) responsivity and detectivity obtained as a function of the substrate position inside the CVD furnace.**

As can be seen from figure 2.8b, the novel shape and morphology (NWRs) of the $MoS_2$ combined with $MoO_2$ has yielded an interesting photoresponse of the photodetector as compared to the literature. Article 2 emphasizes the particular role of the collecting substrate's position in boosting the $MoS_2$ based photodetection performances.

### 2.3.2 Photodetector based $MoS_2/MoO_2$ heterostructure

In light of the previous study, particular attention has been paid to the optimization of $MoS_2/MoO_2$ heterostructures to further enhance optoelectronic performances. In this sense, we have explored the position of the substrate where the heterostructure is often grown but we have made a change in the precursor's preparation. Indeed, a new recipe in terms of the precursor's preparation was used. Namely, a mixture solution of S, $MoO_3$, and ethanol were prepared in order to have a more dispersive solution of the precursor. After sonication, a few droplets of the mixture were added on top of the Si substrate before being introduced into the CVD reactor. The main goal of this protocol was to create multiple nucleation sites of $MoS_2/MoO_2$-based heterostructure. Then, a rapid heating rate was implemented to ensure incomplete sulfurization of MoO3 precursor and therefore secure the fabrication of a high-yield $MoS_2/MoO_2$ heterostructure. Indeed, our result demonstrated the elaboration of a novel $MoS_2/MoO_2$ heterostructure with an interesting morphology consisting of $MoS_2$ microfibers and $MoO_2$ microflowers (e.g., Fig. 2.9). The average diameter of $MoO_2$ microflowers is of a few tens of microns, while the length of $MoS_2$ microfibers can reach up to hundreds of microns impinging in all directions.

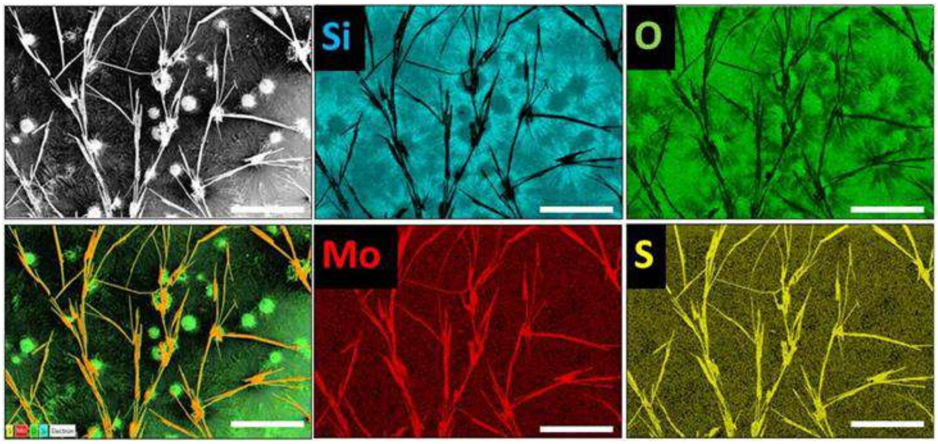

**Figure 2.9: (Top left) SEM image of $MoS_2/MoO_2$ heterostructure, (bottom left) overlapping of EDS maps and SEM image, and EDS mapping considering Si, O, Mo and S as markers (scale bar =100 μm).**

To comprehend the fabrication of $MoS_2/MoO_2$ heterostructure, we have analyzed its microstructure at the early stages of nucleation. Figure 2.10 depicts SEM images showing a few microfibers nucleating at different sites while starting the coalescence process. Due to the precursor preparation, it is expected to have some concentration gradient of the mixture, which is believed to be at the origin of the growth of the $MoO_2$ compound. This diffusing process can result in the formation of $MoO_2$ microflowers.

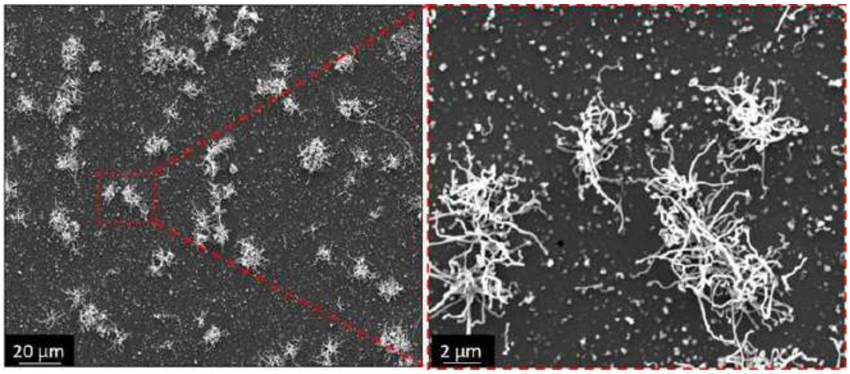

**Figure 2.10: SEM images showing early stages of $MoS_2/MoO_2$ microfiber/microflower nucleation (left is the red box zoom out).**

The obtained heterostructure was subsequently integrated into a photodetection device and evaluated under various wavelength excitations. Interestingly, this heterostructure has exhibited a broadband photoresponse across the 450—630 nm range. The highest R and D* of 0.75 mA/W and $1.45 \times 10^7$ Jones, respectively were obtained under blue light excitation at a very low excitation power of 20 $mW/cm^2$. An extensive study has been carried out on the $MoS_2/MoO_2$ heterostructure summarized in the Article 3.

## 2.4 Optoelectronic properties of $MoS_2$ fabricated by PLD

The PLD is the other approach used for the fabrication of $MoS_2$. The choice of this technique was based on its ability to generate large-scale $MoS_2$ compatible with standard integrated circuit processing, as well as the deposition of $MoS_2$ films. PLD is highly desired for the development of $MoS_2$-based optoelectronic devices with superior performances[49,50], it is unquestionably an appropriate technique in this context, having been successfully used for the deposition of MoS2 ultrathin films onto various substrates, primarily for photodetection applications[27,51]. To examine the influence of the deposition temperature ($T_d$) on the photoresponse of MoS2-based photodetectors, various thin films were prepared at various temperatures. Below, Figure 2.11 depicts a schematic of the PLD system used for the fabrication of $MoS_2$ thin films on Si substrate at room temperature (RT), 300°C, 400°C, 500°C, 600°C, and 700°C using a pulse number $N_{LP}$ = 7000, which corresponds to approximately 100 nm of resulting film thickness.

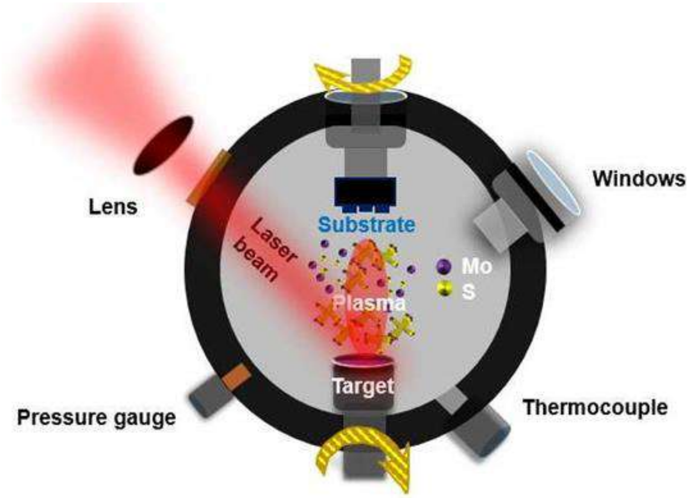

**Figure 2.11: Schematic of the PLD system used for the fabrication of $MoS_2$ thin films.**

In this study, a methodical examination is provided on the effect of $T_d$ on the structure and optoelectronic properties of $MoS_2$ thin films (thickness 100 nm). As a consequence, we were able to identify a film deposition temperature of 500°C that yields highly crystallized and preferentially (002)-oriented $MoS_2$ films with the best photodetection performance and a bandgap of 1.4 eV. Our findings highlight the significance of $T_d$ in influencing not only the crystallinity but also the optoelectronic properties of $MoS_2$ films. Moreover, because $MoS_2$ structures appear to be vertically oriented, the strong photodetection performance of the $MoS_2$ films is comparable to that of a few layers 2D-$MoS_2$. An example of $MoS_2$ thin film surface features deposited by PLD is shown in figure 2.12, consisting of two tilted SEM images of $MoS_2$ structure obtained respectively at RT and 500°C.

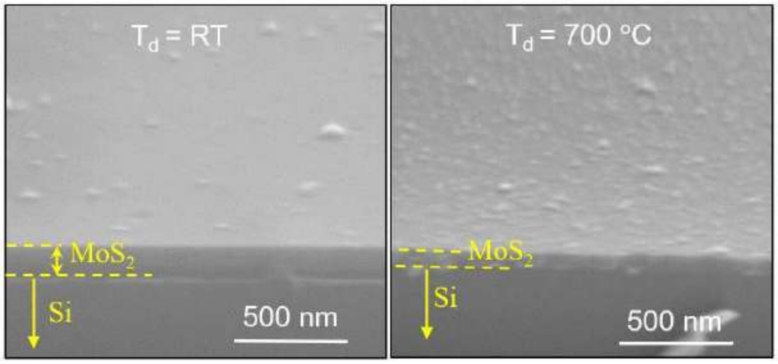

**Figure 2.12: Tilted SEM images of as-grown $MoS_2$ deposited by PLD processed at RT (thickness 100 nm) and 700°C (thickness 60 nm).**

The resulting film thickness appeared to decrease with the increasing $T_d$, from 100 nm to 60 nm, respectively at RT and 500°C. The thickness decrease is mainly due to the temperature- induced crystallization and densification of the films, as previously reported[52]. Moreover, the surface roughness has dramatically augmented at 500°C. Besides, Raman spectra of the $MoS_2$ films as a function of $T_d$ are shown in figure 2.13a.

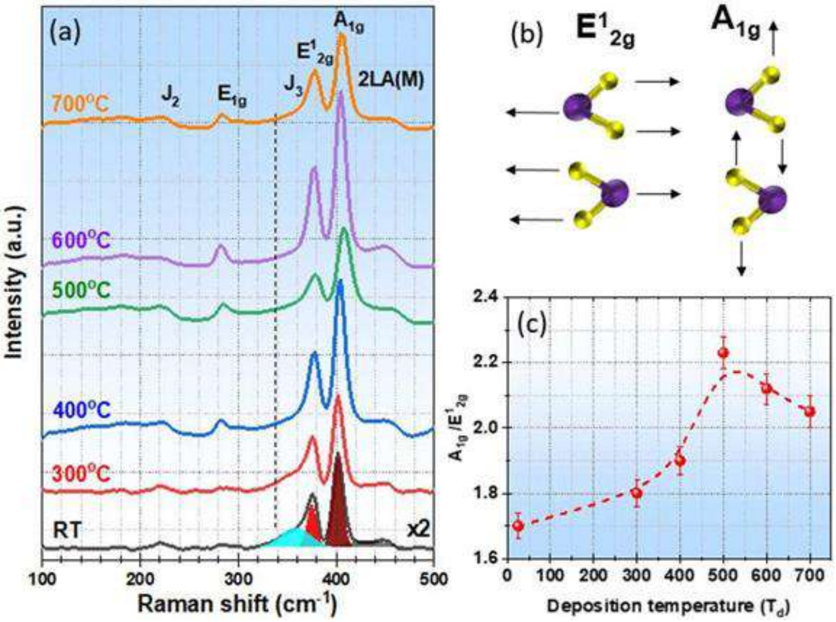

**Figure 2.13: (a) Raman spectra of $MoS_2$ films as a function of $T_d$, (b) schematic of in-plane E12g and out of plane $A_{1g}$ vibration modes of $MoS_2$, (c) $[A_{1g}]/[E^1_{2g}]$ intensity ratio variation as a function of $T_d$.**

Broad peaks representing the vibrational modes of the 2H-$MoS_2$ phase indicated by the $E^1_{2g}$ and the $A_{1g}$ are clearly observed even for the $MoS_2$ films deposited at RT. figure 2.13b shows a schematic image of $E^1_{2g}$ and the $A_{1g}$ mode vibrations for illustration. Because of the improved crystallinity of the films with increasing Td, the characteristic peaks of the 2H-$MoS_2$ phase become narrower and more intense at high Td. Moreover, When the $[A_{1g}]/[E^1_{2g}]$ peak intensity ratio of the $MoS_2$ films is plotted as a function of Td (see Figure 2.13c), it is discovered that the ratio reaches its maximum at $T_d$ = 500°C. The vertical orientation of the $MoS_2$, as revealed by high-resolution transmission electron microscopy (HRTEM) as shown in Figure 2.14, is associated with an increase in the intensity ratio of out-of-plane to in-plane S-atom vibrations. The HRTEM micrographs show a well-crystallized $MoS_2$ film at 500°C where it is amorphous at RT (Figure

2.14a). Interestingly, the $MoS_2$ crystals appeared to nucleate horizontally at the substrate interface and then grow vertically perpendicular to the substrate surface as shown in Figure 2.14b-c.

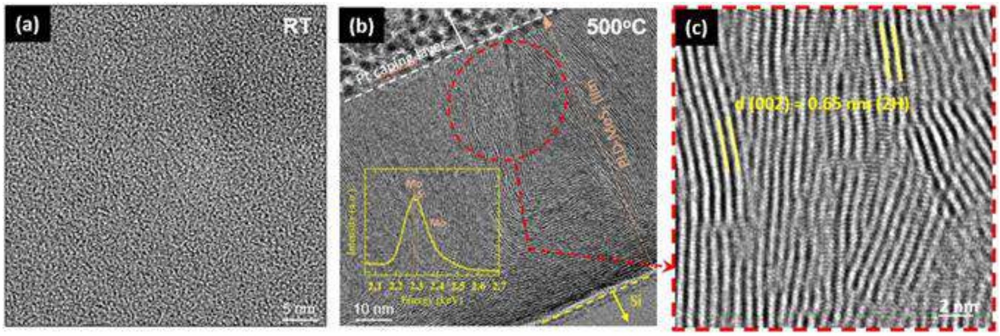

**Figure 2.14: HRTEM image of $MoS_2$ films fabricated at (a) RT and (b-c) 500°C.**

To evaluate the optoelectronic performances of $MoS_2$ samples, the fabricated $MoS_2$ films were integrated into a functional photodetection device (Figure 2.15a) and tested in dark and under illumination. Figure 2.15b shows the halogen lamp spectrum used. Typical results obtained on $MoS_2$ thin films are shown in figure 2.15c. The plot illustrates the J-V curve recorded in dark and under halogen lamp illumination for the best-performing sample fabricated at 500°C.

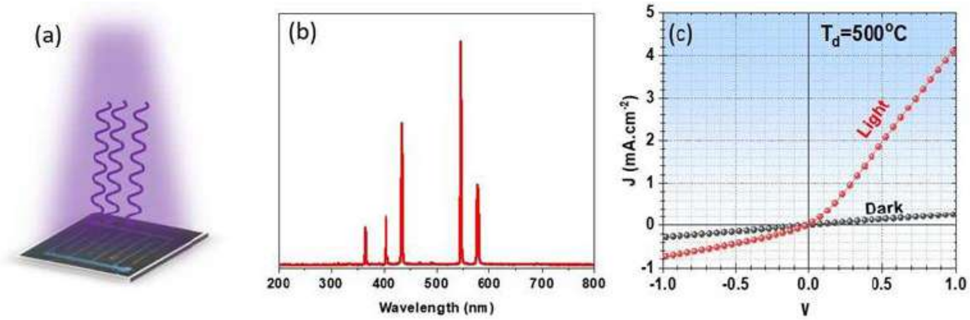

**Figure 2.15: (a) Typical $MoS_2$ based photodetector fabricated by PLD at 500°C, (b) halogen lamp spectrum used for the excitation, (c) J-V curve recorded in dark and under illumination.**

The best device has exhibited a responsivity and a detectivity of 125 mA/W and $9 \times 10^9$ Jones, respectively. Moreover, R (or D*) and the $[A_{1g}]/[E^1_{2g}]$ ratio have a constant-plus-linear relation- ship (see figure 2.16). This clearly shows that the photodetection performance (R and D*) of the $MoS_2$ films linearly scales with the degree of the vertical orientation of the $MoS_2$ sheets in the films. This result demonstrates PLD's enormous potential to obtain high-performing $MoS_2$-based photodetectors as discussed in detail in the Article 4.

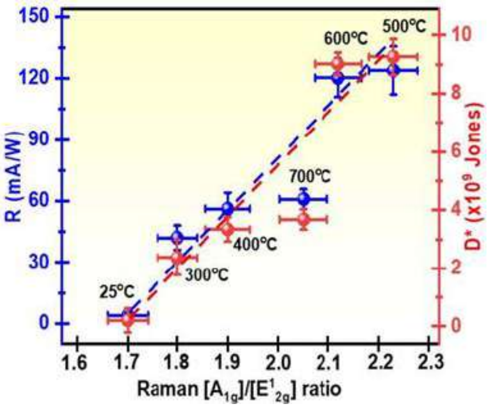

**Figure 2.16: Linear dependence of the optical bandgap of the $MoS_2$ films upon the $[A_{1g}]/[E^1_{2g}]$ ratio.**

## 2.5 CVD-$MoS_2$ versus PLD-$MoS_2$ based photodetectors

Our systematic investigations of the optoelectronic properties of $MoS_2$ nanostructures grown by both CVD and PLD and their in-depth characterizations have enabled us to better comprehend the main benefits and drawbacks of every processing route on the photodetection applications in terms of performances. By tuning various variables influencing the CVD growth of $MoS_2$, we were able to monitor the photodetection performances through the control of the $MoS_2$ crystalline structure and its morphology or even by using it combined with other oxides in the form of the heterostructure. As already discussed previously, the resulting structures have shown high photoresponse and fast response owing to the low dark current and the incident light trapping leading to increased light harvesting. Although the CVD technique has yielded high-performing $MoS_2$-based photodetectors, the low control of the obtained $MoS_2$ nanosheets thickness poses a real challenge. In this sense, the PLD route has appeared as an alternative for controllable $MoS_2$ film thickness as demonstrated. Moreover, an interesting result was obtained using the PLD technique, consisting of its ability to produce vertically aligned $MoS_2$ structures with excellent optical properties. Nonetheless, the density of the $MoS_2$ film has generated a high dark current, limiting the photodetection performances. To capture the advantages and the drawbacks of CVD and PLD toward the fabrication of high-performing $MoS_2$-based photodetectors, we have summarized in Table. 2.3 the outputs of each fabrication process.

**Table 2.3: Advantages and limitations of CVD and PLD process toward the fabrication of high performing $MoS_2$ based photodetectors.**

| Fabrication | Advantages | Limitations |
|---|---|---|
| **CVD** | Morphology control<br>Low dark current<br>High charge transfer | By-products issue<br>High deposition temperature<br>Thickness control |
| **PLD** | Thickness control<br>High photocurrent<br>High phase control | Morphology control<br>High dark current<br>Expensive |

Several concepts could spring to mind considering the comparison between CVD and PLD toward the development of the best performing $MoS_2$-based photodetector that needs further investigations. For instance, the low photocurrent recorded in the $MoS_2$ photodetectors fabricated by the CVD process could be significantly increased by coupling $MoS_2$ excitons with plasmonic metallic nanoparticles[32,43] or using $MoS_2$-based heterostructures in combination with other 2D materials. Besides, one can take also advantage of the $MoS_2$ NWRs beneficial effects on the photoresponse to develop core-shell-based $MoS_2$ NWRs incorporated indirect band gap semiconductors such as III-V materials to further improve the responsivity while achieving the broadband photoresponse[13,42]. This can be also a base for further development using the PLD technique to deposit $MoS_2$ nanostructures on template substrates such as vertical silicon NWRs or metal NPs. This strategy would also benefit to MoS2 deposited by PLD to achieve low dark current due to light trapping as observed with CVD MoS2 NWRs while showing high photocurrent. Additionally, the diameter of $MoS_2$ NPs can be tuned by changing the NLP during the PLD deposition which will be very useful in terms of achieving high photoresponse[53,54]. Furthermore, the ability to fabricate $MoS_2$ at various temperatures using PLD could be of great interest to yield combined phase structures of $MoS_2$[6], which in turn, might enhance the optical absorption and charge carriers' mobility[27].

# CHAPTER 3 : HYBRID 1T/2H-MOS$_2$ FOR PHOTOCATALYSIS

To take advantage of the good broadband light harvesting and conversion of our developed MoS$_2$ nanostructures, we have examined hybrid MoS$_2$ heterostructure made of 2H- MoS$_2$ and 1T- MoS$_2$ toward photocatalytic water decontamination. Indeed, based on previously reported data in the literature, MoS$_2$ was demonstrated to exhibit very interesting photodegradation properties owing to its high optical absorption and large surface area. Hence, we expect to achieve better photodegradation performances of our hybrid sample as they have exhibited high photogenerated current.

Our photodegradation measurements were carried out on methylene blue (MB) organic dye known as one of the major pollutants of drinking water. The selection of MB was based on its high use to dye most fabrics and more importantly, its high toxicity. Some reported data have already showcased the removal of MB using MoS$_2$-based photocatalyst[8,55,56]. However, most of these works suffer from complex processing routes without achieving a significant increase in performance. Hence other strategies have been adopted to accelerate the photodegradation of MB such as the use of hybrid systems based on In$_2$S$_3$ functionalized MoS$_2$[57] or MoS$_2$ doped with nobel metal NPs[8]. Despite the increased performances achieved by these heterostructures, their fabrication methods are costly and require multi-step processes.

Recently, the association of 2H-MoS$_2$ with its polymorph form, i.e., the metallic 1T-MoS2 phase has emerged as an exciting alternative solution to develop high-performing catalyst ascribed to the high carriers mobility in 1T-MoS$_2$ that can be transferred to 2H-MoS$_2$ via Z-scheme mechanism[9,17]. In this sense, using the ability of the CVD fabrication tunability, we have elaborated a high-quality hybrid heterostructure based on 1T-MoS$_2$/2H-MoS$_2$ to be evaluated for MB photodegradation. Figure 3.1a shows HRTEM image of the hybrid 1T-MoS$_2$/2H-MoS$_2$ structure. The heterostructure nature of the fabricated compound is also confirmed by Raman spectroscopy as shown in figure 3.1b. 2H-MoS$_2$ is indicated by $A_{1g}$ and $E^1_{2g}$ vibrational modes located at 405 and 385 cm$^{-1}$, respectively, and the fingerprint peaks of the 1T-MoS$_2$ phase i.e.; $J_1$, $J_2$, $E_{1g}$, and $J_3$ vibrational modes are located at 147, 228, 283, and 330 cm$^{-1}$, respectively, as already reported[6,8].

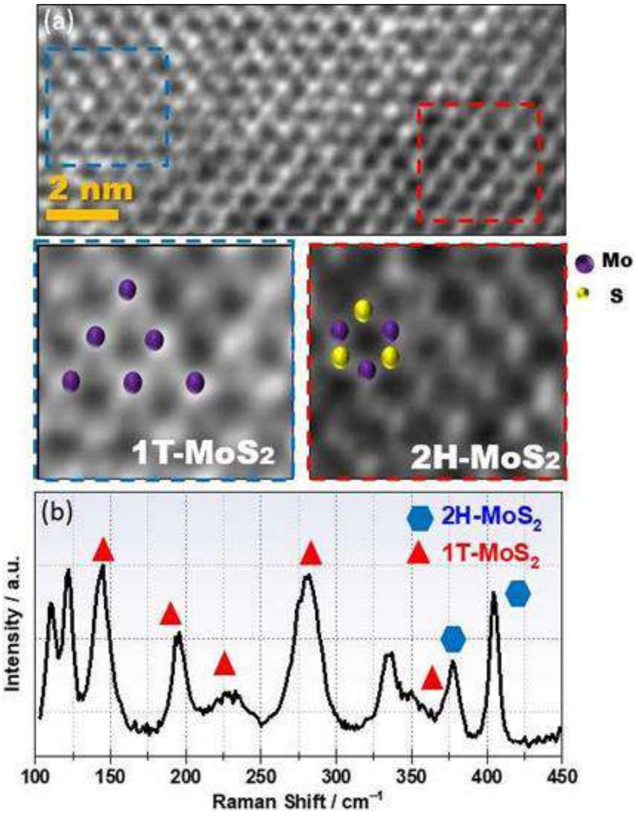

**Figure 3.1: (a) HRTEM image and (b) Raman spectroscopy of 1T-MoS$_2$/2H-MoS$_2$ heterostructure**

Our article describes in more detail the importance of the use of the hybrid 1T-MoS$_2$/2H- MoS$_2$ in the photodegradation of MB. The proposed following photodegradation mechanism underlies the high photocatalytic performance of the 1T-MoS$_2$/2H- MoS$_2$ heterostructure (figure 3.2). According to this mechanism, the 2H-MoS$_2$ phase acts as a photosensitizer whereas the metallic 1T-MoS$_2$ phase acts as a co-catalyst, enhancing carriers transfer. Basically, the electron- hole pairs with a narrow bandgap are photogenerated in 2H-MoS$_2$ under illumination, and the excited electrons from 2H-MoS$_2$ valence band are likely to be trapped by 1T-MoS$_2$ eqn(3.1), hence reducing their recombination rate and extending their lifetime. This is intended to dramatically decrease the recombination of the photogenerated charges, thus extending the redox reaction’s lifetime, which in turn, enables the reduction of $O_2$ molecules to $O_2^*$ eqn(3.2). $O_2$ undergoes multi- electron and proton redox reactions eqns(3.3) and (3.4). The created $OH^*$ molecule participates actively in the photodegradation of MB eqn(3.5).

(3.1) $$1T\text{-}MoS_2/2H\text{-}MoS_2 + h\nu \longrightarrow h^+_{VB} + e^-_{CB}$$

(3.2) $$e^- + O_2 \longrightarrow O_2^{*-}$$

(3.3) $$O_2 + 2e^- + 2H^+ \longrightarrow H_2O_2$$

(3.4) $$H_2O_2 + e^-_{CB} + H^+_2 + h\nu \longrightarrow OH^* + H_2O$$

(3.5) $$O_2^{*-}, OH^*, H^+ + \text{MB Dye} \longrightarrow CO_2 + H_2O + \text{inorganic molecules}$$

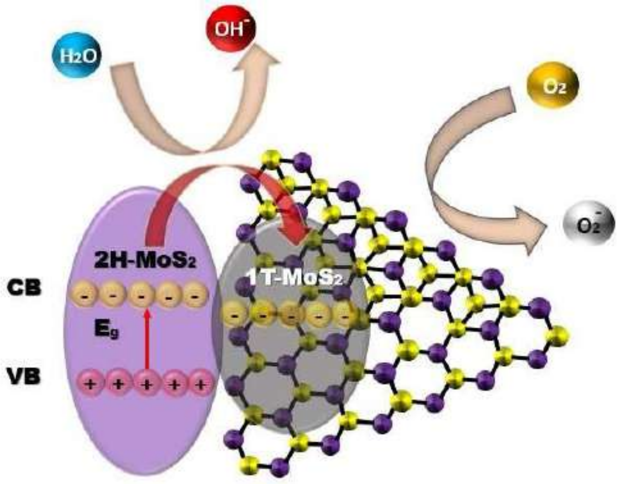

**Figure 3.2: Proposed 1T-MoS$_2$ /2H-MoS$_2$ activity during the photodegradation of MB.**

In contrast to previously reported works in the literature, the present study presented in Article 5 enables the MB photodegradation using a hybrid 1T-MoS$_2$/2H-MoS$_2$ heterostructure fabricated by a one-step CVD process[58], which is demonstrated to achieve more than 80% photodegradation of MB at a rate-constant of $12.5 \times 10^{-3}$ min$^{-1}$ and $9.2 \times 10^{-3}$ min$^{-1}$, under UV and visible light excitations, respectively. This is ~ 1.2 times higher than reported performances in the literature.

Finally, this study allowed us to establish that the intermixing of both phases 1T-MoS$_2$ and 2H-MoS$_2$, using a controlled one-step-CVD fabrication route is a simple way to highly improve the photodegradation of MB and paves the way to the use of this hybrid 1T-MoS$_2$/2H-MoS$_2$ heterostructure in other photocatalysis applications such as water splitting and green hydrogen production.

# CHAPTER 4 : RÉSUMÉ DE LA THÈSE EN FRANÇAIS

## 4.1. Introduction générale

Les dernières décennies ont été marquées par une augmentation sans précédent de la consommation mondiale d'énergie en raison d'une croissance frénétique de la technologie et d'une augmentation continue de la population mondiale. Les combustibles fossiles tels que le pétrole, le charbon et le gaz naturel ont été utilisés pendant des années comme ressources essentielles pour répondre à la demande croissante d'énergie. Malheureusement, cette pratique a entraîné une hausse spectaculaire des émissions de $CO_2$, ce qui a fait peser de graves risques de pollution sur l'avenir de notre planète. Pour faire face à cette menace environnementale mondiale, les gouvernements ont eu recours à des solutions innovantes en adoptant plusieurs stratégies basées sur l'utilisation de ressources énergétiques non polluantes et/ou sur l'atténuation de l'empreinte $CO_2$. Par exemple, l'utilisation massive d'énergies renouvelables et l'élimination des effluents polluants avant leur émission dans l'environnement sont les deux principales stratégies adoptées dans le monde.

Les technologies vertes basées sur la récupération de l'énergie solaire et la photocatalyse sont parmi les méthodes les plus populaires utilisées pour limiter les émissions de $CO_2$. Historiquement, le silicium a été utilisé de manière dominante comme matériau semi-conducteur, ce qui a favorisé le développement de ces technologies. Néanmoins, d'autres semi-conducteurs à base de matériaux III-V ont également été proposés comme une nouvelle génération de matériaux pour les applications énergétiques vertes dans de nombreux domaines, notamment la photovoltaïque, l'électrocatalyse et la photocatalyse. Malgré les progrès considérables réalisés dans ces directions, le processus de mise à l'échelle de ces technologies reste très coûteux. Une avancée scientifique majeure, réalisée avec la première isolation du graphène en 2004, a changé les règles du jeu en introduisant une nouvelle classe de matériaux semi-conducteurs bidimensionnels (2D) dotés de propriétés compositionnelles, structurelles ou interfaciales. Le graphène a été le premier matériau 2D doté de propriétés exceptionnelles. Plus dur que l'acier, le graphène possède une très grande surface spécifique et une conductivité électrique et thermique supérieures à celle du cuivre. En outre, il est transparent et flexible. L'émergence du graphène a incité les scientifiques à s'intéresser davantage à cette classe de matériaux. Depuis lors, une large gamme de matériaux 2D est apparue avec diverses propriétés physiques, notamment des isolants, des semi-conducteurs, des conducteurs et des supraconducteurs tels que le nitrure de bore (hBN), les dichalcogénures de métaux de transition (TMD), le phosphorène noir, les MXènes et d'autres hétérostructures de Van der Waals. En particulier, la famille des TMD a suscité un intérêt croissant en raison de la possibilité de moduler leur bande interdite en fonction du nombre de couches. En particulier, le disulfure de molybdène ($MoS_2$) est l'un des matériaux les plus étudiés de la famille des TMDs en raison de son abondance dans la nature. Le $MoS_2$ se caractérise également par une forte interaction lumière-matière, une absorption optique élevée dans le visible et une mobilité élevée des porteurs (200 $cm^2V^{-1}s^{-1}$). Toutes ces propriétés ont fait du $MoS_2$ un bon candidat pour de nombreuses applications dans la conversion de la lumière et la photocatalyse, ce qui explique l'augmentation continue du nombre de publications sur le $MoS_2$ au cours de la dernière décennie (Fig. 0.1).

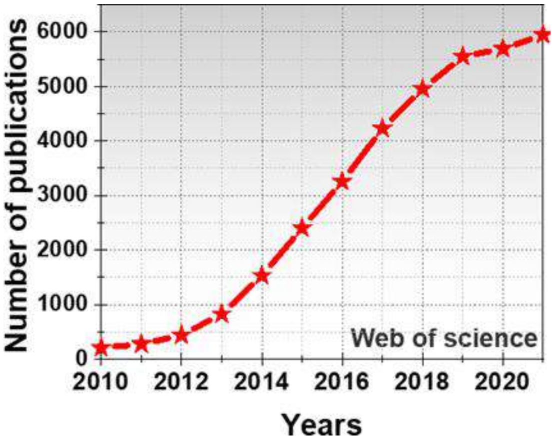

**Figure 0.1. Nombre de publications sur le $MoS_2$ au cours des dix dernières années.**

Les travaux de cette thèse portent sur l'étude du $MoS_2$ sous sa forme pure et/ou associé à d'autres composés tels que le $MoO_3$ ou le $MoO_2$ afin d'améliorer ses propriétés optoélectroniques et photocatalytiques. Pour atteindre cet objectif, des films de $MoS_2$ ont été synthétisés par deux voies de traitement, à savoir le dépôt chimique en phase vapeur (CVD) et le dépôt par laser pulsé (PLD). En étudiant les microstructures obtenues du $MoS_2$ par ces méthodes, nous avons identifié et examiné les paramètres/mécanismes régissant la croissance de ces films très performants en termes de propriétés optoélectroniques et photocatalytiques. Les principaux objectifs de ce projet de thèse sont les suivants :

(i) Synthèse et contrôle de films de $MoS_2$ par des techniques CVD et PLD et caractérisation systématique des microstructures et morphologies résultantes, et réalisation de mesures photoélectriques.

(ii) Identification et étude de la corrélation entre les microstructures obtenues et les propriétés optoélectroniques.

(iii) Intégration de films $MoS_2$ dans des dispositifs de photodétection et optimisation de leurs performances.

(iv) Evaluation de ces films pour la photodégradation de polluants tels que le bleu de méthyle.

(v) Décoration de films $MoS_2$ avec des nanoparticules d'Ag afin d'exploiter les effets plasmoniques de l'Ag pour améliorer les propriétés optoélectroniques.

Le manuscrit est présenté sous forme d'articles, qui peuvent être lus indépendamment les uns les autres. Chaque chapitre se compose d'un bref résumé mettant en évidence le contexte et la motivation de l'étude, la méthodologie et les principaux résultats, suivi de la version intégrale de l'article en question.

Le chapitre 1 présente les aspects fondamentaux des nanostructures de $MoS_2$. Par exemple, les structures cristallines de $MoS_2$ les plus connues, les techniques de traitement pertinentes de MoS2, y compris leurs avantages et leurs inconvénients, les propriétés physiques de $MoS_2$ et les applications ciblées potentielles de $MoS_2$. L'utilisation du $MoS_2$ dans les dispositifs optoélectroniques et dans les applications photocatalytiques est plus particulièrement présentée.

Le chapitre 2 est divisé en deux sections principales. La première partie est consacrée à la fabrication et au contrôle de nanostructures de $MoS_2$ présentant différentes microstructures et morphologies à l'aide de la technique CVD. En fonction des propriétés physiques, une microstructure est sélectionnée et utilisée pour le développement de photodétecteurs. La deuxième partie concerne l'utilisation de la technique PLD pour le contrôle de l'épaisseur et la qualité des films minces de $MoS_2$. La meilleure structure sélectionnée, est évaluée en termes de performances optoélectroniques.

Une discussion générale confrontant les résultats des techniques CVD et PLD tout en soulignant les principales valeurs ajoutées de chaque méthode de fabrication pour le développement de photodétecteurs performants. Les paramètres clés contrôlant le rendement de chaque technique seront discutés et des recommandations seront formulées.

Le chapitre 3 est consacré au développement de films minces hybrides de $MoS_2$ destinés à être utilisés comme photocatalyseurs efficaces. L'objectif de ce chapitre est de démontrer la pertinence du dépôt CVD dans la fabrication de microstructures hybrides de $MoS_2$, à savoir des hétérostructures 1T-$MoS_2$/2H-$MoS_2$ avec des capacités photocatalytiques élevées pour la photodégradation du polluant « le bleu de méthyle ».

La conclusion de la thèse donne un aperçu général de nos résultats et méthodologies tout en mettant en avant l'importance de nos recherches dans le développement de nouveaux nanomatériaux $MoS_2$ via deux méthodes de synthèse ainsi que leur intégration dans des dispositifs optoélectroniques ou pour être utilisés comme photocatalyseurs. Une perspective dédiée aux pistes de recherche qui pourraient émerger de ce travail sera donnée spécifiquement pour le développement de photodétecteurs présentant un temps de réponse rapide.

En particulier, nous avons trouvé une perspective intéressante qui a donné lieu à une procédure concernant l'association de matériaux plasmoniques avec le $MoS_2$ CVD.

## 4.2. Nanostructures à base de $MoS_2$ - État de l'art

### 4.2.1. Structure cristalline du $MoS_2$

Le disulfure de molybdène ($MoS_2$) fait partie de la famille des dichalcogénures de métaux de transition (TMD) dont la formule standard est $MX_2$, où M désigne un métal de transition (Mo, W, etc.) et X un chalcogène (Se, S, etc.). Le $MoS_2$ massif est un matériau stratifié formé d'un empilement de couches bidimensionnelles (2D) de 0.65 nm d'épaisseur[1]. Faiblement liées par les forces de Van Der Waals, ces couches peuvent être facilement exfoliées à l'aide de la méthode d'exfoliation mécanique, comme c'est le cas pour la plupart des matériaux 2D. Les ions Mo+4 et S−2 sont disposés dans une structure en sandwich connectés par des liaisons covalentes suivant une séquence S-Mo-S. Le $MoS_2$ se présente sous forme de trois structures cristallines polymorphes, à savoir le 2H (hexagonale), le 3R (rhomboédrique) et le 1T (tétragonale), qui appartiennent respectivement aux groupes de points $D_{6h}$, $C_{3v}$ et $D_{6d}$, comme illustré sur la figure 1.1. Il convient de noter que la structure 2H-$MoS_2$ est considérée comme la phase thermodynamiquement stable. Elle présente un avec la structure 3R-$MoS_2$ un comportement semi-conducteur[2–4]. Par ailleurs, la structure métastable 1T-$MoS_2$ [5] se comporte comme un conducteur. C'est pourquoi plusieurs études ont été consacrées à la transition de phase et à la modulation entre la phase 1T-$MoS_2$ et la phase 2H-$MoS_2$ [5–10] en vue des applications en optoélectroniques et photocatalytiques.

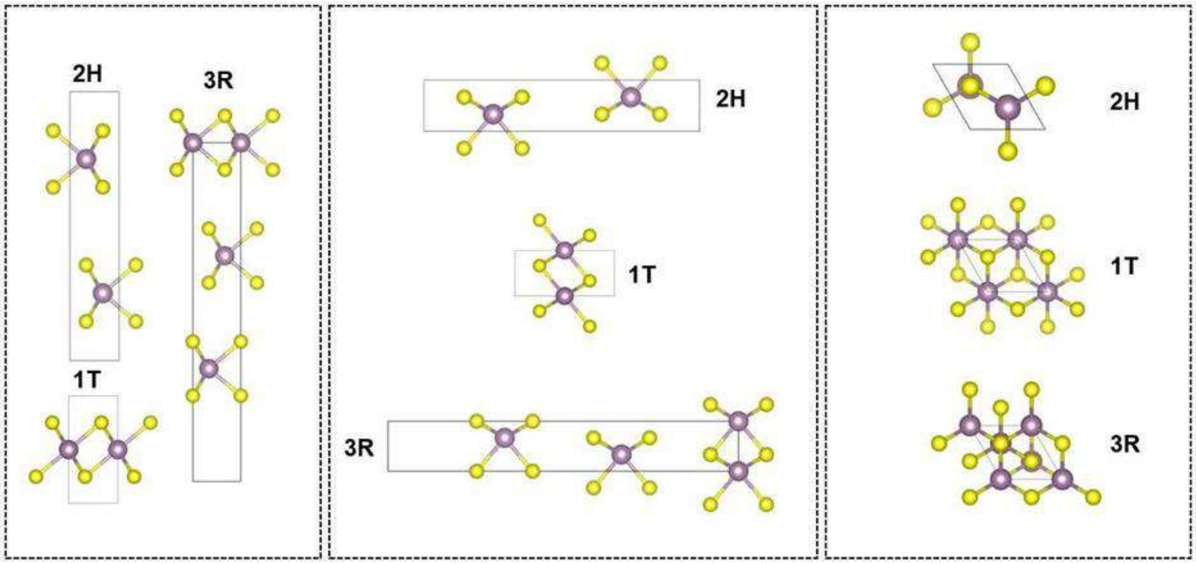

**Figure 1.1. Structures cristallines polymorphes du $MoS_2$ vues sous différentes projections.**

### 4.2.2. Propriétés du $MoS_2$

Comme pour la plupart des matériaux TMDs, le principal avantage de l'utilisation du 2D-$MoS_2$ est la possibilité de contrôler sa bande interdite[11]. Contrairement au graphène à bande inter- dite nulle, la bande interdite du $MoS_2$ peut être modifiée en contrôlant le nombre de couches, comme le montre la figure 1.2.

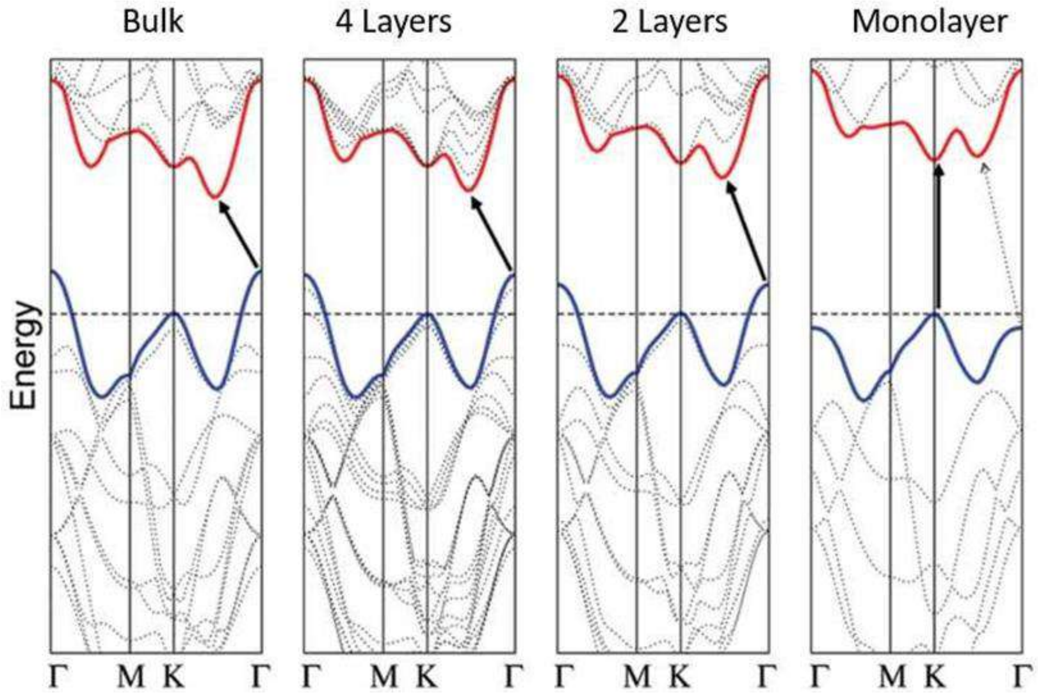

**Figure 1.2. Variation de la bande passante 2D-MoS$_2$ en fonction du nombre de couches. Notez la transition de la bande passante indirecte pour le MoS$_2$ multicouche à la bande passante directe pour le MoS$_2$ monocouche[11].**

En général, le MoS$_2$ massif (>10 couches) présente une bande interdite indirecte de ~ 1.23 eV, et il ne montre pas systématiquement une réponse de photoluminescence (PL). En revanche, le MoS$_2$ monocouche (ML) possède une bande interdite directe de ~ 1.88 eV et une réponse PL systématique, comme l'illustre la figure 1.3[12]. En outre, les spectres PL de ML-MoS$_2$ présentent deux pics d'excitons, attribués à la duplication de la bande de valence au point K (première zone de Brillouin) en raison du couplage spin-orbite, ce qui provoque deux transitions optiquement actives. La première est observée autour de ~ 675 nm (exciton : A), tandis que la seconde apparaît autour de ~ 625 nm (exciton : B)[4,13,14].

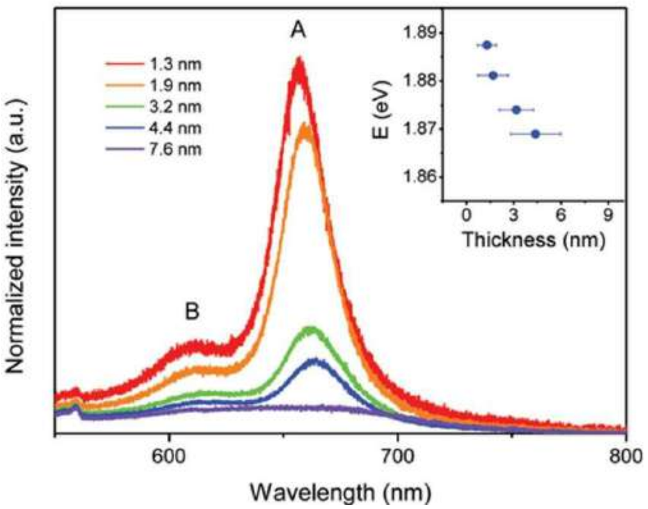

**Figure 1.3. Spectres PL du $MoS_2$ en fonction de l'épaisseur des couches [12].**

La spectroscopie Raman est couramment utilisée comme outil pertinent pour identifier le nombre de couches 2D-$MoS_2$. Pour se faire, on s'appuie sur la différence de décalage de fréquence ($\Delta\omega$) entre les deux modes vibrationnels caractéristiques du $MoS_2$[15,16] à savoir le mode planaire $E^1_{2g}$ apparaissant généralement dans la gamme de fréquence 383-385 $cm^{-1}$ et le mode hors plan $A_{1g}$ apparaissant dans la gamme de fréquence 402-408 $cm^{-1}$ comme le montre la figure 1.4.

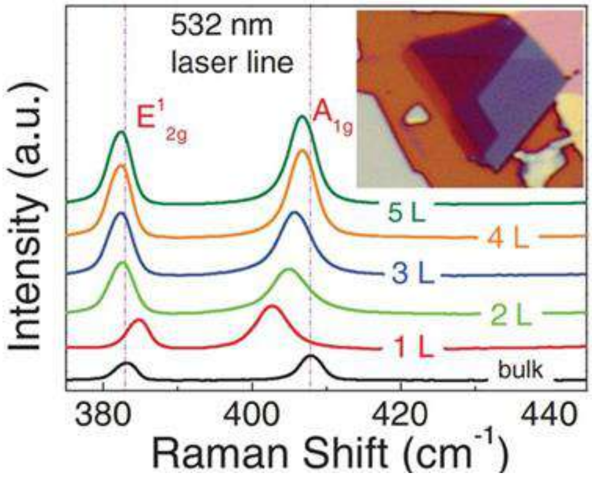

**Figure 1.4: Décalage Raman enregistré pour le $MoS_2$ en vrac et en quelques couches[16].**

Pour le $MoS_2$ ML, $\Delta\omega$ est généralement inférieur à 20 $cm^{-1}$, et augmente progressivement avec le nombre avec de couches. En outre, la spectroscopie Raman est utilisée pour identifier d'autres formes polymériques de $MoS_2$, telles que 1T-$MoS_2$ sur la base des modes $E_{1g}$, $J_1$, $J_2$, et $J_3$ qui apparaissent à 283, 152, 213, et 330 cm$^{-1}$, respectivement[17]. Par conséquent, la spectroscopie Raman est un outil fiable pour évaluer la transition de phase et le rapport de phase de 1T-$MoS_2$/2H $MoS_2$[10]. Au-delà de la modulation de la bande interdite, le nombre de couches affecte les constantes optiques du $MoS_2$[18] comme le montre la figure 1.5. L'indice de réfraction et le coefficient d'extinction sont étroitement liés aux ondes d'excitation et plus particulièrement ils sont variables dans le domaine du visible.

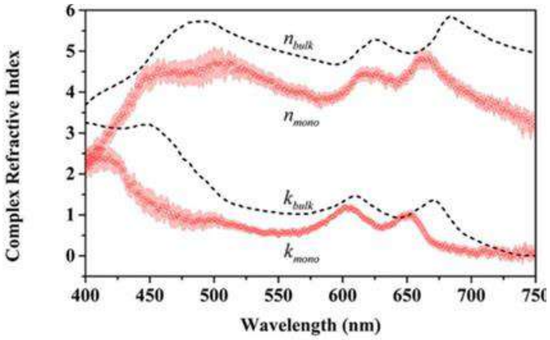

**Figure 1.5: Variation de l'indice de réfraction et du coefficient d'extinction des ML en vrac et $MoS_2$ dans le visible[18].**

### 4.2.3. Fabrication de $MoS_2$

Un large éventail de méthodes de fabrication a été utilisé pour produire du $MoS_2$. L'exfoliation mécanique, comme d'ailleurs pour les autres matériaux 2D, a été l'une des premières méthodes de synthèse utilisées pour étudier les propriétés photoélectriques du $MoS_2$[19]. Cependant, cette technique n'offre pas un contrôle précis de l'épaisseur et de l'uniformité des feuilles de $MoS_2$ exfoliées[20]. Par ailleurs, plusieurs groupes ont utilisé l'exfoliation chimique à l'aide de l'intercalation de Li- pour générer des $MoS_2$ à grande échelle[2,21]. Cette méthode permet de préparer le $MoS_2$ avec une grande homogénéité, mais les couches ainsi produites sont souvent altérées par le Li[12]. Dans ce contexte, la fabrication du $MoS_2$ par l'approche du dépôt chimique en phase vapeur (CVD) est apparue comme l'une des méthodes de fabrication les plus populaires pour produire du $MoS_2$ à un coût raisonnable et avec une large gamme de morphologies, telles que des triangles planaires[22] et des nanofeuillets verticales (NS)[23]. Ces morphologies sont nécessaires pour améliorer les propriétés optoélectroniques et photocatalytiques du $MoS_2$. Néanmoins, le problème du CVD réside parfois dans la pureté altérée des films obtenus, qui peut être due à la réaction incomplète des précurseurs et à des réactions chimiques secondaires difficiles à contrôler[24]. En revanche, les approches de dépôt physique en phase vapeur (PVD) ont montré un grand potentiel en termes de génération de films continus et stœchiométriques avec une large surface spécifique grâce à leur capacité à transférer la stœchiométrie de la cible au substrat[25]. Cela montre qu'il est possible de produire des films minces avec une forte répétabilité et un contrôle des propriétés des matériaux[26]. Le processus PLD, par exemple, a montré un grand potentiel pour la fabrication de $MoS_2$ avec une bonne qualité cristalline et un contrôle de l'épaisseur[27]. Cependant, le coût de la fabrication est relativement élevé et il reste le principal inconvénient de ce procédé[28].

### 4.2.4. Domaines d'application du de $MoS_2$

Le $MoS_2$ a d'abord été utilisé comme lubrifiant solide sous forme de particules de 1 à 100 nm de diamètre en raison de ses bonnes propriétés lubrifiantes et de sa stabilité thermique jusqu'à 350°C même dans un environnement agressif[29]. Cependant, l'émergence des matériaux 2D au-delà du graphène a favorisé l'apparition du $MoS_2$ dans de nombreuses applications. Par exemple, en raison de sa forte absorbance optique et de son faible courant d'obscurité, le $MoS_2$ a été considéré comme un bon candidat pour la photodétection[30]. En outre, la capacité de fabriquer divers $MoS_2$ à base d'hétérostructures a été extrêmement utile pour le développement de nouveaux photodétecteurs avec une réponse dans une large bande allant de l'UV à l'IR[31]. Par conséquence, de nombreuses stratégies ont été adoptées pour stimuler les performances des photodétecteurs à base de $MoS_2$, par exemple l'amélioration de son absorption optique et en augmentant le transfert de charges à l'aide de l'ajout de nanoparticules métalliques[32], ou le dopage[33] ou encore en l'associant à d'autres hétérostructures à base de matériaux type Van Der Waals[34]. Le $MoS_2$ est aussi considéré comme un bon candidat pour la microélectronique en raison de la mobilité très élevée des porteurs de charge, ce qui permet d'obtenir des rapports de courant on/off élevés[35,36]. Il est aussi très désiré comme un matériau très intéressant pour la détection de gaz en raison de sa surface spécifique élevée[37]. Récemment, des photocatalyseur à base de $MoS_2$ ont commencé à susciter l'intérêt pour la production d'hydrogène par photocatalyse en raison de sa bande interdite lui procurant une grande capacité d'absorption de la lumière visible. Dans ce sens, plusieurs études ont été menées sur l'utilisation du $MoS_2$ pour la séparation des molécules de l'eau et la production d'hydrogène[38], la photodégradation[39], et dans les cellules photovoltaïques[40] comme cela est récapitulé sur la figure 1.6. L'article 1 constitue le contexte de la thèse. Il offre un aperçu détaillé de la fabrication, de la caractérisation et des applications les plus pertinentes récemment associées au $MoS_2$.

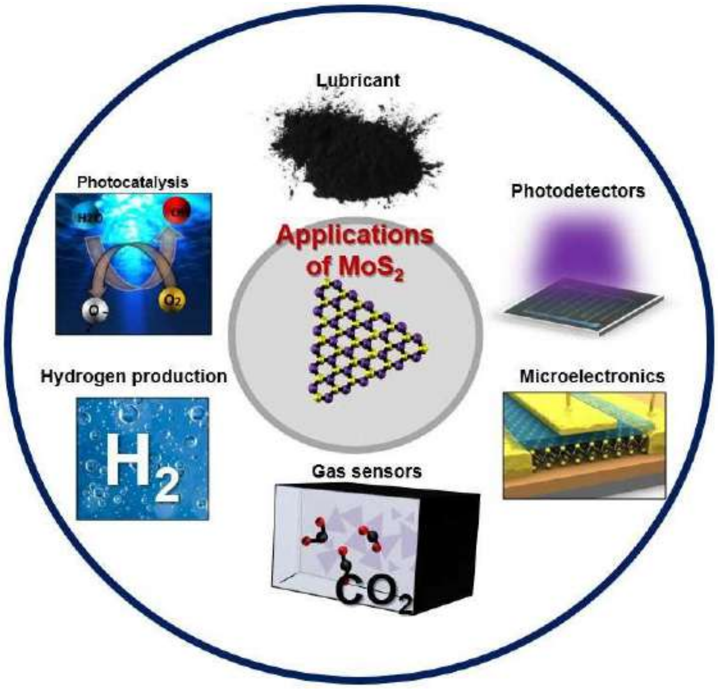

**Figure 1.6: Applications les plus courantes du $MoS_2$.**

## 4.3. Photodétecteurs à base des nanostructures de $MoS_2$

### 4.3.1. Principe de la photodétection

Les photodétecteurs sont des composants essentiels des dispositifs optoélectroniques qui utilisent des matériaux semi-conducteurs pour convertir la lumière absorbée en signal électrique. En général, les matériaux photodétecteurs sont sélectionnés en fonction du domaine d'absorption de la lumière requise pour l'application visée. Le photodétecteur fonctionne donc dans une gamme de longueurs d'onde spécifique. Cependant, les photodétecteurs basés sur des hétérostructures peuvent être conçus pour une photodétection à large bande. La figure 2.1 présente les applications les plus communes à base de photodétecteurs.

La figure 2.2 illustre la responsivité d'un dispositif photodétecteur commercialisé basé sur le Si et l'InGaAs. La photodétection est étroitement liée à la bande interdite de chaque matériau photodétecteur. Cela explique la large acceptation de l'utilisation du Si pour les applications photovoltaïques, par opposition à l'InGaAs, qui est couramment utilisé dans les applications de communication.

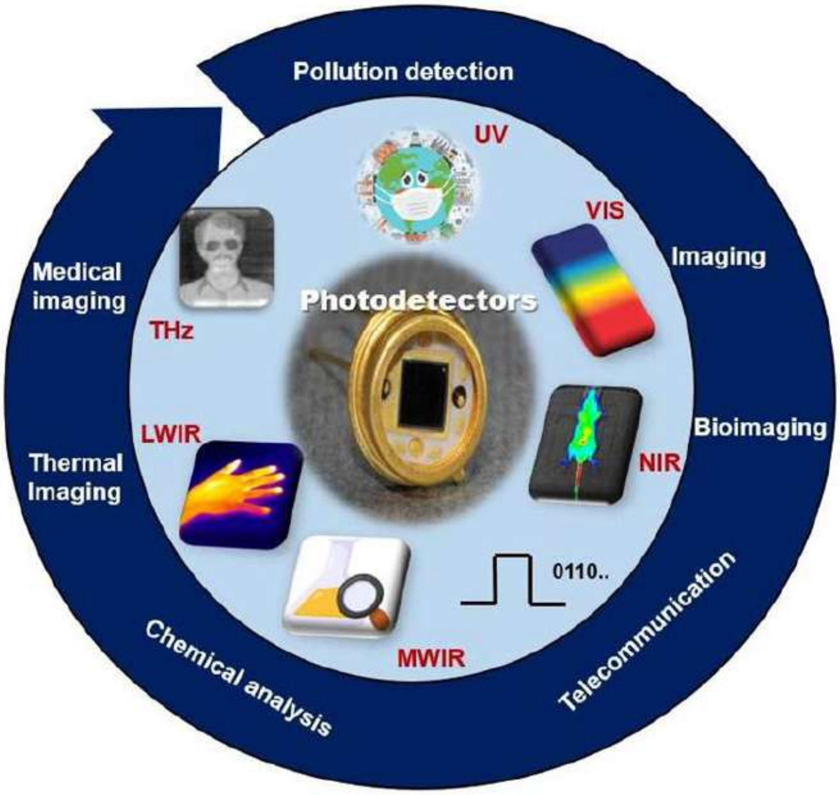

Figure 2.1: Quelques applications courantes des photodétecteurs

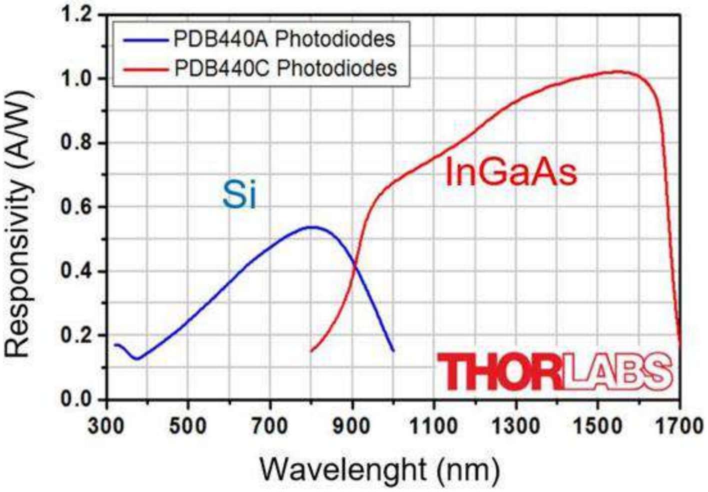

Figure 2.2: Responsivité du Si et de l’InGaAs en fonction des longueurs d’onde.

Le processus de captage de la lumière et de sa conversion dans les photodétecteurs repose sur deux mécanismes connus. À savoir, un processus de conversion de l’énergie thermique basé sur l’effet photo-thermoélectrique, et une conversion basée sur l’excitation optique générant un champ électrique, concernant les effets photovoltaïques et photoconducteurs, comme illustré à la figure 2.3.

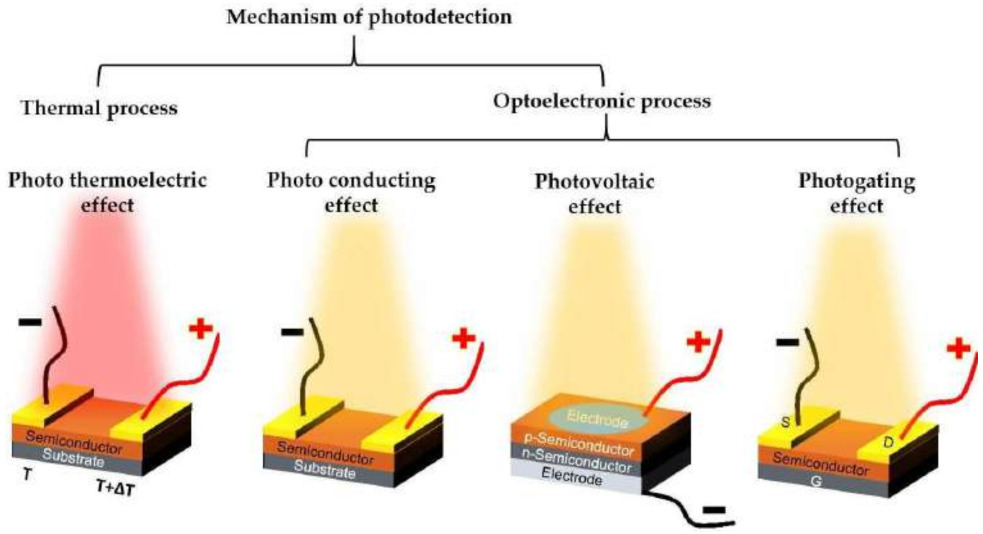

**Figure 2.3: Différents types de photodétecteur et leur mécanisme de photodétection.**

En général, les choix technologiques sont principalement dictés par l’application souhaitée. D’une part, les dispositifs à base de photoconducteurs sont les plus couramment utilisés en raison de leur facilité de fabrication. Cette technologie nécessite des films semi-conducteurs hautement cristallins possédant une absorption optique élevée et une bonne susceptibilité à la création de paires électron-trou. Néanmoins, le courant d’obscurité élevé et la nécessité d’une polarisation externe restent des inconvénients importants de cette technologie. Les dispositifs photovoltaïques, en revanche, sont les plus efficaces en raison du faible courant d’obscurité obtenu à polarisation nulle grâce au champ électrique interne incorporé par la jonction p-n. Le tableau 2.1 résume les effets de photoconversion susmentionnés en indiquant leurs avantages et leurs limites.

**Tableau 2.1: Type de mécanisme de photodétection on et leurs caractéristiques.**

| Mécanisme | Caractéristiques | Avantages | Limites |
|---|---|---|---|
| **Effet photo thermo-électrique** | La différence de température induit l'effet Seebeck, qui est traduit par des photogénérés. | Pas de biais externe | Détection dans une gamme spécifique |
| **Effet photo-conductive** | Les porteurs photogénérés sont déclenchés par un champ externe qui modifie la conductivité du dispositif. | Dispositifs simples et flexibles | Nécessite une polarisation externe ; courant d'obscurité élevé |
| **Effet photo-voltaïque** | Les porteurs photogénérés sont générés par un champ électrique intégré dû à la jonction p-n | Pas de polari-sation externe ; faible courant d'obscurité | Fabrication fastidieuse et coûteuse |
| **Effet de photogrille** | Les porteurs piégés dans les états localisés agissent comme une porte locale supplémentaire, modulant la conductance du canal. | Faible courant d'obscurité ; réponse à large bande;<br>réponse rapide | Nécessite une polarisation externe ; fabri- cation fastidieuse; coûteuse |

La figure 2.4 illustre le mécanisme de photoconduction impliqué dans un semi-conducteur lorsqu'il génère un excès de porteurs de charge libres en absorbant des photons. Les énergies des photons sont généralement supérieures à la bande interdite, ce qui entraîne une augmentation de la conductivité électrique. La figure 2.4a illustre la conception de base d'un photoconducteur, qui consiste en un semi-conducteur avec deux contacts métalliques. Le courant d'obscurité est généralement mesuré en l'absence d'excitation. Lorsque le dispositif est exposé à des photons dont l'énergie est supérieure à sa bande interdite, les excitons photogénérés (paires électron-trou) sont créés et leur séparation et leur mobilité sont assurées par une polarisation appliquée, comme le montre la figure 2.4b. La différence entre les courants lumineux et sombres permet de déterminer la valeur du photocourant et donc les performances optoélectroniques du dispositif (par exemple, figure 2.4c).

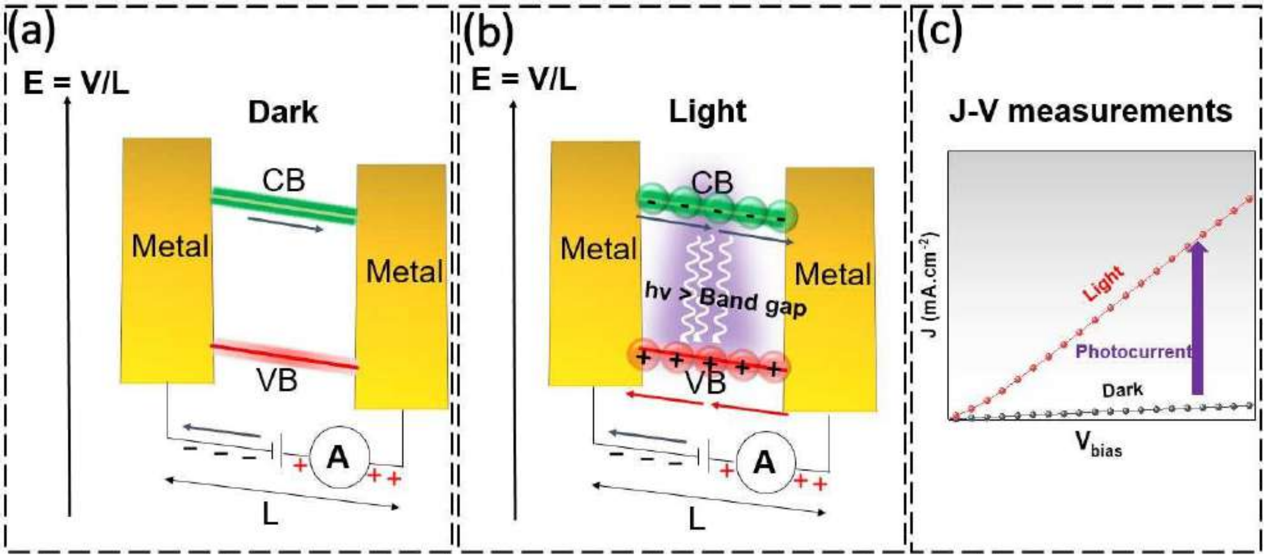

**Figure 2.4: Schéma de la génération de porteurs de charge en (a) l'absence d'illumination (courant d'obscurité), (b) en présence d'une excitation lumineuse et (c) courbes J-V résultantes dans l'obscurité et sous illumination.**

La performance d'un photodétecteur consiste à évaluer son courant d'obscurité ($I_d$) mesuré en l'absence de toute illumination externe pendant une durée donnée jusqu'à ce que la stabilité soit atteinte. L'importance de $I_d$ découle du fonctionnement de base d'un photodétecteur qui consiste à évaluer sa photoréponse, définie comme le rapport entre les porteurs photogénérés induits par l'excitation lumineuse indiquée par un photocourant ($I_{Ph}$) et les porteurs intrinsèques indiqués par $I_d$. Ces courants mesurés sont ensuite utilisés pour calculer la réactivité (R) et la détectivité spécifique (D*). R indique la sensibilité du photodétecteur à la génération de $I_{Ph}$ pour une puissance incidente donnée et D* fournit une évaluation globale des performances du dispositif. Le temps de réponse (τ) est un autre paramètre utilisé pour évaluer la rapidité avec laquelle une photoréponse est obtenue et l'efficacité quantique (EQE) traduit le rapport entre les porteurs générés et les photons incidents (par exemple, tableau 2.2).

**Tableau 2.2: Paramètres physiques utilisés pour sonder les performances optoélectroniques d'un photodétecteur.**

| Paramètres | Formule | Unité | Description |
|---|---|---|---|
| **Courant d'obscurité** | $I_d$ | A | Courant mesuré en absence d'éclairage |
| **Photocourant** | $I_{Ph} = I - I_d$ | A | La différence entre le courant sous illumination et le courant d'obscurité |
| **Photoréponse** | $100 x I_{Ph} / I_d$ | % | Le rapport entre le photocourant et le courant d'obscurité |
| **Responsivité** | $R = I_{Ph}/P$ | A/W | Le rapport entre le photocourant obtenu et la puissance d'excitation |
| **Détectivité** | $D^* = R/(2e\lambda I_d)^{0.5}$ | Jones | Capacité d'un photodétecteur à capter les signaux les plus faibles |
| **EQE** | $100hc\ I_{Ph} / e\lambda P$ | % | Rapport entre le nombre de porteurs de charge collectés par le photodétecteur et le nombre de photocharges sous une puissance donnée. |
| **Temps de réponse** | $\tau_r$ and $\tau_d$ | s | Temps écoulé pour que le photocourant augmente ou diminue entre 10% à 90% |

#### 4.3.2. Photodétecteurs à base de $MoS_2$

Pour évaluer ses propriétés optoélectroniques, le $MoS_2$ pur a été intégré, seul ou combiné à d'autres composés, dans des dispositifs photodétecteurs suivis de mesures photoélectriques. La littérature fait état d'une multitude de stratégies visant à améliorer l'efficacité de la photodétection des dispositifs à base de $MoS_2$. La plupart de ces stratégies reposent sur l'augmentation de l'absorption optique et de l'efficacité de la photodétection, y compris son utilisation dans des hétérostructures hybrides[34,41] ou avec des nanostructures plasmoniques[42,43]. L'amélioration des propriétés optoélectroniques du $MoS_2$ a également été aussi obtenue par dopage chimique[33] ou encore la fonctionnalisation de la surface[31]. Dans ce sens, nous avons utilisé deux approches de fabrication différentes, CVD et PLD, pour obtenir diverses nanostructures de $MoS_2$ en termes de microstructure, de morphologie, de taille et de forme, à mettre en relation avec les performances optoélectroniques. L'approche CVD a été choisie en raison de sa capacité à générer des $MoS_2$ hautement cristallins avec différentes morphologies[44–46] tandis que le processus PLD a été utilisé pour fabriquer des films minces de $MoS_2$ de haute qualité avec un contrôle de l'épaisseur[47]. En raison de leur très faible épaisseur (matériaux d'une épaisseur d'un atome), on s'attend à ce que le courant d'obscurité soit très faible dans les matériaux 2D, ce qui améliorerait considérablement leur photoréponse. Sur la base de leurs bandes interdites respectives, ces matériaux présentent un grand potentiel pour la prochaine génération de photodétecteurs, comme le montre la figure 2.5. En particulier, le $MoS_2$ a généralement été utilisé pour la photodétection dans l'UV et le visible. Entre-temps, de nombreuses hétérostructures basées sur le $MoS_2$ ont été reportées permettant d'étendre ses performances dans une gamme de photodétection large.

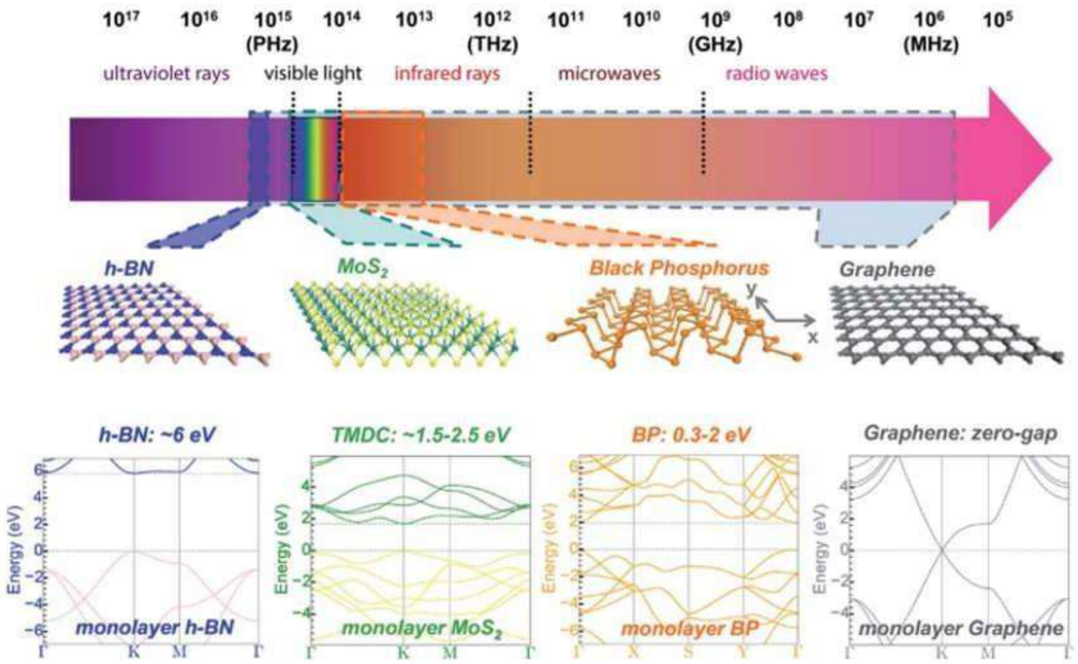

**Figure 2.5: Matériaux 2D pour les applications de photodétection couvrant une large gamme du spectre lumineux. De gauche à droite, la structure cristalline du h-BN, du $MoS_2$, du phosphore noir (BP) et du graphène, ainsi que leurs bandes électroniques respectives[31].**

### 4.3.3. Propriétés optoélectroniques du $MoS_2$ fabriqué par CVD

### a. Effet de la position du substrat

La morphologie du matériau utilisé dans un photodétecteur s'est avérée avoir un impact significatif sur l'amélioration de ses performances. De nombreux efforts ont été consacrés à la fabrication de $MoS_2$ avec des formes variées telles que des paillettes planes[48], des nanofeuillets verticaux (NSs)[37] des microfibres[46] et des nanofils[45]. Par exemple, les $MoS_2$ NS verticaux fabriqués par CVD ont présenté un comportement d'émission de lumière similaire à celui des $MoS_2$ ML exfolié mécaniquement sur une grande surface (2 $cm^2$)[23]. L'alignement vertical du $MoS_2$ fournit une structure idéale, exposant un grand nombre de sites actifs conduisant à un comportement similaire à celui du ML $MoS_2$. Compte tenu de ces données intéressantes, nous avons élaboré une stratégie pour contrôler et surveiller les conditions de croissance à l'aide du système CVD en identifiant les paramètres clés qui influencent le processus de fabrication. Pour ce faire, le substrat collecteur a été placé dans différentes positions à l'intérieur du four tubulaire du système CVD (Fig 2.6) afin d'examiner l'effet de la position du substrat sur la croissance des hétérostructures $MoS_2$ et sur leurs morphologies.

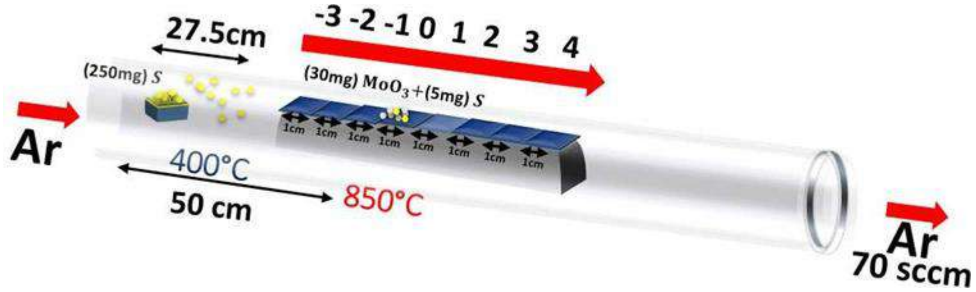

**Figure 2.6: Installation de fabrication d'hétérostructures à base de $MoS_2$ par procédé CVD.**

Par conséquent, des hétérostructures de $MoS_2$ et de $MoS_2/MoO_2$ présentant diverses morphologies ont été obtenues simultanément en fonction de la position du substrat collecteur. En particulier, l'hétérostructure $MoS_2/MoO_2$ composée de nanofils hautement cristallins (NWR) d'un diamètre de 100 nm (figure 2.7) a montré des performances élevées en matière de photodétection.

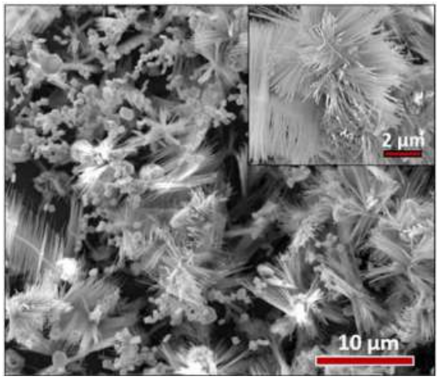

**Figure 2.7: Image par électron secondaire des nanofils de $MoS_2$.**

La figure 2.8a montre un schéma du dispositif fabriqué. Deux électrodes Au de 50 nm d'épaisseur ont été déposées par pulvérisation cathodique afin d'abaisser la barrière de contact et d'améliorer le transport des charges avec le $MoS_2$. En effet, lorsqu'ils sont exposés à l'éclairage d'une lampe halogène, les NWR $MoS_2/MoO_2$ ont montré la photoréponse la plus élevée par rapport à d'autres microstructures, atteignant jusqu'à $10^4$ %, une R élevée de 1.13 mA/W et une D* de $2.6 \times 10^9$ Jones à une tension de fonctionnement aussi basse que 1V (la figure 2.8b).

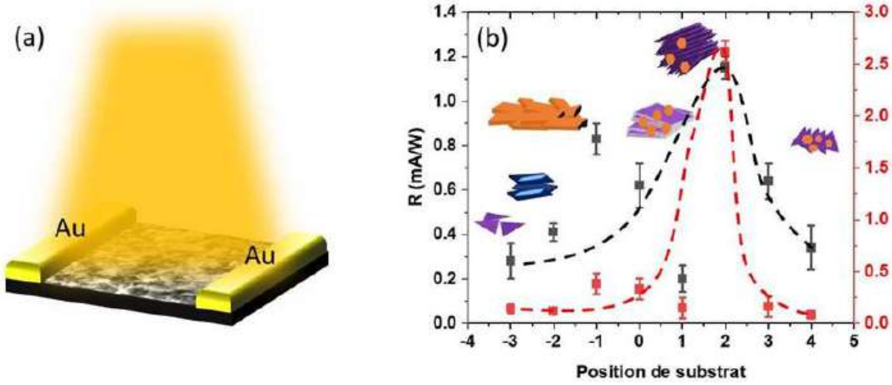

**Figure 2.8: R et D* obtenues en fonction de la position du substrat à l'intérieur du four CVD.**

Comme le montre la figure 2.8b, la forme et la morphologie nouvelles (NWRs) du système combiné $MoS_2$ et $MoO_2$ ont produit une photoréponse intéressante du photodétecteur par rapport à la littérature. La publication suivante souligne le rôle particulier de la position du substrat collecteur dans l'amélioration des performances de photodétection des hétérostructures basées sur le $MoS_2$. Article 2 met l'accent sur le rôle particulier de la position du substrat de collecte dans l'amélioration des performances de la photodétection à base de $MoS_2$.

### b. Photodétecteur basé sur une hétérostructure $MoS_2/MoO_2$

À la lumière des études précédentes, une attention particulière a été accordée à l'optimisation des hétérostructures $MoS_2/MoO_2$ afin d'améliorer davantage les performances optoélectroniques. Dans ce sens, nous avons exploré la position du substrat où l'hétérostructure est souvent obtenue, mais nous avons apporté un changement dans la préparation du précurseur. En effet, une nouvelle recette en termes de préparation du précurseur a été utilisée. A savoir, une solution de mélange de S, $MoO_3$, et d'éthanol a été préparée afin d'avoir une solution plus dispersive du précurseur. Après sonication, quelques gouttelettes du mélange ont été ajoutées sur le dessus du substrat Si avant d'être introduites dans le réacteur CVD. L'objectif principal de ce protocole était de créer de multiples sites de nucléation de l'hétérostructure $MoS_2/MoO_2$. Ensuite, un chauffage rapide a été mis en œuvre pour assurer une sulfuration incomplète du précurseur $MoO_3$ et ainsi garantir la fabrication d'une hétérostructure $MoS_2/MoO_2$ à haut rendement. En effet, nos résultats ont démontré l'élaboration d'une nouvelle hétérostructure $MoS_2/MoO_2$ avec une morphologie intéressante composée de microfibres de $MoS_2$ et de microfleurs de MoO2 (figure 2.9). Le diamètre moyen des microfibres de $MoO_2$ est de quelques dizaines de microns, tandis que la longueur des microfibres de $MoS_2$ peut atteindre des centaines de microns dans toutes les directions.

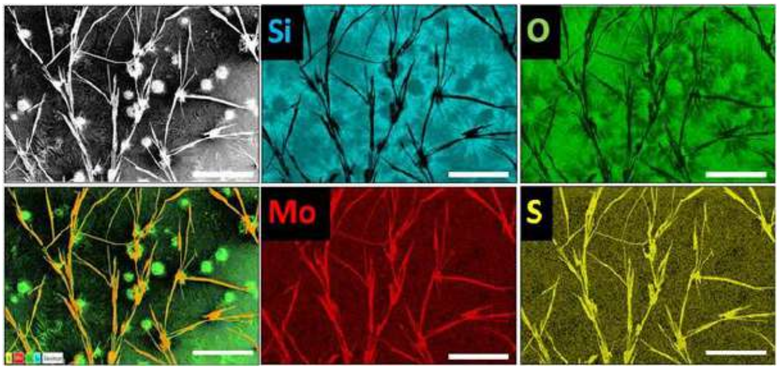

**Figure 2.9: (En haut à gauche) image SEM de l'hétérostructure $MoS_2/MoO_2$, (en bas à gauche) superposition des cartes EDS et de l'image SEM. Le reste c'est des cartographies EDS en considérant Si, O, Mo et S comme marqueurs (barre d'échelle =100 µm).**

Pour comprendre la fabrication de l'hétérostructure $MoS_2/MoO_2$, nous avons analysé sa microstructure aux premiers stades de la nucléation. La figure 2.10 présente des images SEM montrant quelques microfibres nucléées à différents endroits au début du processus de coalescence. En raison de la préparation du précurseur, on s'attend à ce qu'il y ait un certain gradient de concentration dans le mélange, ce qui est supposé être à l'origine de la croissance du composé $MoO_2$. Ce processus de diffusion peut aboutir à la formation de micro-fleurs de $MoO_2$.

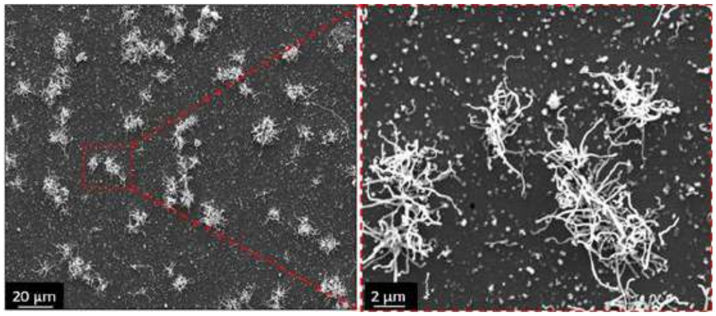

**Figure 2.10: Images SEM montrant les premières étapes de la nucléation $MoS_2/MoO_2$ Microfibre/ microfleur (à gauche est un grossissement du carré rouge de droite).**

L'hétérostructure obtenue a ensuite été intégrée dans un dispositif de photodétection et évaluée sous diverses excitations de longueur d'onde. Il est intéressant de noter que cette hétérostructure a présenté une photoréponse à large bande dans la gamme 450-630 nm. R et D* les plus élevées de 0.75 mA/W et de $1.45x10^7$ Jones, respectivement, ont été obtenues sous excitation de lumière bleue à une puissance d'excitation très faible de 20 $mW/cm^2$. Une étude approfondie a été réalisée sur l'hétérostructure MoS2/MoO2, résumée dans l'Article 3.

### 4.3.4. Propriétés optoélectroniques du $MoS_2$ fabriqué par PLD

La technique de PLD est l'autre approche utilisée pour la fabrication de $MoS_2$. Le choix de cette technique repose sur sa capacité à générer du $MoS_2$ sur des grandes surfaces, compatible avec le traitement des circuits intégrés standard. La PLD est très recherchée pour le développement de dispositifs optoélectroniques basés sur le $MoS_2$[49,50]. La PLD est incontestablement une technique appropriée dans ce contexte, puisqu'elle a été utilisée avec succès pour le dépôt de films ultraminces de $MoS_2$ sur divers substrats, principalement pour des applications de photodétection[27,51]. Pour examiner l'influence de la température de dépôt ($T_d$) sur la photoréponse des photodétecteurs $MoS_2$, divers films minces ont été préparés à différentes températures. La figure 2.11 ci-dessous présente un schéma du système PLD utilisé pour la fabrication de films minces de $MoS_2$ sur un substrat de Si à température ambiante (RT), 300°C, 400°C, 500°C, 600°C et 700°C en utilisant un nombre d'impulsions $N_{LP}$ = 7000, ce qui correspond à une épaisseur de film d'environ 100 nm.

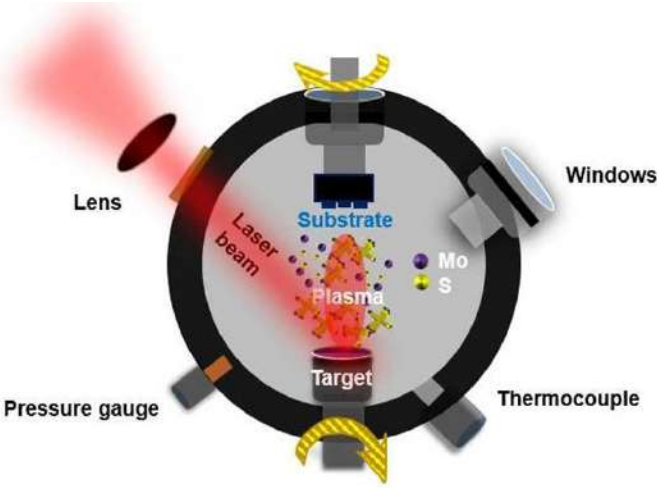

Figure 2.11: Schéma du système PLD utilisé pour la fabrication de films minces $MoS_2$.

Notre étude examine méthodiquement l'effet de la $T_d$ sur la structure et les propriétés optoélectroniques des films minces de $MoS_2$ (épaisseur 100 nm). En conséquence, nous avons pu identifier une température de dépôt de film de 500°C qui donne des films de $MoS_2$ hautement cristallisés et préférentiellement orientés suivant (002) avec une meilleure performance de photodétection et une bande interdite de 1.4 eV. Nos résultats soulignent l'importance de $T_d$ pour influencer non seulement la cristallinité mais aussi les propriétés optoélectroniques des films $MoS_2$. En outre, comme ces structures semblent être orientées verticalement, la forte performance de photodétection des films $MoS_2$ est comparable à celle observée dans les monocouches $MoS_2$. Un exemple des caractéristiques de surface des films minces $MoS_2$ déposés par PLD est illustré à la figure 2.12. Il s'agit de deux images SEM inclinées de la structure $MoS_2$ obtenues respectivement à RT et à 500°C.

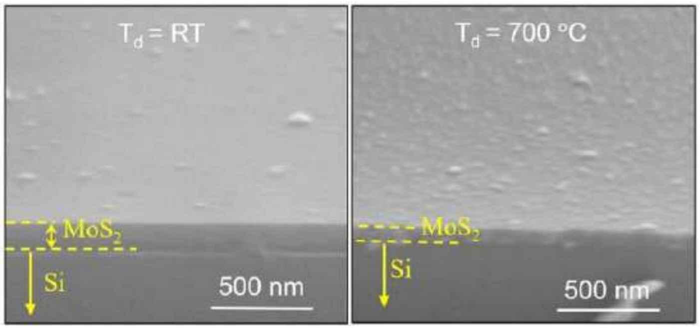

Figure 2.12: Images SEM inclinées de $MoS_2$ déposé par PLD à RT (épaisseur 100 nm) et 500°C (épaisseur 60 nm).

L’épaisseur du film obtenu semble diminuer avec l’augmentation de $T_d$, de 100 nm à 60 nm, respectivement de RT à 500°C. La diminution de l’épaisseur est principalement due à la cristallisation et à la densification des films induites par la température, comme cela a été rapporté précédemment[52]. En outre, la rugosité de la surface a considérablement augmenté à 500°C. De plus, la spectroscopie Raman a été utilisée pour étudier les modes vibrationnels des films $MoS_2$ tels que présentés dans la figure 2.13a.

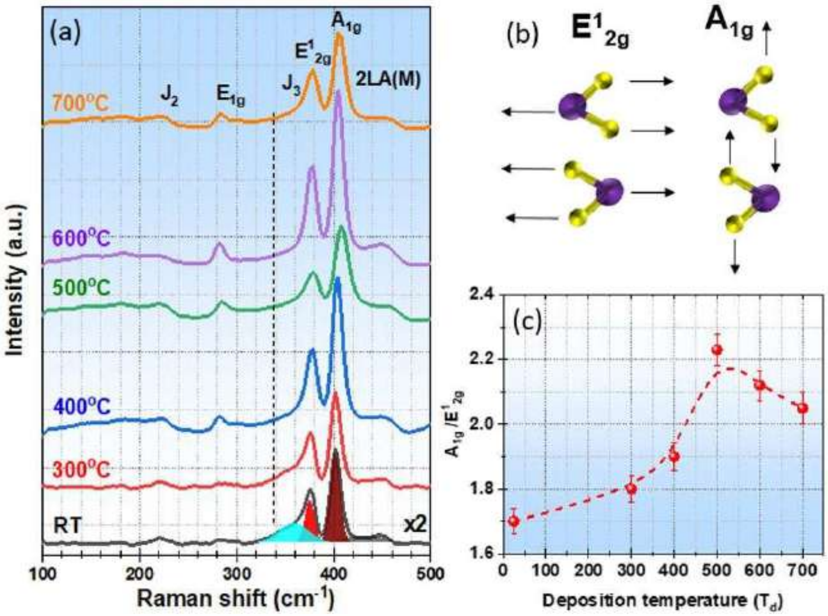

**Figure 2.13: (a) Spectres Raman des films $MoS_2$ en fonction de $T_d$, (b) schéma des modes de vibration dans le plan $E^1_{2g}$ et hors du plan $A_{1g}$ du $MoS_2$, (c) variation du rapport d’intensité $[A_{1g}]/[E^1_{2g}]$ en fonction de $T_d$.**

Des pics Raman large représentant les modes vibrationnels de la phase 2H-$MoS_2$ indiqués par le $E^1_{2g}$ et le $A_{1g}$ sont clairement observés même pour les films $MoS_2$ déposés à RT. La figure 2.13b montre le schéma des modes vibrationnels $A_{1g}$ en $E^1_{2g}$ pour les illustrations. En raison de l’amélioration de la cristallinité des films avec l’augmentation de la $T_d$, les pics caractéristiques de la phase 2H-$MoS_2$ deviennent plus étroits et plus intenses à $T_d$ élevée. En outre, lorsque le rapport d’intensité du pic $[A_{1g}]/[E^1_{2g}]$ des films $MoS_2$ est tracé en fonction de $T_d$ (voir figure 2.13c), on découvre que le rapport atteint son maximum à $T_d$ = 500°C.

Les micrographies HRTEM montrent des films de $MoS_2$ bien cristallisés à 500°C, alors qu’ils sont amorphes à RT (figure 2.14a). Il est intéressant de noter que les cristaux de $MoS_2$ semblent se former horizontalement à l'interface du substrat, puis se développer verticalement, perpendiculairement à la surface du substrat, comme le montre la figure 2.14b-c.

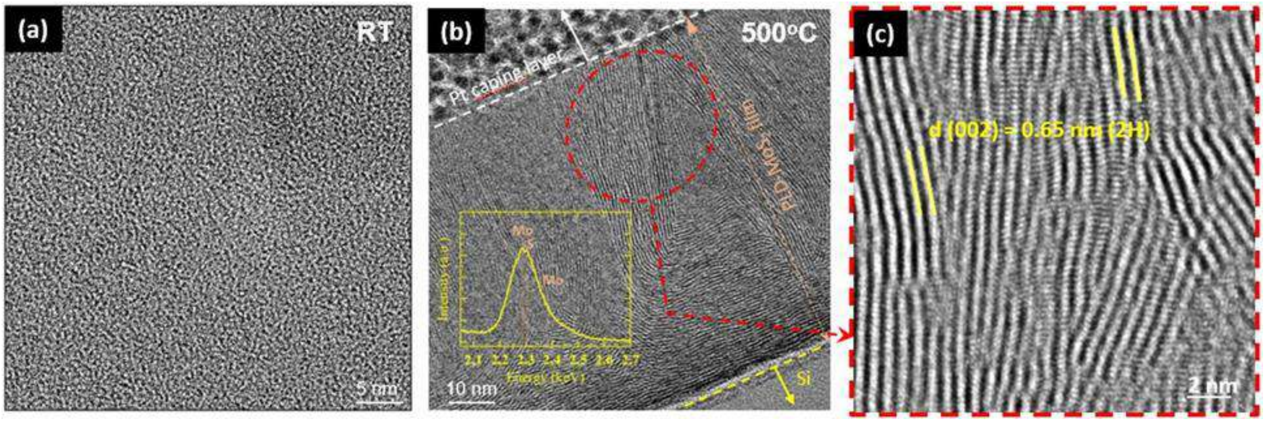

**Figure 2.14: Image TEM des films $MoS_2$ fabriqués à 25°C (a) et 500°C (b-c).**

Pour évaluer les performances optoélectroniques des échantillons de $MoS_2$, ils ont été intégrés dans des dispositifs de photodétection fonctionnels (figure 2.15a) et testés dans l'obscurité et sous illumination. La figure 2.15b montre le spectre de la lampe halogène utilisée. Les résultats typiques obtenus sont présentés dans la figure 2.15c. Le graphique illustre la courbe J-V enregistrée dans l'obscurité et sous éclairage d'une lampe halogène pour l'échantillon le plus performant fabriqué à 500°C.

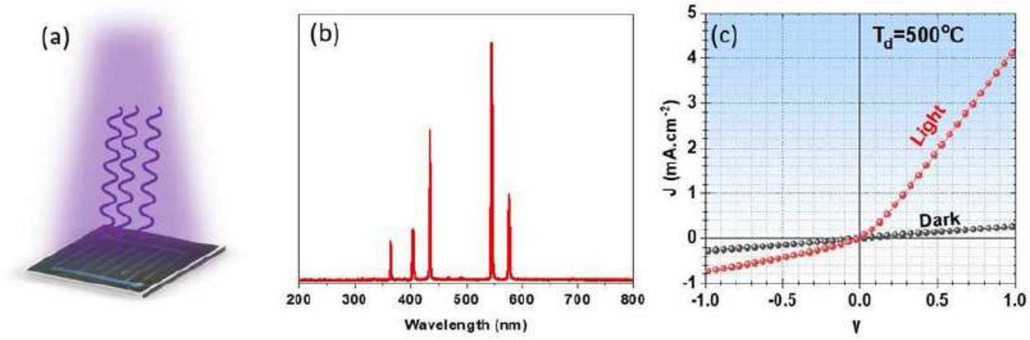

**Figure 2.15: (a) Photodétecteur typique à base de $MoS_2$ fabriqué par PLD à 500°C, (b) spectre de la lampe halogène utilisée pour l'excitation, (c) courbe J-V enregistrée dans l'obscurité et sous illumination.**

Le meilleur dispositif a présenté une R et une D* de 125 mA/W et de $9x10^9$ Jones, respectivement. En outre, R (ou D*) et le rapport $[A_{1g}]/[E^1_{2g}]$ ont une relation constante linéaire (voir figure 2.16). Cela montre clairement que les performances de photodétection (R et D*) des films $MoS_2$ varient linéairement en fonction du degré d'orientation verticale des feuilles $MoS_2$ dans les films. Ce résultat démontre le potentiel énorme du PLD pour obtenir des photodétecteurs à base de $MoS_2$ performants, comme discuté en détail dans l'Article 4.

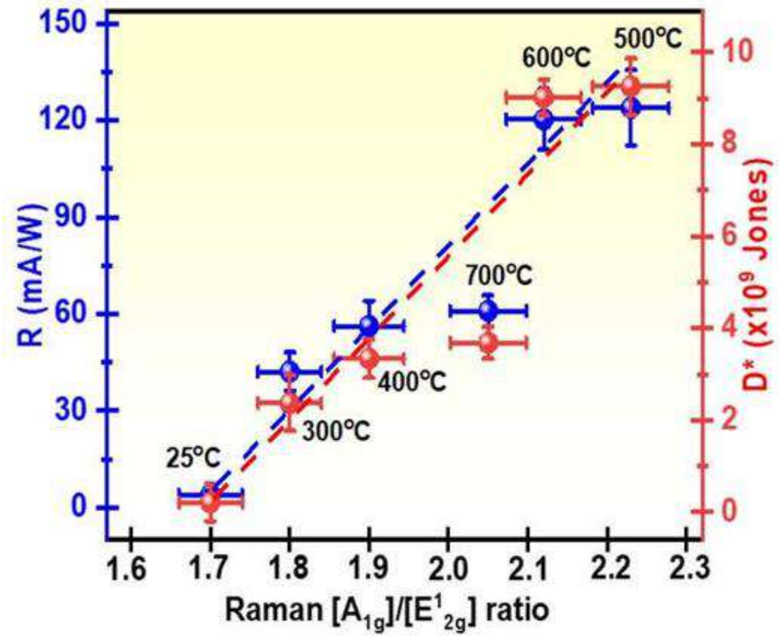

**Figure 2.16: Dépendance linéaire de la bande interdite optique des films MoS2 en fonction du rapport $[A_{1g}]/[E^1_{2g}]$.**

Ce résultat démontre l'énorme potentiel de la PLD pour obtenir des photodétecteurs à base de $MoS_2$ très performants, comme c'est détaillé dans l'article suivant.

### 4.3.5. Photodétecteurs à base de CVD-$MoS_2$ versus PLD-$MoS_2$

Nos études systématiques des propriétés optoélectroniques des nanostructures de MoS2 synthétisés par CVD et PLD et leurs caractérisations nous ont permis de mieux comprendre les principaux avantages et inconvénients de chaque voie de fabrication sur les applications de photodétection en termes de performances. En réglant les diverses variables influençant la croissance CVD du $MoS_2$, nous avons pu peaufiner les performances de la photodétection par le biais du contrôle de la structure cristalline du $MoS_2$ et de sa morphologie ou encore en l'associant avec d'autres oxydes pour former une hétérostructure. Comme indiqué précédemment, les structures obtenues ont montré une photoréponse élevée et une réponse rapide en raison du faible courant d'obscurité et du piégeage de la lumière incidente, ce qui a permis d'augmenter le captage de la lumière. Bien que la technique CVD ait permis d'obtenir des photodétecteurs à base de $MoS_2$ très performants, le faible contrôle de l'épaisseur des nanostructures de $MoS_2$ obtenus constitue un véritable défi. Dans ce sens, la voie PLD se présente comme une alternative fiable pour contrôler l'épaisseur des films de $MoS_2$, comme cela a été démontré. En outre, la technique PLD a permis d'obtenir un résultat intéressant, à savoir la capacité de produire des structures $MoS_2$ alignées verticalement et dotées d'excellentes propriétés optiques. Néanmoins, la densité du film de $MoS_2$ a généré un courant d'obscurité élevé, limitant les performances de la photodétection. Pour récapituler les avantages et les inconvénients de la CVD et de la PLD dans la fabrication de photodétecteurs à base de $MoS_2$ très performants, nous avons résumé dans le Tableau 2.3 les résultats de chaque processus de fabrication.

Tableau 2.3: Avantages et limitations des procédés CVD et PLD pour la fabrication de photodétecteurs performants à base de $MoS_2$.

| **Fabrication** | **Avantages** | **Inconvénients** |
|---|---|---|
| **CVD** | Contrôle de la morphologie<br>Faible courant d'obscurité<br>Transfert de charge élevé | Problème des produits dérivés<br>Température de dépôt élevée<br>Contrôle de l'épaisseur |
| **PLD** | Meilleur contrôle de l'épaisseur<br>Photocourant élevé<br>Meilleur contrôle de phase | Contrôle de la morphologie<br>Courant d'obscurité élevé<br>Coûteuse |

Plusieurs concepts pourraient venir à l'esprit si l'on considère la comparaison entre CVD et PLD pour le développement des photodétecteurs à base de $MoS_2$, ce qui nécessite des recherches plus approfondies. Par exemple, le faible photocourant enregistré dans les photodétecteurs $MoS_2$ fabriqués par procédé CVD pourrait être considérablement augmenté en couplant les excitons $MoS_2$ avec des nanoparticules métalliques plasmoniques[32,43] ou en utilisant des hétérostructures à base de $MoS_2$ en combinaison avec d'autres matériaux 2D. En outre, on peut également tirer parti des effets bénéfiques des NWR $MoS_2$ sur la photoréponse pour développer des NWR $MoS_2$ à base de cœur- coquille incorporés dans des semi-conducteurs à bande interdite directe tels que des matériaux III-V afin d'améliorer encore la réactivité tout en obtenant une photoréponse à large bande[13,42]. Cela peut également servir de base à d'autres développements utilisant la technique PLD pour déposer des nanostructures $MoS_2$ sur des substrats typiques tels que des NWR verticaux en silicium ou des NPs métalliques. Cette stratégie permettrait également au $MoS_2$ déposé par PLD d'obtenir un faible courant d'obscurité dû au piégeage de la lumière, comme cela a été observé avec les NWR de $MoS_2$ déposés par CVD, tout en présentant un photocourant élevé. En outre, le diamètre des NPs de $MoS_2$ peut être réglé en modifiant le $N_{LP}$ pendant le dépôt PLD, ce qui pourrait garantir une photoréponse élevée[53,54]. Par ailleurs, la possibilité de fabriquer du $MoS_2$ à différentes températures à l'aide de la PLD pourrait être d'un grand intérêt pour obtenir des structures de phases combinées de $MoS_2$[6] qui, à leur tour, pourraient améliorer l'absorption optique et la mobilité des porteurs de charge[27].

## 4.4. Structure 1T/2H-$MoS_2$ pour la photocatalyse

Les bonnes performances de conversion de la lumière de nos nanostructures $MoS_2$ développées ainsi que leur large bande interdite, nous ont motivés pour examiner un composé hétérostructure $MoS_2$ à base de 2H-$MoS_2$ et de 1T-$MoS_2$ pour la décontamination photocatalytique de l'eau. En effet, d'après les données précédemment rapportées dans la littérature, il a été démontré que le MoS2 possède des propriétés de photodégradation très intéressantes en raison de sa forte absorption optique et de sa grande surface spécifique. Par conséquent, nous comptons obtenir de meilleures performances de photodégradation avec nos échantillons car ils ont montré un courant photogénéré très élevé.

Nos mesures de photodégradation ont été effectuées sur le bleu de méthylène (MB), un colorant organique connu pour être l'un des principaux polluants de l'eau potable. Le choix du MB a été basé sur sa forte utilisation pour la teinture de la plupart des tissus et, plus important encore, à cause sa forte toxicité. Certaines données rapportées ont déjà montré la possibilité de l'élimination du MB par un photocatalyseur à base de $MoS_2$[8,55,56]. Cependant, la plupart de ces travaux souffrent de la complexité des processus de fabrication sans parvenir à une augmentation significative des performances. D'autres stratégies ont donc été adoptées pour améliorer les performances de photodégradation du MB, tels que l'utilisation de systèmes hybrides basés sur le $MoS_2$ fonctionnalisé[57] ou le $MoS_2$ dopé avec des NP métalliques[8]. Malgré les performances intéressantes obtenues par ces hétérostructures, leurs méthodes de fabrication sont coûteuses et nécessitent des processus de fabrication en plusieurs étapes.

Récemment, l'association du 2H-$MoS_2$ avec sa forme polymorphe, c'est-à-dire la phase métallique 1T-$MoS_2$, est apparue comme une solution alternative pour le développement de catalyseur performant grâce à la mobilité élevée des porteurs de charge dans 1T-$MoS_2$ et que ces porteurs peuvent être transférés à 2H-$MoS_2$[9,17]. Dans ce sens, en utilisant la capacité de réglage de la fabrication CVD, nous avons élaboré une hétérostructure hybride de haute qualité basée sur 1T-$MoS_2$/2H-$MoS_2$ qui sera utilisée pour la photodégradation de la MB. La figure 3.1a montre une image de microscopie électronique en transmission à haute résolution (HRTEM) de cette structure. La nature hétérostructure du composé fabriqué est également confirmée par la spectroscopie Raman, comme le montre la figure 3.1b. Comme le 2H-$MoS_2$ est repéré grâce aux modes vibrationnels $A_{1g}$ et $E^1_{2g}$ situés à 405 et 385 $cm^{-1}$, respectivement. Cependant, la phase 1T-$MoS_2$ est caracterisé par les modes vibrationnels $J_1$, $J_2$, $E_{1g}$ ,et $J_3$ qui sont situés à 147, 228, 283, et 330 $cm^{-1}$ , respectivement, comme cela a déjà été montré[6,8].

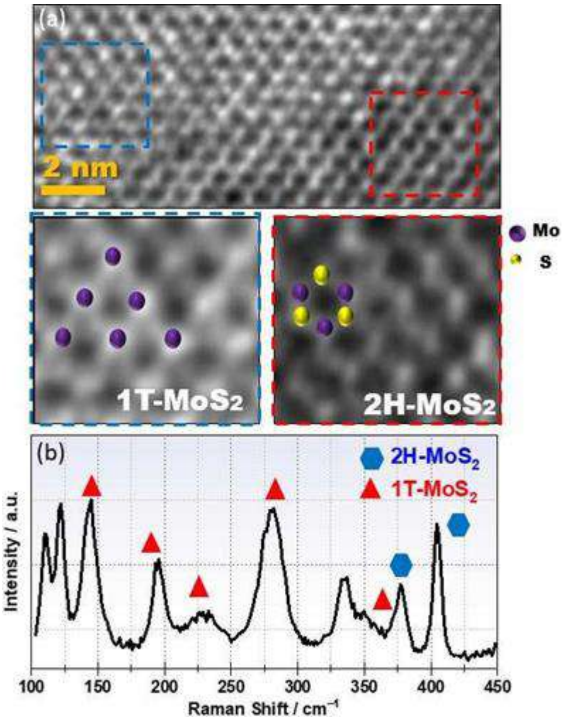

**Figure 3.1: (a) Image HRTEM et (b) spectroscopie Raman de l'hétérostructure 1T-$MoS_2$/2H-$MoS_2$**

Dans ce qui suit, nous avons proposé, comme le montre la figure 3.2, un mécanisme de photodégradation qui sous-tend les performances photocatalytiques élevées de l'hétérostructure 1T-$MoS_2$/2H-$MoS_2$. Selon ce mécanisme, la phase 2H-$MoS_2$ agit comme un photo-sensibilisateur et la phase métallique 1T-$MoS_2$ agit comme un co-catalyseur, favorisant le transfert des porteurs. Les paires électron-trou sont photogénérées dans le 2H-$MoS_2$ sous excitation lumineuse et les électrons excités de la bande de valence de 2H-$MoS_2$ sont plus susceptibles d'être piégés par 1T-$MoS_2$ eq.(4.1), réduisant ainsi leur taux de recombinaison et prolongeant leur durée de vie. L'objectif est de réduire considérablement la recombinaison des charges photogénérées et d'allonger ainsi la durée de vie de la réaction d'oxydoréduction qui permet la réduction des molécules de $O_2$ en $O_2^{*-}$ (eq.(4.2)). $O_2$ subit des réactions d'oxydoréduction multi-électroniques et protoniques (eq.(4.3) et (4.4) ), la molécule OH* formée à son tour, participe activement à la photodégradation de MB eq.(4.5).

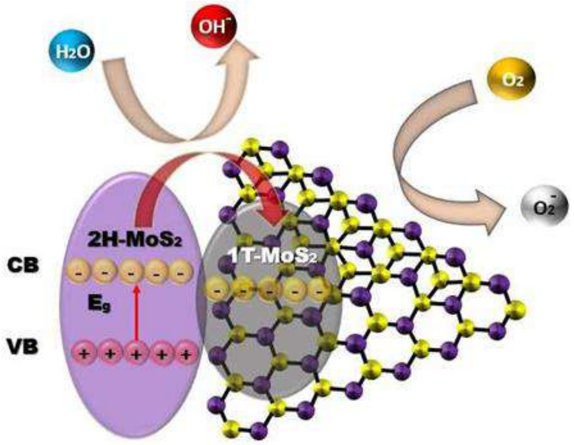

**Figure 3.2: Mécanisme de photogénération par 1T-MoS2/2H-MoS2**

(4.1) $$\text{1T-MoS}_2\text{/2H- MoS}_2 + h\nu \longrightarrow h^+_{VB} + e^-_{CB}$$

(4.2) $$e^- + O_2 \longrightarrow O_2^{*-}$$

(4.3) $$O_2 + 2e^- + 2H^+ \longrightarrow H_2O_2$$

(4.4) $$H_2O_2 + e^-_{CB} + H^+_2 + h\nu \longrightarrow OH^* + H_2O$$

(4.5) $$O_2^{*-}, OH^*, H^+ + MB \longrightarrow CO_2 + H_2O + \text{molécules inorganiques}$$

Contrairement aux travaux précédemment rapportés, la présente étude présenté en Article 5 permet la photodégradation de la MB à l'aide d'une hétérostructure hybride 1T-$MoS_2$/2H-$MoS_2$

fabriquée par le procédé CVD en une seule étape[58]. Elle permet d'obtenir une efficacité de photodégradation de plus de 80% du MB à une constante de photodégradation de $12.5\text{x}10^{-3}$ $\text{min}^{-1}$ et de $9.2\text{x}10^{-3}$ $\text{min}^{-1}$, sous excitation UV et lumière visible, respectivement, soit 1,2 fois plus que les performances rapportées dans la littérature. Ce travail a démontré que le mélange des deux phases 1T-$MoS_2$ et 2H-$MoS_2$, par la méthode de fabrication CVD contrôlée en une seule étape, est un moyen simple pour activer la photodégradation du MB et ouvre la voie à d'autres applications en photocatalyse.

## 4.5. Conclusion et perspectives

Le travail de thèse visait à étudier et à comprendre la relation entre les paramètres de fabri- cation des nanostructures à base de $MoS_2$ par deux méthodes CVD et PLD et leurs propriétés structurelles, morphologiques, électriques et optoélectroniques, ainsi que leurs performances de photodétection.

La première partie de la thèse concernait l'utilisation de la méthode CVD pour générer des nanostructures à base de $MoS_2$ de différentes compositions et morphologies et l'évaluation de leurs propriétés photoélectriques. A cet égard, nous avons démontré un bon contrôle de la morphologie, de la structure cristalline et des propriétés optiques du $MoS_2$. En particulier, nos résultats ont indiqué que les nanofils à base de $MoS_2$ et intégrés dans des dispositifs photoconducteurs, ont montré un photoréponse élevé de 20000% et une D* de $2.6 \times 10^9$ Jones. Ces performances ont été attribuées à la morphologie des nanofils de $MoS_2$ et à leur grande surface spécifique, qui ont considérablement augmenté l'absorption et le piégeage de la lumière, conduisant à un courant d'obscurité très faible. En outre, le rapport des dimensions de ces nanostructures s'est également avéré avantageux pour améliorer le transport des charges le long des nanofils. Par ailleurs, en tirant parti du faible courant d'obscurité obtenu, la photoréponse élevée atteinte par les nanofils de $MoS_2$ a également conduit à une détection élevée sous une faible excitation. Pour améliorer encore les propriétés de photodétection du $MoS_2$ et obtenir une photodétection à sur toute la gamme spectrale, nous avons développé une nouvelle hétérostructure basée sur le $MoS_2$ et le $MoO_2$ avec une morphologie originale composée de microfleurs de $MoO_2$ et de microfibres de $MoS_2$. Les mesures de photodétection ont été effectuées sous différentes longueurs d'onde d'excitation dans la gamme 450-630 nm. Les R et D* très élevées de 0.75 mA/W et 1.45x$10^7$ Jones, respectivement, ont été obtenues sous une excitation de lumière bleue à une puissance d'excitation très faible de 20 mW/$cm^2$.

La deuxième partie de la thèse concerne le développement de photodétecteurs basés sur des films minces de $MoS_2$ élaborés par PLD. Une étude systématique a été menée pour examiner l'effet de la température de dépôt sur les propriétés optoélectroniques et de photodétection des films minces de $MoS_2$. D'après nos résultats, les performances de photodétection les plus élevées ont été obtenues à la température de dépôt optimale de 500°C, avec des valeurs R et D* remarquables atteignant 125 mA/W et 9.2 x $10^9$ Jones, respectivement. Nous avons pu établir, pour la première fois, une corrélation linéaire entre R et D* et l'alignement vertical du $MoS_2$ en notant la corrélation frappante entre $T_d$, R, D*, $E_g$ et le rapport d'intensité Raman $[A_{1g}]/[E^1_{2g}]$.

Il ressort clairement de ce qui précède que le faible courant d'obscurité obtenu par les nanostructures de $MoS_2$ obtenues par CVD a joué un rôle déterminant dans leurs performances élevées en matière de photodétection. Cela est attribué aux morphologies intéressantes des nanostructures de $MoS_2$ générées par le contrôle des paramètres de la CVD. Ces morphologies ont également montré une amélioration de l'absorption optique et du transfert de charge grâce au piégeage de la lumière et à une large surface spécifique. D'autre part, les performances optoélectroniques élevées, obtenues pour le $MoS_2$ fabriqué par PLD ont été principalement dues au photocourant élevé généré, attribué à l'alignement vertical du $MoS_2$.

Les performances de captage et de conversion de lumière par le $MoS_2$ élaboré, nous ont conduit à développer une hétérostructure hybride 1T-$MoS_2$/2H-$MoS_2$, testée ensuite pour la photodégradation du bleu de méthylène. Cette hétérostructure hybride a montré une efficacité de photodégradation de plus de 80% du bleu de méthylène à une constante de photodégradation élevée de 12.5x$10^{-3}$ $min^{-1}$ et 9.2x$10^{-3}$ $min^{-1}$, sous l'excitation de lumière UV et visible, respectivement. Ces résultats suggèrent que la combinaison de la phase conductrice 1T-$MoS_2$ avec la phase semi-conductrice 2H-$MoS_2$ favorise non seulement la photogénération des paires électron-trou, mais améliore également le transfert de charge, accélérant ainsi la photodégradation du bleu de méthylène. Par ailleurs, un mécanisme de photodégradation par l'hétérostructure hybride a été proposé.

Ce travail fournit différents scénarios pour permettre et promouvoir les capacités du $MoS_2$ à capter de la lumière dans une large gamme de fréquence tout en réalisant une photoconversion élevée en termes de porteurs de charge qui peuvent être exploités dans deux applications majeures telles que la photodétection et la photodégradation. Les scénarios proposés sont basés sur des méthodes d'élaboration simples et directes. D'autres développements sont indéniablement nécessaires pour fabriquer un dispositif fonctionnel basé sur ces résultats.

## Perspectives

### 1/ Décoration du $MoS_2$ avec des matériaux plasmoniques

L'idée ici, est d'améliorer les nanostructures de $MoS_2$ en utilisant des matériaux plasmoniques afin d'augmenter sa capacité d'absorption de la lumière ainsi que le transfert de charge et la mobilité. À cet égard, la décoration du $MoS_2$ avec un métal noble est une méthode simple et accessible pour atteindre cet objectif. Des travaux antérieurs ont déjà démontré que les couches de $MoS_2$ enrobées de nanoparticules métalliques peuvent améliorer considérablement les propriétés optiques. Afin d'examiner cet effet sur nos nanostructures de $MoS_2$, nous avons lancé une étude préliminaire sur l'effet des nanoparticules d'argent (Ag-NP) sur la croissance du $MoS_2$ et leur impact sur les performances de photodétection.

Au préalable, des Ag-NP ont été déposées sur un substrat de quartz par PLD, puis des nanostructures de $MoS_2$ ont été déposées par CVD conventionnelle. Le $MoS_2$ obtenu semble croître verticalement sur les précurseurs Ag-NPs.

Nos premiers résultats montrent que ces nouveaux nanocomposites Ag-NPs/$MoS_2$ présentent des propriétés de photodétection étendues sur l'ensemble du spectre visible, ce qui se traduit par une augmentation de D* allant jusqu'à 516% par rapport au performance enregistré sur le $MoS_2$ seul. Ces résultats préliminaires pourraient ouvrir la voie à la conception et au développement de dispositifs optoélectroniques très réactifs basés sur des nanostructures combinées avec des NPs métalliques et de $MoS_2$. Le résultat est accepté dans la conférence EUROCON 2023 qui se tient à Torino est fournie dans l'Article 6.

### 2/ Evaluation du $MoS_2$ fabriqué par PLD dans le domaine photovoltaïque

Le photocourant élevé obtenu sur les films minces de $MoS_2$ obtenus par PLD pourrait être capitalisé dans des applications photovoltaïques. Dans ce sens, il est d'un grand intérêt d'acquérir des cibles PLD à base de $MoS_2$ dopé n et p afin de réaliser des jonctions p-n de haute qualité.

### 2/ Evaluation du $MoS_2$ fabriqué par CVD pour la détection de gaz

Les morphologies originales révélées sur les nanostructures de $MoS_2$ obtenues par CVD pourraient être utilisées pour évaluer leurs performances dans la détection des gaz toxiques. Ces morphologies pourraient offrir de grandes possibilités de sites pour les interactions gaz-$MoS_2$.

# CONCLUSION AND OUTLOUKS

The thesis work aimed at investigating and comprehending the relationship between the fabrication parameters of $MoS_2$ based nanostructures by both methods CVD and PLD and their structural, morphological, electrical, and optoelectronic properties, as well as their performances once they are integrated into functional photodetection devices.

The first part of the thesis concerned the use of the CVD method to generate $MoS_2$-based nanostructures of various compositions and morphologies and the evaluation of their photoelectric properties. In this regard, we have demonstrated a good control of the morphology, the crystalline structure, and the optical properties of $MoS_2$. In particular, our findings have indicated that the $MoS_2$-based nanowires and integrated into photoconductive devices, have shown a $P_{hr}$ as high as 20000% and a D* of 2.6 x $10^9$ Jones. These performances were ascribed to the $MoS_2$ nanowires' morphology and large effective surface area, which have significantly increased the light absorption and trapping leading to very low dark current. Moreover, the aspect ratio of these nanostructures has also appeared to be advantageous for improved charge transport along the nanowires. Furthermore, taking advantage of the low dark current obtained, the high $P_{hr}$ achieved by the $MoS_2$ nanowires, has also led to high detectivity at a very low power excitation. To further enhance the photodetection properties of our $MoS_2$ and attain a broadband photodetection, we have developed novel heterostructure based on $MoS_2$ and $MoO_2$ with an original morphology consisting of $MoO_2$ microflowers and MoS2 microfibers. The photodetection measurements were conducted under various wavelength excitations in 450—630 nm range. The highest responsivity and detectivity of 0.75 mA/W and 1.45x$10^7$ Jones, respectively were obtained under blue light excitation at very low excitation power of 20 mW/$cm^2$.

The second part of the thesis concerns the development of photodetectors based on $MoS_2$ thin films elaborated by PLD. A systematic investigation was carried out to examine the effect of deposition temperature on the structure, optoelectronic, and photodetection properties of $MoS_2$ thin films. Based on our findings, the highest photodetection performances of were achieved at the optimal deposition temperature of 500$^o$C, with remarkable R and D* values as high as 125 mA/W and 9.2 x $10^9$ Jones, respectively. We were able to establish, for the first time, a constant-plus-linear correlation between R and D* and the vertical alignment of the $MoS_2$ by noting the striking correlation between $T_d$, R, D*, $E_g$ and Raman intensity $[A_{1g}]/[E^1_{2g}]$ ratio.

From all above, it is clear that the low dark current achieved by the CVD-grown $MoS_2$ nanostructures, has played a key role in their high photodetection performances. It is attributed to the interesting $MoS_2$ nanostructures morphologies generated by the control of CVD technique parameters. These morphologies have also shown an improved optical absorption and charge transfer ascribed to light trapping and high surface area. On the other hand, the obtained high optoelectronic performances of the PLD grown $MoS_2$ were mainly due to the high generated photocurrent, ascribed to the vertically aligned $MoS_2$.

Taking benefit of the very good light harvesting and conversion of elaborated $MoS_2$, we have elaborated a hybrid 1T/2H-$MoS_2$ heterostructure, used for methylene blue photodegradation. This hybrid heterostructure has shown more than 80% photodegradation of methylene blue at a high rate-constant of $12.5\text{x}10^{-3}$ $\text{min}^{-1}$ and $9.2\text{x}10^{-3}$ $\text{min}^{-1}$, under UV and visible light excitations, respectively. These findings suggest that combining the conductive 1T-$MoS_2$ phase with the semi-conducting 2H-$MoS_2$ phase not only supports photogeneration of electron-hole pairs but also enhances charge transfer and thereby accelerates methylene blue photodegradation. Moreover, a mechanism of MB photodegradation by the hybrid heterostructure was proposed.

This work provides various scenarios to enable and promote the $MoS_2$ capabilities in broad- band light harvesting while achieving high photoconversion in terms of valuable charge carriers that can be exploited in two major applications such as photodetection and photodegradation. The scenarios proposed, are based on facile and straightforward elaboration methods. Further developments are undeniably still required to construct a functional device based on these findings.

## Outlooks

### 1/ Decoration of $MoS_2$ with plasmonic materials

The idea here is to upgrade $MoS_2$ nanostructures using plasmonic materials in order to increase their light absorption as well as charge transfer and mobility. In this regard, decorating $MoS_2$ with Nobel metals is a straightforward and accessible method to achieve this goal. Previous works have already demonstrated that $MoS_2$ layers embedded with metallic nanoparticles can dramatically improve optical properties. To examine such an effect on our $MoS_2$ nanostructures, we have initiated a preliminary study on the effect of silver nanoparticles (Ag-NPs) on the $MoS_2$ growth and their impact on photodetection performances.

Beforehand, Ag-NPs were deposited on quartz substrate using the PLD process, then $MoS_2$ nanostructures were subsequently grown by conventional CVD method. The obtained $MoS_2$ appeared to grow on Ag-NPs seeds vertically.

Our first results show that these novel Ag-NPs/$MoS_2$ nanocomposite exhibits improved photodetection properties across the entire visible spectrum, resulting in an increased specific detectivity (D*) of up to 516% compared to sole $MoS_2$. These preliminary findings could pave the way for the design and development of highly responsive optoelectronic devices based on combined metal NPs and $MoS_2$ nanostructures. The result is accepted as a proceeding in EUROCON 2023 conference held at Torino. The entire proceeding is provided in Article 6.

### 2/ Evaluation of the PLD grown $MoS_2$ in photovoltaics

The obtained high photocurrent obtained on PLD-grown $MoS_2$ thin films could be capitalized in photovoltaics applications. In this sense, it is of great interest to acquire PLD targets based on n and p-doped $MoS_2$ to secure p-n junction with high quality.

### 3/ Evaluation of CVD grown $MoS_2$ in gas sensing

The novel morphologies revealed on CVD-grown $MoS_2$ nanostructures could be used to evaluate their performances in detecting toxic gases. These morphologies could provide large site possibilities for gas-$MoS_2$ interactions.

# BIBLIOGRAPHIE

[1] Krishnan U, Kaur M, Singh K, Kumar M and Kumar A 2019 A synoptic review of MoS 2 : Synthesis to applications *Superlattices Microstruct.* **128** 274–97

[2] Kim S, Park W, Kim D, Kang J, Lee J, Jang H Y, Song S H, Cho B and Lee D 2020 Novel exfoliation of high-quality 2H-MoS2 nanoflakes for solution-processed photodetector *Nanomaterials* **10** 1045

[3] Dan Tan, Willatzen M and Wang Z L 2019 Prediction of strong piezoelectricity in 3R-MoS2 multilayer structures *Nano Energy* **56** 512–5

[4] Paradisanos I, Shree S, George A, Leisgang N, Robert C, Watanabe K, Taniguchi T, Warburton R J, Turchanin A, Marie X, Gerber I C and Urbaszek B 2020 Controlling interlayer excitons in MoS2 layers grown by chemical vapor deposition *Nat. Commun.* **11** 1–7

[5] Wang R, Shao Q, Yuan Q, Sun P, Nie R and Wang X 2020 Direct growth of high-content 1T phase MoS2 film by pulsed laser deposition for hydrogen evolution reaction *Appl. Surf. Sci.* **504** 144320

[6] Barvat A, Prakash N, Singh D K, Dogra A, Khanna S P, Singh S and Pal P 2018 Mixed Phase Compositions of MoS2 Ultra Thin Film Grown by Pulsed Laser Deposition *Mater. Today Proc.* **5** 2241–5

[7] Xu H, Yi J, She X, Liu Q, Song L, Chen S, Yang Y, Song Y, Vajtai R, Lou J, Li H, Yuan S, Wu J and Ajayan P M 2018 2D heterostructure comprised of metallic 1T-MoS2/Monolayer O-g-C3N4 towards efficient photocatalytic hydrogen evolution *Appl. Catal. B Environ.* **220** 379–85

[8] Tian L, Wu R and Liu H Y 2019 Synthesis of Au-nanoparticle-loaded 1T@2H-MoS 2 nanosheets with high photocatalytic performance *J. Mater. Sci.* **54** 9656–65

[9] Yao Y, Ao K, Lv P and Wei Q 2019 MoS2 coexisting in 1T and 2H phases synthesized by common hydrothermal method for hydrogen evolution reaction *Nanomaterials* **9** 1–12

[10] Pradhan G and Sharma A K 2019 Temperature controlled 1T/2H phase ratio modulation in mono- and a few layered MoS 2 films *Appl. Surf. Sci.* **479** 1236–45

[11] Splendiani A, Sun L, Zhang Y, Li T, Kim J, Chim C Y, Galli G and Wang F 2010 Emerging photoluminescence in monolayer MoS2 *Nano Lett.* **10** 1271–5

[12] Eda G, Yamaguchi H, Voiry D, Fujita T, Chen M and Chhowalla M 2011 Photoluminescence from chemically exfoliated MoS 2 *Nano Lett.* **11** 5111–6

[13] Mawlong L P L, Paul K K and Giri P K 2021 Exciton-plasmon coupling and giant photoluminescence enhancement in monolayer MoS2 through hierarchically designed TiO2/Au/MoS2 ternary core − Shell heterostructure *Nanotechnology* **32** 215201

[14] Mukherjee B, Tseng F, Gunlycke D, Amara K K, Eda G and Simsek E 2015 Complex electrical permittivity of the monolayer molybdenum disulfide (MoS_2) in near UV and visible *Opt. Mater. Express* **5** 447

[15] Pradhan G and Sharma A K 2018 Anomalous Raman and photoluminescence blue shift in mono- and a few layered pulsed laser deposited MoS2 thin films *Mater. Res. Bull.* **102** 406–11

[16] Li H, Zhang Q, Yap C C R, Tay B K, Edwin T H T, Olivier A and Baillargeat D 2012 From bulk to monolayer MoS 2: Evolution of Raman scattering *Adv. Funct. Mater.* **22** 1385–90

[17] Nam G H, He Q, Wang X, Yu Y, Chen J, Zhang K, Yang Z, Hu D, Lai Z, Li B, Xiong Q, Zhang Q, Gu L and Zhang H 2019 In-Plane Anisotropic Properties of 1T′-MoS2 Layers *Adv. Mater.* **31** 2–7

[18] Zhang H, Ma Y, Wan Y, Rong X, Xie Z, Wang W and Dai L 2015 Measuring the Refractive Index of Highly Crystalline Monolayer MoS2 with High Confidence *Sci. Rep.* **5** 1–7

[19] Lee C, Yan H, Brus L E, Heinz T F, Hone J and Ryu S 2010 Anomalous lattice vibrations of single- and few-layer MoS2 *ACS Nano* **4** 2695–700

[20] Gupta A, Sakthivel T and Seal S 2015 Recent development in 2D materials beyond graphene *Prog. Mater. Sci.* **73** 44–126

[21] Janica I, Iglesias D, Ippolito S, Ciesielski A and Samorì P 2020 Effect of temperature and exfoliation time on the properties of chemically exfoliated MoS2nanosheets *Chem. Commun.* **56** 15573–6

[22] Zhu D, Shu H, Jiang F, Lv D, Asokan V, Omar O, Yuan J, Zhang Z and Jin C 2017 Capture the growth kinetics of CVD growth of two-dimensional MoS2 *npj 2D Mater. Appl.* **1** 1–7

[23] Deokar G, Rajput N S, Vancsó P, Ravaux F, Jouiad M, Vignaud D, Cecchet F and Colomer J F 2017 Large area growth of vertically aligned luminescent MoS2 nanosheets *Nanoscale* **9** 277–87

[24] Zeng T, You Y, Wang X, Hu T and Tai G 2016 Chemical vapor deposition and device application of two-dimensional molybdenum disulfide-based atomic crystals *Prog. Chem.* **28** 459–70

[25] Muratore C, Voevodin A A and Glavin N R 2019 Physical vapor deposition of 2D Van der Waals materials: a review *Thin Solid Films* **688** 137500

[26] Kaindl R, Bayer B C, Resel R, Müller T, Skakalova V, Habler G, Abart R, Cherevan A S, Eder D, Blatter M, Fischer F, Meyer J C, Polyushkin D K and Waldhauser W 2017 Growth, structure and stability of sputter-deposited MoS2 thin films *Beilstein J. Nanotechnol.* **8** 1115–26

[27] Xi J, Huang X, Hu M and Xiang W 2020 Dependence of laser parameters on structural properties of pulsed laser-deposited MoS2 thin films applicable for field effect transistors *J. Mater. Sci. Mater. Electron.* **31** 21118–27

[28] Bertoldo F, Unocic R R, Lin Y C, Sang X, Puretzky A A, Yu Y, Miakota D, Rouleau C M, Schou J, Thygesen K S and Geohegan D B 2021 Intrinsic Defects in MoS2Grown by Pulsed Laser Deposition: From Monolayers to Bilayers *ACS Nano* **15** 2858–68

[29] Hai-Dou W, Bin-Shi X, Jia-Jun L and Da-Ming Z 2005 Characterization and anti-friction on the solid lubrication MoS 2 film prepared by chemical reaction technique *Sci. Technol. Adv. Mater.* **6** 535–9

[30] Taffelli A, Dirè S, Quaranta A and Pancheri L 2021 Mos2 based photodetectors: A review

*Sensors* **21** 2758

[31] Nalwa H S 2020 A review of molybdenum disulfide (MoS2) based photodetectors: From ultra-broadband, self-powered to flexible devices *RSC Adv.* **10** 30529–602

[32] Rahmati B, Hajzadeh I, Taheri M, Karimzadeh R, Mohajerzadeh S and Mohseni S M 2019 Plasmonic improvement photoresponse of vertical-MoS2 nanostructure photodetector by Au nanoparticles *Appl. Surf. Sci.* **490** 165–71

[33] Kim Y, Bark H, Kang B and Lee C 2019 Wafer-Scale Substitutional Doping of Monolayer MoS 2 Films for High-Performance Optoelectronic Devices *ACS Appl. Mater. Interfaces* **11** 12613–21

[34] Islam A, Lee J and Feng P X L 2018 Atomic Layer GaSe/MoS2 van der Waals Heterostructure Photodiodes with Low Noise and Large Dynamic Range *ACS Photonics* **5** 2693–700

[35] Wu W, De D, Chang S C, Wang Y, Peng H, Bao J and Pei S S 2013 High mobility and high on/off ratio field-effect transistors based on chemical vapor deposited single-crystal MoS2 grains *Appl. Phys. Lett.* **102** 142106

[36] Gomes F O V, Pokle A, Marinkovic M, Balster T, Anselmann R, Nicolosi V and Wagner V 2019 High mobility solution processed MoS2 thin film transistors *Solid. State. Electron.* **158** 75–84

[37] Deokar G, Vancsó P, Arenal R, Ravaux F, Casanova-Cháfer J, Llobet E, Makarova A, Vyalikh D, Struzzi C, Lambin P, Jouiad M and Colomer J F 2017 MoS2–Carbon Nanotube Hybrid Material Growth and Gas Sensing *Adv. Mater. Interfaces* **4** 1–10

[38] Xin X, Song Y, Guo S, Zhang Y, Wang B, Wang Y and Li X 2020 One-step synthesis of P-doped MoS2 for efficient photocatalytic hydrogen production *J. Alloys Compd.* **829** 154635

[39] Long L L, Chen J J, Zhang X, Zhang A Y, Huang Y X, Rong Q and Yu H Q 2016 Layer-controlled growth of MoS2 on self-assembled flower-like Bi2S3 for enhanced photocatalysis under visible light irradiation *NPG Asia Mater.* **8** 1–9

[40] S. I R, Xu X, Yang W, Yang F, Hou L and Li Y 2016 Highly active and reflective MoS2 counter electrode for enhancement of photovoltaic efficiency of dye sensitized solar cells *Electrochim. Acta* **212** 614–20

[41] Goel N, Kumar R, Roul B, Kumar M and Krupanidhi S B 2018 Wafer-scale synthesis of a uniform film of few-layer MoS2 on GaN for 2D heterojunction ultraviolet photodetector *J. Phys. D. Appl. Phys.* **51** 374003

[42] Li Y, Distefano J G, Murthy A A, Cain J D, Hanson E D, Li Q, Castro F C, Chen X and Dravid V P 2017 Superior Plasmonic Photodetectors Based on Au@MoS2 Core-Shell Heterostructures *ACS Nano* **11** 10321–9

[43] Selamneni V, Raghavan H, Hazra A and Sahatiya P 2021 MoS2/Paper Decorated with Metal Nanoparticles (Au, Pt, and Pd) Based Plasmonic-Enhanced Broadband (Visible-NIR) Flexible Photodetectors *Adv. Mater. Interfaces* **8** 1–12

[44] Deokar G, Vignaud D, Arenal R, Louette P and Colomer J 2016 Synthesis and characterization of MoS2 nanosheets *Nanotechnology* **27** 075604

[45] Mouloua D, Rajput N S, Blach J-F, Lejeune M, El Marssi M, El Khakani M A and Jouiad M 2022 Fabrication control of MoS2/MoO2 nanocomposite via chemical vapor deposition for optoelectronic applications *Mater. Sci. Eng. B* **286** 116035

[46] Mouloua D, Rajput N S, Saitzek S, Kaja K, Hoummada K, El Marssi M, El Khakani M A and Jouiad M 2022 Broadband photodetection using one-step CVD-fabricated MoS2/MoO2 microflower/microfiber heterostructures *Sci. Rep.* **12** 1–13

[47] Yang Z and Hao J 2016 Progress in pulsed laser deposited two-dimensional layered materials for device applications *J. Mater. Chem. C* **4** 8859–78

[48] Barvat A, Prakash N, Satpati B, Singha S S, Kumar G, Singh D K, Dogra A, Khanna S P, Singha A and Pal P 2017 Emerging photoluminescence from bilayer large-area 2D MoS2 films grown by pulsed laser deposition on different substrates *J. Appl. Phys.* **122** 015304

[49] Late D J, Shaikh P A, Khare R, Kashid R V., Chaudhary M, More M A and Ogale S B 2014 Pulsed laser-deposited MoS2 thin films on W and Si: Field emission and photoresponse studies *ACS Appl. Mater. Interfaces* **6** 15881–8

[50] Tumino F, Casari C S, Passoni M, Russo V and Li Bassi A 2019 Pulsed laser deposition of single-layer MoS2 on Au(111): From nanosized crystals to large-area films *Nanoscale Adv.* **1** 643–55

[51] Kumar S, Sharma A, Ho Y T, Pandey A, Tomar M, Kapoor A K, Chang E Y and Gupta V 2020 High performance UV photodetector based on MoS2 layers grown by pulsed laser deposition technique *J. Alloys Compd.* **835** 155222

[52] Serna M I, Yoo S H, Moreno S, Xi Y, Oviedo J P, Choi H, Alshareef H N, Kim M J, Minary-Jolandan M and Quevedo-Lopez M A 2016 Large-Area Deposition of MoS2 by Pulsed Laser Deposition with in Situ Thickness Control *ACS Nano* **10** 6054–61

[53] Ka I, Le Borgne V, Fujisawa K, Hayashi T, Kim Y A, Endo M, Ma D and El Khakani M A 2016 Multiple exciton generation induced enhancement of the photoresponse of pulsed-laser-ablation synthesized single-wall-carbon-nanotube/PbS-quantum-dots nanohybrids *Sci. Rep.* **6** 1–11

[54] Trabelsi K, Hajjaji A, Gaidi M, Bessais B and El Khakani M A 2017 Enhancing the photoelectrochemical response of TiO2 nanotubes through their nanodecoration by pulsed-laser-deposited Ag nanoparticles *J. Appl. Phys.* **122** 064503

[55] Khan I, Saeed K, Zekker I, Zhang B, Hendi A H, Ahmad A, Ahmad S, Zada N, Ahmad H, Shah L A, Shah T and Khan I 2022 Review on Methylene Blue: Its Properties, Uses, Toxicity and Photodegradation *Water* **14** 242

[56] Rani A, Patel A S, Chakraborti A, Singh K and Sharma P 2021 Enhanced photocatalytic activity of plasmonic Au nanoparticles incorporated MoS2 nanosheets for degradation of organic dyes *J. Mater. Sci. Mater. Electron.* **32** 6168–84

[57] Singh J and Soni R K 2021 Enhanced sunlight driven photocatalytic activity of In2S3 nanosheets functionalized MoS2 nanoflowers heterostructures *Sci. Rep.* **11** 1–14

[58] Mouloua D, Lejeune M, Rajput N S, Kaja K, Marssi M El, Khakani M A El and Jouiad M 2023 One-step chemically vapor deposited hybrid 1T-MoS2/2H-MoS2 heterostructures towards methylene blue photodegradation *Ultrason. Sonochem.* **95** 106381

# APPENDIX: CHARACTERISATION TECHNIQUES

## X-ray diffraction

X-ray diffraction (XRD) is a versatile, non-destructive analytical method for the identification of the crystallographic structure and the analysis of the crystallinity of a variety of materials (bulk, thin film, powder, etc.). It also provides a wide range of information on the structural properties of the analyzed material, such as crystallite size estimation and lattice parameter calculation. Diffraction occurs when waves interact with a regular structure with a repeat distance approxi- mately equal to the Wavelenght.

The phenomenon is widespread in nature and occurs on a wide range of scales. The distance between the interarticular planes $d_{hkl}$ (see figure 4.1), for a family of crystal planes (h,k,l) (h,k,l designate the Miller indices), can be calculated using the Bragg diffraction formula below:

$$2d_{hkl} \sin\theta = n\lambda \tag{4.1}$$

Where θ is the incidence angle, n is an integer, and λ is the x-ray wavelength. The XRD analyses conducted in this thesis were carried out on D8 Discover diffractometry BrukerTM (KαCu = 1.54 Å).

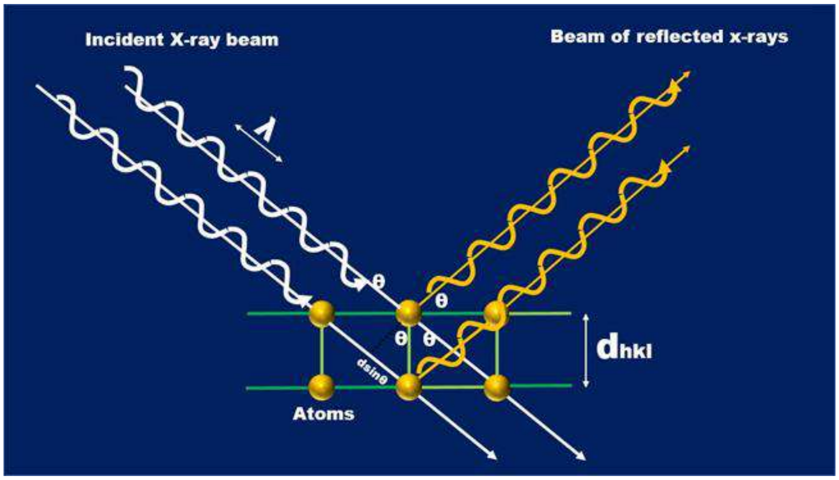

Figure 4.1: Principle of XRD mechanism.

## Raman spectroscopy

Raman spectroscopy is a non-destructive method for the characterization of the vibrational modes of a considered material (see figure 4.2). Raman is supplementary to XRD for secondary phase characterizing. It is a spectroscopic method for detecting vibrational, rotational, and other states in a molecular system. This method is based on a phenomenon known as inelastic light scattering. When a medium interacts with an impinging wavelength, it does change its frequency. Hence, the Raman effect is the result of this frequency shift. Typically, Raman spectroscopy consists of the interaction of a monochromatic light (such as a laser) with the known frequency with the sample surface. The incident radiation's energy $E_0$ is defined by the following relationship:

$$E_0 = hv_0 = hc/\lambda \tag{4.2}$$

h is Planck's constant ($6.63 \times 10^{-34}$ J s), v is the frequency of the incident light, c is the light celerity in vacuum ($3.10^8$ m/s), and λ: wavelength of the incident beam. The wavelength of the scattered light essentially depends on the excitation wavelength. As the Raman scattering wavelength is an impractical number for comparison between spectra measured using different lasers, an offset given by:

$$\Delta\omega = 10^7 \left( (1/\ \lambda l_{aser}) - (1/\ \lambda) \right) \tag{4.3}$$

$\Delta\omega$ is the Raman shift in $cm^{-1}$, $\lambda l_{aser}$ is the laser excitation wavelength in nm and λ is the Raman scattering wavelength in nm.

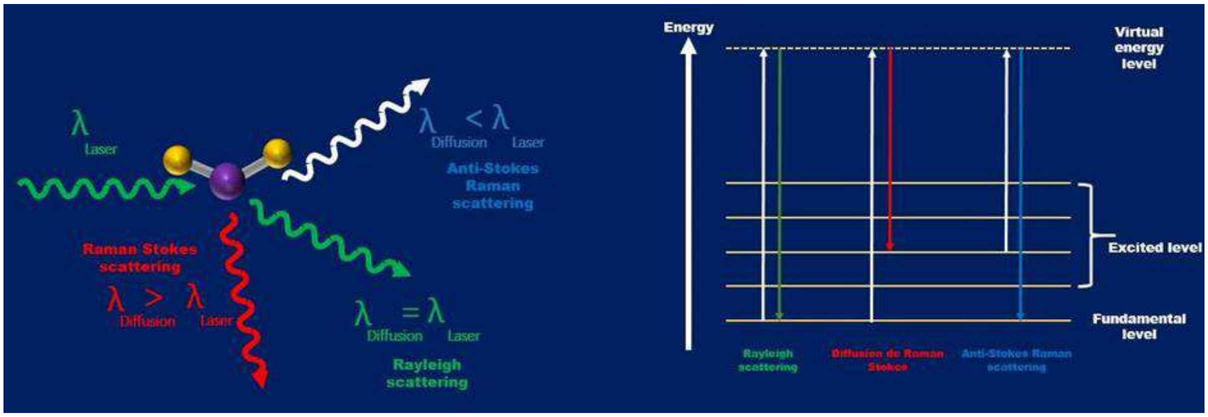

**Figure 4.2: Scattering effects involved in Raman spectroscopy**

When the incident light interacts with a molecule and does not change its energy, so the frequency of scattered light v is the same as that of incident light $v_0$. We then have $v= v_0$. This is called Rayleigh scattering.

If the interaction causes the light photon to gain vibrational energy $v_v$ from the molecule, then the frequency of the scattered light will be higher than that of the incident light. Hence we have: $v=v_0+v_v$. This is anti-Stokes Raman scattering.

If the interaction causes the molecule to gain energy from the incident photon, then the frequency of the scattered light will be lower than that of the incident light. We then have: $v=v_0-v_v$. This phenomenon is Raman Stokes scattering.

The vibrational modes of various $MoS_2$ phases were obtained using a micro-Raman spectrometer, Renishaw$^{TM}$.

### UV-Vis-near IR spectrometer

The UV-Vis near IR spectrometer allows measuring the intensity (I) of light transmitted through a thin layer at different wavelengths (λ). UV, Visible, and Infrared spectral lamp is placed in front of a monochromator. The absorption spectrum across a given range of wavelengths is obtained by determining the intensity versus wavelength (I(λ)) before and after the interaction with the sample. The absorption spectra of the sample can be used to calculate the value of the band gap of semiconductor materials. The optical absorption in this thesis was obtained using a UV-Vis-near IR spectrometer JASCO$^{TM}$ V-670.

### X-ray photoelectron spectroscopy (XPS)

X-ray photoelectron spectroscopy (XPS) is an invaluable tool in the field of material science for probing the electronic states and the elemental composition of the sample. It is a semi-quantitative method for obtaining information on the composition and chemical state of a material's surface, as well as identifying the elements present, chemical bonds, and concentrations. Because it is a surface-sensitive technique with low kinetic energies, XPS experiments are carried out in an ultra-high vacuum environment ($10^{-9}$ - $10^{-10}$ Torr). The photoelectric effect underpins the XPS principle. Indeed, it entails irradiating the sample with an X-ray beam to ionize the atoms (see figure 4.3).

After a direct transfer of energy from the photon to the electrons within the electron stream, the latter will emit electrons. The kinetic energy of the emitted electrons is used to calculate the binding energy, nature, and environment of the atom from which it is emitted. Indeed, by knowing the incident energy of the X-ray beam (hv: h is Planck's constant and v is the frequency of the X-rays used) and the kinetic energy ($E_C$) of the detected electron, the binding energy ($E_{BE}$) of this electron bound to the atomic orbital of the element sought can be calculated using the following equation:

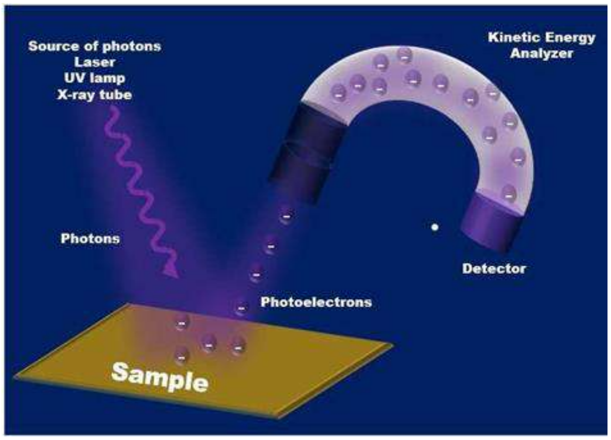

**Figure 4.3: Mechanism of XPS analysis**

## Scanning electron microscopy (SEM)

Scanning electron microscopy (SEM) was used to characterize the morphology and thickness of $MoS_2$ thin films. SEM consists of using the electron-matter interaction principle. Secondary electrons and backscattered electrons are emitted when an electron beam is focused on the surface of a material as illustrated in figure 4.4. The secondary electrons originate from the free outer electrons and are very weakly bonded to the atom's nucleus.

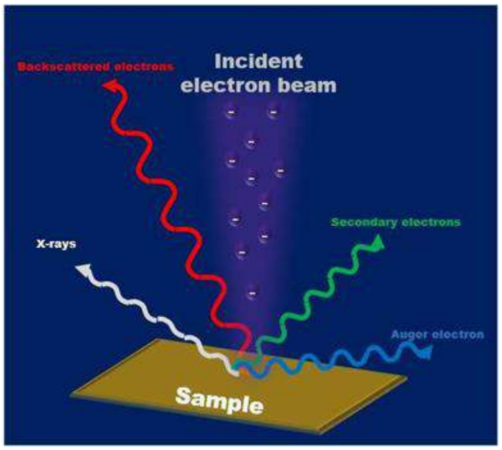

Figure 4.3: Mechanism of SEM analysis

The number of secondary electrons collected is strongly influenced by the surface orientation, which must be parallel to the incident beam. The detection of secondary electrons ejected by the incident electron beam provides information about the sample's topography. Backscattered electrons are the result of a quasi-elastic interaction between the incident beam and material atomic nuclei, and they provide a qualitative analysis of the chemical composition and orientation of the sample.

### Energy dispersive x-ray spectroscopy (EDS)

Energy dispersive x-ray spectroscopy (EDS) is an analytical tool for the elemental analysis of solid materials. It involves examining the X-ray photons re-emitted by the de-excitation of the sample's constituent atoms under the SEM electron beam. The radiation emitted during the interaction between the X-rays and the sample material is rendered as a spectrum, with variable intensity peaks corresponding to the elements present in the sample. Because X-ray photons penetrate quite deeply, the measured composition corresponds to about 1µm depth.

### Transmission electron microscopy

The morphology, crystallinity, and size of $MoS_2$ have been studied using transmission electron microscopy (TEM). It is a highly effective material science tool. A high-energy electron beam is shone through a very thin sample, and the interactions between the electrons and the atoms can be used to observe features such as crystal structure and structure features. Chemical analysis is also possible. In semiconductors, TEM can be used to investigate layer growth, structure, and defects. The TEM principle is based on the interaction of electrons beam accelerated by a potential difference of about 80 to 300 kV with a sample, which results in the formation of an image. The TEM works on the same basic principles as a light microscope, but instead of light, it uses electrons. Because electrons have a much smaller wavelength than light, the optimal resolution of TEM images is millions of magnitudes higher than that of a light microscope. Thus, TEMs can reveal the most minute details of internal structure, even down to individual atoms. In this thesis, the samples were analyzed using a Titan Thermofisher Scientific image Cs-corrected TEM system operating at 300 kV, and the TEM lamellas were prepared by the standard FIB lift-out technique using Helios Thermofisher Scientific's dual-focused ion beam system.

# CHAPTER 6: ARTICLES

## Article 1: D. Mouloua, A. Kotbi, G. Deokar, K. Kaja, M. EL Marssi, M. A. El Khakani, M. Jouiad, Materials-MDPI. 2021, 14, 3283.

materials

MDPI

*Review*

# Recent Progress in the Synthesis of $MoS_2$ Thin Films for Sensing, Photovoltaic and Plasmonic Applications: A Review

**Driss Mouloua [1,2], Ahmed Kotbi [1], Geetanjali Deokar [3], Khaled Kaja [4], Mimoun El Marssi [1], My Ali EL Khakani [2,*] and Mustapha Jouiad [1,*]**

[1] Laboratory of Physics of Condensed Matter, University of Picardie Jules Verne, 33 Saint Leu, 80039 Amiens, France; driss.mouloua@etud.u-picardie.fr (D.M.); ahmed.kotbi@u-picardie.fr (A.K.); mimoun.elmarssi@u-picardie.fr (M.E.M.)
[2] Institut National de la Recherche Scientifique, Centre-Énergie, Matériaux et Télécommunications, 1650, Blvd, Lionel–Boulet, Varennes, QC J3X-1S2, Canada; driss.mouloua@inrs.ca
[3] Physical Science and Engineering Division, Kaust University, Thuwal 23955-6900, Saudi Arabia; geetanjali.deokar@kaust.edu.sa
[4] Laboratoire National de métrologie et d'essais (LNE), 29 av. Roger Hannequin, 78197 Trappes, France; khaled.kaja@lne.fr
* Correspondence: m.a.elkhakani@inrs.ca (M.A.E.K.); mustapha.jouiad@u-picardie.fr (M.J.)

**Abstract:** In the surge of recent successes of 2D materials following the rise of graphene, molybdenum disulfide (2D-$MoS_2$) has been attracting growing attention from both fundamental and applications viewpoints, owing to the combination of its unique nanoscale properties. For instance, the bandgap of 2D-$MoS_2$, which changes from direct (in the bulk form) to indirect for ultrathin films (few layers), offers new prospects for various applications in optoelectronics. In this review, we present the latest scientific advances in the field of synthesis and characterization of 2D-$MoS_2$ films while highlighting some of their applications in energy harvesting, gas sensing, and plasmonic devices. A survey of the physical and chemical processing routes of 2D-$MoS_2$ is presented first, followed by a detailed description and listing of the most relevant characterization techniques used to study the $MoS_2$ nanomaterial as well as theoretical simulations of its interesting optical properties. Finally, the challenges related to the synthesis of high quality and fairly controllable $MoS_2$ thin films are discussed along with their integration into novel functional devices.

**Keywords:** layered materials; 2D-$MoS_2$; pulsed laser deposition; chemical vapor deposition; photovoltaic; gas sensors; plasmonics

check for updates

**Citation:** Mouloua, D.; Kotbi, A.; Deokar, G.; Kaja, K.; El Marssi, M.; EL Khakani, M.A.; Jouiad, M. Recent Progress in the Synthesis of $MoS_2$ Thin Films for Sensing, Photovoltaic and Plasmonic Applications: A Review. *Materials* **2021**, *14*, 3283. https://doi.org/10.3390/ma14123283

Academic Editor: Rafik Addou

Received: 16 May 2021
Accepted: 10 June 2021
Published: 14 June 2021

## 1. Introduction

Two-dimensional (2D) materials are generally defined as crystalline substances with a few atoms thickness [1]. Graphene was the first 2D crystal to be ever isolated in 2004 and has since been extensively investigated by many groups around the world [2–6]. In fact, graphene became known as the material of superlatives showing a mechanical strength hundreds of times larger than steel [7] while maintaining a high mechanical flexibility [8] and superior electrical and thermal conductivities [9]. Following the discovery of graphene [10], a very large spectrum of 2D materials possessing a wide range of highly attractive properties have emerged [8,10]. For instance, two-dimensional transition metal dichalcogenide (2D-TMDs) semiconducting (SC) materials have exhibited unique optical and electrical properties [11,12], resulting from the quantum confinement effect attributed to their shapes and sizes with respect to the Bohr radius [13–17], in addition to their surface effects, which is due to the transition from an indirect bandgap in the "bulk form" to a direct bandgap for the "mono- to few-layer" ultrathin film form [18]. The layered configuration of the 2D-TMDs materials is at the origin of their strong interaction with light [19] and the relatively high mobility of their charge carriers [20], which in turn prompted their use in many optoelectronic applications, such as ultra-thin field-effect transistors [21], photo-detectors [22], light emitting diode [23], and solar-cells [24]. Generally, 2D-TMDs form a family of graphite-like layered thin semiconducting structures with the chemical formula of $MX_2$, where M refers to a transition metal atom (Mo, W, etc.) and X is a chalcogen atom (Se, S, etc.). The layered nature of this class of 2D materials induces a strong anisotropy in their electrical, chemical, mechanical, and thermal properties. In particular, molybdenum disulfide ($MoS_2$) is the most studied layered 2D-TMD [25–30]. From a crystalline point of view, layered $MoS_2$ exists in three polymorphic crystalline structures: 1T (tetragonal) [31], 2H (hexagonal) [32], and 3R (rhombohedral) [33] (Figure 1). The crystallographic parameters associated to these crystalline forms are summarized in Table 1. In the case of mono- to few-layer structures, 2H-$MoS_2$ is the most thermodynamically stable phase and thus the most commonly encountered. When the $MoS_2$ is in the monolayer form, it takes an octahedral or a trigonal prismatic coordination phase.

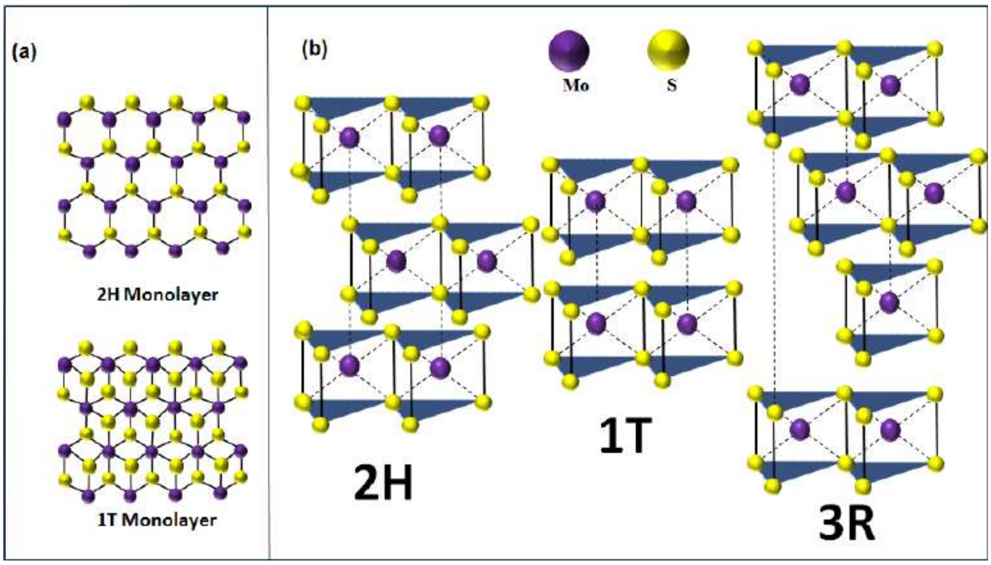

**Figure 1.** (**a**) Top view of 2H/1T $MoS_2$ monolayer. (**b**) Polymorphic structures of $MoS_2$ (2H is the hexagonal crystal form, 1T is the tetragonal crystal form, and 3R is the rhombohedral crystal form).

**Table 1.** Crystal parameters and the nature of polymorphic structures of 2D-$MoS_2$.

| Polymorphic Structure | Lattice Parameter | Point Group | Electronic Behavior | Ref |
|---|---|---|---|---|
| 1T | a = 5.60 Å, c = 5.99 Å | $D_{6d}$ | Metal | [31] |
| 2H | a = 3.15 Å, c = 12.30 Å | $D_{6h}$ | Semiconductor | [32] |
| 3R | a = 3.17 Å, c = 18.38 Å. | $C_{3v}$ | Semiconductor | [33] |

Furthermore, $MoS_2$ layered materials were observed to exhibit various shapes and morphologies, such as planar [34–36] and vertically aligned nanosheets (NSs) [37], nanoflowers [38], nanotubes [39], nanowires [40], and nanoplatelets [41,42]. This variety of forms could be controlled by choosing suitable synthesis routes with optimized operating parameters [38–41,43–47]. Thus, it is possible to adjust the 2D-$MoS_2$ properties to develop high performance devices i energy storage [47], electronics [46], photonics [45], sensing [48], and field emission [49] applications. Recently, up to few-layer $MoS_2$ nanosheets have been shown to be highly efficient for electronic, optoelectronic, and solar energy harvesting devices [50–52] because of their tunable direct bandgap [53], strong light-absorption, and prominent photoluminescence with energies lying in the visible range (1.8–1.9 eV) [54].

Although Mo and S are strongly covalently bonded within an individual layer, adjacent sheets are linked together only by the very weak van der Waals interaction. This weak bonding provides a facile processing route such as mechanical or chemical exfoliation to form few- to monolayer $MoS_2$ films. Unlike graphene, 2D-$MoS_2$ is much less prone to surface contaminations, which offers a superior chemical stability to 2D-MoS2, making it more attractive for the above-mentioned applications [55–57].

This review is timely to report on the state of the art of 2D-$MoS_2$ from synthesis, properties, and applications viewpoints. It also intends to provide insights on the remaining challenges to widen the applications range of this fantastic 2D-$MoS_2$ material. It is organized as follows. In Section 2, various fabrication routes are highlighted with a special focus on physical vapor deposition (PVD) methods. Key processing parameters are pinpointed and their influence on the material characteristics, i.e., thickness, crystallinity, morphology, etc., and properties are underlined. In Section 3, relevant techniques used to investigate the complex structure and morphology of 2D-$MoS_2$ are presented and discussed. In particular, its unique and outstanding optical properties are put forward through theoretical simulations based on the complex permittivity of the $MoS_2$ monolayer. In Section 4, density functional theory (DFT) calculations were carried out on both the bulk and the monolayer $MoS_2$ using Quantum Expresso™ code and one-dimensional solar cell capacitance simulator SCAPS-1D™. These calculations were used to determine, respectively, the optoelectronic properties and photovoltaic performances in solar cell configuration. Then, interesting applications in three selected fields where 2D-$MoS_2$ has shown promising outcomes, namely solar energy conversion, gas sensing, and plasmonics, are presented in Section 5. In the last section, we discuss the reported works and point towards new directions and applications in which 2D-$MoS_2$ would potentially play a key technological role.

## 2. Fabrication Techniques of 2D-$MoS_2$

Tremendous efforts have been devoted to the synthesis of 2D-$MoS_2$ with controllable large-area growth and uniform atomic layers using both top-down and bottom-up approaches. The most commonly used processing routes are detailed in the following sub-sections along with their advantages and limitations.

### *2.1. Mechanical and Chemical Exfoliations*

Mechanical exfoliation, also known as micromechanical cleavage, is a straightforward technique that takes advantage of the weak bonding between layers, for the production of high-quality mono- to few-layer $MoS_2$ [58–60]. It consists of exfoliating thin films of 2D-$MoS_2$ from a bulk $MoS_2$ crystal by using a low surface tension tape to break the weak interlayer bonds in a similar way as for grapheme [61]. Additional exfoliation of the extracted films may be needed to obtain few- to monolayer $MoS_2$. Tapes could be attached to glass slides to achieve planar exfoliation and slow peeling. The obtained monolayers are usually transferred to an appropriate substrate for further analysis and testing.

The advantage of the mechanical exfoliation process lies in its simplicity that requires the sole use of a confocal microscope to localize the 2D-$MoS_2$ layers deposited on the substrate. Conveniently, this technique can produce high crystalline quality mono- to few layers with a lateral size up to few tens of micrometers, making them highly suitable for sensing applications. However, this approach suffers from a lack of a consistent control in producing the 2D monolayers as it is heavily user-dependent and does not permit the control of the size and/or thickness uniformity of the exfoliated 2D-$MoS_2$ layers [62]. Therefore, the mechanical exfoliation technique is not necessarily suitable for the production of 2D-$MoS_2$ layers intended for large-area and high-throughput applications.

Chemical exfoliation, on the other hand, appears as a promising approach to produce large quantities of mono- and few-layer $MoS_2$ nanosheets [60,63–65]. Eda et al. [54] reported a high yield of monolayer crystal synthesis using chemical exfoliation of bulk $MoS_2$ via Li intercalation. However, this approach may induce an alteration in the quality of the produced 2D-$MoS_2$. For instance, the chemically exfoliated $MoS_2$ layers can lose their semiconducting properties because of the structural changes resulting from the Li intercalation process. However, this fabrication route stands by its ease of processing, low production costs, and suitability for catalysis and/or sensing applications [66].

### 2.2. Chemical Vapor Deposition

Chemical vapor deposition (CVD) is one of the most popular routes for large-scale, high-quality, and low-cost 2D-$MoS_2$ material production [49,67–69]. CVD is a bottom-up fabrication method at the equilibrium state, which enables the processing of layered 2D-$MoS_2$ with controlled morphology and good crystallinity while minimizing structural defects. The control of the CVD process is ensured by tuning the deposition parameters such as temperature, pressure, gas flow rate, precursor's quantities, and substrate types. The 2D-$MoS_2$ synthesis via the CVD technique can be achieved by means of thermal vapor sulfurization (TVS), thermal vapor deposition (TVD), and thermal decomposition (TD). Deokar et al. [43] used TVS for high quality and vertically-aligned luminescent $MoS_2$ nanosheets. A similar process could be used to grow 2D-$MoS_2$ layers [36,70] by employing two sources, such as molybdenum thin film (below 20 nm) or molybdenum oxide ($MoO_3$) powder deposited on a $SiO_2$/Si substrate as a first precursor and the sulfur powder or gaseous sulfur source ($H_2S$, etc.) as the second precursor [49,67–69,71,72]. A typical CVD sulfurization process (Figure 2a) is usually performed in a tubular furnace reactor, where a continuous argon flow (typical flow rate 100 sccm) is used as a carrier gas to stream the evaporated sulfur into the Mo source materials.

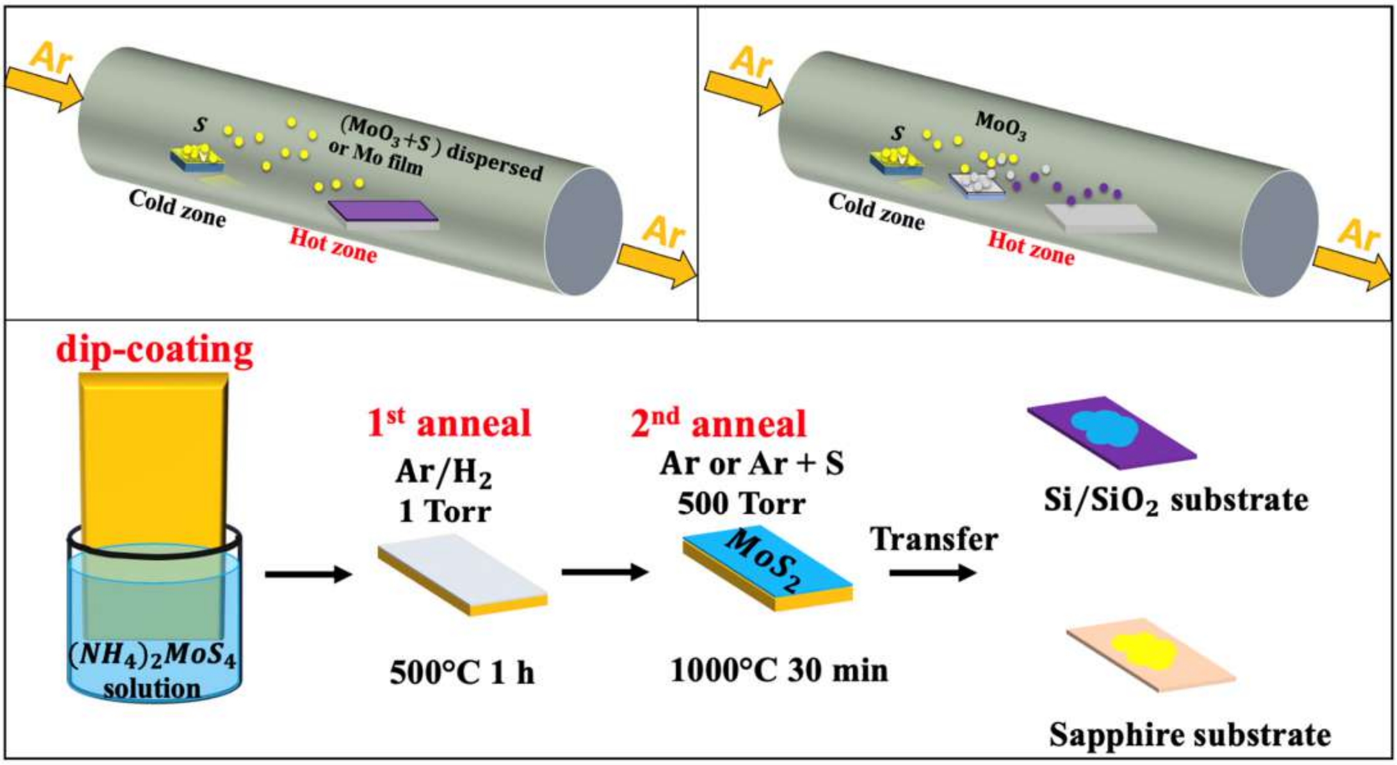

**Figure 2.** Schematic of the chemical vapor deposition techniques: (**a**) thermal vapor sulfurization process using a quartz tube; (**b**) thermal vapor deposition process using a quartz tube; and (**c**) thermal decomposition of $(NH_4)_2MoS_4$ (reproduced and adapted from Ref. [34]).

One of the critical aspects to be controlled in such a CVD tubular reactor is the temperature gradient between the S powder and the substrate. In fact, while the S powder is at 150–200 °C, the substrate's temperature—with or without Mo thin film—should be maintained in the 700–900 °C range to obtain the 2D-$MoS_2$ phase. This technique offers sufficient latitude to fairly control the thickness and the homogeneity of the grown 2D-$MoS_2$. The typical average lateral crystal size obtained by CVD is usually in the 10–30 nm range. Table 2 shows few examples of CVD-TVS grown $MoS_2$ nanostructures along with their associated processing conditions.

**Table 2.** Examples of CVD-TVS grown $MoS_2$ nanostructures.

| Substrate | Precursors | Growth Conditions | Morphology | Ref |
|---|---|---|---|---|
| Si | $MoO_3$ and S powders dispersed on substrate | $MoO_3$ and S powders dispersed on substrate at 850 °C; S powder at 400 °C; Ar-0.725 L/min; time reaction = 30 min | $MoS_2$ nanosheets | [43] |
| Si [001] | S powder and Mo film deposited on substrate | Mo deposited on Silicon at 850 °C, S at 400 °C; Ar-0.725 L/min; time reaction = 30 min | $MoS_2$ nanosheets | [44] |
| Si/$SiO_2$ | S powder and Mo film deposited on substrate | Mo deposited on Silicon at 850 °C, S at 400 °C; Ar-0.725 L/min; time reaction = 30 min | $MoS_2$ nanosheets | [49] |
| Diamond substrate | S powder and Mo deposited on substrate | Mo deposited on Silicon with S powder at 800 °C; $N_2$; ambient pressure; time reaction = 30 min | Horizontally and vertically $MoS_2$ | [73] |
| Si/$SiO_2$ | S powder and $MoO_3$ deposited on substrate | $MoO_3$ film deposited on Silicon at 750–850 °C, 600 mg of S powder at 100 °C; Ar-0.01 L/min; time reaction = 10 min | Mono-to few-layers of $MoS_2$ | [74] |

Table 2 shows the typical morphologies obtained for $MoS_2$, which seem to depend on the carrier gas and the type of the substrate used. The reaction time and the spatial position of the substrate strongly affect the number of resulting layers.

The TVD based $MoS_2$ growth (Figure 2b) involves the concomitant evaporation of both $MoO_3$ and S powders. This approach consists of a stepwise sulfurization of $MoO_3$ to form the $MoS_2$ phase. It has been shown that, by increasing the S vapor flux, the sulfurization proceeds through several phase changes before reaching the final product. First, $MoO_3$ is formed, then $MoO_2$ followed by $MoOS_2$, and finally $MoS_2$. This approach is very useful to obtain 2D $MoS_2$ layers with a lateral size of few tens of microns. The TVD growth conditions of $MoS_2$ under various conditions and with different characteristics are summarized in Table 3.

**Table 3.** Examples of TVD grown $MoS_2$ along with their relevant processing conditions (* D is the distance between the $MoO_3$ and *S* powders inside the tubular furnace).

| Substrate/Setup | $MoO_3$ (mg) | S (mg) | D * (cm) | Gas, Flow (sccm) | T (°C), Time (min) | Morphology | Ref |
|---|---|---|---|---|---|---|---|
| Si face-down | 15 | 80 | 18 | Ar<br>10 to 500 | 700, 30 | Flake size between 5.1–47.9 µm | [75] |
| $SiO_2$/Si face-up | 10 | 200 | 30 | Ar, 100 | 850, 20 | Monolayer, bilayer and trilayer $MoS_2$ | [76] |
| $SiO_2$/Si face-down | 10 | 100 | – | $N_2$, 20 | 650, 20 | $MoS_2$ monolayer | [77] |
| $SiO_2$/Si face-down | 10-30 | – | 25 | Ar, 150 | 800, 10 | $MoS_2$ triangular flakes | [78] |
| $SiO_2$/Si face-up | 50 | 175 | – | $N_2$, 300 | 750, 15 | $MoS_2$ monolayer with lateral size of 50 µm | [79] |

In comparison to the results obtained by CVD-TVS summarized in Table 2, TVD exhibits high-yield fabrication of 2D-$MoS_2$ monolayers generally exhibiting a triangular flakes shape. Besides, one can notice the two possible configurations of the substrate of interest in TVD face-up and face-down compared to CVD-TVS [75–79].

Moreover, the TD-based CVD method presents an alternative approach to produce highly crystalline $MoS_2$ thin layers with superior electrical properties on insulating substrates [34]. Typically, the TD-CVD is based on the high-temperature annealing of a thermally decomposed ammonium thiomolybdate layer $(NH_4)_2MoS_4$ in the presence of S, as illustrated in Figure 2c. It is worth noting that the excess in sulfur introduces changes in the shape, size, and morphology of fabricated $MoS_2$. It also leads to a p-type $MoS_2$ semiconductor by increasing the electrons deficiency. In contrast, the presence of sulfur vacancies in $MoS_2$ was reported to have a direct impact on the catalytic properties of $MoS_2$, suggesting a carriers' mobility alteration [80]

Besides, the addition of S during the high-temperature annealing drastically enhances the crystallinity of $MoS_2$. Relatively, centimeter-sized $MoS_2$ crystals could be formed on $Al_2O_3$ substrates compared to $SiO_2$ ones [35]. The fully covered $Al_2O_3$ substrate with an epitaxial monolayer of $MoS_2$ was achieved at 930 °C. The $MoS_2$ crystals nucleate in a single domain to pursue by domain-to-domain stitching process occurring during annealing at 1000 °C mediated by the oxygen flow. The difference in the self-limited monolayer growth observed between the $SiO_2$ and $Al_2O_3$ substrates is related to the absorption energy barrier on $MoS_2$ [37]. In particular, the growth of $MoS_2$ on $Al_2O_3$ obeys the surface-limited epitaxial growth mode, which is not the case for the $SiO_2$ due to lattice mismatch. Moreover, the patterning of the as-grown $MoS_2$ layers has been reported by means of the polydimethylsiloxane (PDMS) stamps and the reuse of the substrate after transferring the $MoS_2$ layers [35]. Recently, the epitaxial growth of centimeter wafer-scale single-crystal $MoS_2$ monolayers on vicinal Au (111) thin films were also obtained at a processing temperature of 720 °C, by melting and re-solidifying commercial Au foils [36]. This allows overcoming the evolution of antiparallel domains and twin boundaries, leading to the formation of polycrystalline films. It has been proposed that the step edge of Au (111) induced the unidirectional nucleation, growth, and subsequent merging of $MoS_2$ monolayer domains into single-crystalline films.

### 2.3. *Atomic Layer Deposition*

The atomic layer deposition (ALD) technique is known to produce high-quality thin films even at low temperatures, typically between 150 and 350 °C. Since ALD is an atom stepwise growth process, where the reactants are alternately injected into the growth area, it allows the purging of excess species and by-products after each reaction. As a result, high-quality films are obtained by sequential surface reactions. A schematic representation of the ALD synthesis of 2D-$MoS_2$ can be found elsewhere [81].

Despite the challenges related to its synthesis conditions, ALD makes it possible to deposit crystalline $MoS_2$ thin films at a relatively low temperature (<350 °C) followed by annealing. For instance, L.K. Tan et al. [82] reported the possibility to use ALD for the synthesis of highly crystallized $MoS_2$ films on sapphire substrates at 300 °C. They prepared $MoS_2$ films by alternating exposure of the substrate to Mo(V) chlorides ($MoCl_5$) and hydrogen disulfide ($H_2S$) vapors. Similarly, Mattinen et al. [83] proposed the use of a Mo based precursor, namely $Mo(thd)_3$ (thd = 2,2,6,6 tetramethylheptane 3,5-dionato), with $H_2S$ as a sulfur source. They have been able to achieve a self-limiting growth and a linear film thickness control (with a very low growth rate of $\approx$0.025 Å per cycle). While the crystallinity of these $MoS_2$ films was found to be particularly good (taking into account that the deposition was done at a low temperature), their surface was rather rough, consisting of flake-like grains with a size of $\approx$10–30 nm. One of the advantages of this process is the possibility to deposit layered $MoS_2$ films on various substrates. Table 4 summarizes the main processing conditions used by different groups along with the achieved $MoS_2$ film thicknesses.

The ALD appears as a potentially interesting technique for the production of high-quality $MoS_2$ ultrathin films at relatively low temperatures and with the ability to achieve excellent step coverage onto different substrates. However, the very low throughput of the ALD might hinder its scalability and competitiveness in comparison with other physical and/or chemical deposition methods.

**Table 4.** Summary of the ALD deposition conditions and achieved $MoS_2$ film thicknesses.

| Substrate | Precursors | P (Torr) | T (°C) | Cycles | Thickness | Ref |
|---|---|---|---|---|---|---|
| $SiO_2$/Si | Mo hexacarbonyl and dimethyldisulfide | 1.4–3.3 | 100 | 100 | ≈11 nm | [84] |
| $SiO_2$/n-Si | $MoCl_5$ and $H_2S$ | 0.75 | 350–450 | 100 | ≈9 nm | [85] |
| $Al_2O_3$ | $Mo(NMe_2)_4$ and $H_2S$ | – | 60 | 100 | ≈12 nm | [81] |
| $Al_2O_3$ 2-inch wafer | $MoCl_5$ and $H_2S$ | 0.001 | 300 | 50 | ≈9 nm | [82] |
| $SiO_2$/Si | $Mo(thd)_3$ (thd = 2,2,6,6 tetramethylheptane 3,5-dionato) and $H_2S$ | 3.75 | 300 | 100 | ≈25 nm | [83] |
| $Al_2O_3$ c-plane | $MoCl_5$ and hexamethyldisilathiane | 3.75 | 350 | 250 | ≈22 nm | [86] |
| Carbon nanotubes, Si-wafers and glass | bis(tbutylimino)bis(dimethylamino) Mo (VI) and $H_2S$ | 300 | 100–250 | 100 | ≈11 nm | [87] |
| Si, $SiO_2$, $Al_2O_3$ | $MoCl_5$ and $H_2S$ | 3.75 | 430–480 | 1 | 1 layer | [88] |
| Si | $MoCl_5$ and $H_2S$ | – | 390–480 | 100 | ≈21.5 nm | [89] |
| $SiO_2$ | Mo hexacarbonyl and $H_2S$ | – | 175 | 100 | ≈5 nm | [90] |

### *2.4. Pulsed Laser Deposition*

Pulsed laser deposition (PLD) has emerged as one of the most promising physical vapor deposition (PVD) techniques for the deposition of $MoS_2$ thin films. The PLD approach consists of shining a focused high-power laser beam onto the surface of a solid target to be ablated and deposited as a film on a substrate. PLD is a non-equilibrium process that leads to the absorption of very-short (15–20 ns) and highly-energetic laser pulses by the target and to the formation of a directive plasma plume. The laser-ablated species that form the plasma plume condense onto the substrate, leading to the growth of a thin film. The PLD is well known for its large process latitude, high-flexibility, and excellent process controllability. For instance, by controlling the number of laser ablation pulses and/or the background gas pressure, nanoparticles, and/or films with thicknesses varying from few nm to few microns can be synthesized. Figure 3 shows a schematic representation of a PLD system.

Among the advantages and the unique features of the PLD method, we can cite: (i) its ability to achieve a congruent transfer to the films when a multi-element target is used [91]; (ii) its highest instantaneous deposition rate along with the highly-energetic aspect of the ablated species (~10 times higher than in sputtering) enables the growth of metastable phases and/or crystalline phases even at room temperature; and (iii) its process latitude, which makes it easy to control almost independently each of the deposition parameters (laser intensity, number of laser ablation pulses, background gas pressure, and substrate temperature), and hence the properties of the deposited materials [92–94]. While the early studies on the PLD of $MoS_2$ date back to the 1990s [95–100], it is only recently that important advancements have been made in PLD synthesis of 2D-$MoS_2$ films onto various substrates opening thereby the way to their use for different optoelectronic applications. In 2014, PLD was successfully used to grow one to several layers of $MoS_2$ onto different metal, semiconducting, and sapphire substrates [101,102]. Siegel et al. [103] were the first to report, in 2015, the growth of $MoS_2$ films (from 1 to a few 10s of monolayers thick) on centimeter-sized areas. Other attempts were made to deposit ultrathin ($\leq$3 nm) films of nearly-stoichiometric amorphous $MoS_2$ onto irregular surfaces such as silicon and tungsten tips and to study their field electron emission (FEE) properties [95]. The authors stated that the addition of the $MoS_2$ coating is beneficial to the FEE process since lower electric fields were required to extract an electron current density of 10 µA/$cm^2$ (namely, 2.8 V/µm for $MoS_2$-coated Si and ~5.5 V/µm for $MoS_2$-coated W tips). More recently, PLD has been used to fabricate high-quality $MoS_2$ films (monolayer to few layers) and integrated them into functional ultraviolet (UV) photodetectors [104]. The developed photodetectors were found to exhibit a very low dark current (~$10 \times 10^{-10}$ A), low operating voltage (2 V), and good response time (32 ms). Their performance surpassed that previously reported for 2D-$MoS_2$ synthesized by other routes [105–109]. Indeed, under UV irradiation, their detectivity, photoresponse ($I_{on}/I_{off}$ ratio), and responsivity were found to be as high as $1.81 \times 10^{14}$ Jones, $1.37 \times 10^5$, and $3 \times 10^4$ A/W, respectively. Table 5 summarizes most of the papers reported so far on the PLD of $MoS_2$ films. More specifically, it compares the main PLD growth conditions of 2D-$MoS_2$ films along with the obtained crystallographic phase and some of the reported optoelectronic properties.

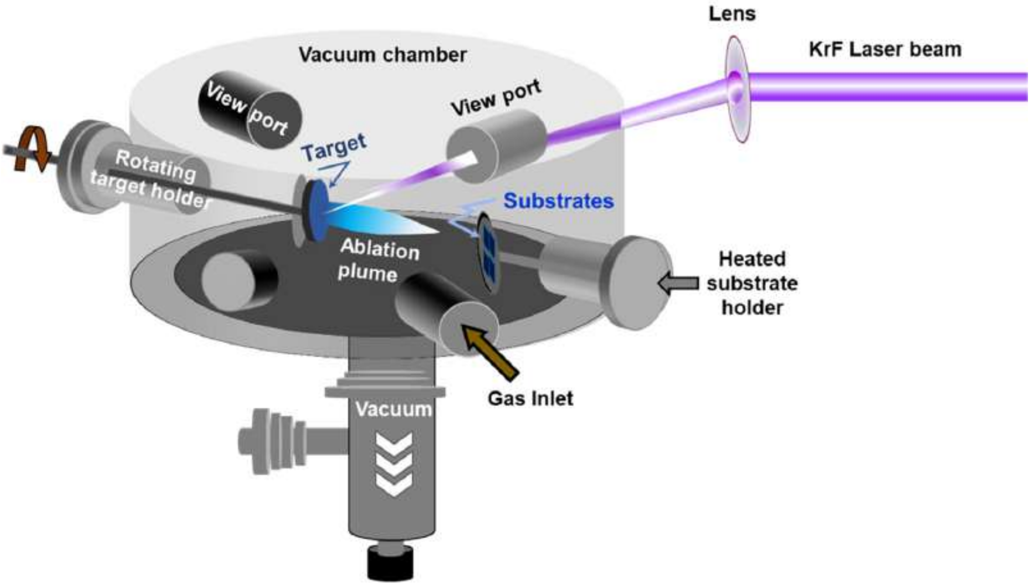

**Figure 3.** Schematic of the pulsed laser deposition chamber.

**Table 5.** Summary of the PLD conditions of $MoS_2$ films along with their thickness and some of their properties.

| Substrate | Target | P(Pa) | T(°C) | Laser Energy | Thickness | Properties | Ref |
|---|---|---|---|---|---|---|---|
| Stainless steel | $MoS_2$ | $2.66 \times 10^{-6}$ | RT/200/300/450 | 5 mJ | ≈400 nm | Granular structure stoichiometric, crystalline $MoS_2$ | [110] |
| Stainless steel | $MoS_2$ | $10^{-6}$ | RT/300 | 100 mJ | ≈70 nm | Stoichiometric single crystal $MoS_2$ | [111] |
| c-$Al_2O_3$ (0001) and Si/$SiO_2$ | 2H-$MoS_2$ | $9.33 \times 10^{-4}$ | 600 | 500 mJ/$cm^2$ | ≈1.4 nm | Stoichiometric<br>2H phase<br>Flake size ≈ 10 µm | [112] |
| GaN/c-$Al_2O_3$ (0001) | 2H-$MoS_2$ | $8 \times 10^{-4}$ | 700 | 50 mJ | Few layers | Mixed phase<br>Roughness ≈0.11 nm | [102] |
| Titanium foil | p-$MoS_2$ | $1.33 \times 10^{-2}$ | RT | – | 0.65 nm | 1T phase $MoS_2$ | [113] |
| $SiO_2$ on Si [100] | $MoS_2$ | $1.33 \times 10^{-2}$ | 800 | 200 mJ/$cm^2$ | ≈20–60 nm | 2H phase $MoS_2$ | [104] |
| Gold-coated carbon cloth | Amorphous $MoS_2$ | $1.33 \times 10^{-2}$ | RT | 220 mJ/$cm^2$ | ≈200 nm | 2H phase $MoS_2$ | [97] |
| Quartz | $MoS_2$ | $9 \times 10^{-5}$ | 300 | 8500 mJ/$cm^2$ | 30 layers | Mixed phase | [114] |
| $Al_2O_3$ (0001) | $MoS_2$+S Powder | $1.33 \times 10^{-2}$ | 700 | 50 mJ | 1–15 Layers of $MoS_2$ | p-$MoS_2$<br>2H phase $MoS_2$<br>Roughness of 0.27 nm | [101] |
| Si | $MoS_2$ | $4 \times 10^{-4}$ | RT | 5/10/100/400 mJ/$cm^2$ | ≈100–200 nm | Various compositions of $MoS_x$ ($x \leq 2.2$) | [115] |

**Table 5.** *Cont.*

| Substrate | Target | P(Pa) | T(°C) | Laser Energy | Thickness | Properties | Ref |
|---|---|---|---|---|---|---|---|
| $SiO_2$ | $MoS_2$ | $3 \times 10^{-5}$ | 700 | 200 mJ | 1–5 layers | 2H phase $MoS_2$ | [116] |
| W (100)-tip | $MoS_2$+poly(vinl) | $5 \times 10^{-3}$ | 700 | 2000 mJ/$cm^2$ | ≈20–60 nm | nearly stoichiometric 2H phase $MoS_2$ | [95] |
| n-Si and p-Si | $MoS_2$+poly(vinl) | $5 \times 10^{-3}$ | 700 | 500 mJ/$cm^2$ | ≈20–60 nm | nearly stoichiometric 2H phase $MoS_2$ | [95] |
| Al, Ag, Ni, Cu | $MoS_2$ | $2.6 \times 10^{-5}$ | 500 | 50 mJ | ≈5 nm | Epitaxial growth of 2H phase $MoS_2$ | [98] |
| Sapphire<br>Quartz<br>$SiO_2$<br>$HfO_2$ | $MoS_2$ +S powder | $1.33 \times 10^{-2}$ | 700 | 30 mJ | 1 monolayer—2.8 nm | large-area growth of stoichiometric layered 2H phase $MoS_2$ | [117] |
| $SiO_2$/Si | $MoS_2$ | $10^{-5}$ | 700 | 200 mJ | few-layer | 2H phase $MoS_2$ | [118] |
| $SiO_2$/Si | $MoS_2$ powder | $5 \times 10^{-4}$ | 600 | 2200 mJ/$cm^2$ | 13 nm | Epitaxial growth of 2H phase $MoS_2$ | [119] |
| Si | $MoS_2$ | $10^{-4}$ | RT | 100 mJ | 129–1900 nm | Stoichiometric films | [120] |
| c-plane sapphire | $MoS_2$ | $10^{-3}$ | 800 | 2000–3000 mJ/$cm^2$ | 1–5 layers | Epitaxial growth of 2H phase $MoS_2$ | [121] |
| Quartz glass | Polycrystalline $MoS_2$ powder | $5 \times 10^{-4}$ | 300 | 8500 mJ/$cm^2$ | 9–10 monolayers | nearly stoichiometric 2H phase $MoS_2$ | [122] |
| Quartz | $MoS_2$ | $8.9 \times 10^{-5}$ |  | 600 mJ | ≈5.8 nm | 2H phase $MoS_2$ | [123] |
| $SiO_2$/Si | $MoS_2$@Ag | $1.33 \times 10^{-7}$ | 500 | 1000–2000 mJ/$cm^2$ | ≈1.3–12.8 nm | 2H phase $MoS_2$ | [124] |
| fluorophlogopite mica | $MoS_2$ | $10^{-5}$ | 700 | 4000 mJ/$cm^2$ | ≈3.3 nm | 2H phase $MoS_2$ | [125] |
| $Al_2O_3$ (0001) | $MoS_2$ | $10^{-3}$ | 650 | 100 mJ | ≈400 nm | 2H phase $MoS_2$ | [126] |

### *2.5. Other Processing Routes*

In addition to the main fabrication methods presented above, other PVD techniques have been used to deposit 2D-$MoS_2$ films. Among these methods, magnetron sputtering has been used to deposit both $MoS_2$ and $WS_2$ films onto polydimethylsiloxane (PDMS) polymer substrates [37,127–130] with controllable defect densities. The PDMS substrate was chosen to fabricate flexible devices based on 2D-semiconducting materials. Interestingly, very smooth $MoS_2$ surfaces, with a roughness of less than 2 nm, were achieved by casting the polymer on a polished silicon wafer. It has also been shown that it is possible to induce subsequent crystallization of $MoS_2$ by exposing it to a pulsed 532 nm laser [127].

Finally, the use of any of the above-discussed techniques to fabricate 2D-$MoS_2$ films is mostly dictated by the availability of the equipment, expertise, and requirements of targeted application. In a general context, the physical-chemical and optoelectronic properties of the final $MoS_2$ films will be determined to select the appropriate synthesis route. Nevertheless, the level of complexity, throughput, and fabrication costs have to be considered to choose the appropriate synthesis technique particularly when a technology has to be adopted. Table 6 provides a general comparison of the preparation techniques of $MoS_2$ described in this review by listing their main advantages and limitations.

**Table 6.** Comparison of the advantages and limitations of different preparation techniques of $MoS_2$.

| Techniques | Advantages | Limitations |
|---|---|---|
| Mechanical exfoliation | - High-quality and good crystallinity.<br>- Mono- to few-layer $MoS_2$<br>- Simple process | - Long processing time (8–84 h)<br>- Tedious and no controllability<br>- Difficult integration with micro/optoelectronic processing |
| Chemical exfoliation | - Large-scale growth<br>- Synthesis of $MoS_2$ monolayer | - Loss of semiconducting properties of $MoS_2$ during Li intercalation. |

**Table 6.** *Cont.*

| Techniques | Advantages | Limitations |
|---|---|---|
| Chemical vapor deposition | - High-quality and crystallinity<br>- Centimeter-scale area growth<br>- Good control of morphologies | - Caution due to the use of toxic precursors<br>- High synthesis temperatures requirement<br>- No lateral uniformity<br>- Mixed phases of 1T, 2H, etc. |
| Atomic layer deposition | - Low-temperature deposition<br>- Uniformity of $MoS_2$ films<br>- High quality of uniformity<br>- Excellent step coverage | - Very low throughput<br>- Long processing time<br>- High cost |
| Pulsed laser deposition | - High-quality and faithful transfer of film stoichiometry<br>- Nanometer-level control of the film thickness<br>- Uniformity onto a large surface (up to 3″ or 4″ diameter wafers)<br>- Quasi-independent control of the growth parameters.<br>- Room-temperature deposition of crystallized $MoS_2$<br>- Compatibility with electronic and optoelectronic device processing | - Relatively costly<br>- Presence of ablated particulates on the surface |
| Sputtering | - High quality and uniformity onto large surface<br>- Compatibility with electronic and opto-electronic device processing.<br>- Fair thickness control | - Relatively costly<br>- Preferential sputtering<br>- Less control on the stoichiometry |

## 3. Characterizations of $MoS_2$ Thin Films

To assess the crystalline quality, microstructure, and optoelectronic properties of the synthesized 2D-$MoS_2$, a variety of characterization techniques have been employed and reported in the literature. These include optical microscopy (OM), scanning electron microscopy (SEM), high-resolution transmission and Scanning transmission electron microscopy (HRTEM and HRSTEM), atomic force microscopy (AFM), energy-dispersive X-ray spectroscopy, X-ray photoelectron spectroscopy (XPS), Raman spectroscopy, and photoluminescence (PL). These methods are often used to investigate the overall 2D-$MoS_2$ surface topography and to qualify the nature of the synthesized material and the shapes of its building blocks (i.e., triangle, nanosheets, and nanoplates) (Figure 4). The observations made by imaging methods are also essential to envision a possible growth mechanism of the micro/nanostructures with respect to the used processing parameters. For instance, Figure 4d shows a schematic representation of the nucleation process of some morphologies of 2D-$MoS_2$.

Subsequently, HRTEM investigations could be carried out to precisely characterize the $MoS_2$ crystalline structure and examine locally its lattice parameters and the presence of defects. In particular, the HRTEM image depicted in Figure 4e is of great importance, as it was recorded in cross-region containing the two possible crystal configurations of $MoS_2$. As it can be seen in Figure 4e–g, the identified phase mixture of 1T@2H-$MoS_2$ could coexist simultaneously in the same fabricated $MoS_2$ thin film [131].

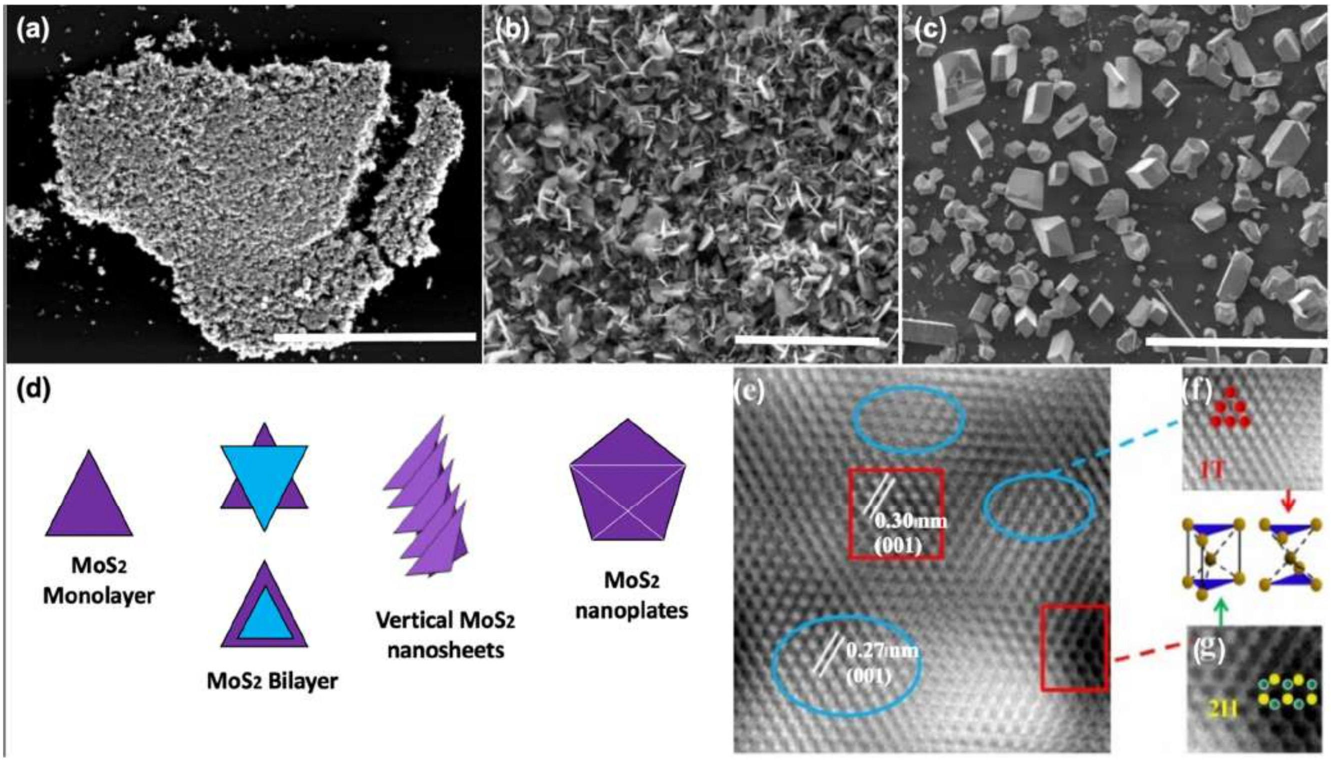

**Figure 4.** Examples of $MoS_2$ microstructures: (**a**) planar triangle flakes scale = 40 µm; (**b**) vertical nanosheets scale = 100 um; (**c**) vertical nanoplates scale = 100 µm; (**d**) schematic of the nucleation process of $MoS_2$; (**e**) HRTEM image of mixed 1T-$MoS_2$ and 2H-$MoS_2$; (**f**) zoom in of blue circled region of the 1T-$MoS_2$ structure, with the unit cell of the 1T phase; and (**g**) zoom in of red circled region of the 2H-$MoS_2$ structure, with the unit cell of the 2H phase. (Figure 4e–g adapted from Ref. [131] Copyright 2019, Springer Nature.)

AFM and its variant methods constitute key characterization tools for the investigation of 2D crystals, mainly due to the atomically thin nature of this layered class of materials. Both vertical and lateral resolutions are fundamentally required to properly investigate the intrinsic properties of 2D materials. AFM is among the few techniques that allow the characterization of 2D-$MoS_2$ in ambient and controlled environments at the nanometer scale. In addition to measuring the local thickness and surface topography, AFM-based electrical methods provide access to additional interesting properties such as the local variations in surface potential of 2D-$MoS_2$. For instance, the Kelvin probe force microscopy (KPFM) method allows the characterization of the sample's surface work function variations. The work function is an extreme surface property, which depends on the energy differences between the Fermi and vacuum levels at the surface. This renders the use of KPFM for the characterization of 2D-$MoS_2$ fundamentally important to investigate band alignments in nanostructures and to study the dependencies of local electronic properties on the number of 2D-$MoS_2$ layers. It also provides key insights into the environmental effects on the state of the sample surface both electronically and morphologically. The KPFM technique was used (Figure 5a) to determine the surface potential variations in mono- and multilayer $MoS_2$, under different humidity conditions.

X-ray photoelectron spectroscopy (XPS) is another relevant surface characterization technique that is widely used to achieve the elemental surface composition of $MoS_2$ films as well as their chemical bonding states. Figure 5b shows typical high-resolution XPS spectra of the $Mo_{3d}$ and $S_{2p}$ core levels. The $Mo_{3d}$ region exhibits two characteristic emission peaks at 232.5 (Mo $3d_{3/2}$) and 229.4 (Mo $3d_{5/2}$) eV. These binding energy values are consistent with electrons of $Mo^{4++}$ corresponding to $MoS_2$. Likewise, the S $2p_{3/2}$ and S $2p_{1/2}$ doublet appearing at binding energies of 162.3 and 163.5 eV is typical for $S^{2-}$ in $MoS_2$ structure. Nan et al. [132] used XPS to show the PL enhancement of monolayer $MoS_2$ through defect engineering and oxygen bonding. The chemical adsorption of oxygen created a heavy p-type doping and the conversion of the Trion into Excitons. Moreover, it caused the suppression of the non-radiative recombination of the excitons at the defect sites. Their results were verified by PL measurements at low temperature, as shown in Figure 5c,d.

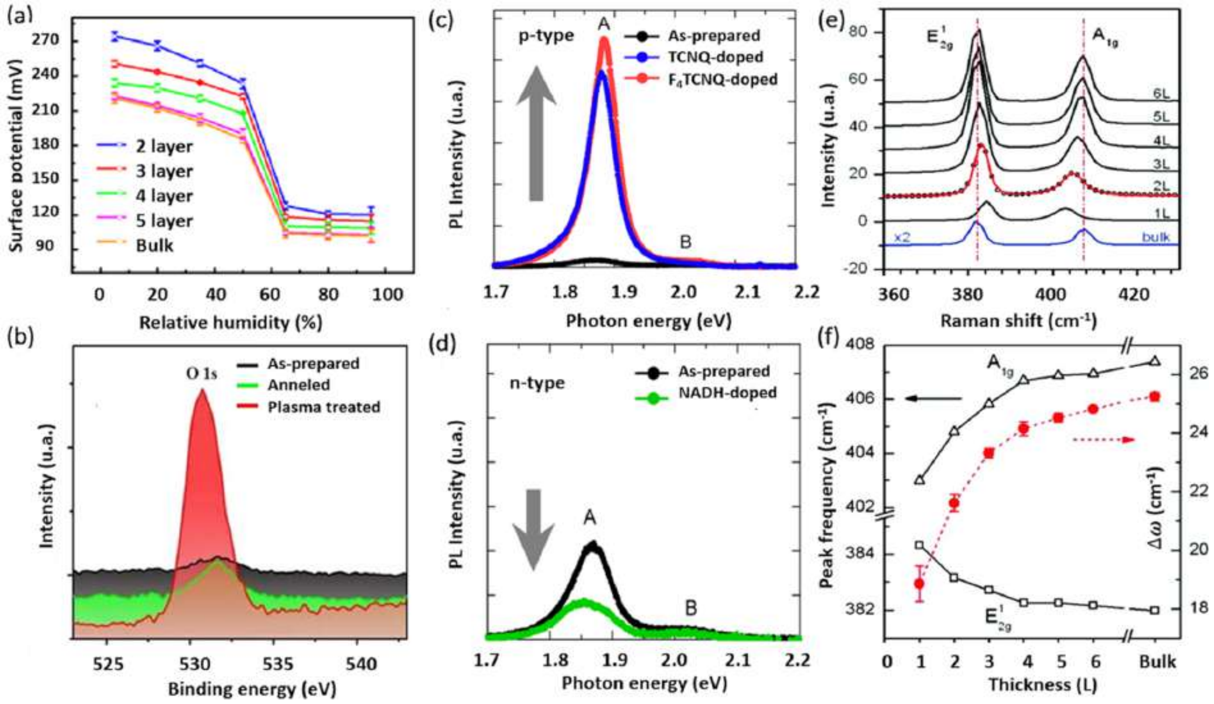

**Figure 5.** (**a**) Surface potential captured by KPFM vs. relative humidity RHs with respect of the number of $MoS_2$ layers (reproduced and adapted from Ref. [133], Copyright 2017, IOP Publishing); (**b**) XPS spectra of Mo 3d and S 2s core levels for different treatment conditions (adapted from Ref. [132] Copyright 2014, American Chemical Society); (**c**,**d**) PL spectra of monolayer $MoS_2$ before and after being doped (reproduced from Ref. [134] Copyright 2013, American Chemical Society); and (**e**,**f**) Raman spectra for various $MoS_2$ films with respect to the number of $MoS_2$ layers (reproduced from Ref. [135] Copyright 2010, American Chemical Society).

Unlike bulk $MoS_2$, the ultrathin 2D-$MoS_2$ (i.e., one to few layers) exhibits a strong PL intensity which increases with reducing the number of layers [136], which has been attributed to quantum confinement effects [53,137]. The PL response can be tuned via several mechanisms including doping [134], plasmonic effect, and defects engineering [132]. For instance, Mouri et al. [134] studied the influence of the thickness on the PL response of $MoS_2$ by using mono-, bi-, and trilayer $MoS_2$ and the PL modulation using doping. They demonstrated that p-type doping with high electron affinity seems to enhance the PL intensity, while the n-type doping tends to reduce it, as illustrated in Figure 5c,d.

Moreover, Raman spectroscopy presents a very sensitive, fast, and non-destructive technique to access valuable information on the chemical structure, phase and polymorphs, crystallinity, and chemical bonding states of 2D-$MoS_2$ materials. It allows the monitoring of the two characteristic peaks of $MoS_2$, namely the in-plane and out-of-plane vibration modes $E^1{}_{2g}$ and $A^1{}_g$ appearing for 514 nm excitation energy at the respective positions of 384.5 and 404.6 $cm^{-1}$ for 2D-$MoS_2$ monolayer [135] (Figure 5e). More interestingly, the difference between the peak positions of $E^1{}_{2g}$, $A^1{}_g$ ($\Delta\omega$) can be used as a robust and effective diagnostic to determine the number of $MoS_2$ layers (up to four layers) or to simply estimate the $MoS_2$ film thickness (Figure 5f). Usually, $\Delta\omega$ is less than 20 $cm^{-1}$ in the presence of a single layer of $MoS_2$, but it increases with increasing $MoS_2$ thickness to reach 25 $cm^{-1}$ for the bulk $MoS_2$ [135]. In fact, a thorough study on the dependence of the characteristic Raman peak positions, width, and intensity of $MoS_2$ films on their thickness have been investigated [103,135,138]. Furthermore, H. Li et al. [138] reported that the frequency of the characteristic peaks is strongly dependent on the excitation energy due to the resonance effect. They showed a red shift of the $E^1{}_{2g}$ mode of about 2.2 $cm^{-1}$ and blue shift of the $A^1{}_g$ mode of about 4.1 $cm^{-1}$. Thus, to effectively determine the exact $MoS_2$ number of layers using Raman spectroscopy, one has to consider the excitation energy and the thickness limit at which the Raman vibrations frequency is reaching a plateau, indicating that it is less sensitive to $MoS_2$ thickness variation above four layers.

## 4. Band Structures and Electronic Properties

We employed density functional theory (DFT) to determine the optoelectronic properties in particular the bandgap energy of both bulk and monolayer $MoS_2$. Perdew–Burke–Ernzerhof (PBE) approach was applied to describe the electronic states of $MoS_2$ using band structure and the density of states (DOS). DFT calculations were implemented in Quantum Espresso™ code [139,140]. The considered 2H-$MoS_2$ has a hexagonal crystal form with the space group P63/mmc (No. 194). The equivalent positions for this structure employed in the calculations are Mo (1/3, 2/3, and 2/8) and S (1/3, 2/3, and 0.621). The valence electron configuration selected for Mo and S atoms are $4p^5$ $5s^1$ and $3s^2$ $3p^4$, respectively. The cutoff wave function and the cutoff charge densities are 70 and 700 Ryd, respectively [140]. The cell parameters and atomic positions were fully relaxed by the process of the total energy minimization. The values of the relaxed lattice constants for bulk $MoS_2$ are a = 3.15 Å and c = 12.3 Å, respectively. The optimized structure was used to perform calculations for band structures and the total density of states for both $MoS_2$ bulk and monolayer. For bulk $MoS_2$ (top left panel of Figure 6a), $9 \times 9 \times 2$ k-points were used to obtain the band structure along the path Γ-K-M-Γ in the Brillouin zone. For $MoS_2$ monolayer (top right panel of Figure 6a), $9 \times 9 \times 1$ k-points were used. A 15 Å vacuum along the z-axis above the monolayer was added to isolate the $MoS_2$ and prevent any interaction between the adjacent layers [141]. The top view of the $MoS_2$ monolayer is shown in the bottom panel of Figure 6a, where sulfur atoms are represented in yellow and molybdenum atoms are shown in purple.

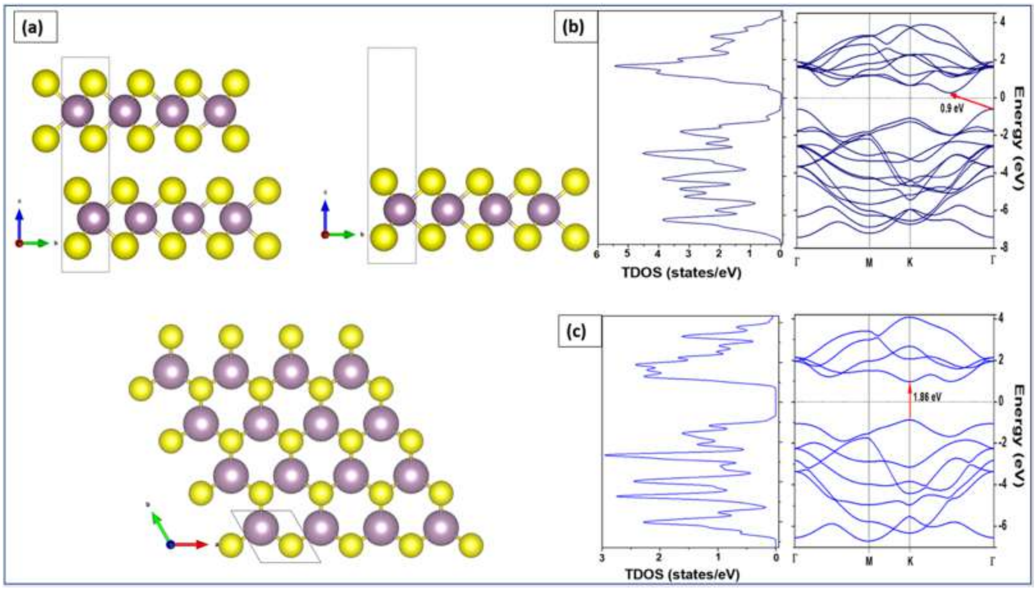

**Figure 6.** (**a**) Bulk $MoS_2$ (**top-left**), monolayer $MoS_2$ (**top-right**), and top view of $MoS_2$ monolayer (**bottom**). Total density of states (**left**) and band structure (**right**) of the (**b**) bulk and (**c**) monolayer.

To obtain the electronic properties, the $MoS_2$ bulk was considered as a set of two hexagonal planes linked together by weak Van Der Waals bonds. The $MoS_2$ monolayer was considered as a single hexagonal plane with covalent bonds between atoms S-Mo-S [142]. The left panel of Figure 6b shows the total DOS calculation results of the bulk $MoS_2$ while the right panel of Figure 6b shows the calculation of its band structure. The energy range is between −8 and 4 eV versus the directions of the highest symmetries in the first Brillouin zone Γ, M, K, and Γ. As observed from the band structure calculations, the $MoS_2$ bulk has an indirect bandgap of 0.9 eV. The minimum of the conduction band is located between K and G and the maximum of valence band at point G. This indirect bandgap obtained for the $MoS_2$ bulk was attributed to the presence of interlayer interactions in the bulk structure [143]. In contrast, Figure 6c shows that the monolayer $MoS_2$ has a direct bandgap of 1.89 eV at the K point. The DOS results are compatible with the results of the band structure. Similar conclusions have been stated in other investigations [141,142].

## 5. $MoS_2$ Applications

Because of their attractive optoelectronic properties, possibly tunable by for example controlling the number of monolayers, $MoS_2$ thin films were tested and validated for a variety of applications including electronics, photonics, solar energy, and energy storage. Here, we give a few examples of some specific successful and promising applications of $MoS_2$ films for solar energy conversion [144,145], gas sensing [44,48,146,147], and plasmonics [148–152].

### 5.1. $MoS_2$ for Solar Energy Harvesting

As demonstrated by DFT calculations, 2D-$MoS_2$ exhibits interesting optoelectronic properties attributed to its direct bandgap ranging from 1.2 to 1.9 eV and an absorption coefficient greater than 105 $cm^{-1}$ throughout the solar spectrum. These key properties are very promising for the use of $MoS_2$ in photovoltaic (PV) applications. Indeed, it has been shown that, when a monolayer of n-type $MoS_2$ is deposited onto a p-type silicon substrate, the resulting p-n junction based PV device is able to yield a power conversion efficiency (PCE) as high as 5.23%, as recorded elsewhere [153]. Such a PV performance is most likely a consequence of the excellent ability of $MoS_2$ to efficiently separate the generated photo-charges at the n-MoS2/p-Si interface of the heterojunction.

To highlight the electrical performance of thin films $MoS_2$-based solar cells in a homojunction form, we used the one-dimensional solar cell capacitance simulator SCAPS-1D™ software 3.3.08 interface [154], developed by M. Burgelman – Department of Electronics and Information Systems at the University of Ghent, Belgium [155,156], to calculate the different PV parameters, i.e., open circuit voltage $V_{OC}$, short-circuit current density $J_{SC}$, fill factor FF, and PCE (η). In this sense, a solar cell made of Ag/p-Si/$MoS_2$/Al structure, as the one represented by a schematic in Figure 7, was implemented in the SCAPS-3308™ environment.

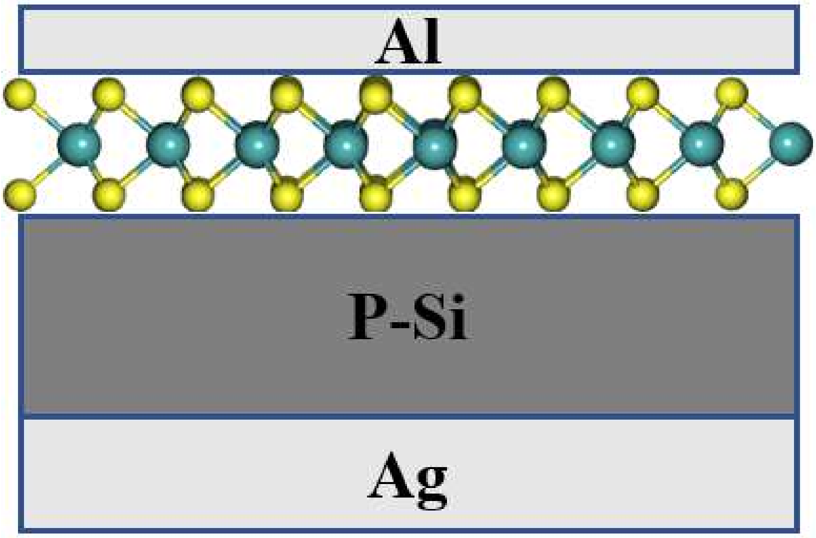

**Figure 7.** Simulated solar cell structure of solar cell.

The simulations were made under AM1.5 illumination conditions at an operating temperature of 300 K. The physical parameters related to the electronic properties of the layers used in the simulation are shown in Table 7. For the considered junction, the thermal speed of the electrons and the holes were fixed at $10^7$ cm/s, the type of defect is neutral, and the capture cross section is $10^{-14}$ cm$^2$.

**Table 7.** Physical parameters of n-$MoS_2$ monolayer and p-Si substrate used in the SCAPS-1D™ simulations.

| Parameters | p-Si [SCAPS] | n-$MoS_2$ |
|---|---|---|
| Thickness (nm) | 200 | 0.32 |
| Bandgap (eV) | 1.12 | 1.9 [153] |
| Electron affinity (eV) | 4.5 | 4.2 [153] |
| Dielectric permittivity (relative) | 11.9 | 10.5 [157] |
| CB effective density of states (1/cm$^3$) | $2.8 \times 10^{19}$ | $2.2 \times 10^{18}$ [158] |
| VB effective density of states (1/cm$^3$) | $1.04 \times 10^{19}$ | $1.8 \times 10^{19}$ [158] |
| Electron thermal velocity (cm/s) | $1 \times 10^7$ | $1 \times 10^7$ [159] |
| Hole thermal velocity (cm/s) | $1 \times 10^7$ | $1 \times 10^7$ [159] |
| Electron mobility (cm$^2$/Vs) | 1500 | 150 [20] |
| Hole mobility (cm$^2$/Vs) | 4500 | 86 [159] |
| Shallow uniform donor density (1/cm$^3$) | 0 | $1 \times 10^{17}$ [159] |
| Shallow uniform acceptor density NA (1/cm$^3$) | $1 \times 10^{16}$ | 0 |

Beyond, the input parameters used in our SCAPS simulations, we provide hereinafter a survey of commonly used physical parameters of $MoS_2$ reported in the literature to simulate the performance of $MoS_2$ in PV applications. As can be seen in Table 8, several combinations are possible which may yield different results.

**Table 8.** A survey of the physical parameters of $MoS_2$ used for the simulation of photovoltaic applications.

| PV Parameters | Reported Values and References | | | |
|---|---|---|---|---|
| Bandgap | 1.29 eV [158,160,161] | 1.2–1.8 eV [159] | 1.23 eV [162] | 1.8 eV [163] |
| Electron affinity | 4.2 eV [158,160–163] | 4–4.7 eV [159] | 4.22 eV [163] | – |
| Relative dielectric permittivity | 3 [164] | 4 [160–162] | 7 [159] | 13.6 [158] |
| Effective density of states in conduction band | $10^{16}$ cm$^{-3}$ [163] | $7.5 \times 10^{17}$ cm$^{-3}$ [160,162] | $2.2 \times 10^{18}$ cm$^{-3}$ [158,161] | $10^{19}$, $2.5 \times 10^{20}$ cm$^{-3}$ [159,164] |
| Effective density of states in valance band | $10^{17}$ cm$^{-3}$ [163] | $1.8 \times 10^{18}$ cm [160,162] | ~$10^{19}$ cm$^{-3}$ [158,161,164] | $2.5 \times 10^{20}$ cm$^{-3}$ [159] |
| Electron thermal velocity | $10^5$ cm/s [162] | $2.12 \times 10^7$ cm/s | – | – |
| Hole thermal velocity | $10^7$ cm/s [162] | $1.18 \times 10^7$ cm/s [161] | – | – |
| Electron mobility | 44 cm$^2$/Vs [159] | 50 cm$^2$/Vs [161] | 100 cm$^2$/Vs [158,160,162] | – |
| Hole mobility | 30 cm$^2$/Vs [161] | 86 cm$^2$/Vs [159] | 150 cm$^2$/Vs [158,160,162] | |
| Shallow uniform donor density | $10^{16}$ [161] | $10^{17}$ [164] | $10^{18}$ [162] | – |
| Shallow uniform acceptor density | 10 cm$^{-3}$ [161] | $10^{17}$ cm$^{-3}$ ($MoS_2$ type P) [158] | $10^{21}$ cm$^{-3}$ ($MoS_2$ type P) [160] | – |

The outcome of our simulations shows that the p-Si/n-$MoS_2$ structure in Figure 7 can yield a PCE value as high as 19.82% when considering 2D-$MoS_2$ with the highest bandgap of 1.9 eV. Figure 8 shows the simulated J-V curve of the p-Si/n-$MoS_2$ cell along with its associated PV parameters. The rather high $V_{oc}$ value of 0.64 V reflects the strong built-in electrical field at the interface between the n-$MoS_2$ layer and p-Si substrate.

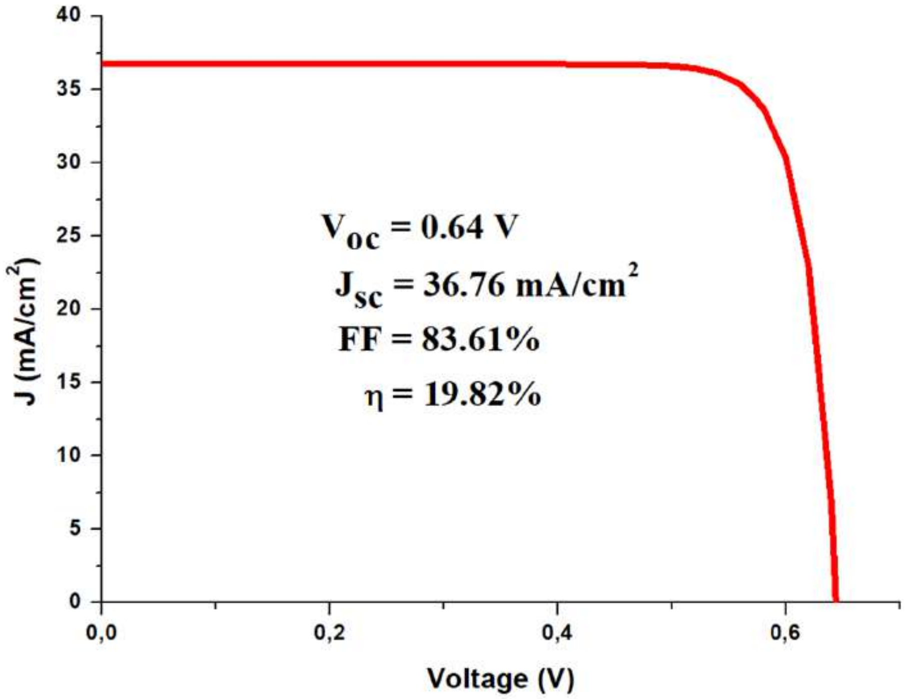

**Figure 8.** Simulated J-V characteristic of p-Si/n-$MoS_2$ solar cell, as calculated by SCAPS-1D™ software.

The high PCE obtained is comparable to the one obtained for well-proven solar cell materials. This is an outstanding yield for an only 0.33 nm thick material used in conjunction with p-Si in the solar cell set up as compared to 250 µm thickness used for conventional Si technology. Moreover, sulfur and molybdenum are abundant and cheaper raw materials as compared to the technologies achieving similar performances such as III-V materials.

Nevertheless, although the simulated PCE performance underlines the great potential of 2D-$MoS_2$ films for PV devices, other challenging issues still need to be addressed or mitigated to develop such devices. For instance, the controlled deposition of $MoS_2$ monolayer, the achievement of a reliable metal contact on $MoS_2$ monolayer free of leakage current or a shortcut with the underlying Si substrate, and the scalability of 2D-MoS2 ultrathin films to the well-established large-size Si wafer technology are among the challenging issues to be addressed in future works.

### 5.2. $MoS_2$ for Gas Sensing Applications

$MoS_2$ nanosheets (NS) have been reported to exhibit enhanced gas sensing performances for a variety of gases, including toxic and hazardous gases such as ammonia ($NH_3$) and nitrogen dioxide ($NO_2$) [43,48,146,165–167]. Thus, $MoS_2$ NS act as a simple chemiresistor that changes its electrical resistance when in contact with reactive gases. The sensing response or sensitivity (S) towards a target gas, at a given operating temperature, is determined from the measured values of resistances of the $MoS_2$-NS sensing element in the presence of atmospheric air resistance ($R_a$) and target gas ($R_g$). Usually, the target gas molecules adsorb onto the $MoS_2$ NS exposed edges and changes its conductivity through the donor/acceptor exchanges process. The sensitivity (S) is defined as follows:

$$\mathbf{S} = \frac{\mathbf{R_a} - \mathbf{R_g}}{\mathbf{R_g}}$$

To design an effective 2D-$MoS_2$ gas sensor, care must be taken to the optimization of its operating temperature, response/recovery times, and selectivity. 2D-$MoS_2$-based gas sensors were found to offer certain advantages, such as high-temperature stability, high resistance to a corrosive environment, and high sensitivity [26,146,165,166]. In addition, 2D-

$MoS_2$ thin film-based sensors were reported to detect $NH_3$ triethylamine (TEA) molecules at the sub-ppm level, at an operating temperature as low as 30 °C [147].

$MoS_2$ thin films obtained by mechanical exfoliation were used for highly sensitive field-effect transistor (FET) sensors [147]. By varying the number of $MoS_2$ layers, the $MoS_2$-based FET sensor exhibited high nitrogen monoxide (NO) sensitivity with a detection limit of 0.8 ppm. Moreover, DFT calculations indicated that NO and $NO_2$ seemed to strongly bind to $MoS_2$ nanosheets in contrast to other molecules such as carbon monoxide (CO), carbon dioxide ($CO_2$), $NH_3$, NO, $NO_2$, and $CH_4$. In addition, the exfoliated $MoS_2$ monolayer showed high response to triethylamine (TEA) at concentrations ranging from 1 to 100 ppm at room temperature (Figure 9a). Due to the strong response and excellent signal-to-noise ratio, a detection limit of TEA as low as 10 ppb was achieved.

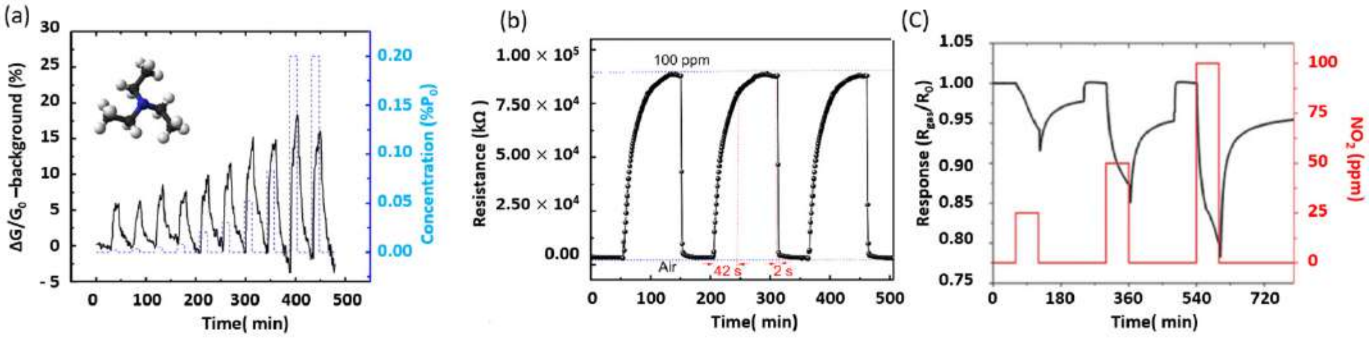

**Figure 9.** (**a**) $MoS_2$ sensor response exposed to TEA (adapted from Ref. [147] Copyright 2013, American Chemical Society); (**b**) repeatability and reversibility of the FLMN gas sensor at 100 ppm $NO_2$ concentration (reproduced and adapted from Ref. [168], Copyright 2019, MDPI); and (**c**) the $MoS_2$/CNT sensor response as a function of three $NO_2$ concentrations (25, 50, and 100 ppm) (reproduced and adapted from Ref. [42], Copyright 2017, Wiley-VCH).

Furthermore, exfoliated few-layer $MoS_2$ nanosheets deposited on a substrate with interdigitated electrodes demonstrated good $NO_2$ detection performances at room temperature [168]. The reported device shows a quick and complete recovery time of 2 s at a rate greater than 97%. Similarly (Figure 9b), DFT calculations indicated that the fairly fast recovery of $MoS_2$ arises from the weak van der Waals interactions between $NO_2$ and the $MoS_2$ surface.

It is worth mentioning that, regardless of their form or morphology, $MoS_2$ thin films remain as robust gas sensors. Indeed, atomic layered $MoS_2$ fabricated by CVD showed excellent sensitivity and high selectivity once exposed to $NH_3$ and $NO_2$ [169]. The resistance of the $MoS_2$ films increases in the case of $NO_2$ adsorption, while it decreases for the $NH_3$ adsorption. The recovery rate of $NO_2$ is higher at 100 °C than at room temperature, while the $NH_3$ sensing signal is negligible at 100 °C. To further exploit the large affinity of $NO_2$ with $MoS_2$ thin films, $MoS_2$ hexagonal-shaped nanoplates (HNPs), with exposed edges allowing significant charge transfer, were grown on the top 20 nm of carbon nanotubes (CNTs). This configuration is advantageous to increase both the surface area and the number of sites for gas adsorption. The hybridization of $MoS_2$ by deposition on CNTs showed an enhanced room-temperature gas-sensing performance [42], attaining a detection limit of a few ppb of $NO_2$ concentration.

### 5.3. $MoS_2$ for Plasmonic Applications

Because of their optical bandgap spread, $MoS_2$ thin films offer interesting opportunities to be coupled with noble metal nanoparticles (NPs) in order to exacerbate the plasmonic properties. Indeed, the coupling effects between the excitons from $MoS_2$ with the plasmons generated within the metal NPs open various prospects for tunable light emitters and absorbers over a wide spectrum. Various $MoS_2$-related plasmonic structures have been developed for different optoelectronic applications, including photodetection [152], photoluminescence modulation [150], photocatalysis [170,171], and photovoltaics [172].

To better understand the origin of the enhancement in light emission/absorption properties of $MoS_2$/metal-NPs hybrid structures, it is necessary to comprehend and estimate the variation of 2D-$MoS_2$ complex permittivity. A mathematical approach based on hybrid Lorentz–Drude–Gaussian (HLDG) model was proposed by Mukherjee et al. [173] to describe the complex permittivity of $MoS_2$ monolayer based on its absorption spectrum (Figure 10a).

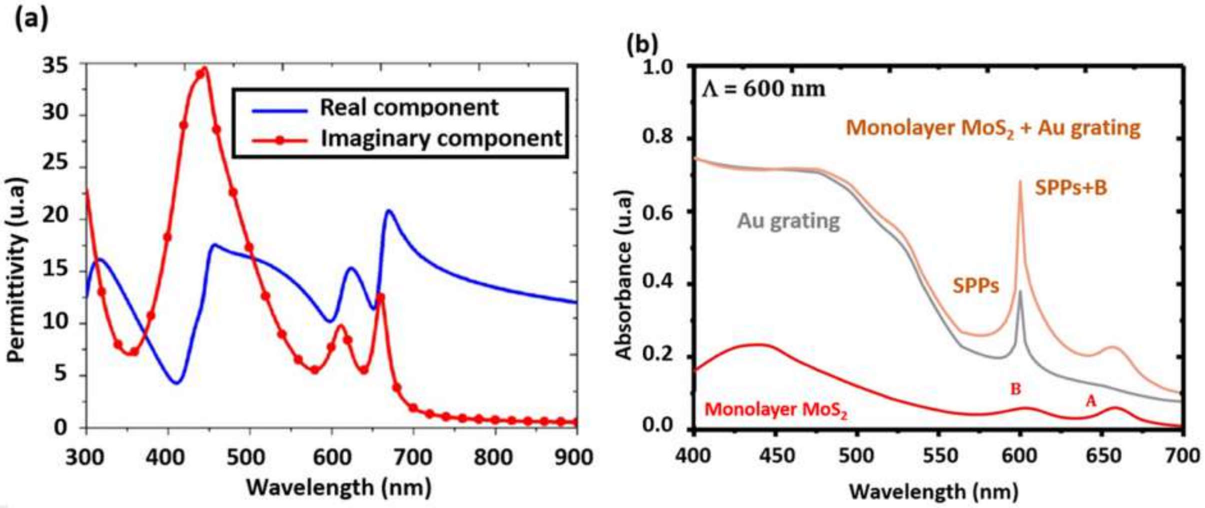

**Figure 10.** (**a**) Complex permittivity vs. wavelength of monolayer $MoS_2$ (reproduced and adapted from [174], Copyright 2018, The Optical Society, OSA); and (**b**) spectral absorptances of an opaque Au plate, a simple 1D Au grating, a suspended monolayer $MoS_2$, and monolayer $MoS_2$-covered Au grating for TM waves with normal incidence from 400–700 nm (reproduced from Ref. [175] Copyright 2018, Elsevier).

The HLDG model can be presented as follows:

$$\varepsilon_c = \varepsilon_c^{LD} + \varepsilon_c^{G},$$

where the superscripts LD and G correspond to Lorentz–Drude and Gaussian permittivity terms, respectively, as described elsewhere [173].

Chen et al. [176] used the HLDG model to design and simulate a perfect absorber based on the local surface plasmon resonance (LSPR) and the coupling properties between Ag patterns and a $MoS_2$ monolayer. Their results show that $MoS_2$ could increase the optical absorption dramatically. In another work, Jiang et al. [174] integrated the generalized interference theory in the HLDG model to investigate the optical properties of a broadband absorber utilizing a $MoS_2$ monolayer. A more rigorous approach, consisting in the use of a coupled-wave analysis algorithm with the HLDG model, has been proposed to study the optical absorption of a composite photonic structure made of $MoS_2$ Au grating [175]. The authors showed that the optical absorption of Au grating can be strongly modified by altering the number of $MoS_2$ layers (Figure 10b), changing the layout of the $MoS_2$ layer (e.g., to a $MoS_2$ nanoribbon array), or inserting a hafnium dioxide spacer. Furthermore, they showed an enhancement of the localized electromagnetic field due to surface plasmon polaritons triggered by Au grating in the presence of few layers of $MoS_2$. The observed enhancement of the $MoS_2$ optical absorption was mainly attributed to the exciton transition. Additionally, the HLDG model was used by Xiaoyong et al. [149] to investigate the tunability of wave propagation in $MoS_2$ supported hybrid surface plasmons waveguides based on dielectric fiber-gap metal substrate structures. By using the finite element method, these authors examined the influence of the structural parameters, the dielectric fiber shape and carrier concentration of the $MoS_2$ layer on the hybrid modes. Their results allow identifying the tunable parameters of the hybrid modes of waveguide structures that could lead to the design of novel surface plasmon devices in the future.

On the other hand, the association of $MoS_2$ with plasmonic NPs was also exploited by Yang et al. [151]. The authors reported on the fabrication of a hybrid nanostructure where a $MoS_2$ monolayer is transferred onto the surface of 10-nm-wide Au nanogap arrays. Interestingly, by adjusting the length of the Au nanogaps, the authors achieved a photoluminescence enhancement as high as ~20 folds. In a more recent work, Mawlong et al. [150] also reported a much higher enhancement factor ~463 folds compared to pristine $MoS_2$ monolayer at ambient of the PL intensity in the case of $TiO_2$/Au/$MoS_2$ ternary core–shell hetero-nanostructures. Such a strong PL enhancement was attributed to the heavy p-doping of the $MoS_2$ lattice along with LSPR initiated exciton–plasmon coupling at the $MoS_2$/Au interface [148]. These results suggest that the hybridization of $MoS_2$ with appropriate metal nanostructures enhances the photoresponse. Indeed, Rahmati et al. [152] also reported an enhancement in the photocurrent generated by vertically aligned $MoS_2$ nanosheets decorated with Au NPs.

## 6. Summary and Outlook

Based on the ever-increasing number of published works on 2D-TMDs materials, there is no doubt that $MoS_2$ will continue to be one of the materials of the choice for the development of innovative and potentially scalable optoelectronic devices.

In term of fabrication, the CVD technique remains a comfortable and affordable route for continuous developments of a variety of shapes and morphologies of 2D-$MoS_2$. By gaining more control of the deposition process itself, it is possible to further tune the optical and electrical properties of $MoS_2$ nanostructures while increasing the size of the sample and the lateral uniformity. Of particular concern is the need to improve the reproducibility of defect-free structures. On the other hand, PLD appears as a highly promising alternative for the production of high-quality $MoS_2$ thin films with a fairly high-level of homogeneity. It also allows tuning the $MoS_2$ strain level during the elaboration, which may lead to exotic physical properties. PLD also offers an additional possibility to optimize, almost quasi-independently, different deposition parameters of $MoS_2$ films, and hence tune at will their properties of interest. Finally, PLD also has the advantage of growing crystalline 2D-TMDS at room temperature, which opens the way to deposit $MoS_2$ films onto flexible and thermo-sensitive substrates, thereby leading to a variety of new applications.

Regarding the applications, apart from those described in this review, 2D-$MoS_2$ exhibits very appealing performances in infrared domains especially in combination with metamaterials such as passive radiative cooling. There are some emerging works [177–180] related to this aspect such as developing hybrid $MoS_2$ thin films with new structures, including metamaterials, metasurfaces, photonic crystals, plasmonics, etc. Similarly, the development of 2D material-based antennas remains unsatisfactory as most of the known achievements on $MoS_2$ in this domain are developed theoretically. Especially, the recent works [181] on terahertz (THz) plasmonics have shown the potential of $MoS_2$ for their application in antenna research. Precisely, the use of $MoS_2$ as a conductive medium in THz antenna appears as a potential direction of recent developments.

**Author Contributions:** Conceptualization, D.M., M.A.E.K., and M.J.; D.M. and A.K. contributed equally to this review; D.M. and G.D. synthesis and plasmonics; A.K and K.K. DFT calculations—SCAPS simulations and KPFM; M.E.M. PL and Raman spectroscopy; supervision, M.E.M., M.A.E.K., and M.J.; and writing—review and editing. All authors have read and agreed to the published version of the manuscript.

**Funding:** This research received no external funding.

**Data Availability Statement:** This review contains both data from literature and own authors' work. The cited data can be consulted in the relevant cited article. The authors data: DFT calculations and SCAPS simulations are available upon request.

**Acknowledgments:** This work was done in the context of a scientific collaboration between INRS and UPJV. D.M. is grateful to both the Region HDF (France) and INRS (QC, Canada) for his PhD fellowship. The authors would like to acknowledge the financial support from the Natural Sciences and Engineering Research Council (NSERC) of Canada.

**Conflicts of Interest:** The authors declare no conflict of interest.

## Abbreviations

| | |
|---|---|
| 1T | Tetragonal |
| 2D | Two-dimension |
| 2H | Hexagonal |
| 3R | Rhombohedral |
| $\Delta\omega$ | Raman shift between the peak positions of $E^1{}_{2g}$ and $A^1{}_g$ |
| ALD | Atomic layer deposition |
| $A^1{}_g$ | $MoS_2$ out-of-plane Raman vibration mode |
| BL | Buffer layer |
| CNTs | Carbon nanotubes |
| CVD | Chemical vapor deposition |
| DFT | Density-functional theory |
| $E^1{}_{2g}$ | $MoS_2$ in-plane Raman vibration mode |
| ETL | Electron transport layer |
| EQE | External quantum efficiency |
| FEE | Field electron emission |
| FET | Field-effect transistor |
| Gr | Graphene |
| HIT | Heterojunction with intrinsic thin layer |
| HLDG | Hybrid Lorentz-Drude-Gaussian model |
| HNPs | Hexagonal-shaped nanoplates |
| HRTEM | High-Resolution Transmission Electron Microscopy |
| J-V | current density versus voltage |
| $J_{sc}$ | Short circuit current density |
| KPFM | Kelvin probe force microscopy |
| LSPR | Localized surface plasmon |
| NPs | Nanoparticles |
| NSs | Nanosheets |
| PCE | Power conversion efficiency |
| PDMS | Polydimethylsiloxane polymer |
| PL | Photoluminescence |
| PLD | Pulsed laser deposition |
| PPB | Particles per billions |
| PPM | Particles per millions |
| PSCs | Perovskite solar cells |
| $R_a$ | Resistance of the sensing element in the presence of atmospheric air |
| $R_g$ | Resistance of the sensing element in the presence of the target gas |
| RH | Relative humidity |
| SCs | Solar cells |
| SEM | Scanning electron microscopy |
| $S_{max}$ | The maximum value of the sensing response |
| SP | Surface potential |
| TCE | Transparent conducting electrode |
| TEM | Transmission electron microscopy |
| TD | Thermal decomposition |
| TMDs | Transition metal dichalcogenides |
| TRPL | Time-resolved photoluminescence |
| TVD | Thermal vapor deposition |
| TVS | Thermal vapor sulfurization |
| UV | Ultraviolet |
| $V_{oc}$ | Open circuit voltage |
| XPS | X-ray photoelectron spectroscopy |

## References

1. Mas-Ballesté, R.; Gómez-Navarro, C.; Gómez-Herrero, J.; Zamora, F. 2D materials: To graphene and beyond. *Nanoscale* **2011**, *3*, 20–30. [CrossRef] [PubMed]
2. Allen, M.J.; Tung, V.C.; Kaner, R.B. Honeycomb carbon: A review of graphene. *Chem. Rev.* **2010**, *110*, 132–145. [CrossRef] [PubMed]
3. Zhu, Y.; Murali, S.; Cai, W.; Li, X.; Suk, J.W.; Potts, J.R.; Ruoff, R.S. Graphene and graphene oxide: Synthesis, properties, and applications. *Adv. Mater.* **2010**, *22*, 3906–3924. [CrossRef] [PubMed]
4. Mattevi, C.; Kim, H.; Chhowalla, M. A review of chemical vapour deposition of graphene on copper. *J. Mater. Chem.* **2011**, *21*, 3324–3334. [CrossRef]
5. Deokar, G.; Avila, J.; Razado-Colambo, I.; Codron, J.L.; Boyaval, C.; Galopin, E.; Asensio, M.C.; Vignaud, D. Towards high quality CVD graphene growth and transfer. *Carbon N. Y.* **2015**, *89*, 82–92. [CrossRef]
6. Deokar, G.; Casanova-Cháfer, J.; Rajput, N.S.; Aubry, C.; Llobet, E.; Jouiad, M.; Costa, P.M.F.J. Wafer-scale few-layer graphene growth on Cu/Ni films for gas sensing applications. *Sens. Actuators B Chem.* **2020**, *305*, 127458. [CrossRef]
7. Minkin, A.S.; Lebedeva, I.V.; Popov, A.M.; Knizhnik, A.A. The Application of Empirical Potentials for Calculation of Elastic Properties of Graphene. *Tech. Phys. Lett.* **2019**, *45*, 111–114. [CrossRef]
8. Gupta, A.; Sakthivel, T.; Seal, S. Recent development in 2D materials beyond graphene. *Prog. Mater. Sci.* **2015**, *73*, 44–126. [CrossRef]
9. Castro Neto, A.H.; Guinea, F.; Peres, N.M.R.; Novoselov, K.S.; Geim, A.K. The electronic properties of graphene. *Rev. Mod. Phys.* **2009**, *81*, 109–162. [CrossRef]
10. Neto Castro, A.H.; Novoselov, K. Two-dimensional crystals: Beyond graphene. *Mater. Express* **2011**, *1*, 10–17. [CrossRef]
11. Tan, C.; Zhang, H. Two-dimensional transition metal dichalcogenide nanosheet-based composites. *Chem. Soc. Rev.* **2015**, *44*, 2713–2731. [CrossRef]
12. Lu, Q.; Yu, Y.; Ma, Q.; Chen, B.; Zhang, H. 2D Transition-Metal-Dichalcogenide-Nanosheet-Based Composites for Photocatalytic and Electrocatalytic Hydrogen Evolution Reactions. *Adv. Mater.* **2016**, *28*, 1917–1933. [CrossRef] [PubMed]
13. Ansari, L.; Monaghan, S.; McEvoy, N.; Coileáin, C.; Cullen, C.P.; Lin, J.; Siris, R.; Stimpel-Lindner, T.; Burke, K.F.; Mirabelli, G.; et al. Quantum confinement-induced semimetal-to-semiconductor evolution in large-area ultra-thin PtSe2 films grown at 400 °C. *npj 2D Mater. Appl.* **2019**, *3*, 1–8. [CrossRef]
14. Stanford, M.G.; Rack, P.D.; Jariwala, D. Emerging nanofabrication and quantum confinement techniques for 2D materials beyond graphene. *npj 2D Mater. Appl.* **2018**, *2*, 1–15. [CrossRef]
15. Butoi, C.I.; Langdon, B.T.; Kelley, D.F. Electron-Transfer Dynamics in DTDCI / MoS 2 and DTDCI / WS 2 Nanoclusters. *J. Phys. Chem. B* **1998**, *102*, 9635–9639. [CrossRef]
16. Wu, X.L.; Fan, J.Y.; Qiu, T.; Yang, X.; Siu, G.G.; Chu, P.K. Experimental evidence for the quantum confinement effect in 3C-SiC nanocrystallites. *Phys. Rev. Lett.* **2005**, *94*, 1–4. [CrossRef] [PubMed]
17. Gan, Z.X.; Liu, L.Z.; Wu, H.Y.; Hao, Y.L.; Shan, Y.; Wu, X.L.; Chu, P.K. Quantum confinement effects across two-dimensional planes in MoS2 quantum dots. *Appl. Phys. Lett.* **2015**, *106*, 233113. [CrossRef]
18. Ellis, J.K.; Lucero, M.J.; Scuseria, G.E. The indirect to direct band gap transition in multilayered MoS 2 as predicted by screened hybrid density functional theory. *Appl. Phys. Lett.* **2011**, *99*, 261908. [CrossRef]
19. Wang, S.W.; Medina, H.; Hong, K.B.; Wu, C.C.; Qu, Y.; Manikandan, A.; Su, T.Y.; Lee, P.T.; Huang, Z.Q.; Wang, Z.; et al. Thermally Strained Band Gap Engineering of Transition-Metal Dichalcogenide Bilayers with Enhanced Light-Matter Interaction toward Excellent Photodetectors. *ACS Nano* **2017**, *11*, 8768–8776. [CrossRef]
20. Yu, Z.; Ong, Z.Y.; Li, S.; Xu, J.B.; Zhang, G.; Zhang, Y.W.; Shi, Y.; Wang, X. Analyzing the Carrier Mobility in Transition-Metal Dichalcogenide MoS2 Field-Effect Transistors. *Adv. Funct. Mater.* **2017**, *27*, 1604093. [CrossRef]
21. Wang, S.; Zhao, W.; Giustiniano, F.; Eda, G. Effect of oxygen and ozone on p-type doping of ultra-thin WSe2 and MoSe2 field effect transistors. *Phys. Chem. Chem. Phys.* **2016**, *18*, 4304–4309. [CrossRef]
22. Wang, X.; Wang, P.; Wang, J.; Hu, W.; Zhou, X.; Guo, N.; Huang, H.; Sun, S.; Shen, H.; Lin, T.; et al. Ultrasensitive and Broadband MoS2 Photodetector Driven by Ferroelectrics. *Adv. Mater.* **2015**, *27*, 6575–6581. [CrossRef]
23. Yin, Z.; Zhang, X.; Cai, Y.; Chen, J.; Wong, J.I.; Tay, Y.Y.; Chai, J.; Wu, J.; Zeng, Z.; Zheng, B.; et al. Preparation of MoS2-MoO3 hybrid nanomaterials for light-emitting diodes. *Angew. Chemie - Int. Ed.* **2014**, *53*, 12560–12565.
24. Liu, Z.; Liu, K.; Zhang, F.; Jain, S.M.; He, T.; Jiang, Y.; Liu, P.; Yang, J.; Liu, H.; Yuan, M. CH3NH3PbI3:MoS2 heterostructure for stable and efficient inverted perovskite solar cell. *Sol. Energy* **2020**, *195*, 436–445. [CrossRef]
25. Wang, H.; Li, C.; Fang, P.; Zhang, Z.; Zhang, J.Z. Synthesis, properties, and optoelectronic applications of two-dimensional MoS2 and MoS2-based heterostructures. *Chem. Soc. Rev.* **2018**, *47*, 6101–6127. [CrossRef]
26. Gupta, D.; Chauhan, V.; Kumar, R. A comprehensive review on synthesis and applications of molybdenum disulfide (MoS2) material: Past and recent developments. *Inorg. Chem. Commun.* **2020**, *121*, 108200. [CrossRef]
27. Krishnan, U.; Kaur, M.; Singh, K.; Kumar, M.; Kumar, A. A synoptic review of MoS 2: Synthesis to applications. *Superlattices Microstruct.* **2019**, *128*, 274–297. [CrossRef]
28. Nalwa, H.S. A review of molybdenum disulfide (MoS2) based photodetectors: From ultra-broadband, self-powered to flexible devices. *RSC Adv.* **2020**, *10*, 30529–30602. [CrossRef]

29. Sun, J.; Li, X.; Guo, W.; Zhao, M.; Fan, X.; Dong, Y.; Xu, C.; Deng, J.; Fu, Y. Synthesis methods of two-dimensional MoS2: A brief review. *Crystals* **2017**, *7*, 198. [CrossRef]
30. Kumar, R.; Sahoo, S.; Joanni, E.; Singh, R.K.; Yadav, R.M.; Verma, R.K.; Singh, D.P.; Tan, W.K.; Pérez del Pino, A.; Moshkalev, S.A.; et al. A review on synthesis of graphene, h-BN and MoS2 for energy storage applications: Recent progress and perspectives. *Nano Res.* **2019**, *12*, 2655–2694. [CrossRef]
31. Xu, H.; Yi, J.; She, X.; Liu, Q.; Song, L.; Chen, S.; Yang, Y.; Song, Y.; Vajtai, R.; Lou, J.; et al. 2D heterostructure comprised of metallic 1T-MoS2/Monolayer O-g-C3N4 towards efficient photocatalytic hydrogen evolution. *Appl. Catal. B Environ.* **2018**, *220*, 379–385. [CrossRef]
32. Backes, C.; Berner, N.C.; Chen, X.; Lafargue, P.; LaPlace, P.; Freeley, M.; Duesberg, G.S.; Coleman, J.N.; McDonald, A.R. Functionalization of liquid-exfoliated two-dimensional 2H-MoS2. *Angew. Chemie - Int. Ed.* **2015**, *54*, 2638–2642. [CrossRef] [PubMed]
33. Tan, D.; Willatzen, M.; Wang, Z.L. Prediction of strong piezoelectricity in 3R-MoS2 multilayer structures. *Nano Energy* **2019**, *56*, 512–515. [CrossRef]
34. Liu, K.K.; Zhang, W.; Lee, Y.H.; Lin, Y.C.; Chang, M.T.; Su, C.Y.; Chang, C.S.; Li, H.; Shi, Y.; Zhang, H.; et al. Growth of large-area and highly crystalline MoS 2 thin layers on insulating substrates. *Nano Lett.* **2012**, *12*, 1538–1544. [CrossRef]
35. Yu, H.; Liao, M.; Zhao, W.; Liu, G.; Zhou, X.J.; Wei, Z.; Xu, X.; Liu, K.; Hu, Z.; Deng, K.; et al. Wafer-Scale Growth and Transfer of Highly-Oriented Monolayer MoS2 Continuous Films. *ACS Nano* **2017**, *11*, 12001–12007. [CrossRef] [PubMed]
36. Yang, P.; Zhang, S.; Pan, S.; Tang, B.; Liang, Y.; Zhao, X.; Zhang, Z.; Shi, J.; Huan, Y.; Shi, Y.; et al. Epitaxial Growth of Centimeter-Scale Single-Crystal MoS2 Monolayer on Au(111). *ACS Nano* **2020**, *14*, 5036–5045. [CrossRef]
37. Chen, X.P.; Xing, G.J.; Xu, L.F.; Lian, H.Q.; Wang, Y. Vertically aligned MoS2 films prepared by RF-magnetron sputtering method as electrocatalysts for hydrogen evolution reactions. *Compos. Interfaces* **2020**, 1–10. [CrossRef]
38. Hu, Z.; Wang, L.; Zhang, K.; Wang, J.; Cheng, F.; Tao, Z.; Chen, J. MoS2 Nanoflowers with Expanded Interlayers as High-Performance Anodes for Sodium-Ion Batteries. *Angew. Chemie - Int. Ed.* **2014**, *53*, 12794–12798. [CrossRef]
39. Chen, J.; Kuriyama, N.; Yuan, H.; Takeshita, H.T.; Sakai, T. Electrochemical hydrogen storage in MoS2 nanotubes. *J. Am. Chem. Soc.* **2001**, *123*, 11813–11814. [CrossRef]
40. Li, W.J.; Shi, E.W.; Ko, J.M.; Chen, Z.Z.; Ogino, H.; Fukuda, T. Hydrothermal synthesis of MoS2 nanowires. *J. Cryst. Growth* **2003**, *250*, 418–422. [CrossRef]
41. Hwang, H.; Kim, H.; Cho, J. MoS2 nanoplates consisting of disordered graphene-like layers for high rate lithium battery anode materials. *Nano Lett.* **2011**, *11*, 4826–4830. [CrossRef]
42. Deokar, G.; Vancsó, P.; Arenal, R.; Ravaux, F.; Casanova-Cháfer, J.; Llobet, E.; Makarova, A.; Vyalikh, D.; Struzzi, C.; Lambin, P.; et al. MoS2–Carbon Nanotube Hybrid Material Growth and Gas Sensing. *Adv. Mater. Interfaces* **2017**, *4*, 1–10. [CrossRef]
43. Deokar, G.; Vignaud, D.; Arenal, R.; Louette, P.; Colomer, J. Synthesis and characterization of MoS2 nanosheets. *Nanotechnology* **2016**, *27*, 075604. [CrossRef]
44. Deokar, G.; Rajput, N.S.; Vancsó, P.; Ravaux, F.; Jouiad, M.; Vignaud, D.; Cecchet, F.; Colomer, J.F. Large area growth of vertically aligned luminescent MoS2 nanosheets. *Nanoscale* **2017**, *9*, 277–287. [CrossRef]
45. Gan, X.; Gao, Y.; Fai Mak, K.; Yao, X.; Shiue, R.J.; Van Der Zande, A.; Trusheim, M.E.; Hatami, F.; Heinz, T.F.; Hone, J.; et al. Controlling the spontaneous emission rate of monolayer MoS2 in a photonic crystal nanocavity. *Appl. Phys. Lett.* **2013**, *103*, 181119. [CrossRef] [PubMed]
46. Eda, G.; Fujita, T.; Yamaguchi, H.; Voiry, D.; Chen, M.; Chhowalla, M. Coherent atomic and electronic heterostructures of single-layer MoS 2. *ACS Nano* **2012**, *6*, 7311–7317. [CrossRef] [PubMed]
47. Wang, T.; Chen, S.; Pang, H.; Xue, H.; Yu, Y. MoS2-Based Nanocomposites for Electrochemical Energy Storage. *Adv. Sci.* **2017**, *4*, 1600289. [CrossRef] [PubMed]
48. Shokri, A.; Salami, N. Gas sensor based on MoS2 monolayer. *Sensors Actuators, B Chem.* **2016**, *236*, 378–385. [CrossRef]
49. Deokar, G.; Rajput, N.S.; Li, J.; Deepak, F.L.; Ou-Yang, W.; Reckinger, N.; Bittencourt, C.; Colomer, J.F.; Jouiad, M. Toward the use of CVD-grown MoS2 nanosheets as field-emission source. *Beilstein J. Nanotechnol.* **2018**, *9*, 1686–1694. [CrossRef]
50. Ma, J.; Bai, H.; Zhao, W.; Yuan, Y.; Zhang, K. High efficiency graphene/MoS2/Si Schottky barrier solar cells using layer-controlled MoS2 films. *Sol. Energy* **2018**, *160*, 76–84. [CrossRef]
51. Arulraj, A.; Ramesh, M.; Subramanian, B.; Senguttuvan, G. In-situ temperature and thickness control grown 2D-MoS2 via pulsed laser ablation for photovoltaic devices. *Sol. Energy* **2018**, *174*, 286–295. [CrossRef]
52. Guo, F.; Li, M.; Ren, H.; Huang, X.; Hou, W.; Wang, C.; Shi, W.; Lu, C. Fabrication of p-n CuBi2O4/MoS2 heterojunction with nanosheets-on-microrods structure for enhanced photocatalytic activity towards tetracycline degradation. *Appl. Surf. Sci.* **2019**, *491*, 88–94. [CrossRef]
53. Splendiani, A.; Sun, L.; Zhang, Y.; Li, T.; Kim, J.; Chim, C.Y.; Galli, G.; Wang, F. Emerging photoluminescence in monolayer MoS2. *Nano Lett.* **2010**, *10*, 1271–1275. [CrossRef] [PubMed]
54. Eda, G.; Yamaguchi, H.; Voiry, D.; Fujita, T.; Chen, M.; Chhowalla, M. Photoluminescence from chemically exfoliated MoS 2. *Nano Lett.* **2011**, *11*, 5111–5116. [CrossRef] [PubMed]
55. Rafiee, J.; Mi, X.; Gullapalli, H.; Thomas, A.V.; Yavari, F.; Shi, Y.; Ajayan, P.M.; Koratkar, N.A. Wetting transparency of graphene. *Nat. Mater.* **2012**, *11*, 217–222. [CrossRef]
56. Kozbial, A.; Zhou, F.; Li, Z.; Liu, H.; Li, L. Are Graphitic Surfaces Hydrophobic? *Acc. Chem. Res.* **2016**, *49*, 2765–2773. [CrossRef]

57. Marbou, K.; Ghaferi, A.A.; Jouiad, M. In-situ Characterization of Wettability Alteration in HOPG. *SOP Trans. Nanotechnol* **2015**, *2374*, 1–10.
58. Huang, Y.; Pan, Y.H.; Yang, R.; Bao, L.H.; Meng, L.; Luo, H.L.; Cai, Y.Q.; Liu, G.D.; Zhao, W.J.; Zhou, Z.; et al. Universal mechanical exfoliation of large-area 2D crystals. *Nat. Commun.* **2020**, *11*, 1–9. [CrossRef]
59. Magda, G.Z.; Petõ, J.; Dobrik, G.; Hwang, C.; Biró, L.P.; Tapasztó, L. Exfoliation of large-area transition metal chalcogenide single layers. *Sci. Rep.* **2015**, *5*, 3–7. [CrossRef]
60. Kim, S.; Park, W.; Kim, D.; Kang, J.; Lee, J.; Jang, H.Y.; Song, S.H.; Cho, B.; Lee, D. Novel exfoliation of high-quality 2h-mos2 nanoflakes for solution-processed photodetector. *Nanomaterials* **2020**, *10*, 1045. [CrossRef]
61. Pirzado, A.A.; Le Normand, F.; Romero, T.; Paszkiewicz, S.; Papaefthimiou, V.; Ihiawakrim, D.; Janowska, I. Few-layer graphene from mechanical exfoliation of graphite-based materials: Structure-dependent characteristics. *ChemEngineering* **2019**, *3*, 1–10. [CrossRef]
62. Novoselov, K.S.; Jiang, D.; Schedin, F.; Booth, T.J.; Khotkevich, V.V.; Morozov, S.V.; Geim, A.K.; Benka, S.G. Two-dimensional atomic crystals. *Phys. Today* **2005**, *58*, 9. [CrossRef] [PubMed]
63. Janica, I.; Iglesias, D.; Ippolito, S.; Ciesielski, A.; Samorì, P. Effect of temperature and exfoliation time on the properties of chemically exfoliated MoS2nanosheets. *Chem. Commun.* **2020**, *56*, 15573–15576. [CrossRef] [PubMed]
64. Guan, Z.; Wang, C.; Li, W.; Luo, S.; Yao, Y.; Yu, S.; Sun, R.; Wong, C.P. A facile and clean process for exfoliating MoS2 nanosheets assisted by a surface active agent in aqueous solution. *Nanotechnology* **2018**, *29*, 425702. [CrossRef]
65. Lin, H.; Wang, J.; Luo, Q.; Peng, H.; Luo, C.; Qi, R.; Huang, R.; Travas-Sejdic, J.; Duan, C.G. Rapid and highly efficient chemical exfoliation of layered MoS2and WS2. *J. Alloys Compd.* **2017**, *699*, 222–229. [CrossRef]
66. Yang, Y.Q.; Tye, C.T.; Smith, K.J. Influence of MoS2 catalyst morphology on the hydrodeoxygenation of phenols. *Catal. Commun.* **2008**, *9*, 1364–1368. [CrossRef]
67. Liu, H.F.; Wong, S.L.; Chi, D.Z. CVD Growth of MoS2-based Two-dimensional Materials. *Chem. Vap. Depos.* **2015**, *21*, 241–259. [CrossRef]
68. Wang, Q.H.; Kalantar-Zadeh, K.; Kis, A.; Coleman, J.N.; Strano, M.S. Electronics and optoelectronics of two-dimensional transition metal dichalcogenides. *Nat. Nanotechnol.* **2012**, *7*, 699–712. [CrossRef]
69. Zeng, T.; You, Y.; Wang, X.; Hu, T.; Tai, G. Chemical vapor deposition and device application of two-dimensional molybdenum disulfide-based atomic crystals. *Prog. Chem.* **2016**, *28*, 459–470.
70. Balendhran, S.; Ou, J.Z.; Bhaskaran, M.; Sriram, S.; Ippolito, S.; Vasic, Z.; Kats, E.; Bhargava, S.; Zhuiykov, S.; Kalantar-Zadeh, K. Atomically thin layers of MoS 2via a two step thermal evaporation-exfoliation method. *Nanoscale* **2012**, *4*, 461–466. [CrossRef]
71. Nam Trung, T.; Kamand, F.Z.; Al tahtamouni, T.M. Elucidating the mechanism for the chemical vapor deposition growth of vertical MoO2/MoS2 flakes toward photoelectrochemical applications. *Appl. Surf. Sci.* **2020**, *505*, 144551. [CrossRef]
72. Ahn, C.; Lee, J.; Kim, H.U.; Bark, H.; Jeon, M.; Ryu, G.H.; Lee, Z.; Yeom, G.Y.; Kim, K.; Jung, J.; et al. Low-Temperature Synthesis of Large-Scale Molybdenum Disulfide Thin Films Directly on a Plastic Substrate Using Plasma-Enhanced Chemical Vapor Deposition. *Adv. Mater.* **2015**, *27*, 5223–5229. [CrossRef]
73. Sojková, M.; Siffalovic, P.; Babchenko, O.; Vanko, G.; Dobročka, E.; Hagara, J.; Mrkyvkova, N.; Majková, E.; Ižák, T.; Kromka, A.; et al. Carbide-free one-zone sulfurization method grows thin MoS 2 layers on polycrystalline CVD diamond. *Sci. Rep.* **2019**, *9*, 2–12. [CrossRef]
74. Withanage, S.S.; Kalita, H.; Chung, H.S.; Roy, T.; Jung, Y.; Khondaker, S.I. Uniform Vapor-Pressure-Based Chemical Vapor Deposition Growth of MoS2 Using MoO3 Thin Film as a Precursor for Coevaporation. *ACS Omega* **2018**, *3*, 18943–18949. [CrossRef] [PubMed]
75. Wang, S.; Rong, Y.; Fan, Y.; Pacios, M.; Bhaskaran, H.; He, K.; Warner, J.H. Shape evolution of monolayer MoS2 crystals grown by chemical vapor deposition. *Chem. Mater.* **2014**, *26*, 6371–6379. [CrossRef]
76. Jeon, J.; Jang, S.K.; Jeon, S.M.; Yoo, G.; Jang, Y.H.; Park, J.H.; Lee, S. Layer-controlled CVD growth of large-area two-dimensional MoS2 films. *Nanoscale* **2015**, *7*, 1688–1695. [CrossRef] [PubMed]
77. Hyun, C.M.; Choi, J.H.; Lee, S.W.; Park, J.H.; Lee, K.T.; Ahn, J.H. Synthesis mechanism of MoS2 layered crystals by chemical vapor deposition using MoO3 and sulfur powders. *J. Alloys Compd.* **2018**, *765*, 380–384. [CrossRef]
78. Lin, Z.; Zhao, Y.; Zhou, C.; Zhong, R.; Wang, X.; Tsang, Y.H.; Chai, Y. Controllable Growth of Large-Size Crystalline MoS2 and Resist-Free Transfer Assisted with a Cu Thin Film. *Sci. Rep.* **2015**, *5*, 1–10. [CrossRef] [PubMed]
79. Rotunno, E.; Bosi, M.; Seravalli, L.; Salviati, G.; Fabbri, F. Influence of organic promoter gradient on the MoS2growth dynamics. *Nanoscale Adv.* **2020**, *2*, 2352–2362. [CrossRef]
80. Le, D.; Rawal, T.B.; Rahman, T.S. Single-Layer MoS2 with Sulfur Vacancies: Structure and Catalytic Application. *J. Phys. Chem. C* **2014**, *118*, 5346–5351. [CrossRef]
81. Jurca, T.; Moody, M.J.; Henning, A.; Emery, J.D.; Wang, B.; Tan, J.M.; Lohr, T.L.; Lauhon, L.J.; Marks, T.J. Low-Temperature Atomic Layer Deposition of MoS2 Films. *Angew. Chemie - Int. Ed.* **2017**, *56*, 4991–4995. [CrossRef]
82. Tan, L.K.; Liu, B.; Teng, J.H.; Guo, S.; Low, H.Y.; Loh, K.P. Atomic layer deposition of a MoS2 film. *Nanoscale* **2014**, *6*, 10584–10588. [CrossRef] [PubMed]
83. Mattinen, M.; Hatanpää, T.; Sarnet, T.; Mizohata, K.; Meinander, K.; King, P.J.; Khriachtchev, L.; Räisänen, J.; Ritala, M.; Leskelä, M. Atomic Layer Deposition of Crystalline MoS2 Thin Films: New Molybdenum Precursor for Low-Temperature Film Growth. *Adv. Mater. Interfaces* **2017**, *4*, 1700123. [CrossRef]

84. Jin, Z.; Shin, S.; Kwon, D.H.; Han, S.J.; Min, Y.S. Novel chemical route for atomic layer deposition of MoS2 thin film on SiO2/Si substrate. *Nanoscale* **2014**, *6*, 14453–14458. [CrossRef]
85. Browning, R.; Padigi, P.; Solanki, R.; Tweet, D.J.; Schuele, P.; Evans, D. Atomic layer deposition of MoS2 thin films. *Mater. Res. Express* **2015**, *2*, 12–17. [CrossRef]
86. Liu, H.; Chen, L.; Zhu, H.; Sun, Q.Q.; Ding, S.J.; Zhou, P.; Zhang, D.W. Atomic layer deposited 2D MoS2 atomic crystals: From material to circuit. *Nano Res.* **2020**, *13*, 1644–1650. [CrossRef]
87. Chen, C.; Raza, M.H.; Amsalem, P.; Schultz, T.; Koch, N.; Pinna, N. Morphology-Controlled MoS2 by Low-Temperature Atomic Layer Deposition. *Nanoscale* **2020**, *12*, 20404–20412.
88. Yang, J.; Liu, L. Nanotribological properties of 2-D MoS2 on different substrates made by atomic layer deposition (ALD). *Appl. Surf. Sci.* **2020**, *502*, 144402. [CrossRef]
89. Huang, Y.; Liu, L.; Sha, J.; Chen, Y. Size-dependent piezoelectricity of molybdenum disulfide (MoS2) films obtained by atomic layer deposition (ALD). *Appl. Phys. Lett.* **2017**, *111*, 063902. [CrossRef]
90. Jang, Y.; Yeo, S.; Lee, H.B.R.; Kim, H.; Kim, S.H. Wafer-scale, conformal and direct growth of MoS 2 thin films by atomic layer deposition. *Appl. Surf. Sci.* **2016**, *365*, 160–165. [CrossRef]
91. Pandiyan, R.; Oulad Elhmaidi, Z.; Sekkat, Z.; Abd-lefdil, M.; El Khakani, M.A. Reconstructing the energy band electronic structure of pulsed laser deposited CZTS thin films intended for solar cell absorber applications. *Appl. Surf. Sci.* **2017**, *396*, 1562–1570. [CrossRef]
92. Brassard, D.; El Khakani, M.A. Pulsed-laser deposition of high- k titanium silicate thin films. *J. Appl. Phys.* **2005**, *98*, 054912. [CrossRef]
93. Daghrir, R.; Drogui, P.; Dimboukou-Mpira, A.; El Khakani, M.A. Photoelectrocatalytic degradation of carbamazepine using Ti/TiO2 nanostructured electrodes deposited by means of a pulsed laser deposition process. *Chemosphere* **2013**, *93*, 2756–2766. [CrossRef]
94. Ka, I.; Le Borgne, V.; Ma, D.; El Khakani, M.A. Pulsed laser ablation based direct synthesis of single-wall carbon nanotube/PbS quantum dot nanohybrids exhibiting strong, spectrally wide and fast photoresponse. *Adv. Mater.* **2012**, *24*, 6289–6294. [CrossRef]
95. Late, D.J.; Shaikh, P.A.; Khare, R.; Kashid, R.V.; Chaudhary, M.; More, M.A.; Ogale, S.B. Pulsed laser-deposited MoS2 thin films on W and Si: Field emission and photoresponse studies. *ACS Appl. Mater. Interfaces* **2014**, *6*, 15881–15888. [CrossRef] [PubMed]
96. Rai, R.H.; Pérez-Pacheco, A.; Quispe-Siccha, R.; Glavin, N.R.; Muratore, C. Pulsed laser annealing of amorphous two-dimensional transition metal dichalcogenides. *J. Vac. Sci. Technol. A* **2020**, *38*, 052201. [CrossRef]
97. Wang, R.; Sun, P.; Wang, H.; Wang, X. Pulsed laser deposition of amorphous molybdenum disulfide films for efficient hydrogen evolution reaction. *Electrochim. Acta* **2017**, *258*, 876–882. [CrossRef]
98. Loh, T.A.J.; Chua, D.H.C. Growth mechanism of pulsed laser fabricated few-layer MoS2 on metal substrates. *ACS Appl. Mater. Interfaces* **2014**, *6*, 15966–15971. [CrossRef] [PubMed]
99. McDevitt, N.T.; Bultman, J.E.; Zabinski, J.S. Study of amorphous MoS2 films grown by pulsed laser deposition. *Appl. Spectrosc.* **1998**, *52*, 1160–1164. [CrossRef]
100. Mosleh, M.; Laube, S.J.P.; Suh, N.P. Friction of undulated surfaces coated with mos2 by pulsed laser deposition. *Tribol. Trans.* **1999**, *42*, 495–502. [CrossRef]
101. Serrao, C.R.; Diamond, A.M.; Hsu, S.L.; You, L.; Gadgil, S.; Clarkson, J.; Carraro, C.; Maboudian, R.; Hu, C.; Salahuddin, S. Highly crystalline MoS2 thin films grown by pulsed laser deposition. *Appl. Phys. Lett.* **2015**, *106*, 052101. [CrossRef]
102. Barvat, A.; Prakash, N.; Singh, D.K.; Dogra, A.; Khanna, S.P.; Singh, S.; Pal, P. Mixed Phase Compositions of MoS2 Ultra Thin Film Grown by Pulsed Laser Deposition. *Mater. Today Proc.* **2018**, *5*, 2241–2245. [CrossRef]
103. Siegel, G.; Venkata Subbaiah, Y.P.; Prestgard, M.C.; Tiwari, A. Growth of centimeter-scale atomically thin MoSfilms by pulsed laser deposition. *APL Mater.* **2015**, *3*, 056103. [CrossRef]
104. Kumar, S.; Sharma, A.; Ho, Y.T.; Pandey, A.; Tomar, M.; Kapoor, A.K.; Chang, E.Y.; Gupta, V. High performance UV photodetector based on MoS2 layers grown by pulsed laser deposition technique. *J. Alloys Compd.* **2020**, *835*, 155222. [CrossRef]
105. Lopez-Sanchez, O.; Lembke, D.; Kayci, M.; Radenovic, A.; Kis, A. Ultrasensitive photodetectors based on monolayer MoS 2. *Nat. Nanotechnol.* **2013**, *8*, 497–501. [CrossRef] [PubMed]
106. Alkis, S.; Öztaş, T.; Aygün, L.E.; Bozkurt, F.; Okyay, A.K.; Ortaç, B. Thin film MoS_2 nanocrystal based ultraviolet photodetector. *Opt. Express* **2012**, *20*, 21815. [CrossRef] [PubMed]
107. Huo, N.; Konstantatos, G. Ultrasensitive all-2D MoS2 phototransistors enabled by an out-of-plane MoS2 PN homojunction. *Nat. Commun.* **2017**, *8*, 1–6. [CrossRef]
108. Tsai, D.S.; Liu, K.K.; Lien, D.H.; Tsai, M.L.; Kang, C.F.; Lin, C.A.; Li, L.J.; He, J.H. Few-layer MoS2 with high broadband photogain and fast optical switching for use in harsh environments. *ACS Nano* **2013**, *7*, 3905–3911. [CrossRef] [PubMed]
109. Goel, N.; Kumar, R.; Roul, B.; Kumar, M.; Krupanidhi, S.B. Wafer-scale synthesis of a uniform film of few-layer MoS2 on GaN for 2D heterojunction ultraviolet photodetector. *J. Phys. D. Appl. Phys.* **2018**, *51*, 374003. [CrossRef]
110. Donley, M.S.; Murray, P.T.; Barber, S.A.; Haas, T.W. Deposition and properties of MoS2 thin films grown by pulsed laser evaporation. *Surf. Coatings Technol.* **1988**, *36*, 329–340. [CrossRef]
111. Walck, S.D.; Donley, M.S.; Zabinski, J.S.; Dyhouse, V.J. Characterization of Pulsed Laser Deposited PbO/MoS2 by Transmission Electron Microscopy. *J. Mater. Res.* **1994**, *9*, 236–245. [CrossRef]

112. Barvat, A.; Prakash, N.; Satpati, B.; Singha, S.S.; Kumar, G.; Singh, D.K.; Dogra, A.; Khanna, S.P.; Singha, A.; Pal, P. Emerging photoluminescence from bilayer large-area 2D MoS2 films grown by pulsed laser deposition on different substrates. *J. Appl. Phys.* **2017**, *122*, 015304. [CrossRef]
113. Wang, R.; Shao, Q.; Yuan, Q.; Sun, P.; Nie, R.; Wang, X. Direct growth of high-content 1T phase MoS2 film by pulsed laser deposition for hydrogen evolution reaction. *Appl. Surf. Sci.* **2020**, *504*, 144320. [CrossRef]
114. Wang, S.; Yu, H.; Zhang, H.; Wang, A.; Zhao, M.; Chen, Y.; Mei, L.; Wang, J. Broadband few-layer MoS2 saturable absorbers. *Adv. Mater.* **2014**, *26*, 3538–3544. [CrossRef]
115. Fominski, V.Y.; Markeev, A.M.; Nevolin, V.N.; Prokopenko, V.B.; Vrublevski, A.R. Pulsed laser deposition of MoSx films in a buffer gas atmosphere. *Thin Solid Films* **1994**, *248*, 240–246. [CrossRef]
116. Jiao, L.; Jie, W.; Yang, Z.; Wang, Y.; Chen, Z.; Zhang, X.; Tang, W.; Wu, Z.; Hao, J. Layer-dependent photoresponse of 2D MoS 2 films prepared by pulsed laser deposition. *J. Mater. Chem. C* **2019**, *7*, 2522–2529. [CrossRef]
117. Serna, M.I.; Yoo, S.H.; Moreno, S.; Xi, Y.; Oviedo, J.P.; Choi, H.; Alshareef, H.N.; Kim, M.J.; Minary-Jolandan, M.; Quevedo-Lopez, M.A. Large-Area Deposition of MoS2 by Pulsed Laser Deposition with in Situ Thickness Control. *ACS Nano* **2016**, *10*, 6054–6061. [CrossRef] [PubMed]
118. Jiao, L.; Wang, Y.; Zhi, Y.; Cui, W.; Chen, Z.; Zhang, X.; Jie, W.; Wu, Z. Fabrication and Characterization of Two-Dimensional Layered MoS2 Thin Films by Pulsed Laser Deposition. *Adv. Condens. Matter Phys.* **2018**, *2018*, 23–28. [CrossRef]
119. Pradhan, G.; Sharma, A.K. Anomalous Raman and photoluminescence blue shift in mono- and a few layered pulsed laser deposited MoS2 thin films. *Mater. Res. Bull.* **2018**, *102*, 406–411. [CrossRef]
120. Walck, S.D.; Zabinski, J.S.; Donley, M.S.; Bultman, J.E. Evolution of surface topography in pulsed-laser-deposited thin films of MoS2. *Surf. Coatings Technol.* **1993**, *62*, 412–416. [CrossRef]
121. Ho, Y.T.; Ma, C.H.; Luong, T.T.; Wei, L.L.; Yen, T.C.; Hsu, W.T.; Chang, W.H.; Chu, Y.C.; Tu, Y.Y.; Pande, K.P.; et al. Layered MoS2 grown on c -sapphire by pulsed laser deposition. *Phys. Status Solidi - Rapid Res. Lett.* **2015**, *9*, 187–191. [CrossRef]
122. Zhang, Y.; Wang, S.; Yu, H.; Zhang, H.; Chen, Y.; Mei, L.; Di Lieto, A.; Tonelli, M.; Wang, J. Atomic-layer molybdenum sulfide optical modulator for visible coherent light. *Sci. Rep.* **2015**, *5*, 1–7. [CrossRef] [PubMed]
123. Zhang, Y.; Wang, S.; Wang, D.; Yu, H.; Zhang, H.; Chen, Y.; Mei, L.; Di Lieto, A.; Tonelli, M.; Wang, J. Atomic-layer molybdenum sulfide passively modulated green laser pulses. *IEEE Photonics Technol. Lett.* **2016**, *28*, 197–200. [CrossRef]
124. Miao, P.; Ma, Y.; Sun, M.; Li, J.; Xu, P. Tuning the SERS activity and plasmon-driven reduction of p-nitrothiophenol on a Ag@MoS2 film. *Faraday Discuss.* **2019**, *214*, 297–307. [CrossRef] [PubMed]
125. Xie, M.Z.; Zhou, J.Y.; Ji, H.; Ye, Y.; Wang, X.; Jiang, K.; Shang, L.Y.; Hu, Z.G.; Chu, J.H. Annealing effects on sulfur vacancies and electronic transport of MoS2 films grown by pulsed-laser deposition. *Appl. Phys. Lett.* **2019**, *115*, 121901.
126. Su, B.; He, H.; Ye, Z. Large-area ZnO/MoS2 heterostructure grown by pulsed laser deposition. *Mater. Lett.* **2019**, *253*, 187–190. [CrossRef]
127. Pang, X.; Zhang, Q.; Shao, Y.; Liu, M.; Zhang, D.; Zhao, Y. A flexible pressure sensor based on magnetron sputtered mos2. *Sensors (Switzerland)* **2021**, *21*, 1130. [CrossRef]
128. Tao, J.; Chai, J.; Lu, X.; Wong, L.M.; Wong, T.I.; Pan, J.; Xiong, Q.; Chi, D.; Wang, S. Growth of wafer-scale MoS2 monolayer by magnetron sputtering. *Nanoscale* **2015**, *7*, 2497–2503. [CrossRef]
129. Kaindl, R.; Bayer, B.C.; Resel, R.; Müller, T.; Skakalova, V.; Habler, G.; Abart, R.; Cherevan, A.S.; Eder, D.; Blatter, M.; et al. Growth, structure and stability of sputter-deposited MoS2 thin films. *Beilstein J. Nanotechnol.* **2017**, *8*, 1115–1126. [CrossRef] [PubMed]
130. Rowley-Neale, S.J.; Ratova, M.; Fugita, L.T.N.; Smith, G.C.; Gaffar, A.; Kulczyk-Malecka, J.; Kelly, P.J.; Banks, C.E. Magnetron Sputter-Coated Nanoparticle MoS2 Supported on Nanocarbon: A Highly Efficient Electrocatalyst toward the Hydrogen Evolution Reaction. *ACS Omega* **2018**, *3*, 7235–7242. [CrossRef]
131. Tian, L.; Wu, R.; Liu, H.Y. Synthesis of Au-nanoparticle-loaded 1T@2H-MoS 2 nanosheets with high photocatalytic performance. *J. Mater. Sci.* **2019**, *54*, 9656–9665. [CrossRef]
132. Nan, H.; Wang, Z.; Wang, W.; Liang, Z.; Lu, Y.; Chen, Q.; He, D.; Tan, P.; Miao, F.; Wang, X.; et al. Strong photoluminescence enhancement of MoS2 through defect engineering and oxygen bonding. *ACS Nano* **2014**, *8*, 5738–5745. [CrossRef]
133. Feng, Y.; Zhang, K.; Li, H.; Wang, F.; Zhou, B.; Fang, M.; Wang, W.; Wei, J.; Wong, H.S.P. In situ visualization and detection of surface potential variation of mono and multilayer MoS2 under different humidities using Kelvin probe force microscopy. *Nanotechnology* **2017**, *28*, 295705. [CrossRef]
134. Mouri, S.; Miyauchi, Y.; Matsuda, K. Tunable Photoluminescence of Monolayer MoS2 via Chemical Doping. *Nano Lett.* **2013**, *13*, 5944–5948. [CrossRef] [PubMed]
135. Lee, C.; Yan, H.; Brus, L.E.; Heinz, T.F.; Hone, J.; Ryu, S. Anomalous lattice vibrations of single- and few-layer MoS2. *ACS Nano* **2010**, *4*, 2695–2700. [CrossRef]
136. Mak, K.F.; Lee, C.; Hone, J.; Shan, J.; Heinz, T.F. Atomically thin MoS2: A new direct-gap semiconductor. *Phys. Rev. Lett.* **2010**, *105*, 2–5. [CrossRef] [PubMed]
137. Cheiwchanchamnangij, T.; Lambrecht, W.R.L. Quasiparticle band structure calculation of monolayer, bilayer, and bulk MoS 2. *Phys. Rev. B - Condens. Matter Mater. Phys.* **2012**, *85*, 205302. [CrossRef]
138. Li, H.; Zhang, Q.; Yap, C.C.R.; Tay, B.K.; Edwin, T.H.T.; Olivier, A.; Baillargeat, D. From bulk to monolayer MoS 2: Evolution of Raman scattering. *Adv. Funct. Mater.* **2012**, *22*, 1385–1390. [CrossRef]

139. Ahmad, S.; Mukherjee, S. A Comparative Study of Electronic Properties of Bulk MoS2 and Its Monolayer Using DFT Technique: Application of Mechanical Strain on MoS2 Monolayer. *Graphene* **2014**, *03*, 52–59. [CrossRef]
140. Erfanifam, S.; Jamilpanah, L.; Sangpour, P.; Haddadi, F.; Hamdi, M.; Erfanifam, M.; Chanda, G.; Herrmannsdörfer, T.; Sazgari, V.; Sadeghi, A.; et al. Electrical and optical properties of MoS2,MoOx=2,3(MoSO)/RGO heterostructure. *arXiv* **2018**, *3*, 1–6.
141. Zhang, Z.; Qian, Q.; Li, B.; Chen, K.J. Interface Engineering of Monolayer MoS2/GaN Hybrid Heterostructure: Modified Band Alignment for Photocatalytic Water Splitting Application by Nitridation Treatment. *ACS Appl. Mater. Interfaces* **2018**, *10*, 17419–17426. [CrossRef]
142. Dolui, K.; Rungger, I.; Das Pemmaraju, C.; Sanvito, S. Possible doping strategies for MoS2 monolayers: An ab initio study. *Phys. Rev. B - Condens. Matter Mater. Phys.* **2013**, *88*, 075420. [CrossRef]
143. Zahid, F.; Liu, L.; Zhu, Y.; Wang, J.; Guo, H. A generic tight-binding model for monolayer, bilayer and bulk MoS 2. *AIP Adv.* **2013**, *3*, 052111. [CrossRef]
144. Liang, M.; Ali, A.; Belaidi, A.; Hossain, M.I.; Ronan, O.; Downing, C.; Tabet, N.; Sanvito, S.; EI-Mellouhi, F.; Nicolosi, V. Improving stability of organometallic-halide perovskite solar cells using exfoliation two-dimensional molybdenum chalcogenides. *npj 2D Mater. Appl.* **2020**, *4*, 1–8. [CrossRef]
145. Singh, E.; Kim, K.S.; Yeom, G.Y.; Nalwa, H.S. Atomically thin-layered molybdenum disulfide (MoS2) for bulk-heterojunction solar cells. *ACS Appl. Mater. Interfaces* **2017**, *9*, 3223–3245. [CrossRef]
146. J rvinen, T.; Lorite, G.S.; Per ntie, J.; Toth, G.; Saarakkala, S.; Virtanen, V.K.; Kordas, K. WS2 and MoS2 thin film gas sensors with high response to NH3 in air at low temperature. *Nanotechnology* **2019**, *30*, 405501. [CrossRef]
147. Perkins, F.K.; Friedman, A.L.; Cobas, E.; Campbell, P.M.; Jernigan, G.G.; Jonker, B.T. Chemical Vapor Sensing with Monolayer MoS2. *Nano Lett.* **2013**, *13*, 668–673. [CrossRef] [PubMed]
148. Mukherjee, B.; Simsek, E. Utilization of monolayer MoS2 in Bragg stacks and metamaterial structures as broadband absorbers. *Opt. Commun.* **2016**, *369*, 89–93. [CrossRef]
149. He, X.; Liu, F.; Lin, F.; Xiao, G.; Shi, W. Tunable MoS2 modified hybrid surface plasmon waveguides. *Nanotechnology* **2019**, *30*, 125201. [CrossRef] [PubMed]
150. Mawlong, L.P.L.; Paul, K.K.; Giri, P.K. Exciton-plasmon coupling and giant photoluminescence enhancement in monolayer MoS2 through hierarchically designed TiO2/Au/MoS2 ternary core − Shell heterostructure. *Nanotechnology* **2021**, *32*, 215201. [CrossRef] [PubMed]
151. Yang, Y.; Pan, R.; Tian, S.; Gu, C.; Li, J. Plasmonic hybrids of mos2 and 10-nm nanogap arrays for photoluminescence enhancement. *Micromachines* **2020**, *11*, 1109. [CrossRef]
152. Rahmati, B.; Hajzadeh, I.; Taheri, M.; Karimzadeh, R.; Mohajerzadeh, S.; Mohseni, S.M. Plasmonic improvement photoresponse of vertical-MoS2 nanostructure photodetector by Au nanoparticles. *Appl. Surf. Sci.* **2019**, *490*, 165–171. [CrossRef]
153. Tsai, M.L.; Su, S.H.; Chang, J.K.; Tsai, D.S.; Chen, C.H.; Wu, C.I.; Li, L.J.; Chen, L.J.; He, J.H. Monolayer MoS2 heterojunction solar cells. *ACS Nano* **2014**, *8*, 8317–8322. [CrossRef]
154. Burgelman, M.; Verschraegen, J.; Minnaert, B.; Marlein, J. Numerical simulation of thin film solar cells: Practical exercises with SCAPS. *Numos Work.* **2007**, 357–366.
155. Burgelman, M.; Verschraegen, J.; Degrave, S.; Nollet, P. Modeling thin-film PV devices. *Prog. Photovoltaics Res. Appl.* **2004**, *12*, 143–153. [CrossRef]
156. Verschraegen, J.; Burgelman, M. Numerical modeling of intra-band tunneling for heterojunction solar cells in scaps. *Thin Solid Films* **2007**, *515*, 6276–6279. [CrossRef]
157. Chen, X.; Wu, Z.; Xu, S.; Wang, L.; Huang, R.; Han, Y.; Ye, W.; Xiong, W.; Han, T.; Long, G.; et al. Probing the electron states and metal-insulator transition mechanisms in molybdenum disulphide vertical heterostructures. *Nat. Commun.* **2015**, *6*, 1–8. [CrossRef]
158. Rashid, H.; Rahman, K.S.; Hossain, M.I.; Tabet, N.; Alharbi, F.H.; Amin, N. Prospects of molybdenum disulfide (MoS2) as an alternative absorber layer material in thin film solar cells from numerical modeling. *Chalcogenide Lett.* **2014**, *11*, 397–403.
159. Deng, Q.; Li, Y.; Shen, Y.; Chen, L.; Wang, G.; Wang, S. Numerical simulation on n-MoS2/p-Si heterojunction solar cells. *Mod. Phys. Lett. B* **2017**, *31*, 1750079. [CrossRef]
160. Tousif, N.; Mohammad, S.; Ferdous, A.A.; Hoque, A. Investigation of Different Materials as Buffer Layer in CZTS Solar Cells Using SCAPS. *J. Clean Energy Technol.* **2018**, *6*, 293–296. [CrossRef]
161. Heidariramsheh, M.; Haghighi, M.; Dabbagh, M.M.; Mahdavi, S.M. Pure sulfide Cu2ZnSnS4 layers through a one-step low-temperature PLD technique: Insight into simulation on modified back contact to overcome the barrier of MoS2. *Mater. Sci. Eng. B Solid-State Mater. Adv. Technol.* **2020**, *262*, 114701. [CrossRef]
162. Bouarissa, A.; Gueddim, A.; Bouarissa, N.; Maghraoui-Meherezi, H. Modeling of ZnO/MoS2/CZTS photovoltaic solar cell through window, buffer and absorber layers optimization. *Mater. Sci. Eng. B Solid-State Mater. Adv. Technol.* **2021**, *263*, 114816. [CrossRef]
163. Zaidi, B.; Ullah, M.S.; Hadjoudja, B.; Gagui, S.; Houaidji, N.; Chouial, B.; Shekhar, C. Role of TCO films in improving the efficiency of CdS/MoS 2 heterojunction solar cells. *J. Nano- Electron. Phys.* **2019**, *11*, 4–7. [CrossRef]
164. Kohnehpoushi, S.; Nazari, P.; Nejand, B.A.; Eskandari, M. MoS2: A two-dimensional hole-transporting material for high-efficiency, low-cost perovskite solar cells. *Nanotechnology* **2018**, *29*, 205201. [CrossRef] [PubMed]

165. Joshi, N.; Hayasaka, T.; Liu, Y.; Liu, H.; Oliveira, O.N.; Lin, L. A review on chemiresistive room temperature gas sensors based on metal oxide nanostructures, graphene and 2D transition metal dichalcogenides. *Microchim. Acta* **2018**, *185*, 1–16. [CrossRef] [PubMed]
166. Donarelli, M.; Ottaviano, L. 2d materials for gas sensing applications: A review on graphene oxide, mos2, ws2 and phosphorene. *Sensors (Switzerland)* **2018**, *18*, 3638. [CrossRef] [PubMed]
167. Ramanathan, A.A. Defect Functionalization of MoS2 nanostructures as toxic gas sensors: A review. *IOP Conf. Ser. Mater. Sci. Eng.* **2018**, *305*, 012001. [CrossRef]
168. Li, W.; Zhang, Y.; Long, X.; Cao, J.; Xin, X.; Guan, X.; Peng, J.; Zheng, X. Gas Sensors Based on Mechanically Exfoliated MoS2 Nanosheets for Room-Temperature NO2 Detection. *Sensors (Basel).* **2019**, *19*, 2123. [CrossRef]
169. Cho, B.; Hahm, M.G.; Choi, M.; Yoon, J.; Kim, A.R.; Lee, Y.J.; Park, S.G.; Kwon, J.D.; Kim, C.S.; Song, M.; et al. Charge-transfer-based gas sensing using atomic-layer MoS2. *Sci. Rep.* **2015**, *5*, 8052. [CrossRef]
170. Zhang, Y.; Guo, S.; Xin, X.; Song, Y.; Yang, L.; Wang, B.; Tan, L.; Li, X. Plasmonic MoO2 as co-catalyst of MoS2 for enhanced photocatalytic hydrogen evolution. *Appl. Surf. Sci.* **2020**, *504*, 144291. [CrossRef]
171. Li, Y.; Wang, H.; Xie, L.; Liang, Y.; Hong, G.; Dai, H. MoS2 Nanoparticles Grown on Graphene: An Advanced Catalyst for the Hydrogen Evolution Reaction. *J. Am. Chem. Soc.* **2011**, *133*, 7296–7299. [CrossRef]
172. Chaojian, H.; Bo, L.; Qingwei, L.; Lijun, Y.; Yang, W.; Zhan, Y.; Lixin, D. Plasmon-Enhanced Photovoltaic Characteristics of Black Phosphorus-MoS 2 Heterojunction. *IEEE Open J. Nanotechnol.* **2021**, *2*, 41–51. [CrossRef]
173. Mukherjee, B.; Tseng, F.; Gunlycke, D.; Amara, K.K.; Eda, G.; Simsek, E. Complex electrical permittivity of the monolayer molybdenum disulfide (MoS_2) in near UV and visible. *Opt. Mater. Express* **2015**, *5*, 447. [CrossRef]
174. Jiang, Y.; Chen, W.; Wang, J. Broadband MoS 2 -based absorber investigated by a generalized interference theory. *Opt. Express* **2018**, *26*, 24403. [CrossRef] [PubMed]
175. Song, J.; Lu, L.; Cheng, Q.; Luo, Z. Surface plasmon-enhanced optical absorption in monolayer MoS2 with one-dimensional Au grating. *J. Quant. Spectrosc. Radiat. Transf.* **2018**, *211*, 138–143. [CrossRef]
176. Chen, W.; Wang, L.; Jiang, Y.; Wang, J. A Perfect Absorber Based on Monolayer MoS2 and Nano-Silver in the Visible Regime. *2018 Int. Conf. Microw. Millim. Wave Technol. (ICMMT). IEEE* **2018**, 1–3.
177. Camellini, A.; Mazzanti, A.; Mennucci, C.; Martella, C.; Lamperti, A.; Molle, A.; Buatier de Mongeot, F.; Della Valle, G.; Zavelani-Rossi, M. Evidence of Plasmon Enhanced Charge Transfer in Large-Area Hybrid Au–MoS2 Metasurface. *Adv. Opt. Mater.* **2020**, *8*, 2000653. [CrossRef]
178. Muhammad, N.; Chen, Y.; Qiu, C.W.; Wang, G.P. Optical Bound States in Continuum in MoS2-Based Metasurface for Directional Light Emission. *Nano Lett.* **2021**, *21*, 967–972. [CrossRef]
179. Deng, M.; Li, Z.; Rong, X.; Luo, Y.; Li, B.; Zheng, L.; Wang, X.; Lin, F.; Meixner, A.J.; Braun, K.; et al. Light-Controlled Near-Field Energy Transfer in Plasmonic Metasurface Coupled MoS2 Monolayer. *Small* **2020**, *16*, 2003539. [CrossRef]
180. Liu, J.T.; Tong, H.; Wu, Z.H.; Huang, J.B.; Zhou, Y.S. Greatly enhanced light emission of MoS2 using photonic crystal heterojunction. *Sci. Rep.* **2017**, *7*, 1–8. [CrossRef]
181. Xie, Y.; Liang, F.; Chi, S.; Wang, D.; Zhong, K.; Yu, H.; Zhang, H.; Chen, Y.; Wang, J. Defect Engineering of MoS2 for Room-Temperature Terahertz Photodetection. *ACS Appl. Mater. Interfaces* **2020**, *12*, 7351–7357. [CrossRef] [PubMed]

**Article 2: D. Mouloua, N. S. Rajput, J.-F. Blach, M. Lejeune, M. El Marssi, M. A. El Khakani, M. Jouiad, Mater. Sci. Eng. B 2022, 286, 116035.**

Materials Science and Engineering B 286 (2022) 116035

Contents lists available at ScienceDirect

Materials Science & Engineering B

journal homepage: www.elsevier.com/locate/mseb

# Fabrication control of $MoS_2/MoO_2$ nanocomposite via chemical vapor deposition for optoelectronic applications

D. Mouloua [a,b], N.S. Rajput [c], J.-F. Blach [d], M. Lejeune [a], M. El Marssi [a], M.A. El Khakani [b,*], M. Jouiad [a,*]

[a] Laboratory of Physics of Condensed Matter, University of Picardie Jules Verne, Scientific Pole, 33 rue Saint-Leu, 80039 Amiens Cedex 1, France
[b] Institut National de la Recherche Scientifique (INRS), Centre-Énergie, Matériaux et Télécommunications, 1650, Blvd, Lionel– Boulet, Varennes, QC J3X-1P7, Canada
[c] Advanced Materials Research Center, Technology Innovation Institute, P.O. Box 9639, Abu Dhabi, United Arab Emirates
[d] Univ. Artois, CNRS, Centrale Lille, ENSCL, Univ. Lille, UMR 8181, Unité de Catalyse et Chimie du Solide (UCCS), F-62300 Lens, France

ARTICLE INFO

*Keywords:*
$MoS_2/MoO_2$ nanocomposite
$MoS_2/MoO_2$ heterostructure
$MoS_2$ nanowires
Chemical vapor deposition
Photocurrent
Photoresponse

ABSTRACT

We report on the fabrication and control of $MoS_2/MoO_2$ nanocomposites exhibiting various optoelectronic properties. We demonstrate the growth of various compositions, shapes and crystalline structures by chemical vapor deposition (CVD). Microplates 1 to 30 μm to highly crystalline nanowires ~ 100 nm in diam. are obtained. Our findings show that depending on the $MoO_2$ content the band gap varies from 2 eV to 2.4 eV, whereas nanowires sample exhibits the lowest reflectance $\leq 10$ % for $\lambda \geq 450$ nm. Furthermore, the photoelectric properties of the produced samples were characterized by integrating them into photoconductive devices. Our results demonstrate a good photoresponse achieving $2 \times 10^4$ %, a responsivity as high as 1.13 mA/W, and a specific detectivity of $2.6 \times 10^9$ Jones for the nanowires, with a relatively rapid rise and decay times 1.6 s and 0.8 s, respectively. This work emphasizes the high potential of $MoS_2/MoO_2$ nanocomposite for the development of highly responsive optoelectronic devices.

## 1. Introduction

Over the past decade, molybdenum disulfide ($MoS_2$) has increasingly attracted attention due to its outstanding electrical and optical properties [1–4]. $MoS_2$ is a layered semiconductor that is sought to be used in optoelectronic devices with high on–off current ratios [5], owing to its tunable band gap [6,7] and its high electronic mobility [8]. When $MoS_2$ is associated with other materials, the resulting heterostructures could lead to a wide range of applications [9–15].

$MoS_2$-based photodetectors have been widely reported in the literature. Notably, engineering $MoS_2$-based heterostructures is among the most investigated strategies for the improvement of the photodetection performances [16]. Their main advantage consists in their ability to enable high charge carrier nucleation and transport and fast photodetection response by generating built-in electric fields [17]. Although a large variety of materials have been coherently associated with $MoS_2$, their elaboration remains relatively tedious, generally requiring a two steps fabrication process, hence raising the overall costs of the photodetector devices [18–20]. In this sense, the chemical vapor deposition (CVD) approach prevails as the most accessible, affordable and straightforward route for producing good-crystalline quality $MoS_2$ [21–23]. Nonetheless, the CVD growth of $MoS_2$ is sensitive to various parameters, including ambient pressure, carrier gas flow, furnace temperature, CVD reaction dwell time, precursor's positions, substrate location, etc. Evaluating each parameter is critical to obtain high-quality crystalline, mono to few $MoS_2$ layers with controlled morphologies and properties [24–28]. A comprehensive review regarding the $MoS_2$ growth via CVD, including growth parameters effects can be found elsewhere [29,30].

Although the CVD method allows the fabrication of highly crystalline $MoS_2$ films with a variety of morphologies, one of its limit is the loss of purity of $MoS_2$ due to incomplete sulfidation of metal precursors [31]. In other words, several intermediate materials, such as $MoO_3$ [32], $MoO_2$ [33], $MoOS_2$ [34] would have been synthesized as already investigated [35]. Recently, other researchers have pointed out the possible beneficial effects of hybridizing such intermediate materials with $MoS_2$ to improve the overall optical performance of the final hybrid materials [36]. Nonetheless, the control of the $MoS_2/MoO_2$ phase ratio throughout

---

* Corresponding authors.
*E-mail addresses:* m.a.elkhakani@inrs.ca (M.A. El Khakani), mustapha.jouiad@u-picardie.fr (M. Jouiad).

https://doi.org/10.1016/j.mseb.2022.116035
Received 23 May 2022; Received in revised form 10 September 2022; Accepted 16 September 2022
Available online 30 September 2022

the CVD process and its effect on the properties of the resulting nanocomposite has not been investigated yet.

In this work, we report a systematic investigation of the $MoS_2/MoO_2$ nanocomposites where the $MoS_2/MoO_2$ phase ratio can be controlled through the tuning of the CVD key parameters. Thus, various variants of the $MoS_2/MoO_2$ nanocomposite with engineered band gaps were achieved and used to for the photodetection.

## 2. Materials and methods

### 2.1. CVD growth

Molybdenum trioxide (MoO3, 99.99 %) and sulfur (S, 99.5 %) were used to synthesize high crystalline planar and vertical $MoS_2$ and $MoO_2$ crystals on silicon (Si) substrates using a CVD system. A ceramic boat with 250 mg of sulfur (S) was placed upstream was placed upstream in a low-temperature zone 27.5 cm from the flow inlet. Eight substrates were cleaned by acetone and ethanol, rinsed by deionized-water and dried out using nitrogen gas flow prior to their introduction in the furnace. The substrates were placed in the high- temperature zone and 30 mg of MoO3 and 5 mg of S were added on the substrate located at position #0 on samples holder which is placed 50 cm from the tube inlet (Fig. 1a). Four other substrates were placed after sample #0 in the same flow direction, positions #1 to #4, and three substrates are placed before sample #0 in the opposite direction of flow, positions # −1 to # −3 (Fig. 1a). Fig. 1b shows the temperature variation in the furnace as a function of time. The center of the furnace was heated from room temperature to 400 °C at a heating rate of 20 °C/min. This rate was selected to achieve a rapid sulfur evaporation and avoid a complete reaction of of MoO3 powder favoring thereby the formation of a hybrid material containing $MoS_2$ and $MoO_2$. Then, a second heating rate of 10 °C/min was applied up to 600 °C, this heating segment is intended to slowdown the evaporation of MoO3. Finally, a third heating rate of 6 °C/min was applied to attain the processing temperature of 850 °C maintained for a total reaction dwell time of 30 min (Fig. 1c). All the syntheses were carried out at atmospheric pressure using ultra-high purity gas carrier Argon (99.998 %) at 70 sccm flow rate during the whole CVD process. Finally, the furnace was shut down and the samples were cooled down naturally to room temperature while keeping the gas flow.

### 2.2. Material characterization

The as-grown $MoS_2/MoO_2$ composites were first examined by optical microscopy using Olympus$^{TM}$ BX51M optical microscope in polarized mode. Then their microstructure was examined by scanning electron microscopy (SEM) Quanta 200 FEG, ThermofisherScientific$^{TM}$ and the chemical composition was determined through elemental mapping of the constituting elements using energy dispersive X-ray spectroscopy (EDX) oxford instruments$^{TM}$. A dual focused ion beam system Helios ThermofisherScientific$^{TM}$ was used to prepare cross-sectional samples and thin lamella for transmission electron microscopy (TEM) investigations. Lamellas were prepared using a standard FIB lift-out technique. TEM analyses of the samples were conducted using an image Cs-corrected TEM system Titan Thermofisher Scientific$^{TM}$ operating at 300 kV. The vibrational modes of the processed samples were used to track the characteristic spectra associated with the various $MoS_2$ phases, using a micro-Raman spectrometer, Renishaw$^{TM}$, with a laser excitation of 532 nm. The crystalline structure was characterized by means of X-ray diffraction (XRD) using a D8 Discover diffractometry Bruker$^{TM}$ ($K\alpha Cu = 1.54$ Å). The optical properties were systematically investigated by means of UV–vis-near IR spectrometer JASCO$^{TM}$ V-670. The spectroscopic ellipsometry was also employed, at room temperature, to complete the optical characterizations by using a phase-modulated ellipsometer UVISEL HR460 from Horiba Scientific$^{TM}$ covering the 300 – 1500 nm wavelength range with a 2 nm step interval and an incidence angle of 70°. Finally, electrical measurements were performed using Palmsens-4 electrochemical workstation under ambient conditions.

## 3. Results and discussion

### 3.1. Optical microscopy and Raman spectroscopy

Fig. 2a shows snapshots of our samples' tray after the fabrication process. The samples #1 to #4 have a blueish color while the samples #-1 to # −3 are greyer. This indicates that the density/thickness of the films is not evenly distributed along the tube furnace length and it is a sample position dependent. As can be seen, samples #1 and #2 are the bluest ones, suggesting a higher thickness or the existence of specific

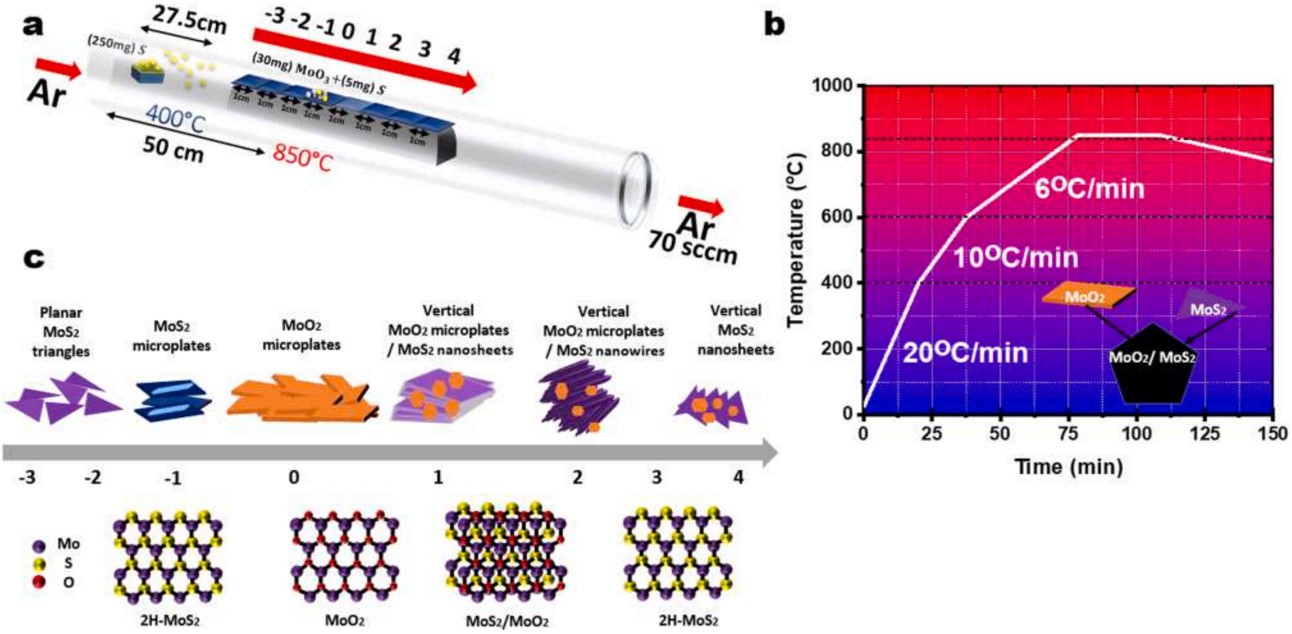

**Fig. 1.** a. Fabrication workflow of $MoS_2/MoO_2$ nanocomposite by CVD process using quartz tube, b. heating rate profile of different heating segments, c. representation of the typical $MoS_2/MoO_2$ morphologies and chemical compositions as a function of the sample position in the furnace.

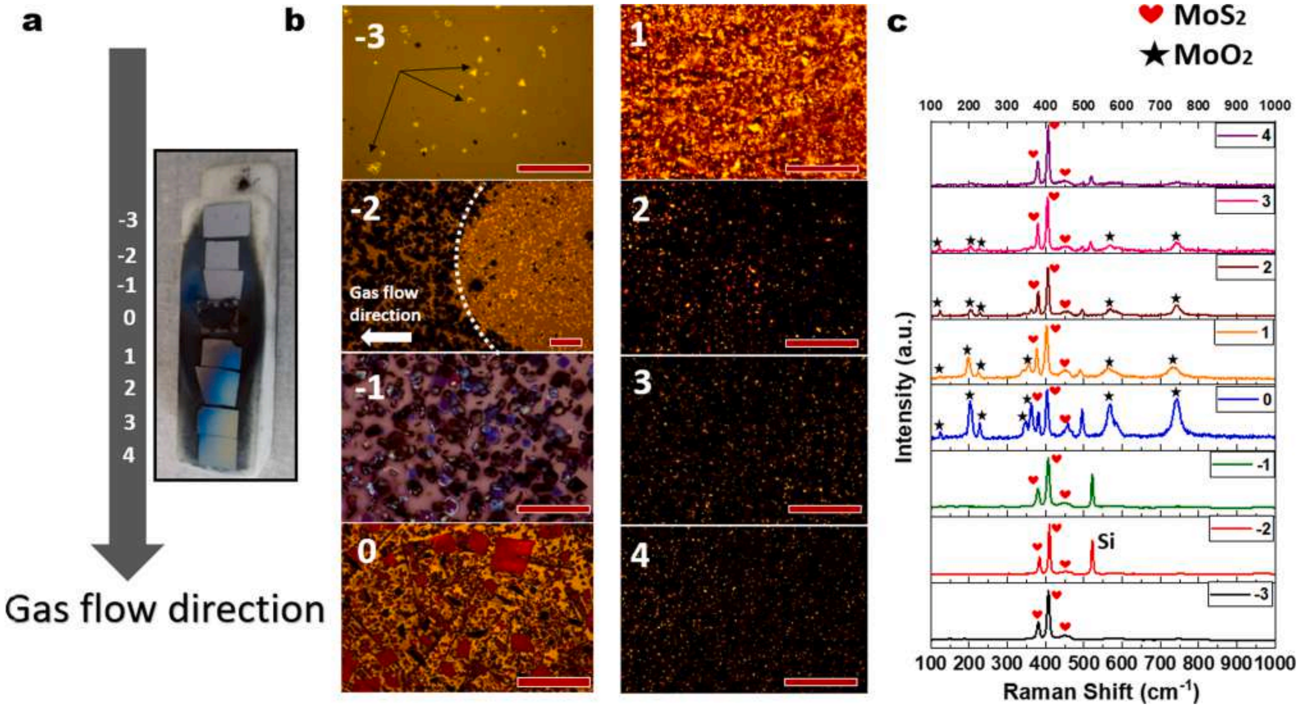

**Fig. 2.** a. A snapshot of the processed samples as collected from the tube furnace b. typical optical images of the $MoS_2/MoO_2$ (scale bar 50 μm) samples at the eight different positions in the furnace; c. corresponding Raman spectra of the as a function of the sample positions.

morphology and/or chemical composition. Fig. 2b displays the optical images of all samples. One can notice that the sample at the position #-3 contains planar $MoS_2$ micro-triangles with low density highlighted by dark arrows on the image. It is important to stress here that this morphology is the most common structure cited in the literature [30,37,38]. By comparing the images of Fig. 2b, a morphology transformation from sample #-3 to sample #-1 can be witnessed, namely from planar micro-triangles to planar microplates $MoS_2$ (with blue color, likely because of their higher thickness). The sample #0 contains a higher surface density of larger $MoO_2$ microplates (with red color) as confirmed by Raman spectroscopy shown in Fig. 2c. As the sample position is changed from sample #1 to sample #4, the optical image color

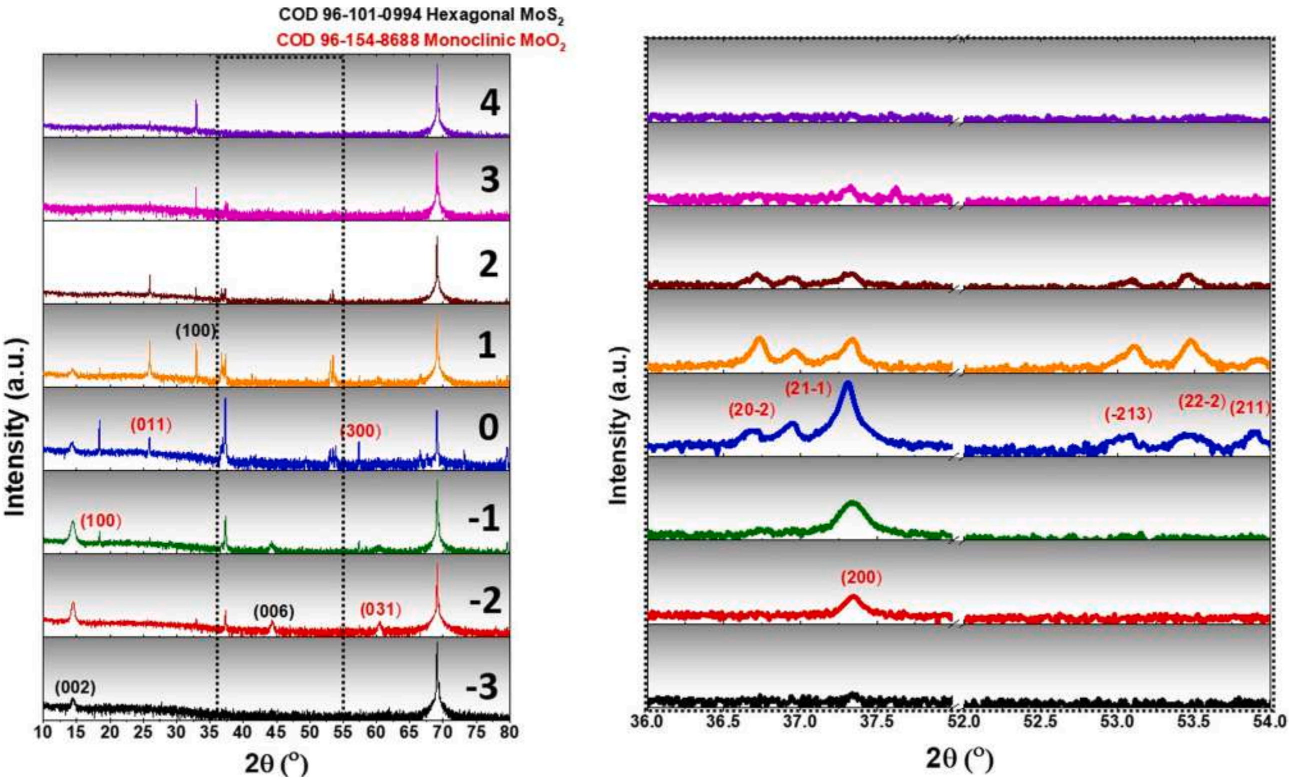

**Fig. 3.** a. Typical XRD diagrams of our CVD grown $MoS_2/MoO_2$ nanocomposites; b. a zoomed view of the (36–54) 2θ range.

changes progressively from yellow-orange-brownish to an increasingly darker tone. As demonstrated using Raman spectroscopy provided in Fig. 2c, this indicates the presence of $MoO_2$ which is vanishing towards the sample #4 where only $MoS_2$ is obtained. Indeed the Raman spectra show the Raman fingerprint of pure hexagonal structure of 2H-$MoS_2$ A1g and $E^1$2g modes [39]. In contrast, the $MoO_2$ spectra are intense and visible for sample #0 indicating the characteristic peaks of monoclinic (m) $MoO_2$ but they are missing for the sample #4.

### *3.2. XRD analysis and XPS spectroscopy*

To confirm the structural and chemical transformation of the $MoS_2$/$MoO_2$ samples as a function of their position in the furnace, we have performed XRD analysis. Fig. 3a shows the obtained XRD diagram, where the Miller indices of diffracted planes are marked in black and in red for the phase 2H-$MoS_2$ (COD-96-101-0994) and m-$MoO_2$ (COD- 96-154-8688), respectively. The sample #-3 exhibits a weak reflection peak corresponding to (0 0 2) plans of 2H- $MoS_2$ and no extra peak is recoded, this result corroborates the Raman spectra obtained for this sample showing the sole formation of $MoS_2$. As we move towards position of sample #-2, we notice the appearance of the (0 0 6) planes reflection of 2H-$MoS_2$ along with two peaks attributed to (2 0 0) and (0 3 1) family plans of m-$MoO_2$ (extra peaks belong to Si substrate). The m-$MoO_2$ associated peaks appear also for the samples #-1, #0, #1 and #2. For instance, (1 0 0) peak appeared for sample #-1 and (2 0 −2), (2 1 −1), (3 0 0), (−2 1 3), (2 2 −2), and (2 1 1) peaks also appeared for sample #0 even if the only defined and intense one is the (2 1 −1) peak (see the zoomed XRD region in Fig. 3b). On the other hand, Fig. 3a shows a progressive vanishing of the 2H-$MoS_2$ (2 0 0) peak intensity when sample position is changing from sample #-2 to sample #1. This suggests an increase in the amount of $MoO_2$ at the expense of $MoS_2$ phase in the direction from sample #-2 to sample #1. It can also be seen that sample #0 shows most of the $MoO_2$ XRD peaks. Finally, for samples #1, #2, #3 and #4, we noticed the recurrence of the (1 0 0) peak of $MoS_2$ and the progressive disappearance of the $MoO_2$ associated peaks, confirming the above-discussed results where the formation of the $MoO_2$ phase is favored around position #0 and the predominance of the $MoS_2$ phase increases as the position is changed towards the sample #4. The unmarked high peak at around $2\theta = 69^\circ$ and $45^\circ$ correspond to the Si substrate, and the other unmarked peaks could be identified properly and are considered to be potentially due to impurities.

Fig. 4a shows the XPS survey of the sample #-3. Note that the XPS investigations were carried out in PHI VersaProbe II scanning XPS microprobe. The system used 15KV electron gun to produce monochromatic and microfocused Al K-alpha X-ray source of 1486.6 eV. All the obtained XPS spectra were calibrated using C1s as reference at 284.6 eV. The background was removed and subsequently the peaks were fitted with Gaussian functions.

The high-resolution XPS spectra of the Mo 3d, S 2 s and O 1 s core levels are displayed in Fig. 4b-4d. In Fig. 4b, the S 2 s core level peak is observed at 227.2 eV in addition to the two peaks at 229.8 and 233.3 eV, which are attributed to the Mo 3d5/2 and Mo 3d3/2 doublet, respectively, corresponding to the $Mo^{4+}$ states in $MoS_2$ [40]. The small Mo 3d core level peak at 236.4 eV is attributed to the $Mo^{6+}$ state of MoO3 [35]. Similarly, the S 2p spectra show the $S^{2-}$ doublet of $MoS_2$ at 162.3 and 163.7 eV (Fig. 4c) [41]. The binding energies of O 1 s (Fig. 4d) are due to S—O/S=O bonding states at 533.5 eV and to C—O bonding states at 531.5 eV [42]. On the other hand, Fig. 4e shows the XPS survey of the sample #0, the Fig. 4f shows the high-resolution XPS prominent peak located at 231.4 eV is due to $Mo^{4+}$ bonding states in $MoS_2$ while the small peak centered around 232.3 eV is associated with of $MoO_2$ [43]. The peak around 234.5 eV represents the 3d5/2 of $Mo^{+10}$ (MoO5) which is consistent with a higher ratio of $MoO_2$ in the sample#0 [37]. The deconvolution of the S 2p core level spectrum (Fig. 4g) suggests that the peak at 162.3 eV is due to MoSX with × < 2 [44], the peak at 163.7 eV is attributed to S 2p3/2, while the peak at 164.9 is attributed to S 2p1/2 in $MoS_2$/$MoO_2$ [43]. Correspondingly, the prominent component of the O1s peak located around 533.7 eV (see Fig. 4h) is likely to be due to S—O/S=O bonding states in MoOS2 [45], while the smaller component centered around 532.3 eV is due to C—O bonding states [46], originating from the unavoidable carbon contamination of the sample surface.

### *3.3. Microstructure analysis*

An interesting aspect of our fabrication method is the possibility to influence the morphology of our samples. Both the simple's position in the furnace and its distance with respect to the precursors are the main parameters determining the composition and crystalline structure of the grown material. Fig. 5 shows the EDX mapping of sample #0 where the planar $MoS_2$/$MoO_2$ microplates with a size in the 10–100 µm range are clearly seen. The maps built on Mo, S, and O elements are clearly seen to reproduce the shapes of the $MoS_2$/$MoO_2$ microplates.

Fig. 6 compares the SEM images of the CVD grown samples selected

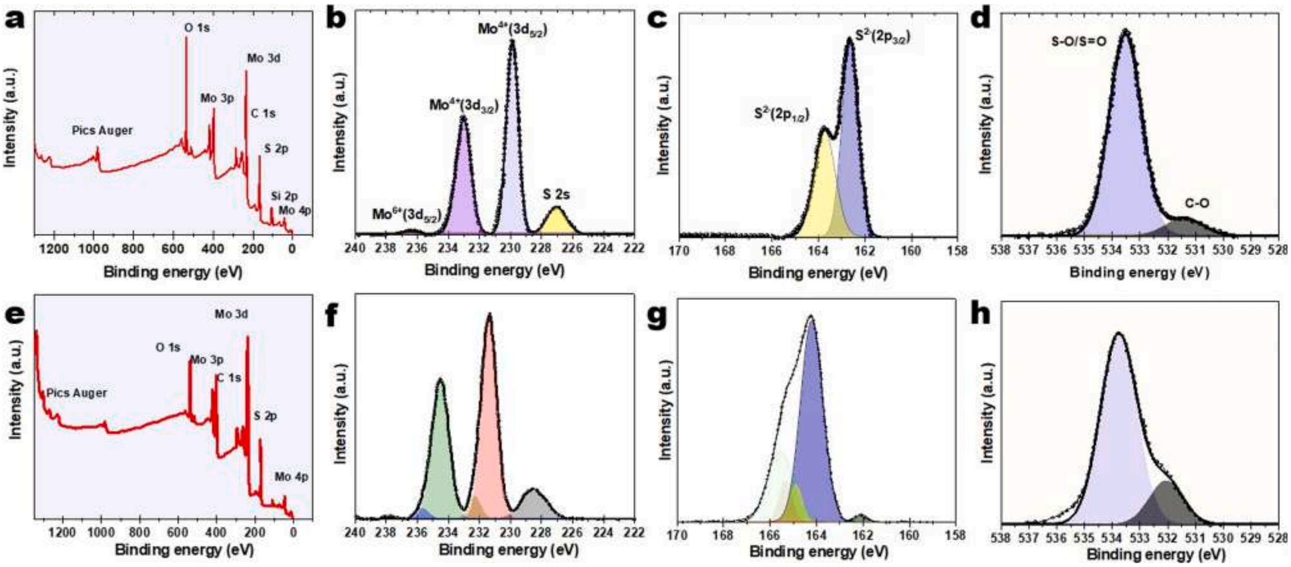

**Fig. 4.** a. Typical XPS survey of sample #-3 and corresponding high-resolution XPS spectra of Mo 3d (b.), S 2 s (c.), and O 1 s (e.) core levels e. XPS survey of the sample #0 with its associated high-resolution Mo 3d (f.), S 2 s (g.) S 2p and O 1 s (h.) core levels.

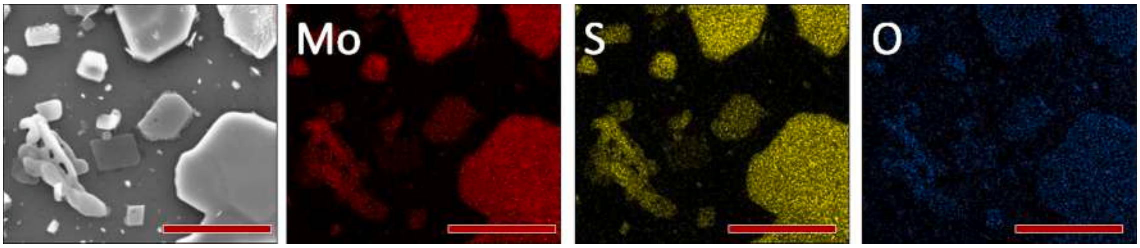

**Fig. 5.** Typical EDX elemental chemical maps of Mo, S and O elements recorded in the sample 0 (scale bar 100 μm).

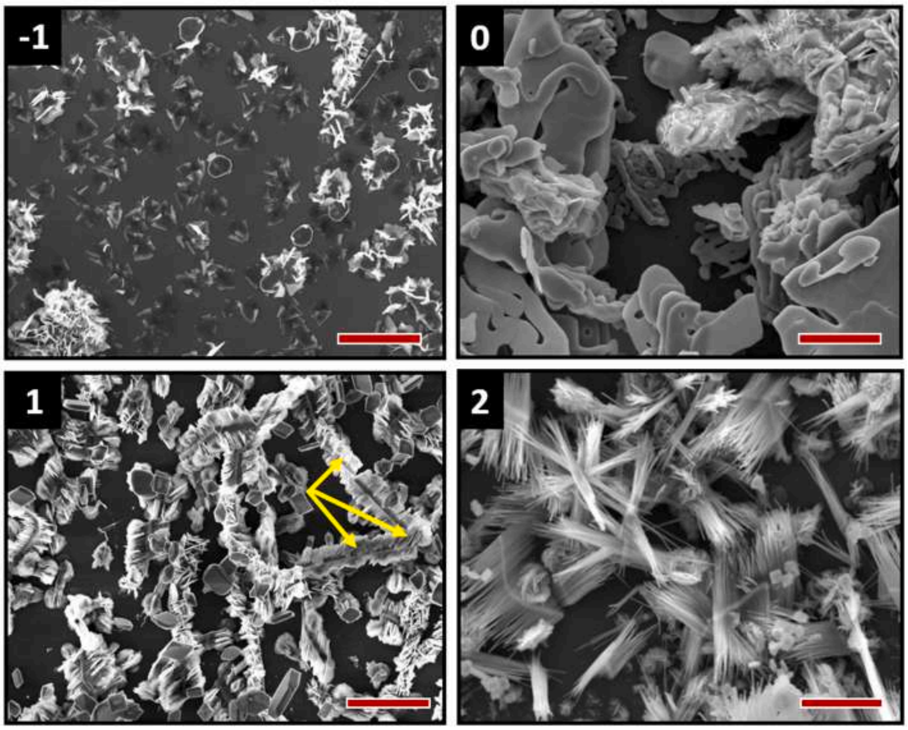

**Fig. 6.** SEM images of the $MoS_2/MoO_2$ samples at the respective positions of #-1, #0, #1 and #2 in the CVD tube furnace (the scale bar for all images is 5 μm).

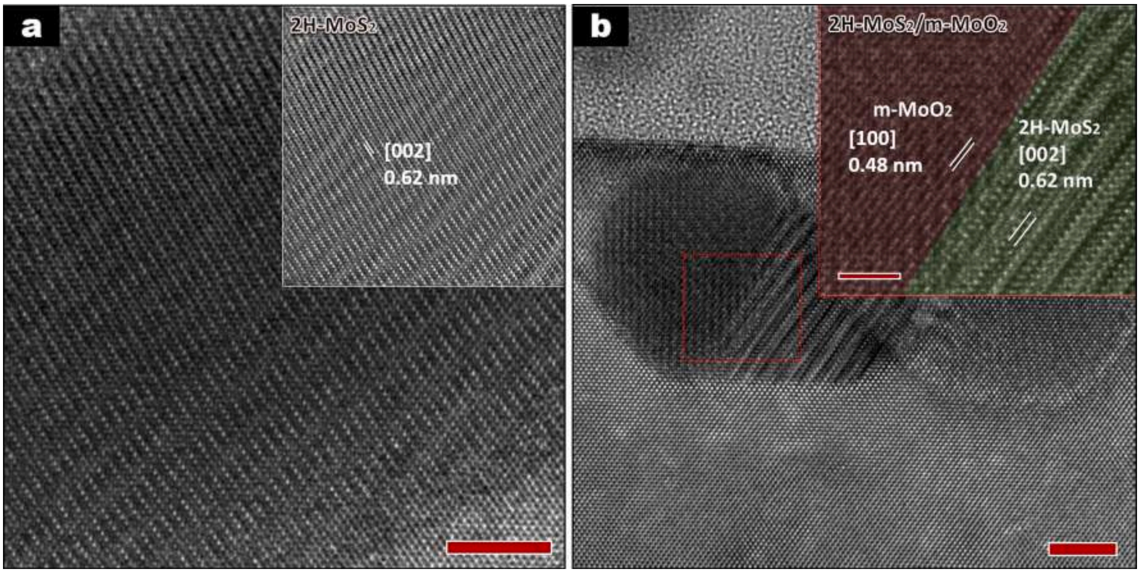

**Fig. 7.** High-resolution TEM images of a. 2H-$MoS_2$ grain taken from sample #-3 and b. 2H-$MoS_2$/m-$MoO_2$ heterostructure from the sample positioned at #1. The scale bar here is 5 nm.

to highlight the chemical composition difference, namely samples #-1, #0, #1 and #2, where significant different morphologies are obtained. Indeed, while sample #-1 shows a planar morphology similar to that of positions #-2 and #-3, sample #0 exhibits a low density of $MoS_2/MoO_2$ microplates because of the high content of $MoO_2$, which is believed to have a significant effect on the planar morphology observed. The size of the $MoS_2/MoO_2$ microplates is in the 5–30 μm range for the sample #0. As we move towards the sample #1, the size of the $MoS_2/MoO_2$ microplates significantly decreases (1–3 μm range) and most interestingly the microplates are seen to pile up vertically as indicated by yellow arrows. This points up a clear morphological transition from planar to vertical $MoS_2/MoO_2$ nanosheets, accompanied with film densification. At the position #2, the $MoS_2/MoO_2$ nanosheets have completely disappeared with increasing of the $MoS_2$ content and giving place to the growth $MoS_2$ nanowires; another important morphological transformation. The vertical and the high aspect ratio of the $MoS_2/MoO_2$ nanostructures (whether nanosheets or nanowire bundles) of samples #1 and #2 along with their apparent inner open path could enhance their ability to absorb light and behave like “ideal” black bodies, as reflected from their very dark apparent color observed by optical microscopy.

The HRTEM image of single-phase high-purity $MoS_2$ is presented in Fig. 7a. The d-spacing of 2H-$MoS_2$ is displayed in the insert of Fig. 7a and was found to be 0.62 nm, corresponding to the [0 0 2] plane. This confirms the high crystallinity of grown $MoS_2$, which supports further the above-discussed Raman and the XRD results. The Fig. 7b, on the other hand, confirms the existence of nanograins consisting of the juxtaposition of 2H-$MoS_2$ and m-$MoO_2$ lattices as confirmed by Raman spectroscopy. The d-spacing of the [1 1 0] planes of m-$MoO_2$ is 0.48 nm, as shown in the inset of Fig. 7b, confirming again both the Raman and XRD results presented hereinbefore.

An interesting outcome from these HRTEM analyses, is the $MoS_2/MoO_2$ heterostructure nature which develops during the CVD growth. This indicates a good coherency between both lattices of $MoS_2$ and $MoO_2$ suggesting a combined macroscopic optical and electrical response. Indeed, the heterostructure could enhance many optical properties-based applications as its response to external light excitation will involve not only each material optical absorption but also it involves the new constructed heterostructure i.e., the combination of the two optical absorptions. In catalysis, this may trigger a Z-scheme reaction [47].

### 3.4. Optical properties

The reflectance spectra of the $MoS_2/MoO_2$ films samples are presented in Fig. 8a. As can be seen, the $MoS_2$ samples #-2 and #-3 exhibit a reflectance that gradually decreases from ~ 35 % to ~ 20 % from UV towards the visible region and the excitons A and B are clearly visible at 636 and 688 nm positions, respectively [48]. The overall.

recorded reflectance of all samples seems to follow a general trend in the full light range 350 nm up to 800 nm consisting of a low light absorption for the sample #-3, followed by a gradual decrease to achieve the maximum light absorption for the sample #1, then a decrease of the light absorption towards the sample #4. One can notice the absence of the excitons A and B in heterostructure samples, provoked by the decrease of the content of planar $MoS_2$ and a concomitant increase in the $MoO_2$ content as seen in Fig. 8b. It is clear that position #1 is offering the lowest reflectance for UV and most of the visible wavelengths. The reflectance spectra of Fig. 8a were also used to determine the optical bandgap of the $MoS_2/MoO_2$ films by using the Kubelka-Munk function [49]. Thus, the direct bandgaps of $MoS_2/MoO_2$ were deduced from the plot of $(F(R)h\nu)^2$ versus photon energy ($h\nu$), as illustrated in Fig. 8c. The position dependence of the bandgap of the $MoS_2/MoO_2$ films is shown in Fig. 8d. It is clearly seen that the bandgap of our $MoS_2/MoO_2$

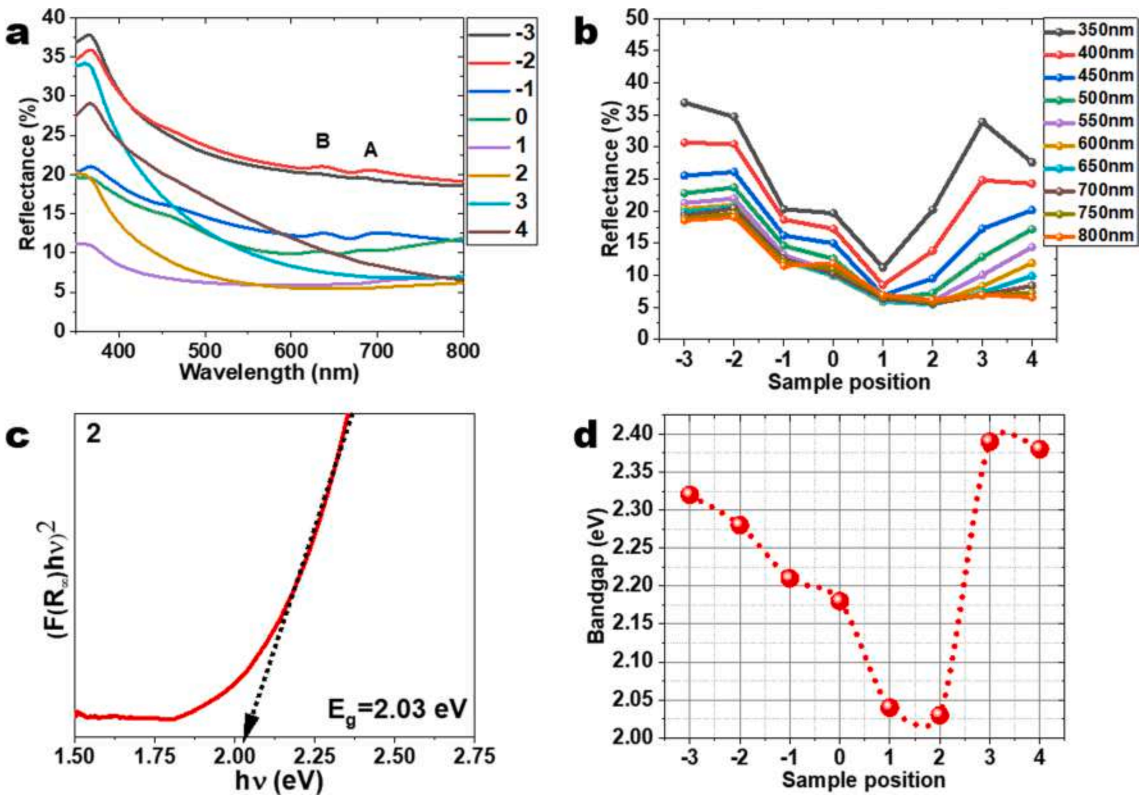

**Fig. 8.** a. Reflectance spectra of the CVD grown $MoS_2/MoO_2$ samples at different positions; b. position dependence of the reflectance of the $MoS_2/MoO_2$ films for selected wavelengths; c. typical Tauc-plot of the Kubelka–Munk function for the determination of the direct bandgap of the sample #2; d. variation of the bandgap as function of the sample position.

heterostructure exhibits the maximum value of 2.4 eV for the sample #1 and a minimum value of 2 eV for the sample #2.

The optical properties of samples #-2 and #2 were further characterized using spectroscopic ellipsometry and the result is depicted in Fig. 9. The sample #-2 and #2 were selected for two main raisons: 1) these two samples are representative in term of the chemical composition of the all samples investigated, namely the sample #-2 represents the sole 2H-$MoS_2$ and the sample #2 the $MoS_2/MoO_2$ heterostructure, 2) both samples exhibit less pronounced roughness which avoid additional approximation to fit the optical ellipsometry spectroscopy results. For the sample #-2, we found several peaks in its ellipsometric spectrum. The presence of these peaks suggests a complex optical function for the thin film representing the convolution of several absorption peaks. In our model, we have considered four layers, namely the Si substrate, a thin interface layer of SiO2 (2 nm), a dense layer of $MoS_2$ and a superficial rough layer (a mixture of $MoS_2$ and voids). The optical functions of silicon and SiO2 are found in the database of the ellipsometer software. Then, we built the optical function of $MoS_2$ with the sum of eight Tauc-Lorentz oscillators as proposed in the work of Diware *et al.* [50]. After the fitting procedure, we found the following results concerning the structural properties of layers (see Table 1 in supplementary information). The Fig. 8d&c summarize the fitting results of sample #-2, such as the refractive index and the extinction coefficient. This result is obtained for a thin film thickness of d1 = 10.5 nm; a roughness layer of d2 = 43 nm and a percentage of void in roughness 43.2 %. In addition, we can note that the optical function for $MoS_2$ found after the fitting procedure is in good agreement with the literature data [50]. In particular, we can note the presence of excitons A, B and C at 670 nm, 604 nm and 364 nm for the sample #-2 and not for the sample #2 as discussed in the optical properties section.

For the sample #2, the ellipsometric spectrum is quite different from that of sample #-2, in the sense that it consists of only one oscillation. Consequently, we were not able to fit correctly the ellipsometric data as for sample #-2. We decided then to change the optical function of the thin film by a Cauchy absorbent function [51]. The best fit of the experimental data yielded the following results concerning the structural properties of layers: thin film thickness d1 = 51.3 nm; roughness layer d2 = 142 nm; percentage of void in roughness 89 %. Moreover, our values of the refractive index n = 2.08 at 632 nm were found to be slightly higher than those quoted in literature those for $MoO_2$ n = 1.81 at 632 nm [52]. Such a small difference can be due to the presence of a little amount of $MoS_2$ in the thin film layer which can increases its effective refractive index.

### 3.5. Photoresponse measurements

To investigate the optoelectronic properties of the $MoS_2/MoO_2$ nanocomposite films, we sputter-deposited a pair of 50 nm thick Au electrodes at their surface (as illustrated in Fig. 10a). Au was chosen because of its favourable work function to minimize the contact barrier and improve the charge transport with $MoS_2$. The current density versus bias voltage (J–V) curves of our samples were acquired for all samples, at room temperature, under dark and illumination with a halogen lamp (70 mW/cm$^2$) as illustrated in Fig. 10b for the sample #2. The effective detection area of our samples was estimated (0.075 cm$^2$). For each sample, the photocurrent density defined by. (*Jlight – Jdark*) is plotted as function of the applied voltage in Fig. 10c.

As can be seen, the sample #2 is found to yield the highest photocurrent density of 70μA/cm$^2$ obtained at voltage bias of 1 V. This high photogenerated current density recorded, is believed to result from its particular nanowires morphology. The nanowire shape appears to not only allow a strongly light absorption but it is also expected to provide a rapid charge transfer because of its one-dimensional structure. Subsequently, the photoresponce (P) at a biasing voltage of 1 V was calculated

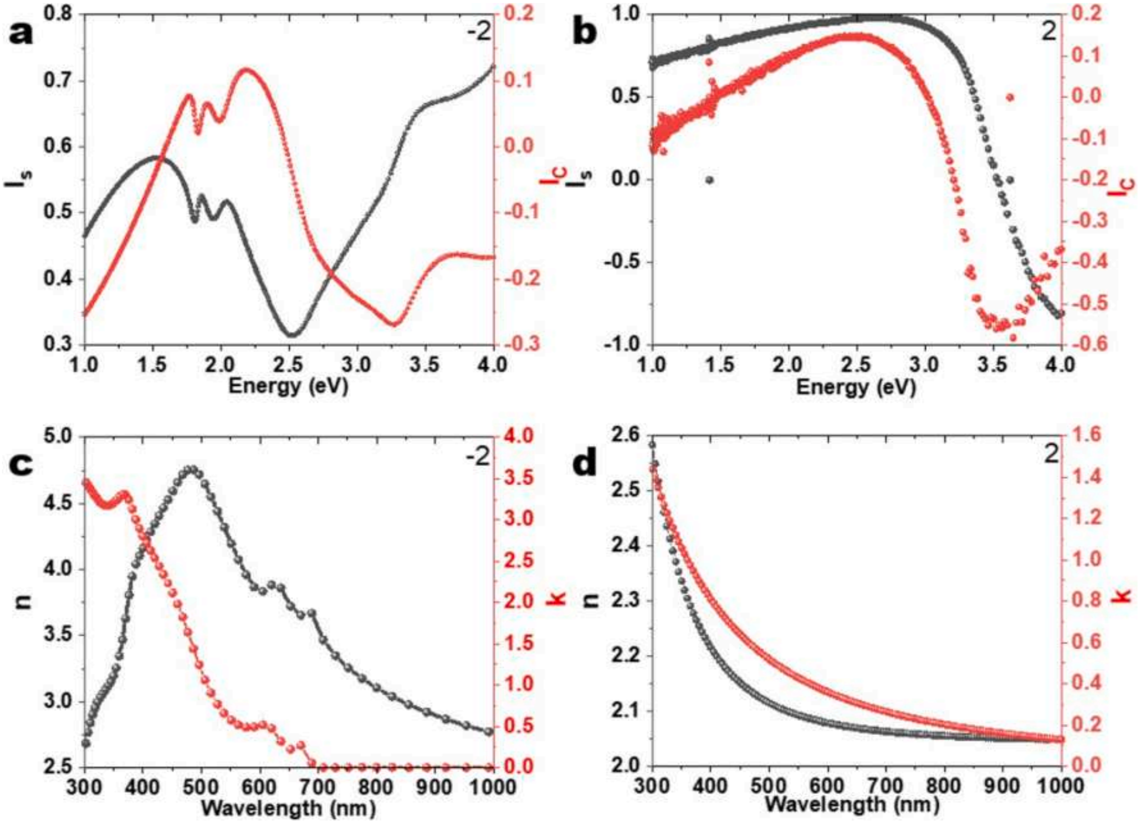

**Fig. 9.** Ellipsometric Is and Ic curves measured on sample #-2 a. and sample #2b. and corresponding refractive indices and extinction coefficients from the ellipsometry spectroscopy, c. sample #-2 and d. sample #2.

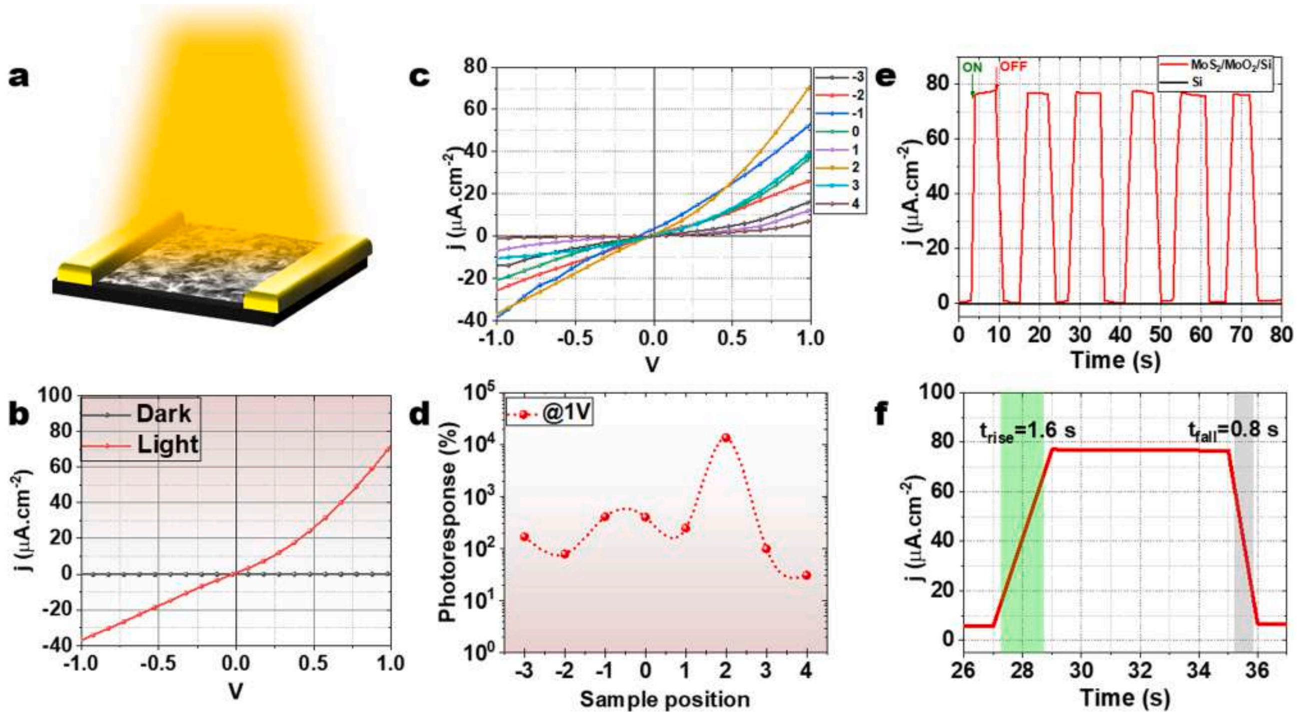

**Fig. 10.** a. $MoS_2/MoO_2$ based photoconductive devices. b. typical J-V curve, here the result is from of the sample 2; c. photocurrent density curves of all samples; d. photoresponse dependence on sample position; e. transient photocurrent response of the sample #2 registered for six cycles ON/OFF every 10 s, under a constant halogen lamp illumination 70 mW.cm$^{-2}$ and at applied bias of 1 V; f. rise and decay times of the photoconductive device recorded for the sample #2.

using P(%) = 100 × [(Ilight-Idark)/I dark] and plotted for all samples in Fig. 10d. It is evident that the sample grown at position #2 has again the highest photoresponse achieving $2.10^4$ %, while the sample #4 has the lowest one of 30 %. As aforementioned, such a high photoresponse is a consequence of the very dense one-dimensional $MoS_2$ nanowires known for their ability to harvest light efficiently and ensure a rapid charge transfer [53–55]. Furthermore, we have calculated the responsivity (R) and the detectivity (D*) for the sample showing the best performances (position #2) at 1 V using the following formula:

$$R = (Ilight - Idark)/PS; D^{*} = R/\sqrt{2qI_{dark}}$$

where P is the incident light's power density, S is the effective illuminated surface, and q is the absolute value of an electron charge ($1.6\ 10^{19}$ Coulombs). For the sample #2, R and D* were found to be equal to 1.14 mA/W and $2.6 \times 10^9$ Jones, respectively. The obtained value of R is comparable to previous reported values [56,57]. It is worth to mention that other studies have reported high R values in the hundreds of A/W range obtained on very small surface area [17,58]. Note that our photoresponse result does not take into account the possible piezophototronic effect that could arise due to the $MoS_2$ interlayers strain as described elsewhere [56,57].

This work, we have mainly focused our attention on the investigation of the photoresponse of various generated microstructures that are simultaneously obtained with CVD while keeping relatively the same surface area. In this way, we can make the appropriate comparison while referring to the specific microstructure. Additional work is needed to examine the effect of excitation energies, active area, power density. Meanwhile, the high value of D* is comparable to other recently reported works [59–62]. Finally, Fig. 10e shows the transient photocurrent response recorded at 1 V bias of the $MoS_2$ based photoconductive device fabricated from the sample #2. The device is also exhibiting a relatively rapid time response as their typical rise and decay times defined as the time required to rise the photocurrent from 10 % to 90 % of its maximum value and vice versa- are found to be 1.6 s and 0.8 s, respectively, as depicted in Fig. 10f. Such response times are comparable with the best values reported in literature for $MoS_2$ [63–65].

## 4. Conclusion

In this work, the potential of the CVD approach to grow various $MoS_2/MoO_2$ nanocomposite structures has been demonstrated simply by changing the position of the substrates in the CVD furnace and controlling their proximity to the precursors. Consequently, various structures, morphologies, compositions and optoelectronic properties were obtained. This work demonstrates the very rich playground offered by the CVD growth approach to develop pure $MoS_2$ to mixed phase $MoS_2/MoO_2$ heterostructure and explore their structural and optoelectronic properties. Our results have pointed out the position #2 to be the most appropriate zone to grow $MoS_2/MoO_2$ nanowires with high crystallinity and very interesting optoelectronic properties. Indeed, the integration of their integration into photoconductive devices enabled us to reveal their capacity to yield a photoresponse as high as $10^4$-fold, a high responsivity of 1.13 mA/W, and specific detectivity of $2.6 \times 10^9$ Jones at an operating voltage as low as 1 V. This suggests that further controlling the CVD growth of such structure is highly promising for the development of highly sensitive photodetectors in the full range of solar spectrum.

## Declaration of Competing Interest

The authors declare no competing interest.

## Data availability

Data will be made available on request.

## *Acknowledgement*

This work was performed in the context of a scientific collaboration between INRS and UPJV. D. Mouloua is grateful to both the Region HDF (France) and INRS (QC, Canada) for his PhD fellowship.

### Financial support

M.A.E and M.J. acknowledge the financial support provided by the Natural Sciences and Engineering Research Council (NSERC) of Canada and Region of Haut-De-France.

### Data availability statement

All data supporting this work are available upon request from the corresponding author: mustapha.jouiad@u-picardie.fr

## Appendix A. Supplementary material

Supplementary data to this article can be found online at https://doi.org/10.1016/j.mseb.2022.116035.

## References

[1] W. Choi, N. Choudhary, G.H. Han, J. Park, D. Akinwande, Y.H. Lee, Recent development of two-dimensional transition metal dichalcogenides and their applications, Vol. 20, Elsevier B.V., 2017, pp. 116–130.
[2] R. Mas-Ballesté, C. Gómez-Navarro, J. Gómez-Herrero, F. Zamora, Nanoscale 3 (2011) 20.
[3] A. Gupta, T. Sakthivel, S. Seal, Prog. Mater. Sci. 73 (2015) 44.
[4] T. Chowdhury, E.C. Sadler, T.J. Kempa, Chem. Rev. 120 (2020) 12563.
[5] Q.H. Wang, K. Kalantar-Zadeh, A. Kis, J.N. Coleman, M.S. Strano, Nat. Nanotechnol. 7 (2012) 699.
[6] A. Splendiani, L. Sun, Y. Zhang, T. Li, J. Kim, C.Y. Chim, G. Galli, F. Wang, Nano Lett. 10 (2010) 1271.
[7] J. Sun, X. Li, W. Guo, M. Zhao, X. Fan, Y. Dong, C. Xu, J. Deng, Y. Fu, Crystals 7 (2017) 1.
[8] D. Gupta, V. Chauhan, R. Kumar, Inorg. Chem. Commun. 121 (2020), 108200.
[9] N. Muhammad, Y. Chen, C.W. Qiu, G.P. Wang, Nano Lett. 21 (2021) 967.
[10] S.A. Svatek, E. Antolin, D.Y. Lin, R. Frisenda, C. Reuter, A.J. Molina-Mendoza, M. Muñoz, N. Agraït, T.S. Ko, D.P. De Lara, A. Castellanos-Gomez, J. Mater. Chem. C 5 (2017) 854.
[11] F. Guo, M. Li, H. Ren, X. Huang, W. Hou, C. Wang, W. Shi, C. Lu, Appl. Surf. Sci. 491 (2019) 88.
[12] S. Lin, X. Li, P. Wang, Z. Xu, S. Zhang, H. Zhong, Z. Wu, W. Xu, H. Chen, Sci. Rep. 5 (2015) 1.
[13] B. Su, H. He, Z. Ye, Mater. Lett. 253 (2019) 187.
[14] Z. Zhang, L. Huang, J. Zhang, F. Wang, Y. Xie, X. Shang, Y. Gu, H. Zhao, X. Wang, Appl. Catal. B Environ. 233 (2018) 112.
[15] Q. Li, N. Zhang, Y. Yang, G. Wang, D.H.L. Ng, Langmuir 30 (2014) 8965.
[16] A. Taffelli, S. Dirè, A. Quaranta, L. Pancheri, Sensors 21 (2021) 2758.
[17] H.S. Nalwa, RSC Adv. 10 (2020) 30529.
[18] H. Gao, C. Du, L. Chen, W. Wang, K. Li, Adv. Mater. Interfaces 9 (2022) 2102350.
[19] M. Peng, Y. Tao, X. Hong, Y. Liu, Z. Wen, X. Sun, J. Mater. Chem. C 10 (2022) 2236.
[20] A. Islam, J. Lee, P.X.L. Feng, ACS Photon. 5 (2018) 2693.
[21] G. Deokar, N.S. Rajput, P. Vancsó, F. Ravaux, M. Jouiad, D. Vignaud, F. Cecchet, J. F. Colomer, Nanoscale 9 (2017) 277.
[22] G. Deokar, P. Vancsó, R. Arenal, F. Ravaux, J. Casanova-Cháfer, E. Llobet, A. Makarova, D. Vyalikh, C. Struzzi, P. Lambin, M. Jouiad, J.F. Colomer, Adv. Mater. Interfaces 4 (2017) 1.
[23] G. Deokar, N.S. Rajput, J. Li, F.L. Deepak, W. Ou-Yang, N. Reckinger, C. Bittencourt, J.F. Colomer, M. Jouiad, Beilstein J. Nanotechnol. 9 (2018) 1686.
[24] I.S. Kim, V.K. Sangwan, D. Jariwala, J.D. Wood, S. Park, K.S. Chen, F. Shi, F. Ruiz-Zepeda, A. Ponce, M. Jose-Yacaman, V.P. Dravid, T.J. Marks, M.C. Hersam, L. J. Lauhon, ACS Nano 8 (2014) 10551.
[25] S. Wang, Y. Rong, Y. Fan, M. Pacios, H. Bhaskaran, K. He, J.H. Warner, Chem. Mater. 26 (2014) 6371.
[26] J. Jeon, S.K. Jang, S.M. Jeon, G. Yoo, Y.H. Jang, J.H. Park, S. Lee, Nanoscale 7 (2015) 1688.
[27] T. Nam Trung, F.Z. Kamand, T.M. Al tahtamouni, Appl. Surf. Sci. 505 (2020).
[28] J. Chen, W. Tang, B. Tian, B. Liu, X. Zhao, Y. Liu, T. Ren, W. Liu, D. Geng, H. Y. Jeong, H.S. Shin, W. Zhou, K.P. Loh, Adv. Sci. 3 (2016) 3.
[29] H.F. Liu, S.L. Wong, D.Z. Chi, Chem. Vap. Depos. 21 (2015) 241.
[30] D. Mouloua, A. Kotbi, G. Deokar, K. Kaja, M. El Marssi, M. Ali, E.L. Khakani, M. Jouiad, Materials (Basel). 14 (2021) 3283.
[31] C.M. Hyun, J.H. Choi, S.W. Lee, J.H. Park, K.T. Lee, J.H. Ahn, J. Alloys Compd. 765 (2018) 380.
[32] Z. Yin, X. Zhang, Y. Cai, J. Chen, J.I. Wong, Y.Y. Tay, J. Chai, J. Wu, Z. Zeng, B. Zheng, H.Y. Yang, H. Zhang, Angew. Chemie - Int. Ed. 53 (2014) 12560.
[33] T. Chiawchan, H. Ramamoorthy, K. Buapan, R. Somphonsane, Nanomaterials 11 (2021) 2642.
[34] J.V. Pondick, J.M. Woods, J. Xing, Y. Zhou, J.J. Cha, ACS Appl. Nano Mater. 1 (2018) 5655.
[35] P. Wang, J. Lei, J. Qu, S. Cao, H. Jiang, M. He, H. Shi, X. Sun, B. Gao, W. Liu, Chem. Mater. 31 (2019) 873.
[36] J. Yan, A. Rath, H. Wang, S.H. Yu, S.J. Pennycook, D.H.C. Chua, Mater. Res. Lett. 7 (2019) 275.
[37] Y. Huang, J. Guo, Y. Kang, Y. Ai, C.M. Li, Nanoscale 7 (2015) 19358.
[38] L.K. Tan, B. Liu, J.H. Teng, S. Guo, H.Y. Low, K.P. Loh, Nanoscale 6 (2014) 10584.
[39] G. Pradhan, A.K. Sharma, Mater. Res. Bull. 102 (2018) 406.
[40] S. Erfanifam, S.M. Mohseni, L. Jamilpanah, M. Mohammadbeigi, P. Sangpour, S. A. Hosseini, A. Iraji Zad, Mater. Des. 122 (2017) 220.
[41] S. Kang, Y.S. Kim, J.H. Jeong, J. Kwon, J.H. Kim, Y. Jung, J.C. Kim, B. Kim, S. H. Bae, P.Y. Huang, J.C. Hone, H.Y. Jeong, J.W. Park, C.H. Lee, G.H. Lee, ACS Appl. Mater. Interfaces 13 (2021) 1245.
[42] R.I. Romanov, A.S. Slavich, M.G. Kozodaev, D.I. Myakota, Y.Y. Lebedinskii, S. M. Novikov, A.M. Markeev, Phys. Status Solidi - Rapid Res. Lett. 14 (2020) 1.
[43] R.D. Nikam, A.Y. Lu, P.A. Sonawane, U.R. Kumar, K. Yadav, L.J. Li, Y.T. Chen, ACS Appl. Mater. Interfaces 7 (2015) 23328.
[44] X. Jiang, M. Fuji, Catal. Lett. (2021) 1.
[45] N. Iqbal, I. Khan, A. Ali, A. Qurashi, J. Adv. Res. 36 (2022) 15.
[46] H. Nan, Z. Wang, W. Wang, Z. Liang, Y. Lu, Q. Chen, D. He, P. Tan, F. Miao, X. Wang, J. Wang, Z. Ni, ACS Nano 8 (2014) 5738.
[47] J. Abed, N.S. Rajput, A. El Moutaouakil, M. Jouiad, Nanomaterials 10 (2020) 1.
[48] B. Mukherjee, F. Tseng, D. Gunlycke, K.K. Amara, G. Eda, E. Simsek, Opt. Mater. Express 5 (2015) 447.
[49] X. Fan, P. Xu, D. Zhou, Y. Sun, Y.C. Li, M.A.T. Nguyen, M. Terrones, T.E. Mallouk, Nano Lett. 15 (2015) 5956.
[50] M.S. Diware, K. Park, J. Mun, H.G. Park, W. Chegal, Y.J. Cho, H.M. Cho, J. Park, H. Kim, S.W. Kang, Y.D. Kim, Curr. Appl. Phys. 17 (2017) 1329.
[51] A.R. Frias, M.A. Cardoso, A.R.N. Bastos, S.F.H. Correia, P.S. André, L.D. Carlos, V. de Z. Bermudez, R.A.S. Ferreira, Energies 12 (2019).
[52] O. De Melo, V. Torres-Costa, A. Climent-Font, P. Galán, A. Ruediger, M. Sánchez, C. Calvo-Mola, G. Santana, V. Torres-Costa, J. Phys. Condens. Matter (2019) 31.
[53] H. Liao, Y. Wang, S. Zhang, Y. Qian, Chem. Mater. 13 (2001) 6.
[54] C. Yu, H. Xu, Y. Sun, X. Zhao, Z. Hui, Y. Gong, R. Chen, Q. Chen, J. Zhou, G. Sun, W. Huang, Carbon N. Y. 170 (2020) 543.
[55] M. Liu, K. Hisama, Y. Zheng, M. Maruyama, S. Seo, A. Anisimov, T. Inoue, E. I. Kauppinen, S. Okada, S. Chiashi, R. Xiang, S. Maruyama, ACS Nano 15 (2021) 8418.
[56] M. Javadi, S. Darbari, Y. Abdi, F. Ghasemi, IEEE Electron Device Lett. 37 (2016) 677.
[57] P.T. Gomathi, P. Sahatiya, S. Badhulika, Adv. Funct. Mater. 27 (2017) 1701611.
[58] R. Ghalamboland, S. Darbari, M. Rashidifar, Y. Abdi, IEEE Sens. J. 21 (2021) 14784.
[59] A. Xie, Y. Jian, Z. Cheng, Y. Gu, Z. Chen, X. Song, Z. Yang, J. Phys. Condens. Matter (2022) 34.
[60] Y. Yin, Y. Guo, D. Liu, C. Miao, F. Liu, X. Zhuang, Y. Tan, F. Chen, Z. xing Yang, Adv. Opt. Mater. 10 (2022) 1.
[61] D. Liu, F. Liu, Y. Liu, Z. Pang, X. Zhuang, Y. Yin, S. Dong, L. He, Y. Tan, L. Liao, F. Chen, Z. xing Yang, Small 18 (2022) 1.
[62] X. Liu, J. Luo, Y. Lin, Z. Lin, X. Liu, J. He, W. Yu, Q. Liu, T. Wei, J. Yang, W. Zhang, J. Guo, ACS Appl. Electron. Mater. 3 (2021) 5415.
[63] Y. Wu, Z. Li, K.-W. Ang, Y. Jia, Z. Shi, Z. Huang, W. Yu, X. Sun, X. Liu, D. Li, Photonics Res. 7 (2019) 1127.
[64] A.E. Yore, K.K.H. Smithe, S. Jha, K. Ray, E. Pop, A.K.M. Newaz, Appl. Phys. Lett. 111 (2017), 043110.
[65] B. Sun, Z. Wang, Z. Liu, X. Tan, X. Liu, T. Shi, J. Zhou, G. Liao, Adv. Funct. Mater. 29 (2019) 1.

## Article 3: D. Mouloua, N. S. Rajput, S. Saitzek, K. Kaja, K. Hoummada, M. El Marssi, M. A. El Khakani, M. Jouiad, Sci. Rep. 2022, 12, 1.

www.nature.com/scientificreports

scientific reports

OPEN

# Broadband photodetection using one-step CVD-fabricated $MoS_2$/$MoO_2$ microflower/microfiber heterostructures

**D. Mouloua[1,2], N. S. Rajput[3], S. Saitzek[4], K. Kaja[5], K. Hoummada[6], M. El Marssi[1], M. A. El Khakani[2]✉ & M. Jouiad[1]✉**

**Molybdenum disulfide ($MoS_2$) has been combined so far with other photodetecting semiconductors as an enhancing agent owing to its optical and electronic properties. Existing approaches demonstrated $MoS_2$-incorporated photodetector devices using complex and costly fabrication processes. Here, we report on simplified one-step on the chemical vapor deposition (CVD) based synthesis of a unique microfiber/microflower $MoS_2$-based heterostructure formed by capturing $MoO_2$ intermediate material during the CVD process. This particular morphology engenders a material chemical and electronic interplay exalting the heterostructure absorption up to ~ 98% over a large spectral range between 200 and 1500 nm. An arsenal of characterization methods were used to elucidate the properties of these novel heterostructures including Raman spectroscopy, X-ray diffraction, X-ray photoelectron spectrometry, high-resolution transmission and scanning electron microscopies, and Kelvin probe force microscopy. Our findings revealed that the $MoS_2$ and the $MoO_2$ crystallize in the hexagonal and monoclinic lattices, respectively. The integration of the $MoS_2$/$MoO_2$ heterostructures into functional photodetectors revealed a strong photoresponse under both standard sun illumination AM1.5G and blue light excitation at 450 nm. Responsivity and detectivity values as high as 0.75 mA $W^{-1}$ and $1.45 \times 10^7$ Jones, respectively, were obtained with the lowest light intensity of 20 mW $cm^{-2}$ at only 1 V bias. These results demonstrate the high performances achieved by the unique $MoS_2$/$MoO_2$ heterostructure for broadband light harvesting and pave the way for their adoption in photodetection applications.**

Undeniably, molybdenum disulfide ($MoS_2$) has proven to be an excellent material for opto-electronic applications among the family of transition metal dichalcogenides (TMDs) two-dimensional (2D) materials[1]. Its outstanding electrical and optical properties[2–6] have made $MoS_2$ one of the most promising candidates for visible light-driven photodetectors[7]. Nonetheless, carriers' recombinations in pristine $MoS_2$ have limited its photodetecion efficiency, despite its good light absorption performance[8,9]. This has driven a general trend during the last decade combining $MoS_2$ with other semiconductors with already known and proven photodetecting capabilities. Efforts done in this direction mainly exploited the high light absorption properties of $MoS_2$ to improve the photodetecting performances of the other semiconductor by favoring carriers separation through the creation of a built-in electric field[6–9]. As example, ZnS/$MoS_2$ heterostructures have been shown to exhibit a large photodetection capability, where ZnS has served as local electric field generator, achieving an increased optoelectronic performances[10]. The the ultra-violet (UV) detection property of ZnS, combined with the strong visible light absorption of $MoS_2$, have led to the fabrication of photodetectors spanning the whole spectrum from UV to the near infrared range. Another strategy consists of using plasmonic metal to create Schottky

[1]Laboratory of Physics of Condensed Matter, University of Picardie Jules Verne, Scientific Pole, 33 Rue Saint-Leu, 80039 Amiens Cedex 1, France. [2]Institut National de la Recherche Scientifique, Centre-Énergie, Matériaux et Télécommunications, 1650, Blvd, Lionel-Boulet, Varennes, QC J3X-1P7, Canada. [3]Advanced Materials Research Center, Technology Innovation Institute, P.O. Box 9639, Abu Dhabi, United Arab Emirates. [4]UMR 8181, Unité de Catalyse et Chimie du Solide (UCCS), Université d'Artois, CNRS, Centrale Lille, Université de Lille, 62300 Lens, France. [5]Laboratoire National de Métrologie et d'essais (LNE), 29 Av. Roger Hannequin, 78197 Trappes, France. [6]IM2NP, Aix Marseille Université, CNRS, Université de Toulon, 13397 Marseille, France. ✉email: m.a.elkhakani@inrs.ca; mustapha.jouiad@u-picardie.fr

contact with $MoS_2$ for hot electrons injection leading to enhanced optical absorption and good photodetection properties[11–13]. Nonetheless, these approaches adopted so far have merely used $MoS_2$ as a supporting agent to catalyze light absorption of other semiconducting photodetector materials. Despite their advantages, these methods still suffer from several challenging limitations to their efficient integration in large scale broadband photodetector applications. Most prominently, fabrication processes of the used semiconductors, such as ZnO or GaN, are highly demanding in terms of resources, time, and cost. Additionally, the resulting functional devices remain restricted to very small dimensions and their efficient photodetection yield is bound to the application of high voltages (i.e. ~ 20 V)[14]. Therefore, innovative solutions to develop large-scale $MoS_2$-based structures with high photodetection performances using affordable and efficient fabrication approaches are required to propel the integration of broadband $MoS_2$-based photodetectors[15,16]. For this, exploiting $MoS_2$-derived semiconductors (such as $MoO_2$ and $MoO_3$), naturally occurring during fabrication processes, constitutes a novel viable route to develop new heterostructures with enhance photodetecting performances. This is motivated by recently reported results showing a great potential of $MoO_2$ as a suitable candidate for optoelectronic applications based heterostructure[17,18]. Recent findings strongly suggest a significant impact of the $MoO_2/MoS_2$ and $MoO_3/MoS_2$ morphology on the increase of optical absorption properties leading to amplified photodetection performances, as found in vertically aligned $MoS_2$ needle-like structures[19,20]. Hence, controlling the morphology of $MoS_2$ is a key for improving photodetection performances[21,22]. Chemical vapor deposition (CVD) has proven to be one of the most promising fabrication techniques to achieve a controlled growth of $MoS_2$[23], owing to its ease of implementation, low-cost and scalability[24–28]. Nevertheless, this requires the control of multiple parameters including pressure, temperature, heating rate, carrier gas flow rate, substrate, precursors positions, and reaction dwell time. All these processing parameters affect the morphology, crystallinity, and thickness of the $MoS_2$ heterostructures, which have been documented elsewhere for the synthesis of high-quality, large-surface-area single and few-layers $MoS_2$[29–31]. Interestingly, $MoO_2$ is intermediate material created during the $MoS_2$ CVD process[32]. Therefore, "capturing" the formation of these materials along with CVD $MoS_2$ would enable an innovative approach to create seamless $MoS_2/MoO_2$ heterostructures in a one single step process.

In this study, we present pioneering results on a single step large-scale controlled CVD growth of a unique $MoS_2/MoO_2$ heterostructure showing giant light absorption (i.e. ~ 98%) over the full spectral range from 200 to 1500 nm. The as-grown heterostructures present a special $MoO_2$ microflowers/$MoS_2$ microfibers morphology, which was found to exhibit a huge specific area along with a strong broadband light absorption spanning from UV to near IR. An arsenal of characterization methods were used to investigate the optical, structural, crystallographic, chemical, electric, and photoelectric properties of the novel heterostructures. We have further integrated the fabricated heterostructure films into a photodetector test configuration to demonstrate their high potential for broadband applications. Applied voltages, one order of magnitude lower that those used for $MoS_2$/GaN structures, enabled a comparable photodetectivity for the unique heterostructures morphology.

## Experimental section

### $MoS_2/MoO_2$ synthesis.

The CVD growth conditions were optimized to control the morphology and ratio of the $MoS_2/MoO_2$ in the heterostructure grown on silicon substrates. First, the intrinsic Si substrate was successively cleaned with acetone and ethanol, rinsed with deionized water, and the dried with a nitrogen jet before introducing it into the furnace. Molybdenum trioxide ($MoO_3$, 99.99%) and sulfur (S, 99.5%) powders were used as reactant and precursor materials, respectively. The cleaned Si substrate was immersed into a mixture solution consisting of 50 mg of S, 50 mg of $MoO_3$, and ethanol. The mixture was kept in an ultrasonicator for 10 min with the Si substrate immersed in it. Then, the substrate was removed from solution and few droplets were added onto its surface before introduction into the horizontal quartz tube of the CVD reactor. A ceramic boat with 200 mg of sulfur was placed upstream in the low-temperature zone of the furnace, 27.5 cm from the flow inlet. Another 2 cm-thick boat was placed face-down downstream in the center of the furnace to exploit its thickness in our growth process. An excess of 20 mg $MoO_3$ was added on the top of the boat at the hot zone (50 cm from the flow inlet). The Si substrate (1 $cm^2$) was placed on the top of this boat 1 cm from the $MoO_3$ powder, as shown in Fig. 1a. Ultra-high purity Ar gas was flown in the furnace at the rate of 70 sccm during the whole growth process. The center of the furnace was heated from room temperature to 850 °C with a rate of 20 °C/min to achieve a non-homogeneous temperature profile inside the quartz tube with an incomplete transformation from $MoO_3$ powder to $MoS_2$ film (Fig. 1b). The furnace was kept at the growth temperature for 30 min. All syntheses were done at atmospheric pressure. Finally, the furnace was allowed to cool down naturally to room temperature with 70 sccm Ar flow. The optical image of the sample surface is given in Fig. 1c showing the homogeneous deposition.

### Characterization.

An Olympus BX51M optical microscope was used to observe the morphology of the $MoS_2/MoO_2$ using bright field mode. Scanning electron microscopy (SEM) (Quanta 200 FEG, ThermofisherScientific) was used to observe the microstructure and examine the nucleation mechanism of our samples growth. The energy-dispersive X-ray spectroscopy (EDS) mappings were carried out in a Scios 2 dual beam system (ThermofisherScientific) equipped with an EDS system (Oxford Instruments). Electron beam parameters of 10 kV energy and 1.6 nA beam current were implemented during investigations. Transmission electron microscopy (TEM) analyses were performed using a Titan G2 (ThermofisherScientific) operating at 300 kV. The tool has Cs corrected beam optics to reduce spherical aberration for ultra-high resolution imaging. A micro-Raman spectrometer (Renishaw) at an excitation wavelength of 532 nm and X-ray diffraction (XRD) using a D8 Discover diffractometry (Bruker) ($K_{\alpha Cu} = 1.54$ Å) were employed to study the vibrational modes and the crystalline quality of the $MoS_2/MoO_2$ heterostructures, respectively. X-ray photoelectron spectroscopy (XPS) analyses were carried out using a ThermofisherScientific K-alpha spectrometer and a PHI VersaProbe III scanning XPS microprobe to investigate the surface composition of our samples. The optical reflectance was measured using

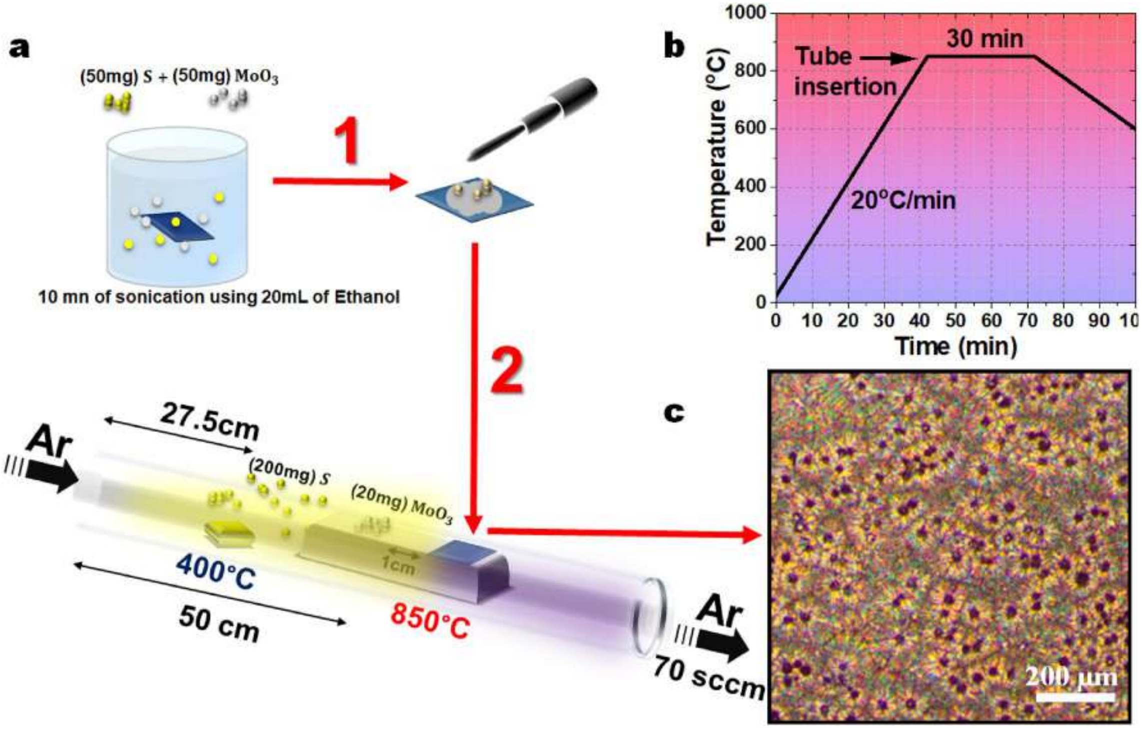

**Figure 1.** (**a**) CVD process set up of $MoS_2/MoO_2$ heterostructure using a tube furnace. (**b**) The temperature profile used for the synthesis of $MoS_2/MoO_2$ heterostructures. (**c**) Optical image of the typically obtained $MoS_2/MoO_2$ heterostructure film on Si substrate.

an UV–Vis-near IR spectrometer (JASCO V-670). Current-voltages (I–V) curves and transient photocurrents were measured using an photoelectrochemical device (Autolab PGSTAT204, Metrohm) coupled either with a solar simulator with Air Mass (AM) 1.5G filter (LOT Quantum Design, 100 mW $cm^{-2}$) or with an LED module (LED Driver kit, Metrohm). The LEDs (450, 470, 505, 590, and 627 nm) used, have a low spectral dispersion and are calibrated with a photodiode to determine their actual power density (mW $cm^{-2}$) received by the sample. To perform photo-electric measurements on our samples, we first exfoliate the $MoS_2/MoO_2$ nano-fibers and then transfer them onto a substrate with a circular interdigitated electrodes pattern[33] with 10 µm spacing. The effective detection area of our sample is equal to $5 \times 10^{-3}$ $cm^2$.Atomic force microscopy (AFM) measurements were carried out in ambient conditions using a Dimension Icon system (Bruker, Santa Barbara, USA) in the peak force Kelvin probe force microscopy (PF-KPFM) method. Conductive Platinum coated silicon AFM probes (Spark150, NuNano, Bristol, UK), with a spring constant $k = 20 \pm 0.2$ N/m, were used. The PF KPFM measurement enables the simultaneous characterization of the sample surface topography and surface potential variations.

## Results and discussion

The CVD grown $MoS_2/MoO_2$ heterostructure was first examined in SEM. The samples display a unique morphology consisting of microflowers attached to microfibers, as shown in Fig. 2a. A close examination of these structures (see sections below) indicate that the microflowers mainly consist of $MoO_2$ with an average diameter size of ~ 50 µm, and the microfibers correspond to $MoS_2$ with a length reaching up to few hundreds of micrometers. Intermixing phases were also observed, especially at the boundaries, as it will be identified later by EDS, HRTEM and KPFM. The inset of Fig. 2b provides a closer look at the morphology of the fabricated $MoS_2/MoO_2$ heterostructures, showing $MoO_2$ microflowers seemingly at the sites of $MoS_2$ microfibers nucleation. This is well illustrated in the EDX elemental maps in Fig. 3. Individual elemental maps for Si, O, Mo, and S are separately shown, whereas their combined mapping was overlaid (color contrast) on the SEM image (bottom-left). The corresponding contrast provides clear indications that the microflowers are rich in oxygen whereas microfibers have a rather high sulfur content, which is signature of $MoS_2$ compound.

To examine the mechanism of $MoS_2/MoO_2$ heterostructure nucleation and growth, the CVD reaction was interrupted at different times while maintaining the same growth conditions. This allows monitoring the CVD reaction kenitics and analyzing the evolving compound miscrostructure. Figure 4. depicts the $MoS_2/MoO_2$ heterostructure after 5 min, 20 min and 30 min reaction time.

One can notice in Fig. 4a that there is first a nucleation sites, two in this micrograph, then random fibers are generated. 20 min later (Fig. 4b) several thicker fibers impinge from the nucleation sites and begin to make the connections between the nucleation sites. At last stage of the CVD reaction 30 min (Fig. 4c), the Si substrate is fully covered by very thick and long fibers as also shown in Fig. 3.

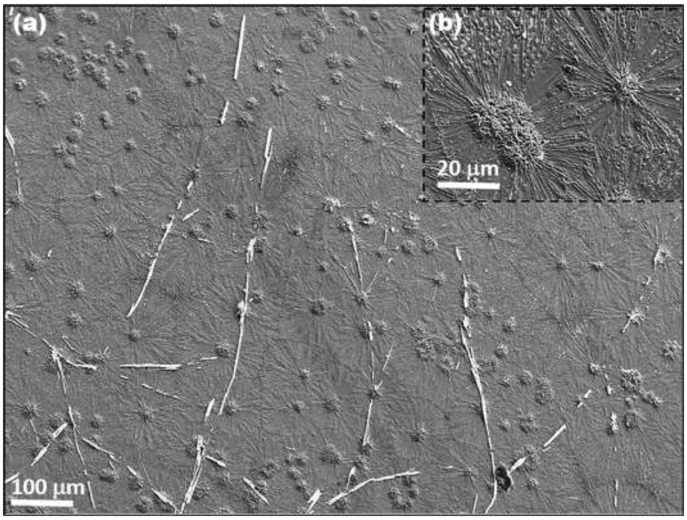

**Figure 2.** (**a**) Large view of the typical microstructure of as-grown $MoS_2/MoO_2$ heterostructures. (**b**) The inset shows a zoomed-in part of the image shown in (**a**), where the microfibers are seen to emerge from the central microflowers.

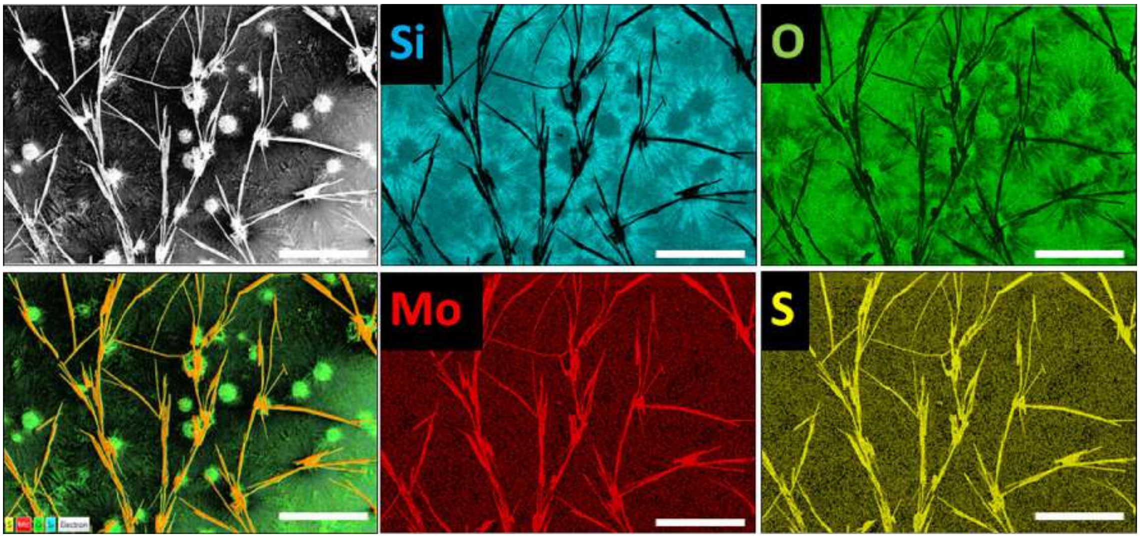

**Figure 3.** EDX mapping of $MoS_2/MoO_2$ heterostructure (scale bar = 100 µm).

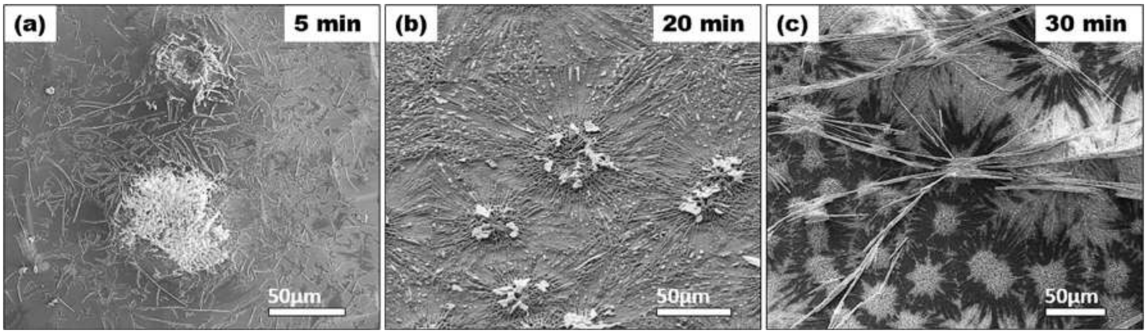

**Figure 4.** CVD reaction performed at different dwel times: (**a**) 5 min, secondary electron SEM image of nucleation sites of $MoS_2/MoO_2$ heterostructure, (**b**) 20 min secondary electron SEM image of $MoS_2/MoO_2$ heterostructure growth, (**c**) 30 min backscattered electron SEM image of well-settled $MoS_2/MoO_2$ heterostructure covering the entire substrate.

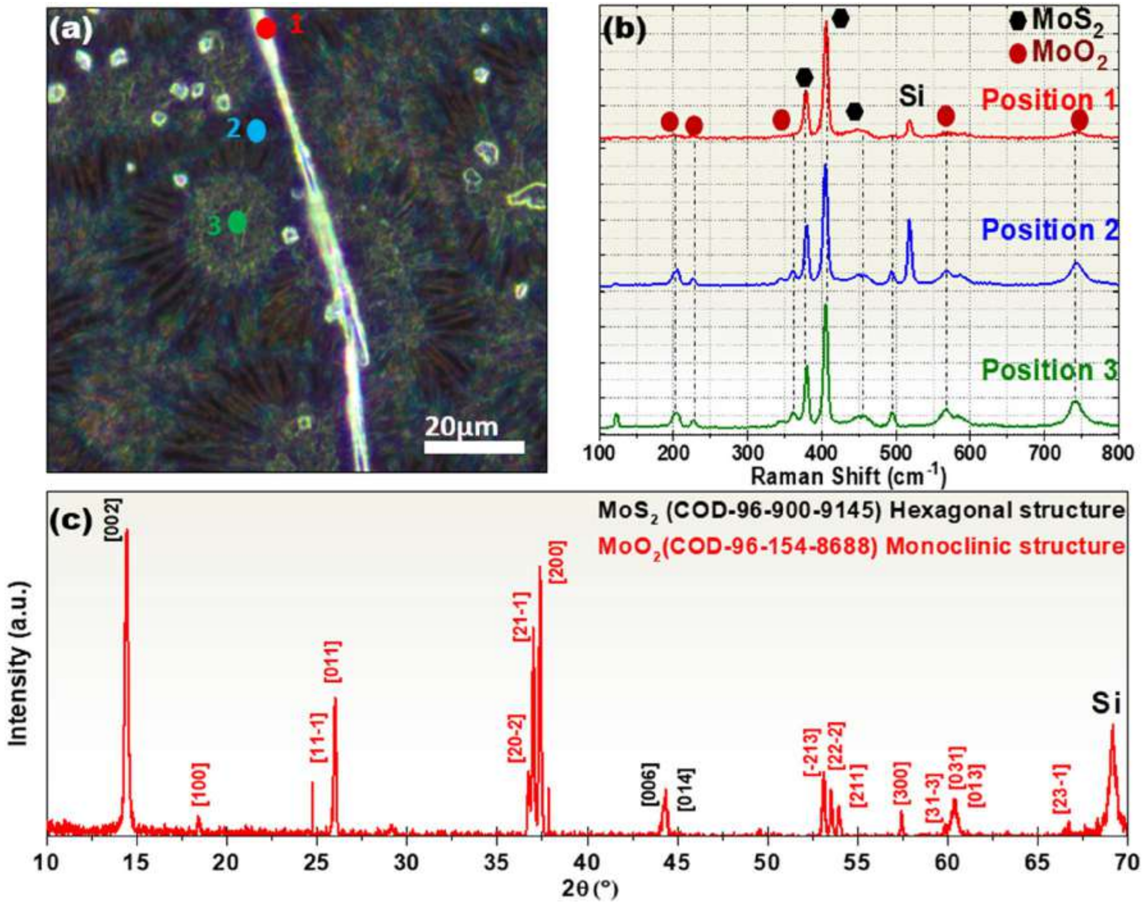

**Figure 5.** (**a**) Optical image showing the positions excited by the laser beam (532 nm) and their (**b**) respective Raman spectra of the $MoS_2/MoO_2$ heterostructures, (**c**) XRD diagram of the same.

The $MoS_2/MoO_2$ heterostructures were further characterized using Raman spectroscopy (laser excitation at 532 nm) and XRD diffraction. Figure 5a shows an optical image indicating the three locations on the sample excited by the laser beam. Figure 5b depicts their respective Raman spectra in the 100–800 $cm^{-1}$. At the position 1, the vibrational modes are associated with known $MoS_2$ peaks, i.e. $E^1_{2g}$ mode at 382 $cm^{-1}$, $A_{1g}$ mode at 406 $cm^{-1}$[34], and Si at 519 $cm^{-1}$, indicating the good purity of $MoS_2$ microfibers. Whereas for the position 2 and 3, corresponding to the microflowers core and edges, the spectra show additional vibrational modes translated by several peaks at 204, 226, 346, 363, 460, 494, 571, 589, and 742 $cm^{-1}$ corresponding the $MoO_2$ compound[32]. It was previously reported that the thermal deposition of $MoO_3$ on Si substrates can lead to the formation of metallic $MoO_2$ microflowers resulting from the thermal reduction of $MoO_3$[35]. The Raman peaks at 204–494 $cm^{-1}$ are due to the stretching modes of doubly coordinated oxygen (Mo–O–Mo)[36], whereas the signals at 571, 589, and 742 $cm^{-1}$ are due to terminal oxygen stretching modes (M=O)[37]. The formation of $MoS_2$ and $MoO_2$ phases is further supported by the XRD results. Indeed, the XRD diagram shown in Fig. 5b reveals the presence of three diffraction peaks (at $2\theta = 14.41°$, 29.11°, and 44.31°; labeled in black), which are ascribed respectively to the (002), (004) and (006) planes of the hexagonal phase $MoS_2$. On the other hand, the multiple peaks located at $2\theta = 18{,}43°$, 25.85, 26°, 36.73°, 36.99°, 37.37°, 53.12°, 53.52°, 53.95°, 57.43°, 59.86°, 60.36°, 60.61°, and 68.25°, are attributed to the (100), $(11\overline{1})$, (011), $(20\overline{2})$, $(21\overline{1})$, (200), $(\overline{2}13)$, $(22\overline{2})$, (211), (300), $(31\overline{3})$, (031), (013), and $(23\overline{1})$ plans of $MoO_2$ monoclinic structure, respectively.

To further examine the microstructure of the $MoS_2/MoO_2$ heterostructure, cross-section samples were prepared (supplementary information) and HRTEM was performed at the $MoO_2$ microflower and $MoS_2$ microfiber interface to identify pure phases and intermixing sites, as shown in the top left image of Fig. 6. Three regions are identified as follows: region R1 corresponding to the base of the $MoO_2$ microflower, as indicated by the central image showing the typical interplanar distance of 0.35 nm and the corresponding diffraction pattern given in the right image. Region R2 corresponding to the first fabricated layer exhibiting a $MoO_3$ crystal structure underlined by the typical interplanar distance 0.48 nm and the corresponding diffraction pattern shown in the right images. This layer most likely acts as a passivation layer between the Si substrate and the $MoS_2/MoO_2$ heterostructure. Finally, region R3 corresponding to the nucleation site of the $MoS_2$ microfiber, as indicated in the top middle image by the typical interplanar distance of 2H-$MoS_2$ of 0.63 nm. In addition, $R_3$ region reveals a thickness of ~ 32 nm, which corresponds to ~ 50 layers of 2H-$MoS_2$. This is consistent with the crystalline structure of the $MoS_2$ microfibers derived from XRD and Raman spectroscopy. More importantly, HRTEM shows that the $MoS_2$ microfibers are intimately interconnected with the $MoO_2$ microflowers. The electron diffraction analyses of the

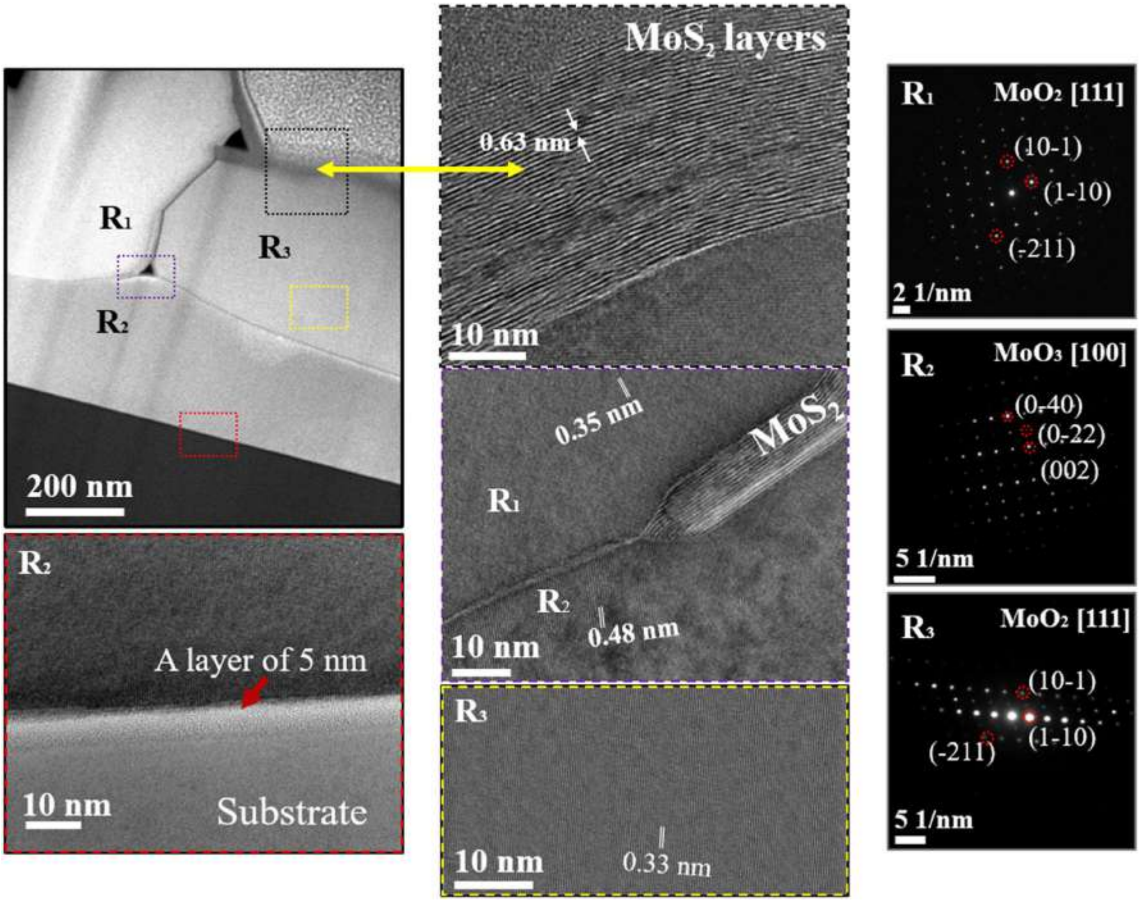

**Figure 6.** HRTEM images of the CVD-grown $MoS_2/MoO_2$ samples. (Top left): overview showing three regions, i.e. base of the $MoO_2$ microflower, passivation substrate, and an impinging $MoS_2$ fiber. (Bottom left): high magnification image of the substrate-grown sample interface. (Middle): crystal structures analyses for the 3 defined regions. (Right): corresponding diffraction patterns.

three regions indicate d-spacing of $(11\bar{1})$, (100), and (011) planes corresponding to monoclinic m-$MoO_2$ crystal. These results confirm the high crystalline quality of the $MoO_2$ microflowers. Interestingly, the central image in Fig. 6 clearly reveals the co-presence of the three zone, indicating the heterostructure character of the $MoS_2$ with both $MoO_2$ and $MoO_3$ on one side and a possible $MoO_2/MoO_3$ heterostructure on the other side. As the thickness of the $MoO_3$ layer is negligible (5 nm: image bottom left) compared to microflowers/microfibers thickness, we assume that the general optical and photodetection behaviors are mainly due to the $MoS_2/MoO_2$ heterostructure.

Figure 7a depicts the XPS survey spectrum of the CVD-grown $MoS_2/MoO_2$ samples. The high-resolution view of both Mo 3d and S 2s core peaks is shown in Fig. 7b. The peak appearing at 226.5 eV is a signature of the S 2s core level. The two peaks located at 229.3 and 232.4 eV are ascribed to the doublets Mo $3d_{5/2}$ and Mo $3d_{3/2}$, corresponding to the $Mo^{4+}$ state in $MoS_2$. Similarly, the $S^{2-}$ doublet is observed in the S 2p spectra at 162.1 and 163.25 eV (Fig. 7c). The binding energies of O 1s are depicted in Fig. 7d. The peak around 530 eV corresponds to $MoO_2$, whereas the peaks at 530.95 and 532 eV are attributed to S–O/S=O and C–O bonds, respectively.

Optical properties of the $MoS_2/MoO_2$ heterostructure samples were investigated by measuring their reflectance in the wavelength range of 200–1500 nm at room temperature. Figure 8a shows that the samples exhibit a very low reflectance over the entire investigated spectral range, increasing from 1% at 200 nm to only ~ 5.5% at 1500 nm. This very low reflectance is could be attributed to the change of $MoS_2$ morphology in the presence of $MoO_2$, as previously reported[38,39]. A weak reduction is observed on the reflectance spectrum around 430 nm attributed to the electron transitions, which occur in the optical band gap. The obtained overall reflectance values were used to evaluate the optical band gap using the Kubelka–Munk function (F(R)), plotted using light absorbance in Fig. 8b. The plot of $(F(R)h\nu)^2$ versus photon energy (hν) and an approximation for direct band gaps of $MoS_2/MoO_2$ allowed extracting two potential values of direct bandgaps, namely $E_g = 2.8$ eV and $E_g = 1.8$ eV, as shown in Fig. 8c.

The band gap $E_g = 2.8$ eV could be ascribed to $MoO_2$[18,40], whereas $E_g = 1.8$ eV is consistent with the values quoted for direct bandgap of mono to few-layers of $MoS_2$[41,42]. The presence of two band gap energies would enhance the probability for electrons to jump to both $MoO_2$ and $MoS_2$ conduction bands once excited by an external light source. This might have likely led to the higher broadband light absorption recorded during the optical absorption measurements. Taking advantage of the presence of band gap energies, Z-scheme electron

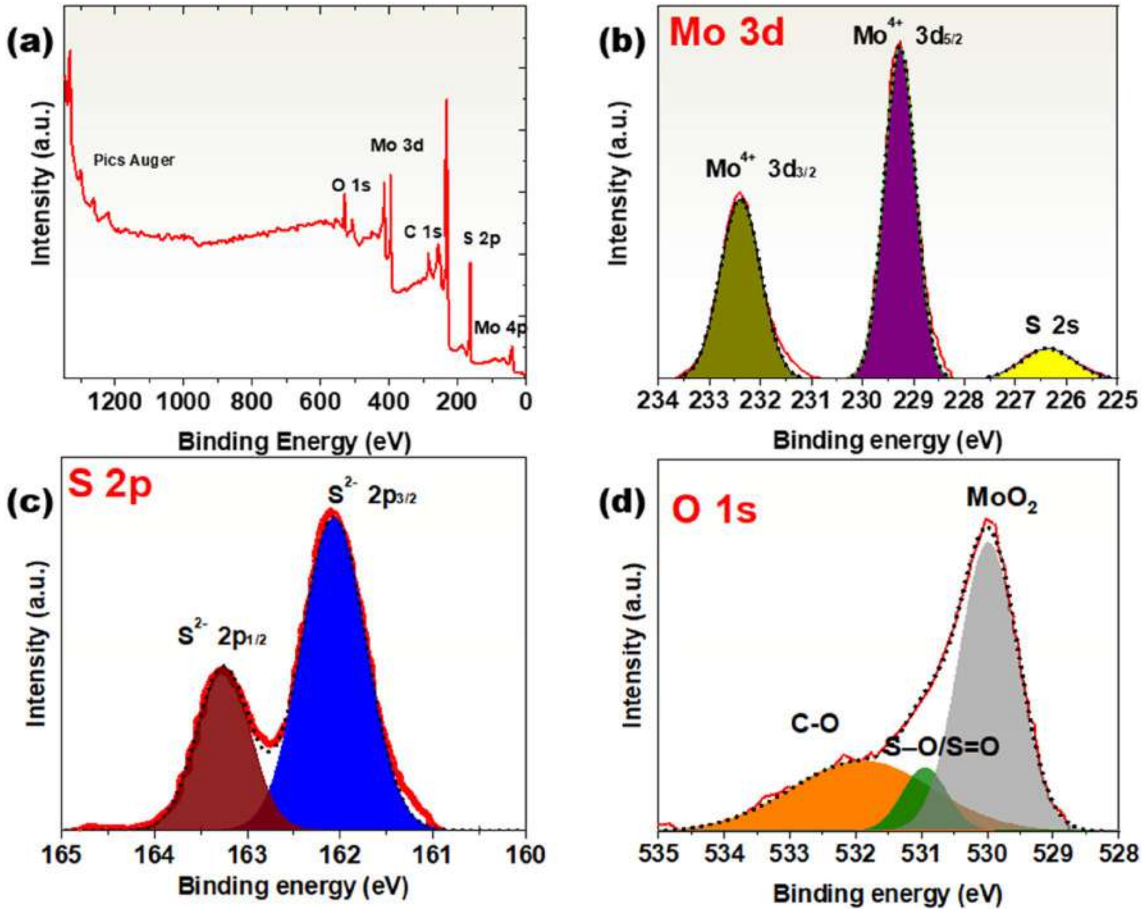

**Figure 7.** (**a**) X-ray photoelectron survey spectrum of the CVD grown $MoS_2/MoO_2$ heterostructures. (**b–d**) High-resolution spectra of the Mo 3d, S 2s, and (**c**) S 2p (**d**) O 1s core level peak region.

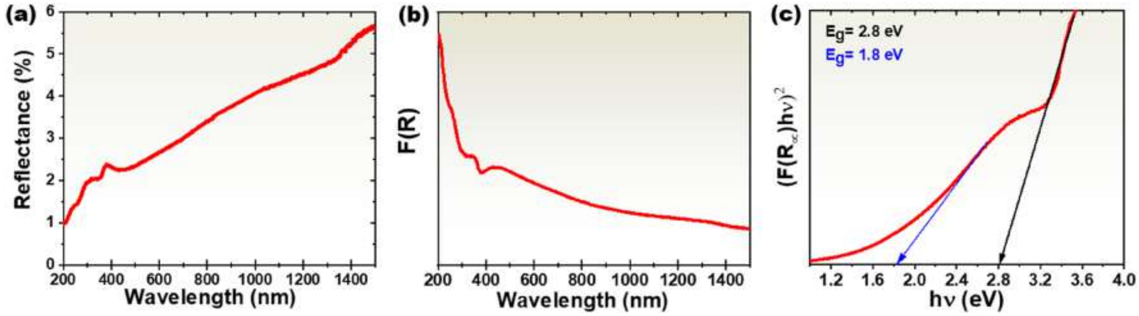

**Figure 8.** (**a**) Measured reflectance of the CVD-grown $MoS_2/MoO_2$ heterostructure samples. (**b**) Light absorbance as derived from the Kubelka–Munk function. (**c**) Bandgap estimation using Kubelka–Munk function plot.

excitation may be also activated. The consequence of such optical properties is discussed further in the photodetection measurement section.

KPFM was used to characterize the surface potential the $MoS_2/MoO_2$ heterostructure. Figure 9 shows topography maps acquired at different scan sizes. The flower-like structure previously observed in SEM is identified on the large scan are (80 μm × 80 μm) in Fig. 9a. Central volcano-like structures, distributed over the surface, from which elongated petal-like structures emanate in all directions forming microflower-like islands can be clearly observed.

The large topography map reveals domain boundaries between islands, which points towards the growth dynamics dictated by surface energies and thermodynamic conditions. Fade dashed lines delimiting one island boundaries (lower right part of the image in Fig. 9a) were overlaid on the topography map to guide the eye. Interestingly, the magnified topography map (scan area: 30 μm × 30 μm) in Fig. 9b reveals the micromorphology of the elongated petal-like structures emanating from the center of the flower-like structure. Multiple microstructures

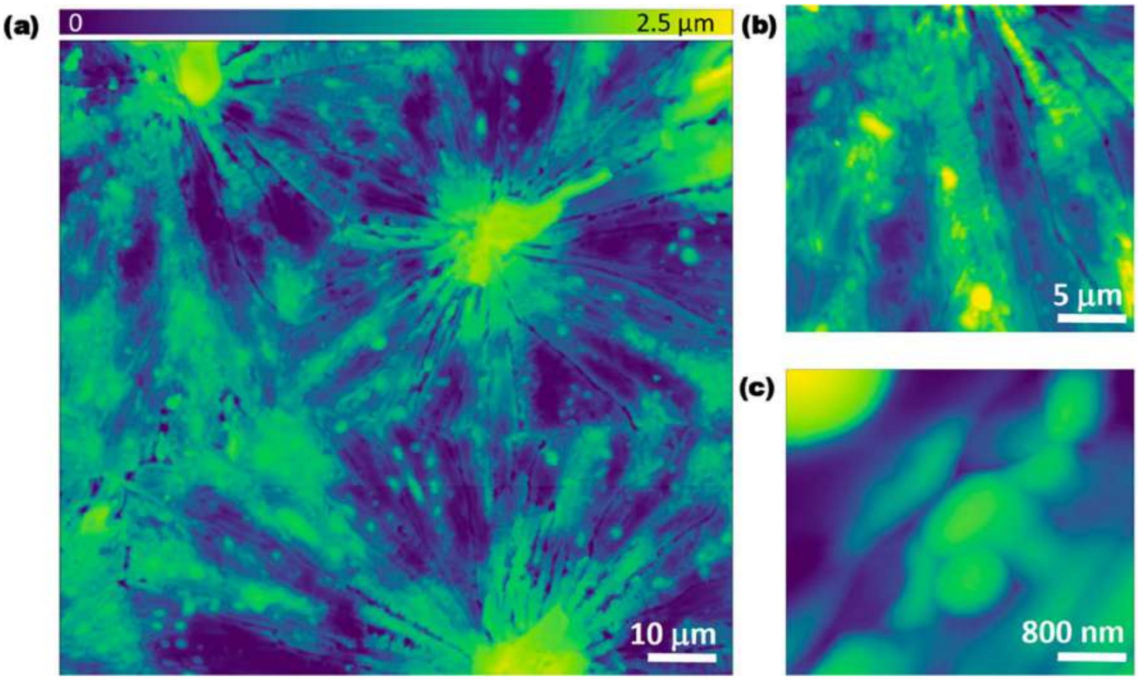

**Figure 9.** (**a**) AFM topography map (scan size: 80 µm$^2$) showing details of the $MoS_2/MoO_2$ structure. (**b**) Area on the elongated structure in form of microfibers (scan size: 30 µm$^2$) emanating from the central volcano structure. (**c**) A zoomed scan (scan size: 4 µm$^2$) over an elongated petal structure showing the inclusion of multiple nanostructures.

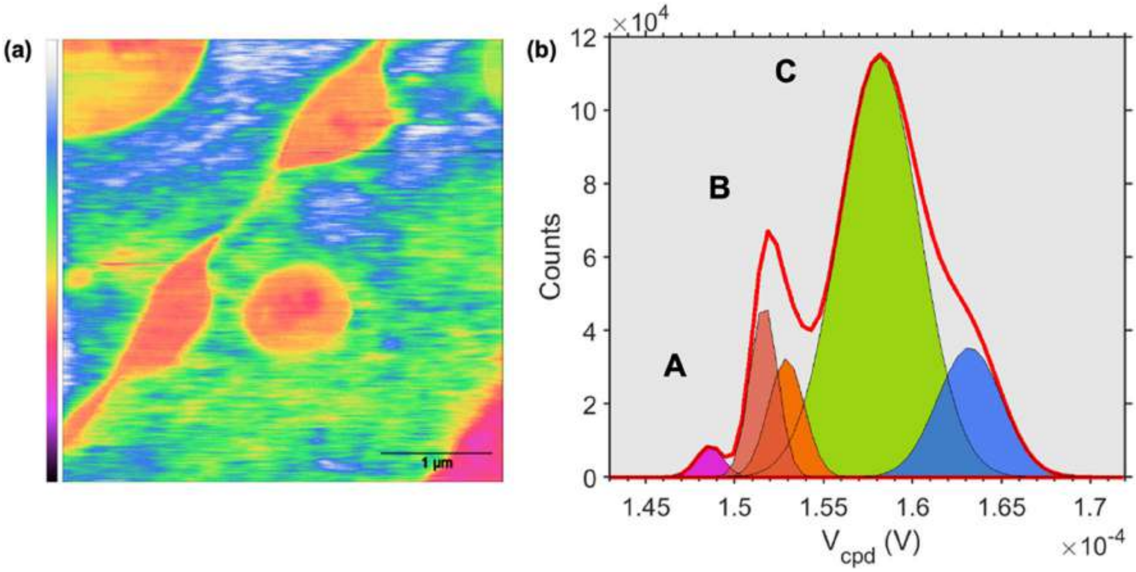

**Figure 10.** (**a**) Surface potential mapping acquired in the FM-KPFM mode on the same spot as in Fig. 8a. (**b**) Histograms of values extracted from the map shown in (**a**).

intercalated in forms of inclusions are clearly observed. To further investigate the origin of this complex structural diversity, a spot with a coexisting mix of microstructures has been imaged (scan size: 4 µm × 4 µm), as shown in Fig. 9c. To investigate the local physical-chemically dependent characteristics of the coexisting structures, surface potential measurements were performed on the same spot in Fig. 9c. The surface potential (or contact potential difference, $V_{cpd}$) stems from the differences in work functions between the AFM probe and the sample. It is an extreme surface-dependent property, highly sensitive to minute variations in the surface chemistry, electronic and crystallographic properties. As described in the experimental section. The AFM electrical measurements, shown here, were conducted in the PF-KPFM mode enabling simultaneous characterization of the surface adhesion to the AFM probe. Figure 10a shows the surface potential variations on the same spot as in Fig. 9c. The observed contrast indicates the coexistence of three different materials with different surface potential values.

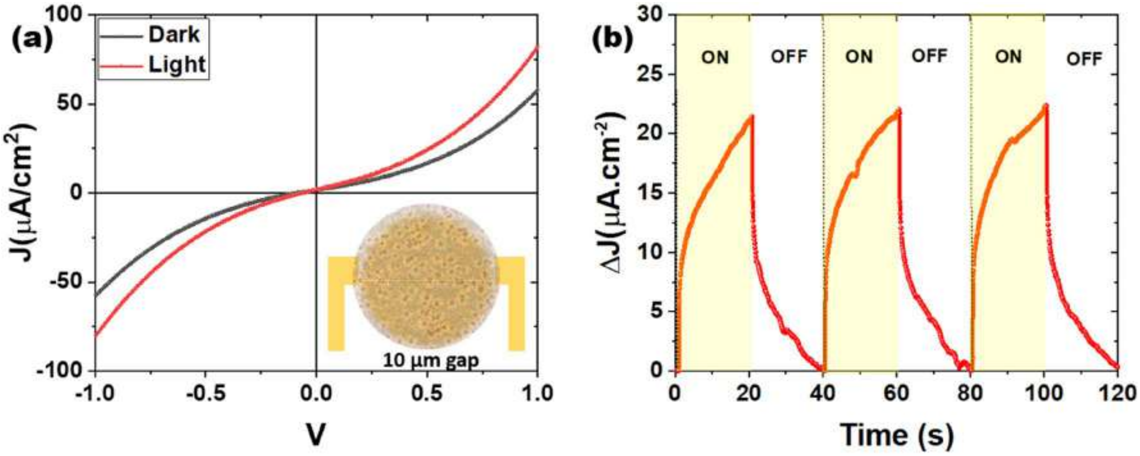

**Figure 11.** (**a**) J–V curves recorded under both dark and simulated sunlight conditions. (**b**) Transient photocurrent density response registered for 3 ON/OFF cycles (every 40 s) under standard sun illumination AM1.5 with an applied voltage $V_{bias} = 1$ V.

A comparison with the central image in Fig. 5, reveals a clear resemblance to the coexisting regions observed in HRTEM images. This strongly suggests a direct corroboration between the surface potential variations and that of the $MoS_2/MoO_2$ heterostructures. The histogram in Fig. 10b reveals three main peaks (A, B, and C) corresponding to the domains observed on the surface potential map (peak colors have been matched to the false color scale in Fig. 10a). The surface potential measurements provide a nanoscale electrical property signature, confirming the observation made above regarding the co-presence of three regions forming the heterostructure.

To investigate the photoelectric properties of our $MoS_2/MoO_2$ heterostructures, the samples were integrated into photoactive devices, and exposed to solar excitation using a solar simulator equivalent to one sun (i.e. 100 $mW.cm^{-2}$ with AM 1.5G filter). Figure 11a shows J-V curves recorded under both dark ($J_{dark}$) and solar excitation ($J_{light}$). It is clearly seen that the $J_{light}$ under sun irradiation is higher than its dark counterpart, confirming the photoactivity of our $MoS_2/MoO_2$ material. Figure 11b depicts the transient photocurrent density ($\Delta J = J_{light} - J_{dark}$) response obtained at 1 V bias with successive ON/OFF cycles. A maximum photocurrent density is obtained after 20 s of sun exposure with a stable photocurrent density of 22 $\mu A\ cm^{-2}$ indicating the high stable photoactivity of the heterostructure. On the J-V curve, a symmetry in the ON/OFF cycles with respect to the origin is observed, suggesting the presence of an ohmic contact between the heterostructure and the gold electrodes, in accordance with previously reported works. This reveals a good electrons' injection at the $MoS_2$/Au interface compatible with the presence of an ohmic contact[12,13], which can be partially explained by the good chemical affinity between the gold and sulfur atoms leading to very weak injection barrier. Nonetheless, J-V curves exhibit a linear variation for low voltages followed by a curvature for higher voltages. Assuming the contacts are indeed ohmic, such curvature is probably due to space-charge-limited current effects[43]. In addition, Fig. 11b shows that the photocurrent undergoes a slow increase under standard sun illumination, and conversely, it shows a slow decay under darkness condition. The observed slow kinetic behavior is an indicator of carrier trapping within the heterostructure under illumination followed by a thermal detrapping of carriers manifested by the slow decay[43].

According to the absorbance spectrum obtained (see Fig. 8a,b) the $MoS_2/MoO_2$ heterostructure exhibits high absorbance capacity in the blue region. To elucidate this optical behavior, we carried photoresponse investigations of our $MoS_2/MoO_2$-based device under 450 nm laser excitation. Figure 12a shows the typical J-V curves recorded in dark and under illumination at variable laser power densities. Our results show that the photogenerated current density under blue light excitation is continuously increasing with increasing power density in the full range between −1 and 1 V. At a power density of 125 $mW\ cm^{-2}$, the photogenerated current density is five times higher than the one recorded in dark. Hence, the high optical absorption of our $MoS_2/MoO_2$ heterostructure is translated to higher photoconversion capacity. The stability and performance of our heterostructure-based photodetector were then further investigated. Figure 12b illustrates the transient photocurrent response steps during light ON/OFF cycles at increasing light power densities $\phi_0$. Results clearly show that the $MoS_2/MoO_2$ heterostructure is stable over time and its photogenerated current is continuously increasing with increasing light power density and/or applied bias. To examine the behavior of the photocurrent change induced by the variation of the incident light intensity, the $\phi_0$ dependence of the photocurrent is depicted in Fig. 12c. Two main behaviors can be identified as follows: (1) For $\phi_0 < 80$ $mW\ cm^{-2}$ the photocurrent density (ΔJ) follows the classical power law $\Delta J = \alpha \Phi_0{}^n$, where α is a wavelength-dependent constant and $n \le 1$ is a constant. (2) For $\phi_0 \geq 80$ $mW\ cm^{-2}$ there is a clear change in the slope of the photocurrent a steep increase of the photocurrent with increasing $\phi_0$. The obtained photocurrent was subsequently used to determine the responsivity and detectivity of our $MoS_2/MoO_2$-based photodetector according to the following equations:

$$R = \frac{I_p}{\phi_0 A} \text{ and } D^* = \frac{R\sqrt{A}}{\sqrt{2qI_{Dark}}},$$

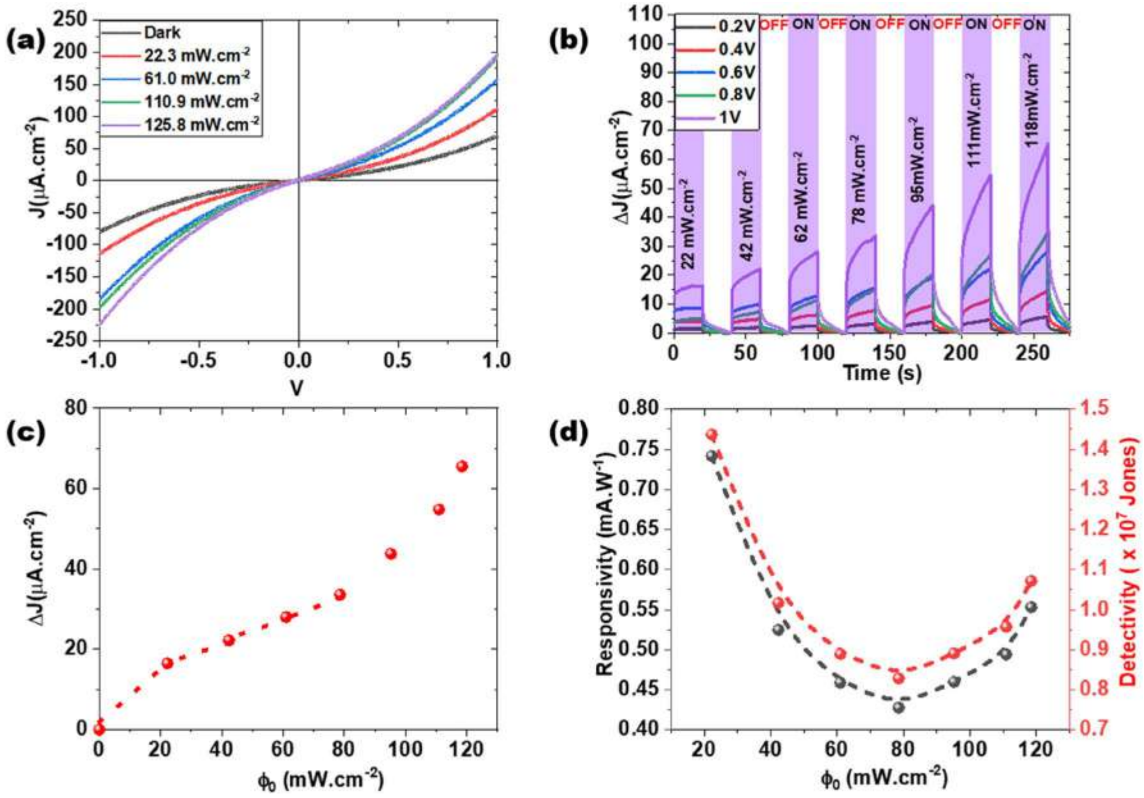

**Figure 12.** (**a**) J–V curves recorded in the dark and under different excitations light intensities at λ = 450 nm. (**b**) Transient photocurrent density for various ON/OFF cycles (40 s each) as a function of light intensity at λ = 450 nm. (**c**) Photocurrent density variation as a function of the light intensity of the blue laser at 1 V bias. (**d**) Responsivity and detectivity change with the incident blue light intensity at 1 V bias.

| Heterostructure | Processing | Excitation (nm) | Bias (V) | R (mA/W) | D* (× $10^7$ Jones) | Ref |
|---|---|---|---|---|---|---|
| $MoS_2/ZnS$ | Hydrothermal | 554 | 1 | 0.17 | – | [10] |
| $MoS_2/SnS$ | Magnetron sputtering | 473 | 1 | 2.4 | 5.7 | [45] |
| $MoS_2/MoTe_2$ | Mechanical exfoliation | 532 | 0 | 111 | 14.8 | [46] |
| $MoS_2/MoO_x$ | CVD | 638 | 10 | 10 | 600 | [47] |
| $MoS_2/MoO_x$ | CVD | 405 | 10 | 1090 | $2.8 \times 10^4$ | [47] |
| $MoS_2/GaN$ | CVD | 460 | 20 | 25 | 56 | [14] |
| $MoS_2/MoO_3$ | Chemical exfoliation | 405 | 5 | 0.134 | – | [48] |
| $MoS_2/MoO_2$ | CVD | 450 | 1 | 0.75 | 1.45 | This work |

**Table 1.** Comparison of $MoS_2$ heterostructures based photodetectors.

where $I_p$ is the generated photocurrent (i.e. difference between the current under illumination and dark current), A is the effective irradiated area, q is the electron charge and $I_{Dark}$ is the dark current.

The obtained responsivity and detectivity as function of the light power densities $\phi_0$ are depicted in Fig. 12d. Our $MoS_2/MoO_2$-based photodetector exhibits maximum values for both responsivity and detectivity at 0.75 mA $W^{-1}$ and $1.45 \times 10^7$ Jones, respectively, achieved at very low blue light intensity excitation of 20 mW $cm^{-2}$. It is woth noting that high optoelectronic performances based on $MoS_2$ were reported[44], however, the fabrication routes cited in this study are tedious, consisting of several fabrication steps. Additionally their photodection responses were achieved on very small active area (~ $10^{-7}$ $cm^2$) and at high applied bias (~ 20 V) compared to our measurements. Generally, our findings concur with the recently reported data as summarized in Table 1.

In this table, we have summarized $MoS_2/MoO_2$ based photodetector performances while providing precision on the fabrication technique used, the excitation energy and the bias voltage. One can notice that our results is comparable to reported data, which indicates the ability of the one-step CVD process to compete with other fabrication techniques.

Nonetheless, Fig. 12d shows that as the incident $\phi_0$increases, both responsivity and detectivity are decreasing until reaching their minimum values at $\phi_0$ =80 mW $cm^{-2}$. Surprisingly, this decrease was followed by a slight augmentation in both the responsivity and detectivity values for higher incident light intensities. This could

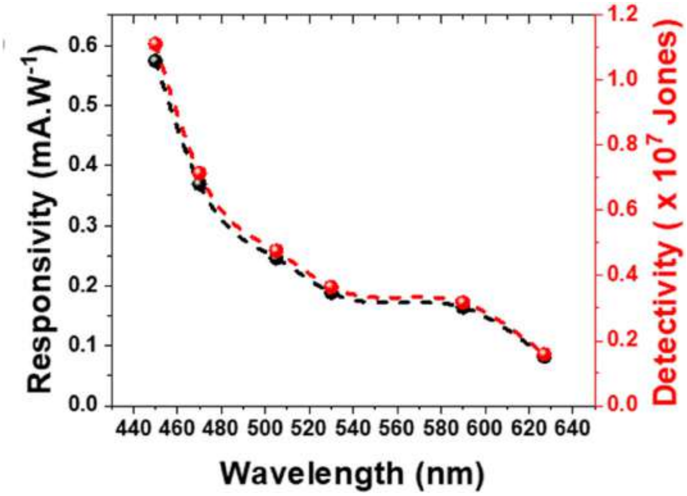

**Figure 13.** Wavelength dependence of the responsivity and detectivity of the $MoS_2/MoO_2$ based photodetector, obtained at 40 mW cm$^{-2}$ light power density and 1 V bias.

be ascribed to the presence of several photoactive layers within the $MoS_2/MoO_2$ heterostructures as suggested by both HRTEM and KPFM surface potential images. The $MoO_2$ photoactive layer anchored to the $MoS_2$ layer contributes to the photocurrent generated when the power density of the light is high enough to pass through the oxide layer. Thus, up to 80 mW cm$^{-2}$, we observe a power law (e.g. Fig. 12c), beyond which we observe the contribution of the $MoO_2/MoS_2$ heterojunction.

Furthermore, The radiation-responsivity and detectivity of the $MoS_2/MoO_2$ heterostructure was studied using various excitation wavelengths at 40 mW.cm$^{-2}$ light power density and 1 V bias as shown in Fig. 13.

The heterostructure photodetection performance is validate for the entire visible spectral range. Nonetheless, it is higher for shorter wavelengths, which is in good agreement with the aforementioned optical measurements. Indeed, the heterostructure is six times more responsive at 450 nm than at 630 nm wavelength. Finally, it is worth noting that the photoresponse performances are measured on the entire sample (microflowers and microfibers). We believe that the photoresponse could be improved if it is recorded using the sole microfibers. Hence different techniques could be put in place to isolate one or few microfibers using mechanical and/or chemical exfoliation or nanofabrication using FIB-SEM to allow developing these microfibers onto photoconductive device.

## Conclusion

In summary, complex $MoS_2/MoO_2$ heterostructures were successfully synthesized using a facile one-step CVD process. The synthesized heterostructures consist mainly of $MoO_2$ microflowers of few 10 s microns in diameter, from which $MoS_2$ microfibers up to 100 s microns-long emanate in all directions. X-ray and electron diffraction techniques have revealed that the crystalline nature of $MoS_2$ and $MoO_2$ in the respective hexagonal 2H-$MoS_2$ and monoclinic m-$MoO_2$ structures. These $MoS_2/MoO_2$ heterostructures were found to exhibit high broadband optical absorption over the entire 200–1500 nm spectral range. This high optical performance is ascribed to the presence of two bandgap energy values measured at 1.8 and 2.8 eV, consistent with those quoted for $MoS_2$ and $MoO_2$, respectively. The strong optical absorption was exploited by integrating the heterostructure samples into functional photodetectors, and interestingly found to exhibit high photoresponsive over the 450—630 nm range. The highest responsivity and detectivity values of 0.75 mA W$^{-2}$and $1.45 \times 10^{7}$ Jones, respectively, were obtained under the blue light excitation at very low light illumination of 20 mW cm$^{-2}$. These results highlight the potential of these CVD-grown $MoS_2/MoO_2$ heterostructures for strong broadband light harvesting and photodetection applications.

## Data availability

All data supporting this work are available upon request from the corresponding author M. Jouiad.

Received: 13 October 2022; Accepted: 12 December 2022

## References

1. Wang, Q. H., Kalantar-Zadeh, K., Kis, A., Coleman, J. N. & Strano, M. S. Electronics and optoelectronics of two-dimensional transition metal dichalcogenides. *Nat. Nanotechnol.* **7**, 699–712 (2012).
2. Mouloua, D. *et al.* Recent progress in the synthesis of MoS2 thin films for sensing, photovoltaic and plasmonic applications : A review. *Materials (Basel)* **14**, 3283 (2021).
3. Ermolaev, G. A. *et al.* Broadband optical properties of monolayer and bulk MoS2. *npj 2D Mater. Appl.* **4**, 1–6 (2020).
4. Jeong, Y. *et al.* Engineering MoSe2/MoS2 heterojunction traps in 2D transistors for multilevel memory, multiscale display, and synaptic functions. *npj 2D Mater. Appl.* **6**, 1–8 (2022).

5. Lu, C. I. *et al.* Moiré-related in-gap states in a twisted MoS2/graphite heterojunction. *npj 2D Mater. Appl.* **1**, 1–6 (2017).
6. Sanjay, S., Hossain, M., Rao, A. & Bhat, N. Super-Nernstian ion sensitive field-effect transistor exploiting charge screening in WSe2/MoS2 heterostructure. *npj 2D Mater. Appl.* **5**, 1–8 (2021).
7. Nalwa, H. S. A review of molybdenum disulfide (MoS2) based photodetectors: From ultra-broadband, self-powered to flexible devices. *RSC Adv.* **10**, 30529–30602 (2020).
8. Ma, J. *et al.* Electrophoretic deposition of ZnSnO3/MoS2 heterojunction photoanode with improved photoelectric response by low recombination rate. *J. Alloys Compd.* **810**, 151845 (2019).
9. Wu, H. *et al.* All-inorganic perovskite quantum dot-monolayer MoS2 mixed-dimensional van der Waals heterostructure for ultrasensitive photodetector. *Adv. Sci.* **5**, 1801219 (2018).
10. Gomathi, P. T., Sahatiya, P. & Badhulika, S. Large-area, flexible broadband photodetector based on ZnS–MoS2 hybrid on paper substrate. *Adv. Funct. Mater.* **27**, 1701611 (2017).
11. Bang, S. *et al.* Augmented quantum yield of a 2D monolayer photodetector by surface plasmon coupling. *Nano Lett.* **18**, 2316–2323 (2018).
12. Radisavljevic, B., Whitwick, M. B. & Kis, A. Integrated circuits and logic operations based on single-layer MoS 2. *ACS Nano* **5**, 9934–9938 (2011).
13. Cunningham, G. *et al.* Photoconductivity of solution-processed MoS2 films. *J. Mater. Chem. C* **1**, 6899–6904 (2013).
14. Liu, X. *et al.* High-performance MoS2 photodetectors prepared using a patterned gallium nitride substrate. *ACS Appl. Mater. Interfaces* **13**, 15820–15826 (2021).
15. Paul, A. K. *et al.* Photo-tunable transfer characteristics in MoTe2–MoS2 vertical heterostructure. *npj 2D Mater. Appl.* **1**, 1–7 (2017).
16. GonzalezMarin, J. F., Unuchek, D., Watanabe, K., Taniguchi, T. & Kis, A. MoS2 photodetectors integrated with photonic circuits. *npj 2D Mater. Appl.* **3**, 1–6 (2019).
17. Wazir, N. *et al.* Vertically stacked MoSe2/MoO2 nanolayered photodetectors with tunable photoresponses. *ACS Appl. Nano Mater.* **3**, 7543–7553 (2020).
18. Guha, P. *et al.* P-type β-MoO2 nanostructures on n-Si by hydrogenation process: Synthesis and application towards self-biased UV-visible photodetection. *Nanotechnology* **30**, 035204 (2019).
19. Deokar, G. *et al.* Large area growth of vertically aligned luminescent MoS2 nanosheets. *Nanoscale* **9**, 277–287 (2017).
20. Guo, Y. *et al.* MoO3–MoS2 vertical heterostructures synthesized via one-step CVD process for optoelectronics MoO3–MoS2 vertical heterostructures synthesized via one-step CVD process for optoelectronics. *2D Mater.* **8**, 035036 (2021).
21. Sriram, P. *et al.* Enhancing quantum yield in strained MoS2 bilayers by morphology-controlled plasmonic nanostructures toward superior photodetectors. *ACS Appl. Mater. Interfaces* **32**, 2242–2252 (2020).
22. Wang, W. *et al.* Photoresponse-bias modulation of a high-performance MoS2 photodetector with a unique vertically stacked 2H-MoS2/1T@2H-MoS2 structure. *ACS Appl. Mater. Interfaces* **12**, 33325–33335 (2020).
23. Zhu, D. *et al.* Capture the growth kinetics of CVD growth of two-dimensional MoS2. *npj 2D Mater. Appl.* **1**, 1–7 (2017).
24. Huang, Y. *et al.* Scalable fabrication of molybdenum disulfide nanostructures and their assembly. *Adv. Mater.* **32**, 2003439 (2020).
25. Deokar, G. *et al.* Towards high quality CVD graphene growth and transfer. *Carbon N. Y.* **89**, 82–92 (2015).
26. Deokar, G. *et al.* MoS2-carbon nanotube hybrid material growth and gas sensing. *Adv. Mater. Interfaces* **4**, 1–10 (2017).
27. Deokar, G., Vignaud, D., Arenal, R., Louette, P. & Colomer, J. F. Synthesis and characterization of MoS2 nanosheets. *Nanotechnology* **27**, 075604 (2016).
28. Deokar, G. *et al.* Toward the use of CVD-grown MoS2 nanosheets as field-emission source. *Beilstein J. Nanotechnol.* **9**, 1686–1694 (2018).
29. Liu, H. F., Wong, S. L. & Chi, D. Z. CVD growth of MoS2-based two-dimensional materials. *Chem. Vap. Depos.* **21**, 241–259 (2015).
30. Zeng, T., You, Y., Wang, X., Hu, T. & Tai, G. Chemical vapor deposition and device application of two-dimensional molybdenum disulfide-based atomic crystals. *Prog. Chem.* **28**, 459–470 (2016).
31. Özden, A., Ay, F., Sevik, C. & Perkgöz, N. K. CVD growth of monolayer MoS2: Role of growth zone configuration and precursors ratio electrical and optical applications and precursors ratio. *Jpn. J. Appl. Phys.* **56**, 06GG05 (2017).
32. Liu, H., Lin, M. & Guo, S. Morphological and structural evolutions of α-MoO3 single crystal belts towards MoS2/MoO2 heterostructures upon post-growth thermal vapor sulfurization. *Appl. Surf. Sci.* **536**, 147956 (2021).
33. Xu, M., Wang, R. & Li, Y. Rapid detection of *Escherichia coli* O157:H7 and *Salmonella typhimurium* in foods using an electrochemical immunosensor based on screen-printed interdigitated microelectrode and immunomagnetic separation. *Talanta* **148**, 200–208 (2016).
34. Lee, C. *et al.* Anomalous lattice vibrations of single- and few-layer MoS2. *ACS Nano* **4**, 2695–2700 (2010).
35. Lin, Y. C. *et al.* Wafer-scale MoS2 thin layers prepared by MoO3 sulfurization. *Nanoscale* **4**, 6637–6641 (2012).
36. Nikam, R. D. *et al.* Three-dimensional heterostructures of MoS2 nanosheets on conducting MoO2 as an efficient electrocatalyst to enhance hydrogen evolution reaction. *ACS Appl. Mater. Interfaces* **7**, 23328–23335 (2015).
37. Nam Trung, T., Kamand, F. Z. & Al Tahtamouni, T. M. Elucidating the mechanism for the chemical vapor deposition growth of vertical MoO2/MoS2 flakes toward photoelectrochemical applications. *Appl. Surf. Sci.* **505**, 1–10 (2020).
38. Infant Raj, S. *et al.* Highly active and reflective MoS2 counter electrode for enhancement of photovoltaic efficiency of dye sensitized solar cells. *Electrochim. Acta* **212**, 614–620 (2016).
39. Li, X. *et al.* Layer-number dependent reflection spectra of MoS2 flakes on SiO2 /Si substrate. *Opt. Mater. Exp.* **8**, 3082 (2018).
40. García-García, M. & Colet-Lagrille, M. Electrochemical fabrication of MoO2/MoO3-based photo-anodes for water splitting. *ECS Meet. Abstr.* **MA2017-01**, 1427–1427 (2017).
41. Lin, S. *et al.* Interface designed MoS2/GaAs heterostructure solar cell with sandwich stacked hexagonal boron nitride. *Sci. Rep.* **5**, 1–9 (2015).
42. Nan, H. *et al.* Strong photoluminescence enhancement of MoS2 through defect engineering and oxygen bonding. *ACS Nano* **8**, 5738–5745 (2014).
43. Bube, R. H. *Photoconductivity of solids* (RE Krieger Pub. Co., 1978).
44. Taffelli, A., Dirè, S., Quaranta, A. & Pancheri, L. Mos2 based photodetectors: A review. *Sensors* **21**, 2758 (2021).
45. Yu, H., Xie, Y., Wei, J., Zhang, P. & Cui, Z. Highly-bendable MoS2/SnS flexible photodetector with broadband infrared response. *Adv. Mater. Interfaces* **2200896**, 1–9 (2022).
46. Ji, X. *et al.* High-performance photodetectors based on MoTe2–MoS2 van der Waals heterostructures. *ACS Omega* **7**, 10049–10055 (2022).
47. Im, H., Liu, N., Bala, A., Kim, S. & Choi, W. Large-area MoS2–MoOx heterojunction thin-film photodetectors with wide spectral range and enhanced photoresponse. *APL Mater.* **7**, 061101 (2019).
48. Wei, Y. *et al.* Robust photodetectable paper from chemically exfoliated MoS2–MoO3 multilayers. *ACS Appl. Mater. Interfaces* **11**, 21445–21453 (2019).

## Acknowledgements

M.A.E and M.J. acknowledge the financial support provided by the Natural Sciences and Engineering Research Council (NSERC) of Canada and by the Region of Haut-De-France (HDF). This work was performed in the context of a scientific collaboration between INRS and UPJV. DM is grateful to both the Region HDF (France) and INRS (QC, Canada) for his PhD fellowship.

## Author contributions

D.M. and M.J. conceived the study; D.M., N.S.R., S.S., and K.K. carried out the experimental investigations; D.M., S.S., M.E., K.H., M.A.E. and M.J. analyzed the data. D.M. and M.J. wrote the first draft and all authors contributed equally on writing, editing, and reviewing the manuscript.

## Competing interests

The authors declare no competing interests.

## Additional information

**Supplementary Information** The online version contains supplementary material available at https://doi.org/10.1038/s41598-022-26185-z.

**Correspondence** and requests for materials should be addressed to M.A.E.K. or M.J.

# Article 4: D. Mouloua, J. Leblanc-Lavoie, L. Pichon, N.S. Rajput, M. El Marssi, M. Jouiad, and M. A. El Khakani, Submitted to Advanced Optical Materials .

# Tuning the strong photoresponse of vertically aligned $MoS_2$ thin films prepared by pulsed laser deposition: influential role of the substrate deposition temperature

D. Mouloua,[1,2] J. Leblanc-Lavoie,[1] L. Pichon,[1] N.S. Rajput,[3] M. El Marssi,[2]
M. Jouiad,[2] and M. A. El Khakani,[1]

[1]*Institut National de la Recherche Scientifique, Centre Énergie, Matériaux et Télécommunications, 1650, Blvd, Lionel–Boulet, Varennes, QC, J3X-1P7, Canada*

[2]*Laboratory of Physics of Condensed Matter, University of Picardie Jules Verne, Scientific Pole, 33 rue Saint-Leu, 80039 Amiens Cedex 1, France*

[3]*Advanced Materials Research Center, Technology Innovation Institute, P.O. Box 9639, Abu Dhabi, UAE*

## Abstract

The pulsed laser deposition (PLD) technique was successfully used to deposit $MoS_2$ films at different deposition temperatures ($T_d$) ranging from 25 to 700°C. Not only the crystalline structure and nanostructural arrangement of the $MoS_2$ monolayers inside the PLD-$MoS_2$ films, but also their optoelectronic properties were shown to vary significantly with $T_d$. The systematic variation of $T_d$ enabled us to point up $T_d$ = 500°C as the optimal temperature that yields PLD-$MoS_2$ films exhibiting a combination of attractive properties. These include a highly crystallized 2H-$MoS_2$ semiconducting phase with a strong (002) preferential orientation, a narrowest optical bandgap of ~1.4 eV and a strong photoresponse as high as 1500%. Raman analyses suggested that the degree of vertical alignment of $MoS_2$ monolayers in the films increases with $T_d$ and reaches its maximum at $T_d$ = 500°C. Indeed, HRTEM provided clear-cut evidence that the PLD-$MoS_2$ films consist of vertically aligned $MoS_2$ monolayers all across the film thickness (~90 nm), enabling those "3D" films to behave as a semiconducting direct-bandgap 2D-$MoS_2$ with excellent optoelectronic properties. Indeed, at $T_d$= 500°C, both the responsivity (R) and detectivity (D*) of the PLD-$MoS_2$ based photodetectors (PDs) are the highest ever-reported for large area ($\geq 1 cm^2$) $MoS_2$-based PDs (with values as high as 125 mA/W and $9.2 \times 10^9$ Jones, respectively, at a low voltage of only 1V). Interestingly, we were able to demonstrate, for the time, a constant-plus-linear relationship between the R and D* and the degree of vertical alignment of the $MoS_2$ monolayers in the PLD-$MoS_2$ films. Such a correlation is fundamental for gaining more control on the PLD growth $MoS_2$ films and for tuning of their optoelectronic properties in view of their integration into devices with standard VLSI processing.

**Keywords:** Pulsed Laser Deposition, PLD, $MoS_2$ films, Bandgap, Photodetection.

## I. Introduction

Following the scientific and technical impact generated by graphene, other 2D semiconducting materials are being investigated because of their unequaled optoelectronic properties and great potential for optoelectronic applications.[1]. Molybdenum disulfide ($MoS_2$) is one of those layered 2D materials that has received considerable attention in the last few years because of its abundance in nature, strong optical absorbance as well as high electrical mobility.[2–4] Moreover, the layered or 2D structures of $MoS_2$ enables very low dark currents,[5] resulting in high on/off ratios[3] and, consequently, high detectivity[5]. Besides, the band gap of $MoS_2$ films can be tuned, to a certain extent, by reducing their thickness to very few monolayers. This is can be used to control the absorption range and thus the detection window of such ultrathin $MoS_2$ films[6].

Given the tremendous potential of $MoS_2$, there have been sustained efforts to master its synthesis by using a variety of techniques[7]. Mechanical exfoliation was the first approach used for the "laborious" isolation of mono to few layers of $MoS_2$[8]. Although this approach permits to access $MoS_2$ flakes with interesting optical and electrical properties, their maximum size remains very small and insufficient for industrial applications[9]. Alternatively, chemical exfoliation-based on Li intercalation was proposed[10], and shown to achieve relatively larger sample sizes. However, the structural and optoelectronic properties of those $MoS_2$ films can be negatively impacted by the defects that are inherent to the chemical processing itself.[10,11] More recently, chemical vapor deposition (CVD) has been intensively used for the synthesis of $MoS_2$ with a variety of forms and morphologies[12–15], because of its relative ease of implementation and low operational cost. Nevertheless, there is still challenging issues in the CVD grown $MoS_2$ films in terms of thickness control, purity, and uniformity of structure/morphology over relatively large substrates, limiting thereby their use for practical device applications. Thus, the use of physical vapor deposition (PVD) techniques is highly appropriate for the growth of uniform $MoS_2$ thin films over large area substrates (up to 3" or 4"-diam. wafers) with fairly controllable thickness (from ~1 to few 100s nm), composition and crystalline structure. In this context, the pulsed laser deposition (PLD) technique has been shown to be very successful for the growth of a variety of thin films with complex stoichiometries and highly attractive properties.[16–19] Indeed, the PLD is well known for its large process latitude where different growth parameters (such as laser intensity, deposition temperature ($T_d$), background pressure, number of laser ablation pulses ($N_{LP}$), etc.) can be quasi-independently controlled to deposit high-quality thin films with different structures and morphologies[20,21]. For instance, nanoparticles and/or thin films (with thicknesses ranging from few nm to few microns) can be PLD-deposited by varying the background gas pressure and/or the $N_{LP}$.[22,23] It is thus possible to PLD-deposit ultrathin films of $MoS_2$ (~2 monolayers-thick) with a predominant hexagonal phase[24]. In fact, when the $MoS_2$ films consist of only very few monolayers, they exhibit a direct bandgap (of 1.8 eV much larger than of the indirect bulk value of 1.2 eV, because of quantum confinement occurrence[2]), making them highly attractive for optoelectronic device applications. Consequently, there has been more attraction for the controlled synthesis of ultrathin films of $MoS_2$ (with mono-to-few 2D-layers with their orientation being in-plane) for photosensitive devices. However, it was recently demonstrated that polycrystalline $MoS_2$ films (with thicknesses in the 15-90 nm range) synthesized by plasma enhanced atomic layer deposition have outperformed the ultrathin films for the hydrogen evolution reaction in electrocatalysis based water splitting experiments.[25] This superior electrochemical performance of relatively thick $MoS_2$ films was associated to the vertical orientation of the monolayers that forms many of their $MoS_2$ grains.[25] The possibility of growing relatively thick (≈100 nm) $MoS_2$ films with out-of-plane orientation of their $MoS_2$ monolayers, which exhibit photoelectric properties equaling or even surpassing those of the in-plane oriented ultrathin films is extremely interesting. This definitely opens a new prospect for the PVD synthesis of "3D" $MoS_2$ films which exhibits the highly sought for properties of 2D-$MoS_2$. In this context, the ionized jet deposition (IJD) with subsequent annealing treatment was recently shown to yield 3D stable and scalable $MoS_2$ films exhibiting excellent electronic and optical properties similar to those of 2D-$MoS_2$.[22] Indeed, Tempel *et al.* have demonstrated that despite the thickness of the IJD-$MoS_2$ films, the latter exhibited a well-resolved photoluminescence emission and a direct bandgap value comparable to the one measured for in-plane 2D-$MoS_2$.[22] Such an extraordinary behavior of the relatively-thick "3D" $MoS_2$ films is believed to result from the vertical orientation of the $MoS_2$ monolayers in the IJD films. Thus, the idea of using PVD techniques, compatible with standard IC processing, to deposit 3D-$MoS_2$ films exhibiting attractive 2D-$MoS_2$ properties is highly exciting for the development of $MoS_2$-based optoelectronic devices with superior performance. In this context, PLD is definitely an appropriate technique that has been successfully used for the deposition of $MoS_2$ ultrathin films onto various substrates mainly for photodetection applications.[20,24,26–28] However, all of these studies have focused on the downsizing of the film thickness (by decreasing the $N_{LP}$) to achieve large area films consisting of 1 to few monolayers of $MoS_2$ and investigate their photodetection properties. Moreover, so far, all of these PLD synthesis related studies used an arbitrary deposition temperature ($T_d$) (sometimes room-temperature followed by post-annealing or a high $T_d$ of 700°C or 800°C), to grow the ultrathin $MoS_2$ films, with no optimization of $T_d$. In this paper, we report on a systematic study of the effect of $T_d$ on the structure and optoelectronic properties of PLD deposited $MoS_2$ thin films (with a thickness of ~100 nm). Thus, we have been able to identify an optimal deposition temperature of 500°C that yields highly-crystallized and preferentially (002)-oriented $MoS_2$ films exhibiting a bandgap of ~1.4 eV and the highest photodetection performance. Our results highlight the significance of $T_d$ for controlling not only the crystallinity of the PLD-$MoS_2$ films but also and their optoelectronic properties. The strong photodetection performance of our "3D" PLD-$MoS_2$ films is similar to what one would expect from few layers 2D-$MoS_2$ because of the vertical orientation of the $MoS_2$ monolayers in the films. Indeed, the HRTEM analyses interestingly revealed the formation of vertically aligned monolayers all through the thickness of our PLD-$MoS_2$ films. Finally, our systematic characterization studies enabled us to establish, for the first time, a fairly linear correlation between the detectivity of the PLD-$MoS_2$ films and their optical bandgap.

## II. Experimental

The $MoS_2$ films were simultaneously deposited onto both Si(100) and quartz substrates by using a GSI-Lumonics KrF excimer laser ($\lambda$ = 248 nm, pulse duration = 15 ns, repetition rate =20 Hz and pulse energy = 120 mJ) focused, at an incidence angle of 45°, on a 2"-diam. $MoS_2$ (99.995% purity) target inside a vacuum chamber. The on-target laser intensity is of ~$2.5 \times 10^8$ W/cm$^2$. The substrates were first cleaned by a standard cleaning procedure (acetone degreasing, isopropanol and de-ionized water cleaning, and N2 jet drying) and then loaded onto a rotating 3"-diameter substrate holder, which is placed parallel to the $MoS_2$ target at a distance of 7 cm. Prior to PLD deposition, the chamber was first pumped with a dry pump (to reach ~50 mTorr residual pressure) and then turbo-pumped down to ~$2 \times 10^{-5}$ Torr. During the deposition process, the $MoS_2$ target was rotated while the laser beam was laterally swept across its surface to ensure a uniform erosion pattern of the target. Concomitantly, the substrate holder was also rotated to achieve a uniform film deposition over all the 3"-daim area. Prior to each deposition, the $MoS_2$ target surface was *in-situ* cleaned by ablating its surface for 5 min while appropriately shielding the substrates holder from the laser ablation plume by a shutter placed close to the target. While all the PLD-$MoS_2$ thin films investigated in this paper were deposited at a fixed $N_{LP}$ of 7000 pulses (corresponding to a film thickness of ~90 nm), their deposition temperature ($T_d$) was systematically varied from 25°C to 700 °C. The morphology, micro/nano-structure and optoelectronic properties of the PLD-$MoS_2$ films were systematically characterized as a function of their $T_d$. First, the local structure of the PLD-$MoS_2$ films was investigated by using a micro-Raman (Renishaw) Spectrometer with the 532 nm excitation line. Their crystalline structure was characterized by x-ray diffraction using a PANalytical diffractometer (with an excitation wavelength of 1.5406 Å). The UV-Vis optical absorbance of the PLD-$MoS_2$ films was measured by using a Perkin-Elmer-Lambda-1050 spectrophotometer, while their thickness and surface morphology were characterized by using a Tescan-Vega3-LMH scanning electron microscopy (SEM) system. For the transmission electron microscopy (TEM) observations, a dual focused ion beam system Helios (Thermofisher Scientific™) was first employed to prepare cross-sectional thin lamellas of the PLD-$MoS_2$ films. The lamellas were prepared using a standard FIB lift-out technique. The TEM analyses of the samples were performed using an image Cs-corrected TEM system (Titan Thermofisher Scientific™) operating at 300 kV. The chemical bonding states of the PLD-$MoS_2$ films were characterized by means of X-ray photoelectron spectroscopy (XPS) using a PHI VersaProbe-III scanning XPS microprobe. A 15 KV electron gun was used in the XPS system to generate a monochromatic and micro-focused Al K-alpha X-ray source of 1486.6 eV. Thus, survey scans in the 0-1100 eV range, as well as high-resolution spectra of Mo and S core levels were acquired. The XPS spectra were calibrated using the C1s peak position reference at 284.6 eV, and peak fittings were performed with the CasaXPS program. The PLD-$MoS_2$ films deposited onto 1”x1” quartz substrates were integrated into photodetection (PD) devices by depositing on their top-surface a pattern of interdigitated Ag electrodes (~150 nm-thick) at room temperature, by means of a PLD process (ablation of a 2”-diam. silver target under a background pressure of $1.5 \times 10^{-5}$ Torr and a laser intensity of $3.5 \times 10^{8}$ W/$cm^{2}10^{8}$ with otherwise the same PLD conditions used for $MoS_2$ deposition). The current density-voltage (J–V) characteristics of these PD devices were acquired under both dark and UV lamp illumination conditions by means of a Keysight-B2901A presicision source/measure unit, while varying the applied voltage from – 1V to +1V. The effective surface of $MoS_2$ based photodetector devices was 1.32 $cm^2$. All the J-V measurements of the PLD-$MoS_2$ based PD devices were systematically carried out as a function of $T_d$, under ambient conditions.

## III. Results and discussion

Figure 1 shows typical SEM images of the PLD-$MoS_2$ films deposited onto silicon substrates at RT, 500°C, 600°C, and 700°C. While the films deposited at RT are seen to exhibit a very dense and smooth surface morphology, the films deposited at $T_d \geq 500°C$ were found to develop a very dense columnar growth. The domes of the $MoS_2$ columns grow in size (while remaining in the few 10s nm range) and contribute to increase the apparent nanoroughness of the film surface. By estimating the film thickness from SEM cross-section views, the deposition rate of the PLD-$MoS_2$ was found to be dependent on $T_d$, as it decreased from 0.0165 nm/pulse at RT, to 0.0133 nm/pulse at 500-600°C and 0.01 nm/pulse at 700°C. This deposition rate decrease (of ~39%) with $T_d$ is thought to result mainly from temperature induced crystallization and densification of the films, as it has been reported previously reported[26].

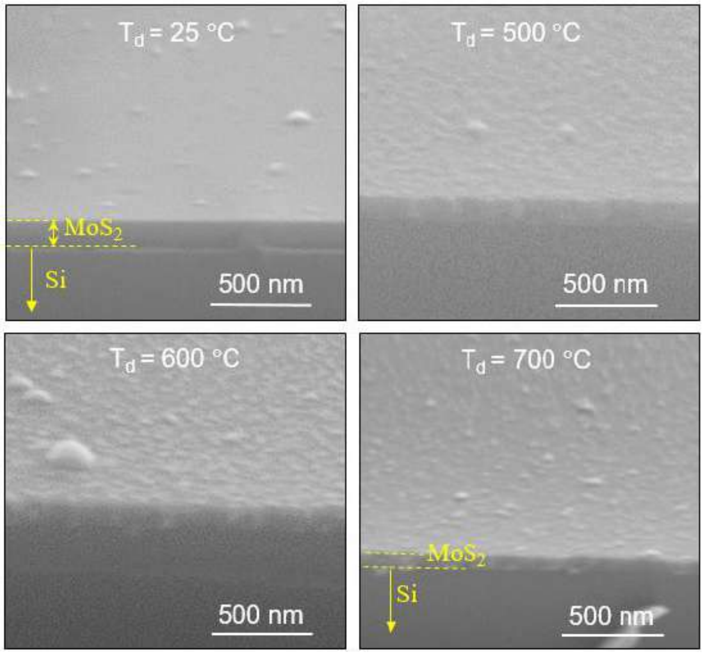

Figure 1: Typical SEM images of the PLD-$MoS_2$ films deposited onto silicon substrates at different $T_d$ (with a fixed $N_{LP} = 7000$).

The XRD spectra of these PLD-$MoS_2$ thin films deposited, as a function of their $T_d$, are shown in figure 2(a). At $T_d = 25°C$, the PLD-$MoS_2$ films are seen to exhibit a weak XRD signal with very broad diffraction peaks (at $2\theta = 14.03^o$ and $37.11^o$), indicating its rather poor crystallinity or amorphous state. By using the Sherrer formula[29], we estimated the size of the (002) $MoS_2$ crystallites to ~1.5 nm. This suggests that the films contain nanocrystals (nucleation seeds also revealed in the Raman spectrum) of $MoS_2$ embedded into an otherwise amorphous/disordered matrix. As $T_d$ is increased to 300°C and 400°C, the polycrystalline nature of the films progressively develops as the (002) and (100) XRD peaks of $MoS_2$ become more defined and their intensity increases. These peaks are the fingerprint of the hexagonal (2H) phase of $MoS_2$[30]. For higher $T_d$ ($\geq$ 500°C), the $MoS_2$ films become highly crystalline with a strong (002) preferential orientation.

To appreciate the $T_d$ favored crystallization of the PLD-$MoS_2$ films, we estimated[25] the size of the (002) $MoS_2$ crystallites and plotted it against $T_d$ in figure 2(b). The $MoS_2$ crystallite size is seen to increase slowly from 1.5 to 4 nm when $T_d$ is raised from RT to 500°C and then ramps up with a higher slope to reach ~12 nm at 700°C. This shows that there is a kink around $T_d$ = 500°C in the growth kinetics of the $MoS_2$ crystals. The $T_d$ increase was also found to be accompanied by a shift of the (002) peak position towards high 2θ values (from 2θ=12.66° to 14.02° when $T_d$ is raised from 300°C to 700°C). This is due to the compressive stress that develops in the $MoS_2$ films as their $T_d$ is increased, as recently reported in the case of atomic layer deposited $MoS_2$ films.[25] In fact, by using the formula reported in Ref. 27 and the recently reported value of thermal coefficient expansion (TCE) of few-layers $MoS_2$ (of ~ $0.5 \times 10^{-6}$ $K^{-1}$,[31] which happens to be quite lower than the TCE of silicon = $2.6 \times 10^{-6}$ $C^{-1}$), the increase of $T_d$ is expected to enhance the compressive stress component of the PLD-$MoS_2$ films. On the other hand, the FWHM of the $MoS_2$ (100) peak at 400°C is seen to be much larger than at $T_d$= 300°C. This could be due to the coexistence of both the 2H (100) peak along with the (100) peak of the tetragonal (1T) $MoS_2$ phase. Such an overlapping makes it difficult to single out the clear-cut presence of the 1T-$MoS_2$ phase. To investigate further the microstructure of our PLD-$MoS_2$ films, Raman spectroscopy is a very convenient technique which complements well the XRD analysis. Figure 2(c) shows the Raman spectra of the PLD-$MoS_2$ films as a function of their $T_d$. Interestingly, even for the PLD-$MoS_2$ films deposited at RT, the Raman fingerprint of 2H-$MoS_2$ phase represented by the $E^1_{2g}$ (due to the in-plane vibrations

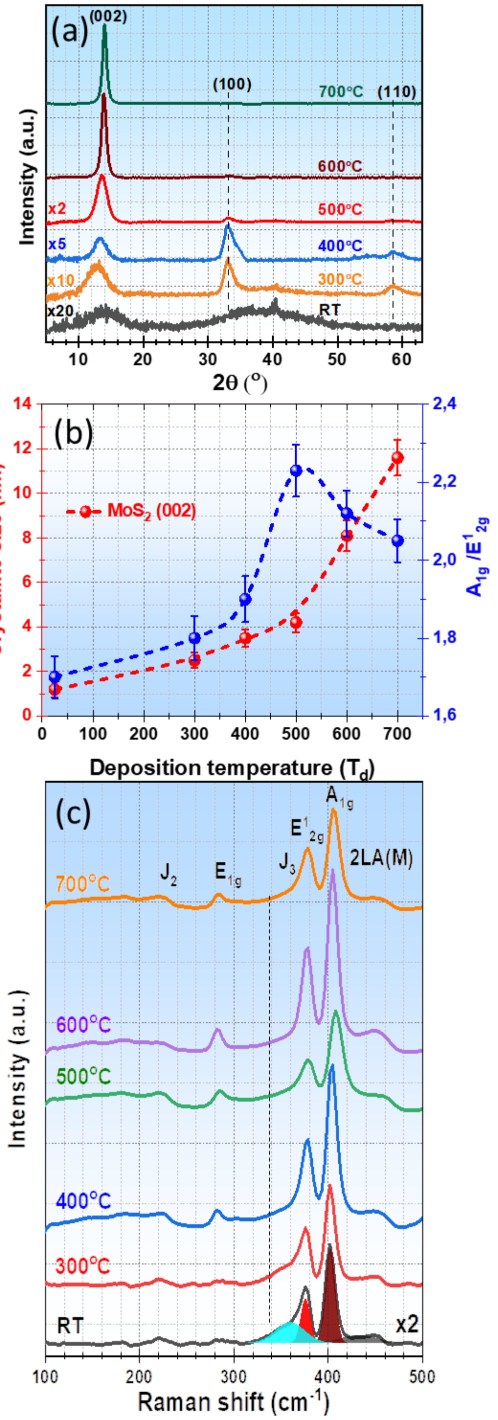

Figure 2: (a) XRD spectra, (b) crystallite size & $[A_{1g}]/[E^1_{2g}]$ ratio, (c) Raman spectra of PLD-$MoS_2$ films as a function of $T_d$.

of the S atoms) and the $A_{1g}$ (due to the out-of-plane vibration of the S atoms) is clearly observed[32]. This corroborates well with the presence of small $MoS_2$ nanodomains, as revealed by the XRD spectrum at RT. When $T_d$ is increased, the characteristic peaks of the 2H-$MoS_2$ phase (namely $E_{1g}$, $E^1_{2g}$, $A_{1g}$ and 2LA(M) appearing at 285, 378, 404, and 450 $cm^{-1}$, respectively) are seen to become narrow and more intense, because of the improved crystallinity of the films with $T_d$, in accordance with the above-discussed XRD results. Moreover, at RT, the $J_3$ peak (light blue component in the RT spectrum of Fig. 2(c)) appearing at 353 $cm^{-1}$ (which is associated with the 1T metallic phase) is seen to overlap with the $E^1_{2g}$ peak (at ~378 $cm^{-1}$, red component in the RT spectrum of Fig. 2(c)) but progressively vanishes with $T_d$ to completely disappear at $T_d \geq 500°C$, in agreement with the previous XRD results. On the other hand, one can notice that the ratio of the main $A_{1g}$ and $E^1_{2g}$ peaks representing the 2H-$MoS_2$ phase are changing with $T_d$. Thus, by plotting the $[A_{1g}]/[E^1_{2g}]$ peak intensity ratio of the PLD-$MoS_2$ films as a function of their $T_d$ (see figure 2(b)), it is found that that ratio reaches its maximum at $T_d$ = 500°C. The increase of the intensity ratio of the out-of-plane to the in-plane of S-atoms vibrations was associated with the vertical orientation of the $MoS_2$ monolayers[33]. These results suggest that our PLD-$MoS_2$ films deposited at the optimal temperature of 500°C exhibit a highly crystallized 2H phase with a tendency to have their $MoS_2$ monolayers vertically oriented. To ascertain the formation of such an original nanostructure in our PLD-$MoS_2$ films, we have performed high-resolution TEM (HRTEM) observations on the films deposited at the optimal $T_d$ of 500°C. Indeed, Figure 3(a) shows the HRTEM image of the PLD-$MoS_2$ films where the PLD-$MoS_2$ film is found to consist, at the interface with the Si-substrate of several horizontally-oriented (in-plane) $MoS_2$ monolayers, onto which vertically-oriented (out-of-

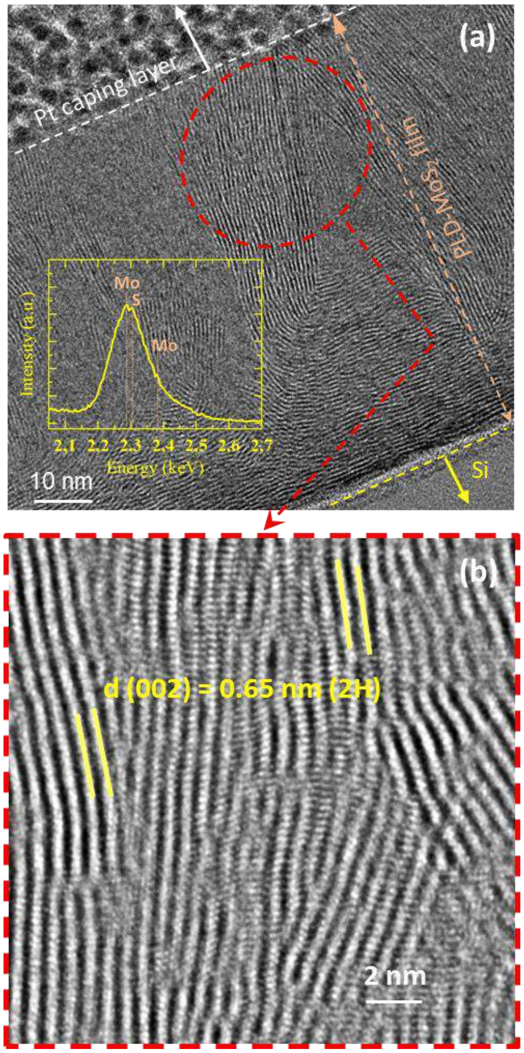

Figure 3: (a) Typical TEM image of the PLD-$MoS_2$ films deposited at $T_d$ = 500°C with its associated EDS spectrum (inset); (b) HRTEM image of the vertically aligned $MoS_2$ monolayers.

plane) $MoS_2$ layers grow all over the rest of the film thickness. Impressively, the quasi-totality of the film is found to be composed of large $MoS_2$ grains with their lattice fringes being perpendicular to the surface of the underlying silicon substrate. Some lattice twinning and dislocation are observed at the grains boundaries. This original nanostructure is thought to be due to the compressive stress of the PLD-$MoS_2$, as pointed out from the XRD analysis. This might be also caused by the supersaturated flux of ablated species which lead to an extremely high density of nucleation sites.[34] Thus, since the in-plane surface of the growing film is "crowded" by the $MoS_2$ grain seeds, the only available direction for them to grow and to relax, to a certain extent, their strain is the out-of-plane direction. This would explain the preferential vertical orientation of the MoS2 monolayers in the PLD-$MoS_2$ films. The higher magnification of the HRTEM image of Fig. 3(b) clearly reveals the vertical alignment of the $MoS_2$ lattice fringes with a spacing of 0.65 nm, which corresponds to the (002) planes of $MoS_2$, confirming thus the preferred orientation observed by XRD. The EDS spectrum (yellow line) superimposed on Fig. 3(a) confirms the presence of both Mo and S elements, but the overlapping of their X-ray emission peaks makes it difficult to determine precisely the local composition of the grains.

The XPS technique was also used to characterize the local bonding states of the PLD-$MoS_2$ films as a function of their $T_d$. Figure 4 shows the high-resolution XPS spectra of the Mo 3d and S 2s core levels at increasing $T_d$ values of 25, 400, 500 and 600°C. The films deposited at RT exhibited broad peaks for both Mo 3d and S2p core levels, indicating some local disordering and variability in the local bondings, consistent with the predominant amorphous structure revealed by XRD. As $T_d$ is increased, the FWHM of all the XPS core level peaks progressively decreases until it reaches its minimum value at $T_d = 500°C$ and then slightly increases for $T_d= 600°C$, as clearly shown in the inset of Fig. 4. This is indicative of significant improvement in the local ordering of the local chemical environments along with the highest crystallinity of the PLD-$MoS_2$ films deposited at $T_d = 500°C$, in agreement with the above-discussed XRD and Raman results (cf. Fig 2.). The high-resolution spectrum of Mo 3d is clearly seen to comprise four distinct components. The weakest Mo 3d peak centered around 235.4 eV is attributed to the $Mo^{6+}$ state of Mo in some surface oxides[35] (likely due to some surface oxidation of the samples as they were continuously exposed to air once they were taken out from the PLD vacuum chamber). The two prominent peaks (appearing at 228.8 and 232.1 eV) are attributed to the Mo $3d_{5/2}$ and Mo $3d_{3/2}$ doublet, respectively,[36] which are due to the predominant $Mo^{4+}$ in the $MoS_2$ structure. Finally, the

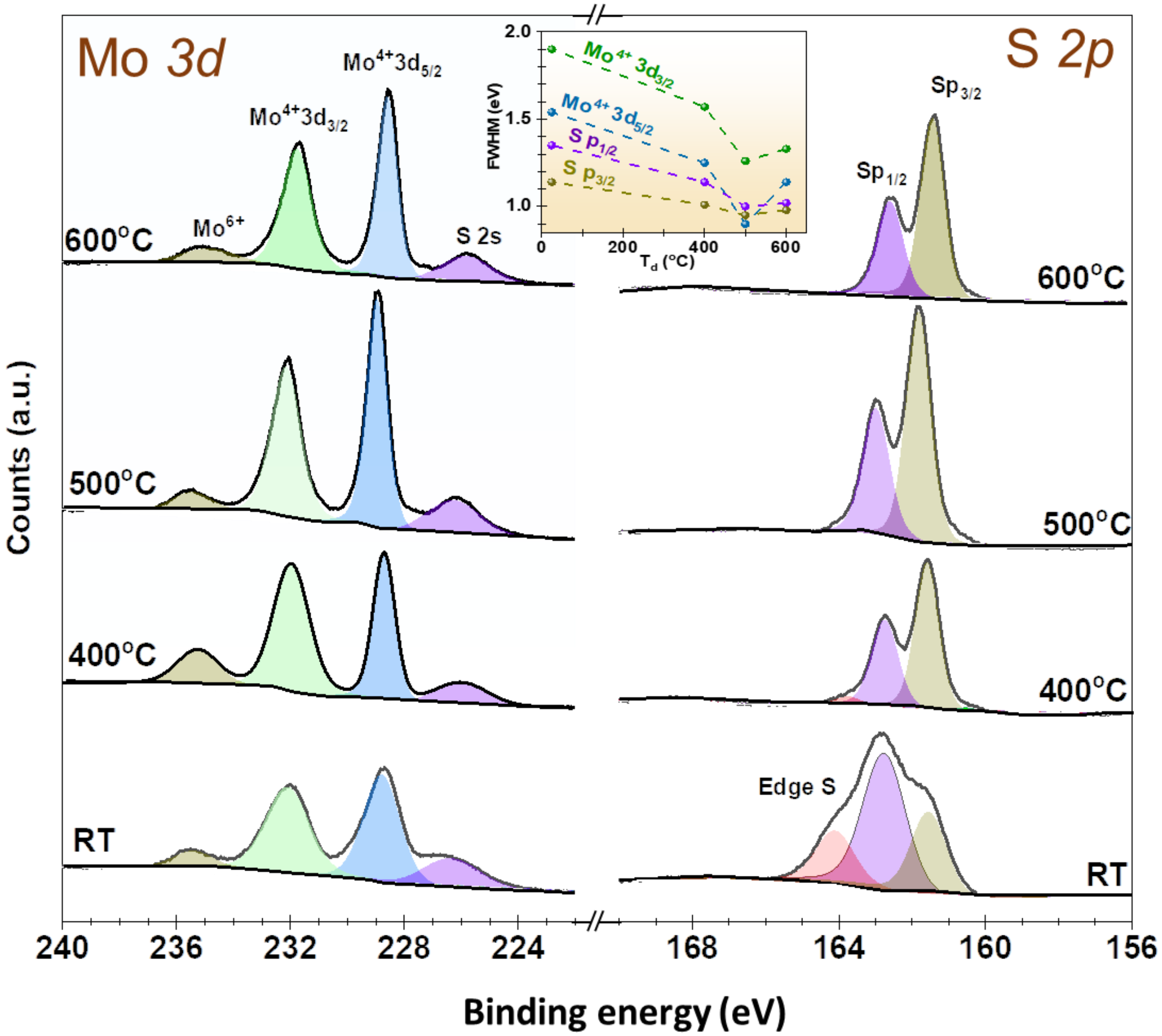

Figure 4: X photoelectron spectroscopy core-level spectra of Mo 3d and S 2p of the PLD-MoS$_2$ films deposited at T$_d$ = RT, 400°C, 500°C, and 600°C.

neighboring peak appearing at 226.4 eV is due to the S 2s states[37]. On the other hand, the high resolution spectrum of the S 2p core level of the films deposited at RT is found to consist of three overlapping components at 161.2, 162.8, and 164.1 eV binding energies. Those peaks are attributed to the S 2p$_{3/2}$, S 2p$_{1/2}$, (S$^{2-}$ in the MoS$_2$ structure)[38] and Edge S (which is generally associated with amorphous and/or defective MoS$_2$ strutures[39]), respectively. When T$_d$ is increased (from RT to 500$^o$C), both Mo 3d and S 2p core levels showed a shift of ~1 and ~0.4 eV towards higher binding energies. This is thought to reflect the crystallinity improvement, hence better local environments ordering, of the films at the optimal T$_d$ of 500°C. However, when T$_d$ is further increased from 500$^o$C to 600$^o$C, the Mo 3d and S 2p peaks shift back by 0.5 and 0.4 eV, respectively, toward lower energy values This might be associated with some local changes in the vertical alignment of $MoS_2$ monolayers (as suggested by Raman analyses in Fig. 2(b)), which causes steric hindrance and/or distortions of Mo-S bonds, lowering thereby the binding energy. Finally, one can note the complete disappearance of the Edge-S peak for $T_d \geq 500^oC$, which is consistent with the improvement of long-range ordering in the $MoS_2$ films.[40]

Figure 5(a) shows the optical transmittance spectra, over the 400–1400 nm wavelength range, of the PLD-$MoS_2$ films deposited on transparent quartz substrates a different $T_d$ ranging RT to 700°C. While the PLD-$MoS_2$ films have comparable thicknesses, their optical absorbance and particularly their onset absorption wavelength are seen to be $T_d$ dependent. To estimate the optical bandgap ($E_g$) of the PLD-$MoS_2$ films, we first calculated the absorption coefficient (α) of the PLD-$MoS_2$ films using the equation $\alpha(\lambda) = \frac{1}{f}\ln\left[\frac{1}{T}(\lambda)\right]$, where $f$ is the film thickness of $MoS_2$ and T (λ) is the transmittance at a given wavelength λ. The calculated values were of $\sim 1\text{x}10^5$ $cm^{-1}$ (for $\lambda \geq 800$ nm) and reach much higher values for shorter wavelengths (up to $\sim 9\text{x}10^5$ $cm^{-1}$ at λ = 450 nm). This confirms the very high absorption capacity of our PLD-$MoS_2$ films, in accordance with literature.[32, 32a]. From the absorption coefficient data, Eg was calculated using the Tauc formula:[42] $(\alpha h\nu)^n = A(h\nu - E_g)^n$, where hν is photon energy and A is a constant. We used n = 2 for the direct bandgap transition. This choice was based on the HR-TEM revealed vertical alignment of the $MoS_2$ monolayers in our films which bodes well with the photoluminescence (not shown here) exhibited by our samples. Thus, the Tauc plots (illustrated in the inset of Fig. 5(a)) enables us to extract the $E_g$ values of the PLD-$MoS_2$ films for each $T_d$ condition. Figure 5(b) shows the $T_d$ dependence of the optical bandgap of the PLD-$MoS_2$ films. It is found that the $E_g$ of the PLD-MoS2 films slightly decreases from 1.7 to 1.65 eV, when $T_d$ is raised from RT to 400°C, then significantly drops to ~1.4 eV at $T_d$ = 500°C before rising again towards to a value of 1.55 eV at $T_d$ = 700°C. Similar

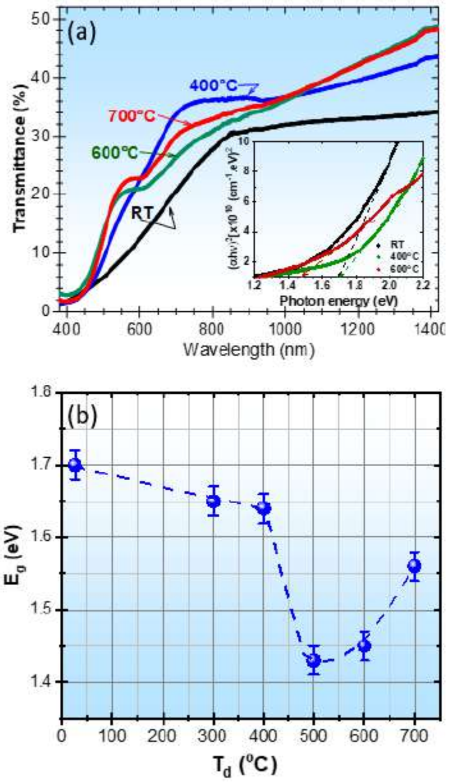

Figure 5: (a) UV-Vis transmittance spectra of the PLD-$MoS_2$ films as a function of their $T_d$. The inset shows their corresponding Tauc plots; (b) $T_d$ dependence of their optical bandgap.

direct optical $E_g$ values (in the 1.3-1.8 eV range) were scatteredely reported for $MoS_2$ films grown by different methods,[43–45] but no systematic $T_d$ dependence of $E_g$ (as in Fig. 5(b)) has been documented so far. This $E_g$ variation is definitely dictated by the crystallinity and the nanostructural arrangement of our PLD-$MoS_2$ films. The fact that $E_g$ is at its lowest value at the optimal $T_d$ condition of 500°C at which the $[A_{1g}]/[E^1_{2g}]$ ratio (in Raman spectra) reaches its maximum, suggests that the degree of vertical orientation of the $MoS_2$ layers along with the associated strain generated in the $MoS_2$ lattice are highly likely responsible for the bandgap narrowing observed at $T_d$=500°C (strikingly, the $E_g$ variation curve of Fig. 5b is almost the inverted image of the $T_d$-dependence of the $[A_{1g}]/[E^1_{2g}]$ ratio of Fig. 2(b)). Even if a clear-cut explanation of the observed bandgap narrowing can not be offered at this point, it is conjectured that the maximum of vertical orientation occurring at $T_d$ = 500C is accompanied with structural defects and dislocations (as revealed by HRTEM imaging) that populate the gap with intermediate levels leading to an apparent narrowing of the gap. As $T_d$ is further increased, some of the strain in the $MoS_2$ nanostruture is released and part of the structural defects are healed, which would open back the bandgap. Again, $T_d$= 500°C stands out as the deposition temperature that yields PLD-$MoS_2$ films with the narrowest bandgap. This will prove to be very interesting for photodetection application, as it is shown hereafter.

By integrating the PLD-$MoS_2$ films into photodetection (PD) functional devices (see their actual photo in the inset of Fig. 6(a)), we were able to assess their photodetection properties as a function of their $T_d$. Figure 6(a) shows typical J-V curves (under dark and UV-lamp illumination) for the PDs fabricated with PLD-$MoS_2$ films deposited at $T_d$ = 500°C. This sample is seen to generate a relatively high photocurrent density ($J_{Ph}$) of ~4.3 mA.cm$^{-2}$ with an applied voltage as low as 1V. This clearly shows the very high photosensitivity of our PLD-$MoS_2$ films. By comparing the $J_{Ph}$ ($J_{Ph} = J_{light} - J_{dark}$) of all samples, as a function of their $T_d$, Fig. 6(b) shows that the generated photocurrent density (black curve) is strongly sensitive to $T_d$, with a bell shape dependence. Indeed, while the films deposited at RT generated a $J_{Ph}$ of only 0.1 mA.cm$^{-2}$, those deposited at 500-600°C yielded the highest $J_{Ph}$ values of ~4.3 mA.cm$^{-2}$. When $T_d$ is further increased towards 700°C, $J_{Ph}$ drops back to ~1.95 mA.cm$^{-2}$. To better qualify the photodetection performance of our devices, we have calculated their associated photoresponse ($Ph_r$) by using the following formula: $Ph_r\,\% = 100 * \frac{I_{Light} - I_{Dark}}{I_{Dark}}$, where $I_{Dark}$ and $I_{Light}$ are the current measured under dark and illumination

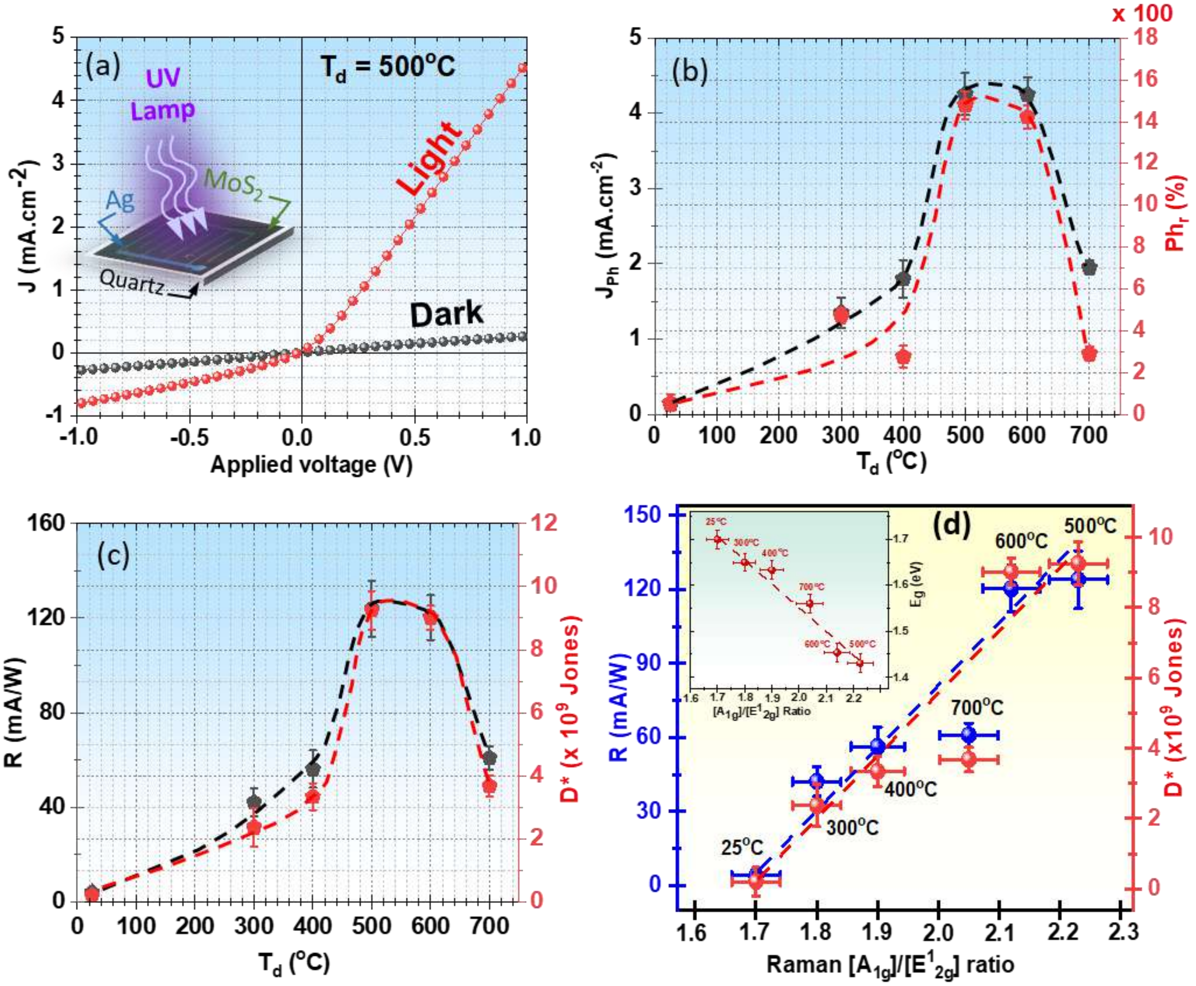

Figure 6: (a) Typical J-V curves (under light and UV lamp illumination) of our PLD-MoS$_2$ based PDs (deposited at T$_d$ = 500°C; (b) T$_d$ dependence of both J$_{Ph}$ and Ph$_r$; of the PLD-MoS$_2$ films based PDs; (c) their corresponding R and D* variations as a function of T$_d$; (d) Constant-plus-linear correlation between both R and D* of the PLD-MoS$_2$ films and their Raman [A$_{1g}$]/[E$^1_{2g}$] peak intensity ratio; The inset of (d) shows a linear dependence of the optical bandgap of the PLD-MoS$_2$ films upon the [A$_{1g}$]/[E$^1_{2g}$] ratio.

conditions, respectively. Figure 6(b) depicts the variation of the Ph$_r$ of all the devices as a function of their T$_d$ (red curve). The shape of the T$_d$ dependence of Ph$_r$ is quite similar to that of J$_{Ph}$. It is found that the photoresponse of the PLD-MoS$_2$ films markedly increases from ~55% (for T$_d$ = RT) to reach a value as high as ~1500% for the optimal T$_d$ of 500°C, after which it starts decreasing to reach ~300% at T$_d$ = 700°C. Besides, responsivity (R) and specific detectivity (D*) are significant metrics to qualify the photodetection performance of MoS$_2$ based photodetectors. Thus, R and D* are calculated by using the two following formulas:[Refs] $\mathrm{R} = \frac{\mathrm{I_{Ph}}}{\mathrm{P.S}}$, and $\mathrm{D}^* = \frac{\mathrm{R}}{\sqrt{2\mathrm{qI_{Dark}}}}$; where P is the power density of the incident light, S is the effective illuminated surface, q is the electron charge ($1.6 \times 10^{-19}$ Coulombs), R units are A/W, while D* is expressed in Jones units. Figure 6(c) shows the R and D* variations of the PLD-$MoS_2$ films as a function of their $T_d$. Consistently, the PLD-ddMoS$_2$ films deposited at $T_d$ = 500-600°C are shown to exhibit the highest R and D* values of 125 mA/W and 9.2 x $10^9$ Jones, respectively. While being aware of the difficulty of comparing the performance of different photodetectors developed in different ways and assessed under variable illumination conditions, the fact remains that an overview of the literature of PDs (exploiting the photoconductivity of $MoS_2$ at an applied voltage of 1V and having a surface area of ~1cm$^2$) shows that the R and D* values of the present work are among the highest values reported so far (see Table 1). This clearly highlights the outstanding photodetection performance of our vertically-aligned-PLD-$MoS_2$ films.

| PD device structure | Preparation technique of $MoS_2$ | Detection area (cm$^2$) | Applied voltage (V) | R (mA/W) | D* ($10^9$ Jones) | Refs. |
|---|---|---|---|---|---|---|
| $MoS_2$/p-Si | PLD | 1.32 cm$^2$ | 1 | 120 | 9.2 | This work |
| $MoS_2$/ZnS | Hydrothermal | 1 | 1 | 0.17 | - | [46] |
| $MoS_2$/SnS | Sputtering | ~1 | 1 | 2.4 | 0.057 | [47] |
| $MoS_2$ | PLD | 0.2 | 10 | 21.8 | - | [48] |
| $MoS_2$/Quartz | PLD | - | 10 | 50.7 | 1.55 | [6] |
| $MoS_2$/$MoO_2$ | CVD | 0.075 | 1 | 1.14 | 2.6 | [49] |
| $MoS_2$/ Perovskite | Exfoliation | 0.09 | 1 | 0.977 | 0.69 | [50] |
| $MoS_2$/Au nanoparticles | Hydrothermal | 0.36 | 2V | 99.3 | - | [51] |

Table 1: Comparison of the photodetection performance of various $MoS_2$ based photodetectors the $MoS_2$ films were prepared with various preparation techniques.

Figure 6(c) shows that by raising $T_d$ from RT to 500°C, both R and D* of the PLD-$MoS_2$ based PDs increased 30-fold and ~50-fold, respectively, demonstrating that the higher crystallinity along with the vertical orientation of the $MoS_2$ monolayers are key for not only the effective absorption of light but also for charges photogeneration and their efficient transfer to the metallic electrodes. By comparing the $T_d$ dependence of R and D*, on one hand (see Figs. 6(c)), and that of the Raman $[A_{1g}]/[E^1_{2g}]$ ratio and $E_g$ on the other hand and (see Figs. 2(b) and 5(b), respectively) it strikingly appears that all those variations follow the same "bell-shape" trend (or its reverse), suggesting a strong correlation between these variables. To better evidence such a correlation, we have cross-plotted R and D* against the Raman [$A_{1g}$]/[$E^1_{2g}$] ratio in Figure 6(d). Thus, a constant-plus-linear relationship is established between R (or D*) and the [$A_{1g}$]/[$E^1_{2g}$] ratio. This clearly demonstrates, for the time, that the photodection performance (R and D*) of the PLD-$MoS_2$ films linearly scales with the degree of vertical orientation of the $MoS_2$ monolayers in the films. On the other hand, the optical bandgap of the PLD-$MoS_2$ films is also found to decrease linearly with their Raman-[$A_{1g}$]/[$E^1_{2g}$] ratio (see the inset of Fig. 6(d)). As above-discussed, a high degree of vertical alignment of the $MoS_2$ monolayers inside the films along with its accompanying strain and structural defects affect the electronic structure (e.g. $E_g$) of the PLD-MoS2 films, which in turn influences their photon absorption capacity and hence their photodetection performance. It is therefore concluded that the ability to control the vertical alignment of $MoS_2$ monolayers has the potential to disrupt the integration of relatively thick "3D"-$MoS_2$ films into advanced optoelectronic devices by using the PLD technique.

## IV. Conclusion

We have achieved a successful and systematic study of the effect of the deposition temperature on the structure, optoelectronic and photodetection properties of $MoS_2$ thin films deposited by PLD. Thus, by varying $T_d$ from 25°C to 700°C, we were able to point up $T_d$ = 500°C, as the optimal deposition temperature that yields $MoS_2$ films exhibiting a combination of highly attractive structural and optoelectronic properties. For instance, the PLD-$MoS_2$ films deposited at 500°C are found to exhibit a very high crystalline structure of the 2H-$MoS_2$ phase with a strong (002) preferential orientation and an average crystallite size of ~4nm. Moreover, those PLD-$MoS_2$ films were found to exhibit the narrowest optical bandgap of ~1.4 eV, and most interestingly an impressive nanostructure which consists of vertically aligned $MoS_2$ monolayers across all over the ~90 nm film thickness, as revealed by HRTEM images. On the other hand, by integrating systematically the PLD-$MoS_2$ films into functional devices, their photodetection properties were assessed as a function of their $T_d$. We were thus able to show their photoresponse is highly dependent on their deposition temperature. Our results show that the highest photodetection performance of our PLD-$MoS_2$ films is achieved at the optimal $T_d$ of 500°C, with remarkable R and D* values as high as 125 mA/W and $9.2 \times 10^9$ Jones, respectively. By noting the striking similarity of the $T_d$ dependence of R, D*, on one hand, and $E_g$ and Raman-[$A_{1g}$]/[$E^1_{2g}$] ratio, on the other hand, we were able to establish, for the first time, a constant-plus-linear correlation between

R and D* and the degree of vertical alignment of the $MoS_2$ monolayers inside the PLD-$MoS_2$ films. It is concluded that controlling the vertical alignment (as demonstrated here via $T_d$ optimization) is key to tune the optoelectronic properties of PLD-$MoS_2$ films. Finally, this work demonstrates that the PLD technique enables the growth of "3D"-$MoS_2$ films exhibiting excellent optoelectronic properties and can foster their integration into devices by using standard VLSI processing.

## Acknowledgement

The authors acknowledge the financial support provided by the Natural Sciences and Engineering Research Council (NSERC) of Canada and by the Region of Haut-De-France (HDF).

## References

[1] J. S. Ponraj, Z. Q. Xu, S. C. Dhanabalan, H. Mu, Y. Wang, J. Yuan, P. Li, S. Thakur, M. Ashrafi, K. McCoubrey, Y. Zhang, S. Li, H. Zhang, Q. Bao, *Nanotechnology* **2016**, *27*, 462001.

[2] D. Mouloua, A. Kotbi, G. Deokar, K. Kaja, M. EL Marssi, M. A. El Khakani, M. Jouiad, *Materials (Basel).* **2021**, *14*, 3283.

[3] B. Radisavljevic, A. Radenovic, J. Brivio, V. Giacometti, A. Kis, *Nat. Nanotechnol.* **2011**, *6*, 147.

[4] S. Wang, H. Yu, H. Zhang, A. Wang, M. Zhao, Y. Chen, L. Mei, J. Wang, *Adv. Mater.* **2014**, *26*, 3538.

[5] A. Taffelli, S. Dirè, A. Quaranta, L. Pancheri, *Sensors* **2021**, *21*, 2758.

[6] Y. Xie, B. Zhang, S. Wang, D. Wang, A. Wang, Z. Wang, H. Yu, H. Zhang, Y. Chen, M. Zhao, B. Huang, L. Mei, J. Wang, *Adv. Mater.* **2017**, *29*, 1605972.

[7] J. Sun, X. Li, W. Guo, M. Zhao, X. Fan, Y. Dong, C. Xu, J. Deng, Y. Fu, *Crystals* **2017**, *7*, 198.

[8] O. Lopez-Sanchez, D. Lembke, M. Kayci, A. Radenovic, A. Kis, *Nat. Nanotechnol.* **2013**, *8*, 497.

[9] R. Mas-Ballesté, C. Gómez-Navarro, J. Gómez-Herrero, F. Zamora, *Nanoscale* **2011**, *3*, 20.

[10] G. Eda, H. Yamaguchi, D. Voiry, T. Fujita, M. Chen, M. Chhowalla, *Nano Lett.* **2011**, *11*, 5111.

[11] X. Fan, P. Xu, D. Zhou, Y. Sun, Y. C. Li, M. A. T. Nguyen, M. Terrones, T. E. Mallouk, *Nano Lett.* **2015**, *15*, 5956.

[12] D. Mouloua, N. S. Rajput, S. Saitzek, K. Kaja, K. Hoummada, M. El Marssi, M. A. El Khakani, M. Jouiad, *Sci. Rep.* **2022**, *12*, 1.

[13] G. Deokar, N. S. Rajput, J. Li, F. L. Deepak, W. Ou-Yang, N. Reckinger, C. Bittencourt, J. F. Colomer, M. Jouiad, *Beilstein J. Nanotechnol.* **2018**, *9*, 1686.

[14] W. Zhao, X. Liu, X. Yang, C. Liu, X. Qian, T. Sun, W. Chang, J. Zhang, Z. Chen, *Nanomaterials* **2020**, *10*, 1.

[15] D. Mouloua, M. Lejeune, N. S. Rajput, K. Kaja, M. El Marssi, M. A. El Khakani, M. Jouiad, *Ultrason. Sonochem.* **2023**, *95*, 106381.

[16] Z. O. Elhmaidi, R. Pandiyan, M. Abd-Lefdil, E. Saucedo, M. A. El Khakani, *Appl. Surf. Sci.* **2020**, *507*, 145003.

[17] D. Brassard, M. A. El Khakani, *J. Appl. Phys.* **2005**, *98*, 054912.

[18] M. A. El Khakani, M. Chaker, *Thin Solid Films* **1998**, *335*, 6.

[19] M. A. El Khakani, B. Le Drogoff, M. Chaker, *J. Mater. Res.* **1999**, *14*, 3241.

[20] F. Tumino, C. S. Casari, M. Passoni, V. Russo, A. Li Bassi, *Nanoscale Adv.* **2019**, *1*, 643.

[21] R. Dolbec, E. Irissou, M. Chaker, D. Guay, F. Rosei, M. A. El Khakani, *Phys. Rev. B - Condens. Matter Mater. Phys.* **2004**, *70*, 1.

[22] I. Ka, V. Le Borgne, K. Fujisawa, T. Hayashi, Y. A. Kim, M. Endo, D. Ma, M. A. El Khakani, *Sci. Rep.* **2016**, *6*, 1.

[23] Z. Hamoudi, M. A. El Khakani, M. Mohamedi, *Int. J. Electrochem. Sci.* **2012**, *7*, 1666.

[24] A. Barvat, N. Prakash, D. K. Singh, A. Dogra, S. P. Khanna, S. Singh, P. Pal, *Mater. Today Proc.* **2018**, *5*, 2241.

[25] A. Sharma, M. A. Verheijen, L. Wu, S. Karwal, V. Vandalon, H. C. M. Knoops, R. S. Sundaram, J. P. Hofmann, W. M. M. Kessels, A. A. Bol, *Nanoscale* **2018**, *10*, 8615.

[26] M. I. Serna, S. H. Yoo, S. Moreno, Y. Xi, J. P. Oviedo, H. Choi, H. N. Alshareef, M. J. Kim, M. Minary-Jolandan, M. A. Quevedo-Lopez, *ACS Nano* **2016**, *10*, 6054.

[27] G. Siegel, Y. P. Venkata Subbaiah, M. C. Prestgard, A. Tiwari, *APL Mater.* **2015**, *3*, 056103.

[28] S. Kumar, A. Sharma, Y. T. Ho, A. Pandey, M. Tomar, A. K. Kapoor, E. Y. Chang, V. Gupta, *J. Alloys Compd.* **2020**, *835*, 155222.

[29] G. Pradhan, A. K. Sharma, *Mater. Res. Bull.* **2018**, *102*, 406.

[30] M. R. Saber, G. Khabiri, A. A. Maarouf, M. Ulbricht, A. S. G. Khalil, *RSC Adv.* **2018**, *8*, 26364.

[31] Z. Lin, W. Liu, S. Tian, K. Zhu, Y. Huang, Y. Yang, *Sci. Rep.* **2021**, *11*, 1.

[32] B. Gao, X. Zhang, *South African J. Chem.* **2014**, *67*, 6.

[33] H. P. Chang, M. Hofmann, Y. P. Hsieh, Y. S. Chen, J. G. Lin, *RSC Adv.* **2021**, *11*, 34269.

[34] S. Metev, K. Meteva, *Appl. Surf. Sci.* **1989**, *43*, 402.

[35] S. Kang, Y. S. Kim, J. H. Jeong, J. Kwon, J. H. Kim, Y. Jung, J. C. Kim, B. Kim, S. H. Bae, P. Y. Huang, J. C. Hone, H. Y. Jeong, J. W. Park, C. H. Lee, G. H. Lee, *ACS Appl. Mater. Interfaces* **2021**, *13*, 1245.

[36] S. Erfanifam, S. M. Mohseni, L. Jamilpanah, M. Mohammadbeigi, P. Sangpour, S. A. Hosseini, A. Iraji Zad, *Mater. Des.* **2017**, *122*, 220.

[37] H. Nan, Z. Wang, W. Wang, Z. Liang, Y. Lu, Q. Chen, D. He, P. Tan, F. Miao, X. Wang, J. Wang, Z. Ni, *ACS Nano* **2014**, *8*, 5738.

[38] Y. Xue, Y. Zhang, Y. Liu, H. Liu, J. Song, J. Sophia, J. Liu, Z. Xu, Q. Xu, Z. Wang, J. Zheng, Y. Liu, S. Li, Q. Bao, *ACS Nano* **2016**, *10*, 573.

[39] C. Zhang, Z. Wang, S. Bhoyate, T. Morey, B. Neria, V. Vasiraju, G. Gupta, S. Palchoudhury, P. Kahol, S. Mishra, F. Perez, R. Gupta, *C* **2017**, *3*, 33.

[40] C. Backes, R. J. Smith, N. McEvoy, N. C. Berner, D. McCloskey, H. C. Nerl, A. O'Neill, P. J. King, T. Higgins, D. Hanlon, N. Scheuschner, J. Maultzsch, L. Houben, G. S. Duesberg, J. F. Donegan, V. Nicolosi, J. N. Coleman, *Nat. Commun.* **2014**, *5*, 1.

[41] Y. Li, J. Liu, X. Zhao, X. Yuan, G. Hu, X. Yuan, J. Ren, *RSC Adv.* **2020**, *10*, 25136.

[42] M. T. L. Lai, K. M. Lee, T. C. K. Yang, G. T. Pan, C. W. Lai, C. Y. Chen, M. R. Johan, J. C. Juan, *Nanoscale Adv.* **2021**, *3*, 1106.

[43] N. Barreau, J. C. Bernède, *J. Phys. D. Appl. Phys.* **2002**, *35*, 1197.

[44] Q. Deng, Y. Li, Y. Shen, L. Chen, G. Wang, S. Wang, *Mod. Phys. Lett. B* **2017**, *31*, 1750079.

[45] C. H. Chang, X. Fan, S. H. Lin, J. L. Kuo, *Phys. Rev. B - Condens. Matter Mater. Phys.* **2013**, *88*, 1.

[46] P. T. Gomathi, P. Sahatiya, S. Badhulika, *Adv. Funct. Mater.* **2017**, *27*, 1701611.

[47] H. Yu, Y. Xie, J. Wei, P. Zhang, Z. Cui, *Adv. Mater. Interfaces* **2022**, *2200896*, 1.

[48] Y. Xie, F. Liang, D. Wang, S. Chi, H. Yu, Z. Lin, H. Zhang, Y. Chen, J. Wang, Y. Wu, *Adv. Mater.* **2018**, *30*, 2.

[49] D. Mouloua, N. S. Rajput, J.-F. Blach, M. Lejeune, M. El Marssi, M. A. El Khakani, M. Jouiad, *Mater. Sci. Eng. B* **2022**, *286*, 116035.

[50] R. M. Ansari, A. D. Salunke, M. Rahil, S. Ahmad, *Adv. Mater. Interfaces* **2023**, *10*, 2202170.

[51] V. Selamneni, H. Raghavan, A. Hazra, P. Sahatiya, *Adv. Mater. Interfaces* **2021**, *8*, 1.

# Article 5: D. Mouloua, M. Lejeune, N. S. Rajput, K. Kaja, M. El Marssi, M. A. El Khakani, M. Jouiad, Ultrason. Sonochem. 2023, 95, 106381.

Ultrasonics Sonochemistry 95 (2023) 106381

Contents lists available at ScienceDirect

Ultrasonics Sonochemistry

journal homepage: www.elsevier.com/locate/ultson

# One-step chemically vapor deposited hybrid 1T-$MoS_2$/2H-$MoS_2$ heterostructures towards methylene blue photodegradation

D. Mouloua[a,b], M. Lejeune[a], N.S. Rajput[c], K. Kaja[d], M. El Marssi[a], M.A. El Khakani[b,*], M. Jouiad[a,*]

[a] Laboratory of Physics of Condensed Matter, University of Picardie Jules Verne, Scientific Pole, 33 rue Saint-Leu, 80039 Amiens Cedex 1, France
[b] Institut National de la Recherche Scientifique, Centre-Énergie, Matériaux et Télécommunications, 1650, Blvd, Lionel–Boulet, Varennes, QC J3X-1P7, Canada
[c] Advanced Materials Research Center, Technology Innovation Institute, P.O. Box 9639, Abu Dhabi, United Arab Emirates
[d] Laboratoire National de métrologie et d'essais (LNE), 29 av. Roger Hennequin, 78197 Trappes, France

## ARTICLE INFO

*Keywords:*
1T-$MoS_2$/2H-$MoS_2$
Chemical vapour deposition
Photocatalysis
Methylene blue

## ABSTRACT

The photocatalytic degradation of methylene blue is a straightforward and cost-effective solution for water decontamination. Although many materials have been reported so far for this purpose, the proposed solutions inflicted high fabrication costs and low efficiencies. Here, we report on the synthesis of tetragonal (1T) and hexagonal (2H) mixed molybdenum disulfide ($MoS_2$) heterostructures for an improved photocatalytic degradation efficiency by means of a single-step chemical vapor deposition (CVD) technique. We demonstrate that the 1T-$MoS_2$/2H-$MoS_2$ heterostructures exhibited a narrow bandgap ~ 1.7 eV, and a very low reflectance (<5%) under visible-light, owing to their particular vertical micro-flower-like structure. We exfoliated the CVD-synthesised 1T-$MoS_2$/2H-$MoS_2$ films to assess their photodegradation properties towards the standard methylene blue dye. Our results showed that the photo-degradation rate-constant of the 1T-$MoS_2$/2H-$MoS_2$ heterostructures is much greater under UV excitation (i.e., $12.5 \times 10^{-3}$ $min^{-1}$) than under visible light illumination (i.e., $9.2 \times 10^{-3}$ $min^{-1}$). Our findings suggested that the intermixing of the conductive 1T-$MoS_2$ with the semiconducting 2H-$MoS_2$ phases favors the photogeneration of electron-hole pairs. More importantly, it promotes a higher efficient charge transfer, which accelerates the methylene blue photodegradation process.

## 1. Introduction

In the context of global warming and water scarcity, the contamination of drinking water has become one of the societies' most serious pollution issues. The massive growth of industries and pharmaceutical disposals discharging organic dyes into the environment has largely contributed to this global issue, which has an adverse impact on the human ecosystem, including the public health and the living conditions of other organisms [1]. Recent public awareness campaigns have prompted scientists to develop eco-friendly and cost-effective pollution remediation solutions to combat the generated pollution harm to the aquatic environment [2–5]. For instance, the organic compound methylene blue (MB), commonly used for dying fabrics is well-known for its toxicity, causing diarrhea, vomiting, and serious allergic reactions [6]. Thus, textile industrial effluents are now subjected to strict treatment measures before releasing their wastewater into the environment [7]. Meanwhile, the photocatalytic degradation (PD) is one of the most straightforward and cost-effective solutions for MB water decontamination [8–11], leveraging the use of solar energy as a renewable energy-source supply [12]. Although numerous materials have been used so far for the PD of MB [13], the majority of the proposed solution relied on complex heterostructure-based devices, leading to costly PD processes

---

*Abbreviations:* MB, Methyl blue; PD, Photodegradation; 2D, Two dimensional; CVD, Chemical vapor deposition; 1T-MoS2, 1-tetragonal molybdenum disulfide; 2H-MoS2, 2-hexagonal molybdenum disulfide; UV, Ultraviolet; SEM, Scanning electron microscopy; TEM, transmission electron microscopy; EDS, Energy dispersive spectroscopy; HRTEM, High resolution transmission electron microscopy; XRD, X-ray diffraction; XPS, X-ray photoelectron spectroscopy; PL, Photoluminescence; $J_{Ph}$, Photocurrent density; $C_0$, Initial concentration in dark; C, Actual concentration during the photodegradation; η, Degradation efficiency; $\eta_{UV}$, Degradation efficiency under UV illumination; $\eta_{Vis}$, Degradation efficiency under visible illumination; k, Photodegradation rate constant; $k_{UV}$, Photodegradation rate constant under UV illumination; $K_{Vis}$, Photodegradation rate constant under visible illumination; VB, Valence band; CB, Conduction band.

* Corresponding authors.

*E-mail addresses:* m.a.elkhakani@inrs.ca (M.A. El Khakani), mustapha.jouiad@u-picardie.fr (M. Jouiad).

https://doi.org/10.1016/j.ultsonch.2023.106381
Received 31 January 2023; Received in revised form 11 March 2023; Accepted 22 March 2023

with no effective improvement in efficiency. Recently, molybdenum disulfide ($MoS_2$) nanostructures and two-dimensional (2D) layers have sparked a growing interest in scientific and industrial fields due to their unique physicochemical properties [14–16], with numerous applications including photocatalysis [17,18], dye-sensitized solar cells [19], and sensing [20,21]. Layered $MoS_2$ exists in three polymorphic crystal lattices: 1T-$MoS_2$ (tetragonal), where the $MoS_2$ behaves as a metal, and two semiconducting phases, namely the 2H-$MoS_2$ (hexagonal) and the 3R-$MoS_2$ (rhombohedral). A recent focus has been made on tuning the bandgap in 2D-$MoS_2$ by controlling the growth parameters in chemical vapor deposition (CVD) to improve its photocatalytic performances for the production of hydrogen or the degradation of organic contaminants in wastewater [22]. Indeed, the CVD method was identified as the most favored process for producing high-quality and costly-affordable crystalline $MoS_2$ with tunable physical properties [23–26] by controlling an assortment of morphologies, such as planar and vertical nanosheets [27], microplates [28], and nanorods [29]. These morphologies have also been very useful in promoting the optical properties of $MoS_2$ and increasing its PD activity [30,31]. Previous reports underlined the interest in developing $MoS_2$-based heterostructures for the PD of MB and its enhancement using several strategies such as incorporating plasmonic nanoparticles [32] or doping [33]. Nonetheless, these proposed methods implied multi-step fabrication processes, inflicting an increase in the overall fabrication costs and challenging their upscaling.

In this work, we demonstrated a facile fabrication route of 1T-$MoS_2$/2H-$MoS_2$ (1T/2H-$MoS_2$) heterostructures based on a single-step method using the CVD technique. We showed that these heterostructures exhibit high MB PD performances, where it is believed that the semiconducting 2H-$MoS_2$ phase acted as a generator of photo charges, while the metallic 1T-$MoS_2$ phase played the role of a charge-conveyor co-catalyst driving the electrons' transfer. The properties and performances of the 1T/2H-$MoS_2$ heterostructures were demonstrated by long-term photochemical reaction tests a systematic characterization approach using a large arsenal of chemical, structural, and electrical characterization methods.

## 2. Materials and methods

### 2.1. CVD growth

Molybdenum trioxide ($MoO_3$, 99.99%) and sulfur (S, 99.5%) were used as precursors to synthesize high-crystalline $MoS_2$ micro-flowers by means of a CVD process. A first ceramic boat containing 200 mg of S was placed upstream of an Argon flow (70 sccm) in the CVD tube furnace. The S was positioned at 27 cm from the gas inlet and its temperature was maintained at 400 °C. A second ceramic boat containing 20 mg of $MoO_3$ was placed at 50 cm from the gas inlet (Fig. 1a). The reaction product was collected on a silicon (Si) substrate, primarily cleaned with acetone and ethanol. The Si substrate was placed face down on the top of the second ceramic boat, maintained at 950 °C. Fig. 1b shows the heating profile used during the CVD reaction. In the first segment, the rate was set at 20 °C/min up to 400 °C. In the following segment, it was set to 6 °C/min and maintained up to 950 °C. A dwell time reaction of 30 min was applied, during which the $MoS_2$ micro-flowers were grown. Then, the furnace was shut down and allowed to cool down to room temperature.

### 2.2. Exfoliation process

Subsequently, the $MoS_2$ micro-flowers were exfoliated by sonication for 30 min using a mixed solution made 10 mL ethanol, 10 mL acetone, and 10 mL deionized water. The mass of the exfoliated film was determined by weighing the sample before and after the exfoliation procedure. The $MoS_2$ powder was retrieved following solvent evaporation.

### 2.3. Photocatalytic measurements

The PD activity was evaluated using a standard solar simulator (AM1.5) and a UV lamp (365 nm, 1 W). Photocurrent density ($J_{Ph}$) measurements were performed using a compact electrochemical workstation (Palmsens-4, PalmSens, Netherlands) under ambient conditions using UV and visible light illumination. A 1 mg of exfoliated $MoS_2$ powder was added to a 10 mL dye solution with 5 $mg.L^{-1}$ MB content. The solution was stirred in the dark for 30 min to reach an adsorption–desorption equilibrium. The PD reaction was initiated for 180 min and the absorption of the MB dye was monitored, at 30 min intervals, using a UV–Visible spectrometer (JASCO™ V-670, Jasco Inc., USA) at a maximum absorption wavelength of 664 nm.

### 2.4. Material characterization

Scanning electron microscopy SEM (Quanta 200 FEG, Thermo-fisher Scientific, USA) was used to investigate the morphology of $MoS_2$. The chemical composition of the as-prepared sample was determined through elemental mapping of their constituting elements using energy dispersive X-ray spectroscopy (EDS) (oxford instruments, UK). A Helios Thermofisher Scientific dual-focused ion beam system was used to

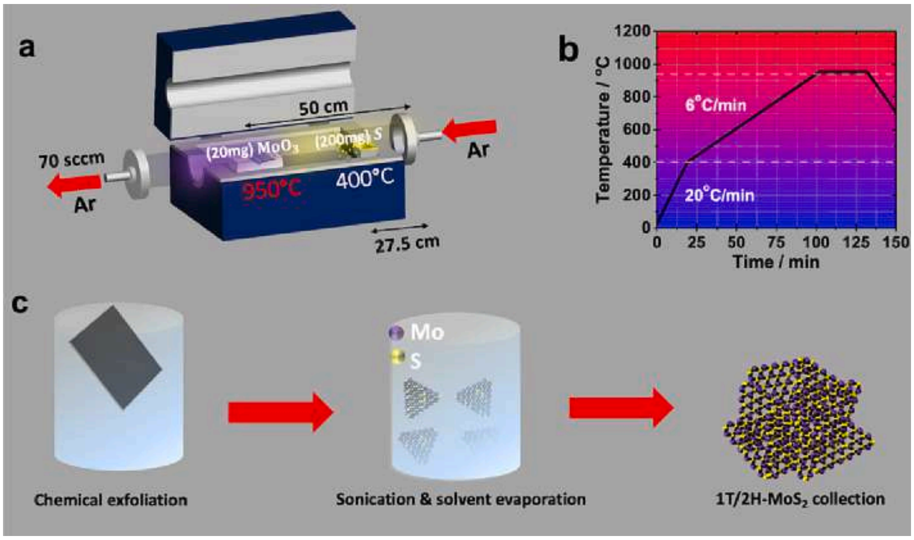

**Fig. 1.** (a) CVD setup for the fabrication of the $MoS_2$ micro-flowers, (b) CVD reaction heating rate profile, and (c) protocol used for the chemical exfoliation of $MoS_2$.

prepare cross-sectional samples. Thin lamella for transmission electron microscopy (TEM) investigations were prepared by the standard FIB lift-out technique. The samples were examined using an image Cs-corrected TEM system (TITAN, Thermo-fisher Scientific, USA) operating at 300 kV. The crystalline structure of $MoS_2$ micro-flowers was characterized by means of X-ray diffraction (XRD), $K_{\alpha Cu} = 1.54$ Å (D8 DISCROVER, Bruker, USA). Raman spectroscopy (Renishaw, UK) was performed to investigate the vibrational modes of the sample and to study the photoluminescence emission of the CVD-grown $MoS_2$. The surface chemical bonding states and composition of the $MoS_2$ deposits were determined by scanning X-ray photoelectron spectroscopy (XPS) microprobe (PHI VersaProbe3, Physical Electronics, USA). The XPS system used a 15 KV electron gun to produce monochromatic and micro-focused Al K-alpha X-ray source of 1486.6 eV. Survey scans in the range of 0–1100 eV and high-resolution core level peaks of Mo and S were carried out. The XPS spectra were calibrated using the C1s peak position at 284.6 eV.

## 3. Results and discussion

A typical SEM micrograph of the CVD deposits in Fig. 2a shows a dense packing of vertically aligned $MoS_2$ micro-flowers uniformly covering the entire surface (1 $cm^2$) of the Si substrate. The nanoleaves of the so-called micro-flowers pointed vertically with a thickness in the range of few tens of nanometers (Fig. 2b-c). Such densely packed micro-cavernous $MoS_2$ structures constitute ideal substrates for high optical absorption via light trapping and scattering [34,35]. The aspect ratio of the $MoS_2$ nanoleaves is expected to promote a fast vertical charge transfer to the electrolyte, as this has been already exploited in the case of photocatalytic vertically aligned $TiO_2$ nanotubes for water splitting [36–38]. Additionally, the intrinsic high in-plane mobility of $MoS_2$ nanosheets is expected to enhance the photocatalytic process. The EDX elemental mapping shown in Fig. 3 indicates that the Mo, S, and Si elements were evenly distributed across the tested area. Furthermore, the free space between micro-flowers significantly increases the surface-area of the samples, which provides additional sites for photocatalysis and improves the conditions for an improved overall PD capacity to degrade the MB dye.

Fig. 4a shows the XRD spectrum of the micro-flowers fabricated sample. The diffraction peaks at 13.74°, 32.9°, 40.5° and 58.8° correspond to the (0 0 2), (1 0 0), (0 0 3) and (1 1 0) planes of $MoS_2$ for both 2H-$MoS_2$ and 1T-$MoS_2$, respectively as already reported [39]. The simultaneous formation of the 1T and 2H $MoS_2$ phases during the CVD process was identified by Raman spectroscopy (Fig. 4b) showing the typical $A_{1g}$ and $E^1_{2g}$ peaks of the 2H-$MoS_2$ phase (due to the out-of-plane and the in-plane vibrations of the S atoms, respectively [40]). The fingerprint peaks of the 1T-$MoS_2$ phase (i.e.; $J_1$, $J_2$, $E_{1g}$, and $J_3$ vibrational modes located at 147 $cm^{-1}$, 228 $cm^{-1}$, 283 $cm^{-1}$, and 330 $cm^{-1}$, respectively [41]) were also clearly identified.

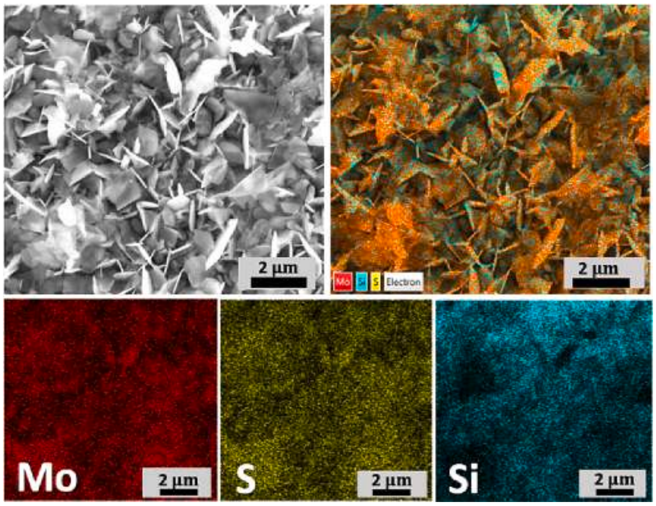

**Fig. 3.** EDS mapping of $MoS_2$ micro-flowers showing a uniform distribution of the Mo, S, and Si elements across the sample's surface.

In the case of packed 2D monolayers, it is well admitted that the $MoS_2$ bandgap is dependent on the number of layers [16]. For instance, from one to few monolayers, $MoS_2$ exhibits a direct bandgap and a measurable photoluminescence (PL) response, while it has an indirect bandgap and do not exhibit any PL emission when the number of monolayers increases [42]. In our case, the CVD-synthesized 1T/2H-$MoS_2$ heterostructures exhibited a PL emission with the typical signature of both excitons $X_A$ and $X_B$ (located at 677 nm and 625 nm, respectively), as shown in Fig. 4c, as reported elsewhere [43]. The quasi-equal intensity of these two-exciton peaks indicates the presence of a multilayer $MoS_2$ structure [44]. It is worth noting that a PL response was recorded using a green laser excitation, despite the fact that the elaborated

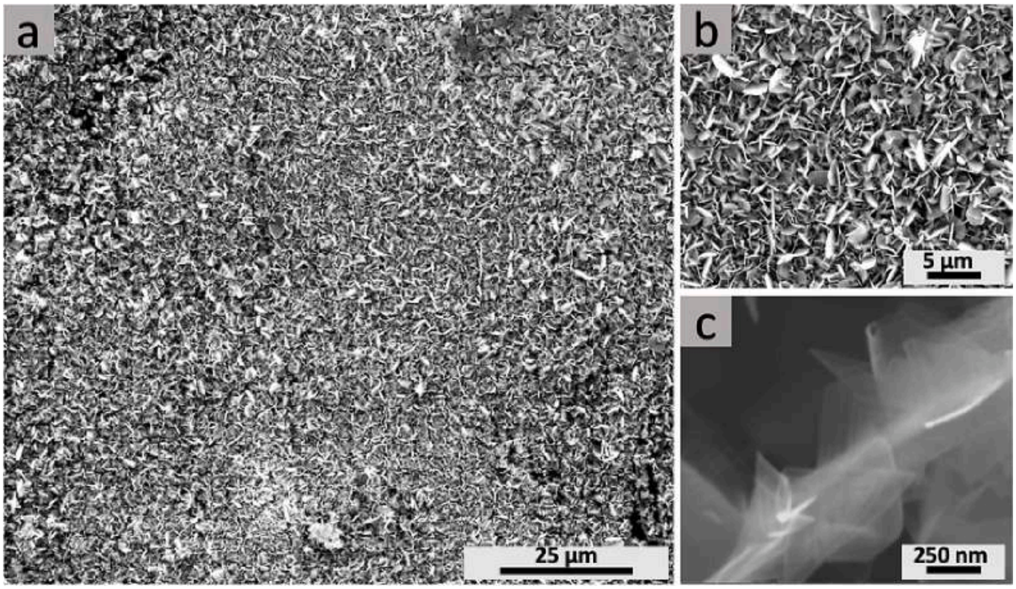

**Fig. 2.** (a) SEM micrograph of the $MoS_2$ micro-flowers deposited on Si substrate, (b) zoom-in showing the vertical shape of the micro-flowers, and (c) SEM micrograph at higher magnification showing the triangular $MoS_2$.

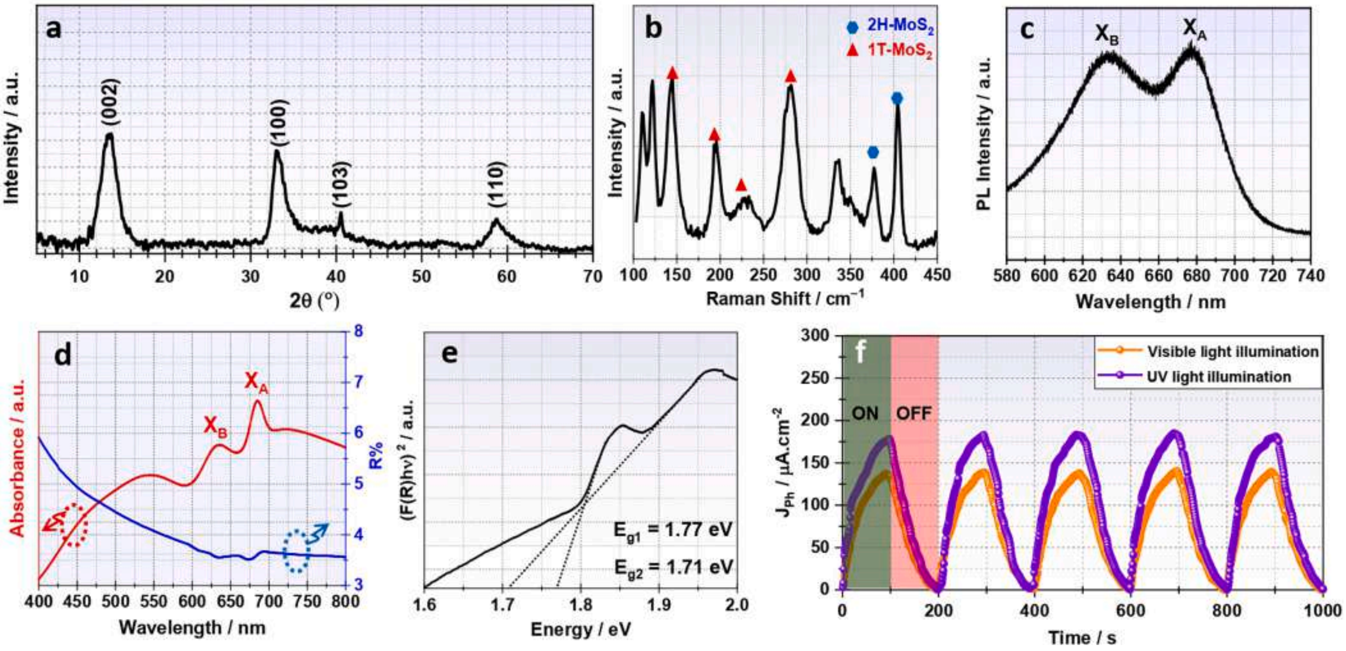

**Fig. 4.** (a) XRD spectrum measured for the 1T/2H-$MoS_2$ sample. (b) Raman spectrum and (c) photoluminescence response recorded under 532 nm excitation. (d) Optical reflectance obtained for the as-deposited film (blue curve) and its corresponding optical absorption after exfoliation (red curve). (d) Tauc-plot of the Kubelka–Munk function for the direct bandgap determination of the 1T/2H-$MoS_2$ heterostructure, and (f) photocurrent measurement of 1T/2H-$MoS_2$ under UV and visible light illumination.

heterostructure is likely consisting of a multilayer $MoS_2$. This behavior was previously observed and attributed to the surface enhancement caused by the vertical configuration of $MoS_2$ [27,45]. Furthermore, the optical reflectance of the $MoS_2$ micro-flowers films, measured over the (400–800) nm wavelength range, exhibited an extremely low reflectance (~6% at 400 nm and decreasing down to ~ 3.5% at 800 nm), as shown in Fig. 4d (black curve). The excitons $X_A$ and $X_B$ were also observed in the reflectance spectrum at 675 nm and 628 nm, respectively. This result indicates the good crystalline quality of the samples, as these excitons are observed in the PL measurements [46]. Optical absorption measurements were conducted on the exfoliated 1T/2H-$MoS_2$ powder (put in deionized water) showing a high absorption and the prominence of both $X_A$ and $X_B$ excitons (Fig. 4d, red curve). This confirms that the exfoliation process preserves the optoelectronic properties of the samples. Subsequently, the optical bandgap of the 1T/2H-$MoS_2$ heterostructure was determined using the optical reflectance spectra as per the Kubelka-Munk function [47]. In this case, the direct bandgap was obtained from the plot of $(F(R)h\nu)^2$ versus the energy of photons $(h\nu)$, as illustrated in Fig. 4f, which gives a bandgap in the range between 1.71 eV and 1.77 eV. This result is in good agreement with the aforementioned PL measurements and other investigations of multilayer $MoS_2$ [48,49]. Moreover, $J_{Ph}$ measurements were performed to examine the sample's photoresponse under UV and visible light illumination. A pair of 50 nm thick Au electrodes were deposited by sputtering on the sample surface with an effective detection area of 0.075 $cm^2$. Fig. 4f shows the transient photocurrent response recorded at a 1 V bias voltage. The $J_{Ph}$ was found equal to 180 and 140 $\mu A/cm^2$ under UV and visible light illumination, respectively, indicating an improved UV photoresponse.

Fig. 5a shows a typical XPS survey spectrum of the CVD-grown $MoS_2$ samples. The 1T/2H-$MoS_2$ micro-flowers were exposed to the ambient atmosphere before being loaded into the XPS system. The O-1 s and Si-2p peaks present in the survey spectrum are due to the Si/$SiO_2$ underlying substrate. The high-resolution binding energy plots of both Mo-3d and S-2 s core level peaks are shown in Fig. 5b and 5c. The deconvolution of the Mo-3d peaks indicated the presence of four different components ascribed to the 1T-$MoS_2$ and 2H-$MoS_2$ phases, as previously reported [39,50]. Additionally, the S-2 s peak was observed, indicating the good crystalline quality of the $MoS_2$ structure. Similarly, the deconvolution of the S-2p peaks revealed the presence of the two components for 1T-$MoS_2$ and one peak for 2H-$MoS_2$ [51]. The peak at 533.5 eV of the O-1 s spectrum (Fig. 5d) is attributed to the S–O bonding, the peak at 532.5 eV corresponds to the C–O bonding, and the peak at 530.7 eV is attributed to $MoO_3$ [52]. The deconvoluted C-1 s spectrum shows a dominant peak at 284.7 eV for C–C/C = C, and a small peak at 285.5 eV for C-O [53].

Further investigations on the 1T/2H-$MoS_2$ CVD deposits were performed using HRTEM analysis, as shown in Fig. 6a. The HRTEM micrograph shows the juxtaposition of both nanocrystals, i.e., the 1T-$MoS_2$ indicated by the (1 0 0) inter-planar spacing of 0.27 nm and the 2H-$MoS_2$ indicated by the (1 0 0) inter-planar spacing of 0.30 nm with a (1 0 0) crystallographic relationship between the two crystals. This strongly suggests the heterostructure character of the composite, as reported elsewhere [54,55]. Fig. 6b and 6c show highly resolved images of the atomic structure of the 2H and 1T phases, respectively (blue and red squares). The high-resolution images indicate that the atoms' positions are consistent with the octahedral coordination (for the 1T-$MoS_2$ phase) and the trigonal prismatic coordination (for the 2H-$MoS_2$ phase). These HRTEM results confirm the formation of intermixed 1T/2H-$MoS_2$ heterostructures at the nanoscale.

To evaluate the photocatalytic performance of the 1T/2H-$MoS_2$ heterostructures for the MB degradation, the PD of the MB dye solution under light excitation, was first conducted without the use of the photocatalyst to assess the MB photolysis. Then, the variation of the MB concentration was monitored in dark with the photocatalyst. Fig. 7 shows the absorbance spectra of the MB solution in the presence of 1T/2H-$MoS_2$ recorded in dark, under visible and UV-light illuminations at variable exposure durations. A series of five replicate measurements was carried out.

The results show a very weak MB's PD in dark, measured during 30 min illumination (Fig. 7a and 7b). This small variation in dark is probably due to the adsorption of MB by 1T/2H-$MoS_2$. Once the sample was

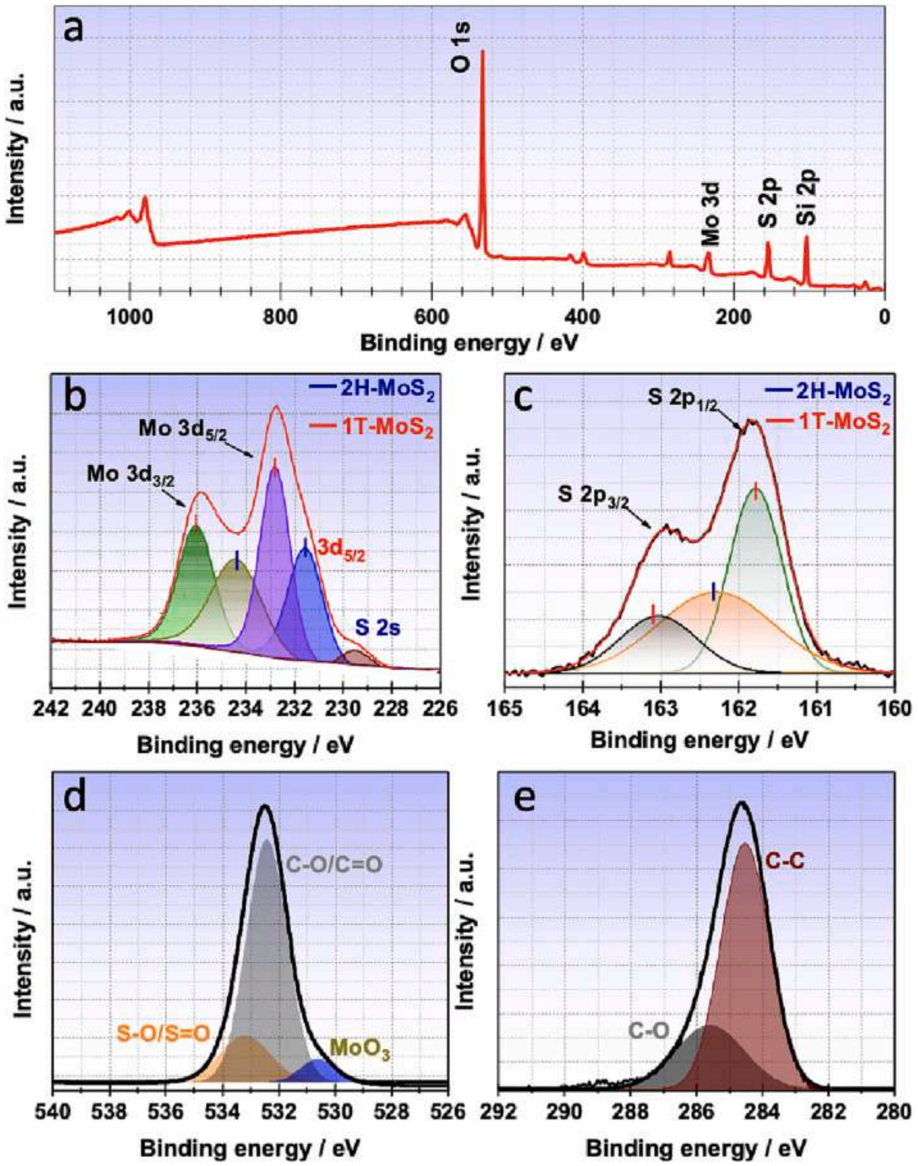

**Fig. 5.** XPS analysis of the 1T/2H-MoS$_2$ heterostructure. (a) XPS survey, (b) Zoom-in on the Mo-3d peaks, and (c) zoom-in on the S-2p peaks. The deconvolution of the Mo-3d and S-2p peaks shows the co-existence of 1T-MoS$_2$ and 2H-MoS$_2$ structures. (d) Zoom-in on the O-1 s peaks and the (e) C-1 s peaks.

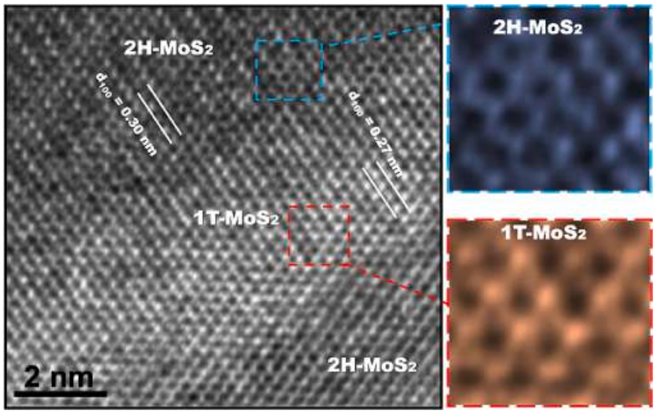

**Fig. 6.** (left) HRTEM image of the 1T/2H-MoS$_2$ sample with respective interplanar spacing. (right) Zoom-in of the regions highlighted by the blue (2H-MoS$_2$) and red (1T-MoS$_2$) squares indicating the atoms' positions.

exposed to illumination, a significantly higher MB photo-degradation was observed, with a higher yield under UV excitation. The MB's degradation efficiency was computed using the UV and visible light illuminations to compare the PD performance under these two conditions. The degradation efficiency, also known as discoloration efficiency η, after t minutes of illumination is given as a function of the MB concentration:

$$\eta(\%) = 100\left(1 - \frac{C}{C_0}\right), \tag{1}$$

where $C_0$ and $C$ represent the initial and the actual MB concentrations in dark and during the PD for a given time t, respectively. Fig. 7c and 7d depict the variation of the concentration ratio $C/C_0$ (black) and the MB's PD efficiency η (red) under UV and visible light illuminations. After 180 min, the MB's concentration was reduced by 90% and 80% of its initial value, respectively, under the UV and visible light illuminations. Nonetheless, the photolysis of MB in absence of the MoS$_2$ photocatalyst was also plotted in Fig. 7c and 7d (dashed lines) to show the influence of the light-source's type on the MB photolysis. We anticipate a $\sim$ 10%–18% under visible light and UV illuminations, respectively, after 180

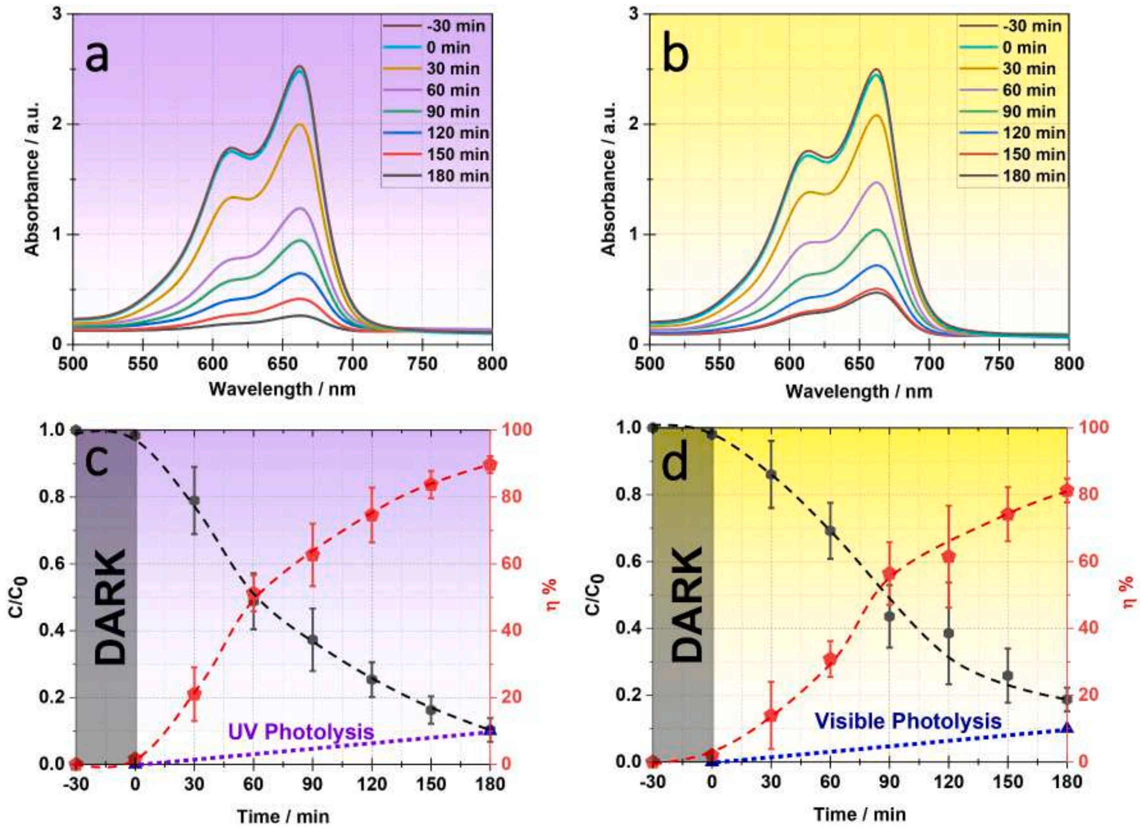

**Fig. 7.** Absorbance of the MB dye solution after different PD durations under illuminations (a) UV and (b) visible. Variation of the dye PD rate and MB concentration ratio under illuminations (c) UV and (d) visible.

min of light exposure in absence of any $MoS_2$ catalyst.

The pseudo-first-order kinetic model was commonly used to evaluate the kinetics of dye degradation at low concentrations. A corresponding rate-constant (k) that characterizes the changes in the concentration over time can be calculated using the following equation:

$$\ln\left(\frac{C}{C_0}\right) = -kt. \tag{2}$$

The PD rate-constants of MB under UV and visible illuminations were determined from the curves' slopes in Fig. 8a using Eq. (2). As can be seen, the photocatalytic activity of the 1T/2H-$MoS_2$ samples is higher under UV light ($\sim 12.5 \times 10^{-3}$ $min^{-1}$) than under visible-light illumination ($\sim 9.2 \times 10^{-3}$ $min^{-1}$). Table 1 compares the first-order kinetic constant of the PD reaction of MB reported in previous works, where $MoS_2$ nanostructures was used as a photocatalyst. These works were compared to the present study, highlighting the benefit of the CVD method in fabricating high crystalline quality $MoS_2$ with a high yield PD activity.

Overall, our results show that the 1T/2H-$MoS_2$ heterostructures presented here are much more efficient for MB photo-degradation than their hydrothermally grown counterparts reported in the literature so far (either under UV or visible light conditions). This gains more importance when considering that our heterostructures were fabricated on large surfaces by a single-step CVD process. This fabrication route offers easier and lower-cost means compared to other tedious processes, such as the hydrothermal fabrication.

The cyclability of our photocatalyst was assessed by subjecting the 1T/2H-$MoS_2$ heterostructures to five consecutive PD cycles (3 h each). After each cycle, the dye solution was replaced with a new one to maintain the same initial dye concentration. In other words, the residual

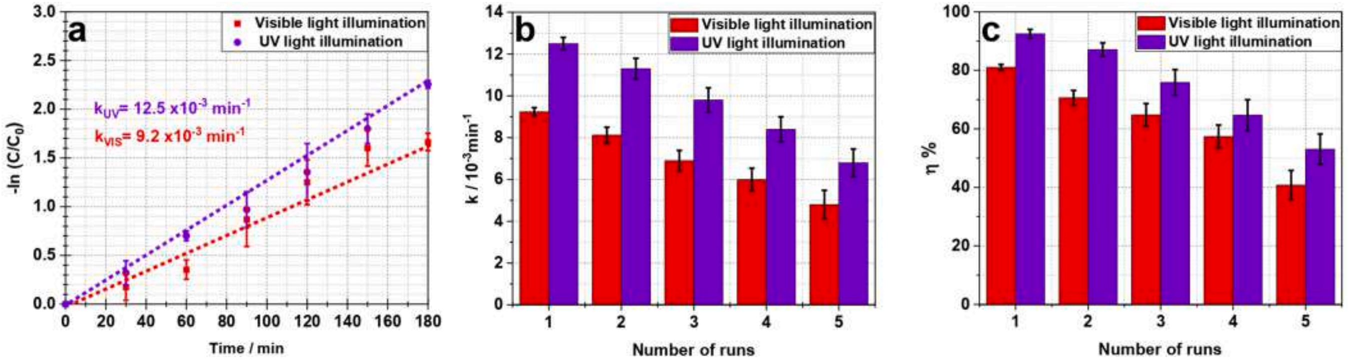

**Fig. 8.** (a) PD rate-constant of 1T/2H-$MoS_2$ under UV and visible light illuminations; (b) reusability of 1T/2H-$MoS_2$ for the rate-constant, and (c) the degradation efficiency.

**Table 1**
Comparison of the PD performance towards MB of different 1T/2H-$MoS_2$ heterostructures synthesized by either hydrothermal or CVD techniques.

| Catalyst dosage mg.$L^{-1}$ | MB concentration mg.$L^{-1}$ | Light source | Time (min) | PD (%) | k ($min^{-1}$) | Ref. |
|---|---|---|---|---|---|---|
| 250 | 40 | Visible | 120 | 69.5 | $7.3 \times 10^{-3}$ | [56] |
| 400 | 200 | Visible | 60 | 28.8 | $5.6 \times 10^{-3}$ | [57] |
| 200 | 20 | Visible | 120 | 98 | $26.2 \times 10^{-3}$ | [58] |
| 300 | 40 | Visible | 60 | 32.5 | $4.8 \times 10^{-3}$ | [59] |
| 100 | 5 | Visible | 180 | 80 | $9.2 \times 10^{-3}$ | This work |
| 100 | 5 | UV | 180 | 90 | $12.5 \times 10^{-3}$ | This work |

dye mass after the degradation of each run was taken into consideration in the analysis of the results~~.~~ Fig. 8b-c show the different rate constant and MB degradation efficiency (η) values obtained for the five consecutive cycles. Both PD rate-constants under UV ($k_{UV}$) and visible ($k_{VIS}$) light illuminations were found to decrease from 12.5 to 9.8 × $10^{-3}$ $min^{-1}$, and from 9.2 to 7.9 × $10^{-3}$ $min^{-1}$, respectively. Consequently, the discoloration rate $\eta_{UV}$ and $\eta_{Vis}$ under UV and visible illuminations (after 180 min of treatment) also decreased from 90% to 85% and from 80% to 74%, respectively, between the first and the 5th cycle. This overall PD efficiency decrease after 5 cycles corresponds to a loss of 1% after each cycle under the UV illumination. Under visible light illumination, the discoloration rate decreased by 1% for the first 3 cycles, and then by 2% for the following ones. These results indicate that the PD efficiency does not decrease significantly after 5 cycles and that the 1T/2H-$MoS_2$ photocatalyst is slightly more active under UV than under visible light (85% versus 74% after 5 cycles). This slight efficiency loss is likely due to the deactivation of $MoS_2$ photocatalytic sites because of some surface contamination/poisoning with degradation by-products.

Based on our findings, the potential mechanism at the origin of the high photocatalytic performance of the 1T/2H-$MoS_2$ structures is illustrated in Fig. 9. The mechanism suggests that the 2H-$MoS_2$ acts as a good photosensitizer and the metallic 1T-$MoS_2$ phase as a co-catalyst, enhancing the electron transfer. Under the illumination, electron-hole pairs are generated in 2H-$MoS_2$ with a narrow bandgap. Electrons ($e^-_{CB}$) are excited from the 2H-$MoS_2$ valence band (VB) to the conduction band (CB), leaving holes ($h^+_{VB}$) in the VB (eqn.3), then, the photo-generated electrons are trapped by 1T-$MoS_2$, which dramatically reduces their recombination rate and extends the redox reaction's lifetime. This facilitates the reduction of $O_2$ molecules to $O_2^{*-}$ (eqn. (4). When the adsorbed $O_2$ undergoes multi-electron and proton redox reactions (eqns. (5) and (6), the OH* molecule is formed, favoring the PD of MB (eqn. (7).

$$1T/2H - MoS_2 + hv \rightarrow h_{VB}{}^{+} + e_{CB}{}^{-} \tag{3}$$

$$e^- + O_2 \rightarrow O_2^{*-} \tag{4}$$

$$O_2 + 2e^- + 2H^+ \rightarrow H_2O_2 \tag{5}$$

$$H_2O_2 + e^- + H^+{}_2 + hv \rightarrow OH^* + H_2O \tag{6}$$

$$O_2^{*-}, OH^*, h^+ + MB\ Dye \rightarrow CO_2 + H_2O + inorganic\ molecules \tag{7}$$

## 4. Conclusion

We have successfully demonstrated the synthesis of 1T-$MoS_2$/2H-$MoS_2$ heterostructures (bandgap ~ 1.7 eV) using a single-step CVD process. The as-grown 1T-$MoS_2$/2H-$MoS_2$ structures consisted of densely packed micro-flowers with vertically oriented nano-leaves. Such cavernous and highly porous morphology is ideal for strong light absorption and trapping, as testified by the very low reflectance (~5%) of our 1T-$MoS_2$/2H-$MoS_2$ heterostructures. By exfoliating the CVD-grown films, we investigated their photocatalytic activity for MB photodegradation under UV and visible light illuminations. Our results showed that their photocatalytic activity surpasses the literature values (for the rate constant) reported so far for similar heterostructures. The PD efficiency of the 1T-$MoS_2$/2H-$MoS_2$ heterostructures towards MB was greater under UV (12.5 × $10^{-3}$ $min^{-1}$) than under visible light illumination (9.2 × $10^{-3}$ $min^{-1}$). Finally, our results suggested that the local intermixing of the 1T and 2H $MoS_2$ phases is favorable for the photocatalysis process. The metallic 1T phase acts as a co-catalyst with

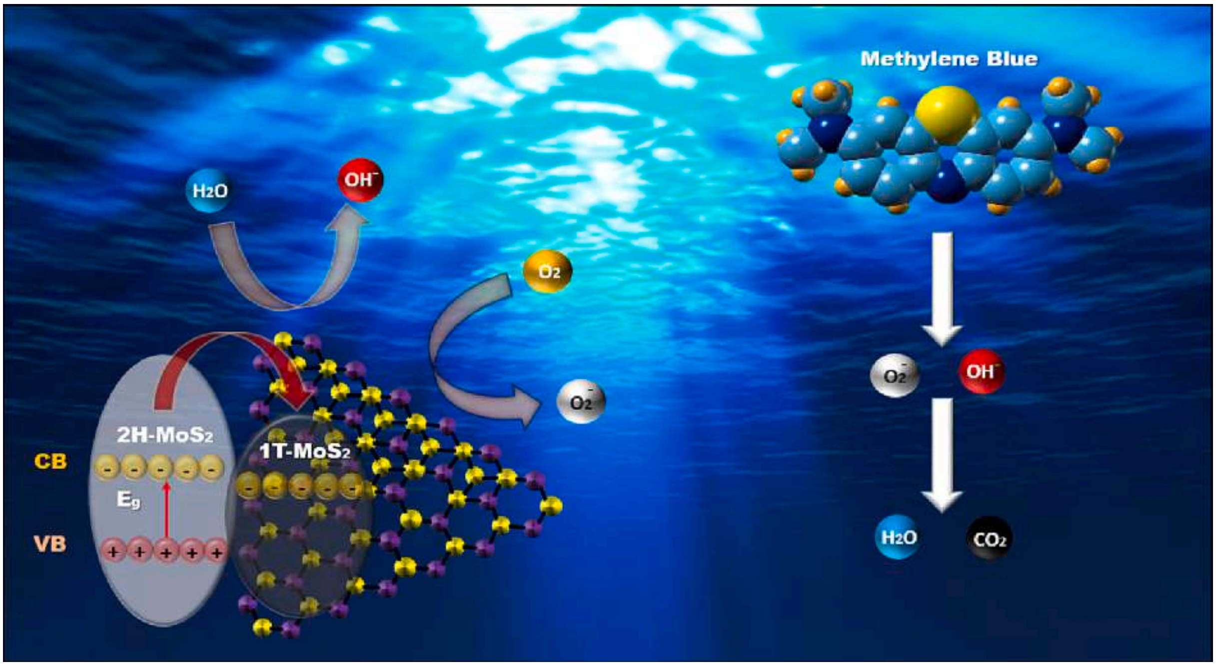

**Fig. 9.** Illustration of the suggested mechanism of MB PD by 1T/2H-$MoS_2$ heterostructures.

the semiconducting 2H phase, by promoting efficient photo charges transfer and limiting their recombination probability. This provides ample available oxidizing groups to photodegrade more MB molecules present in the solution.

## 5. Authors statement

D.M. and M.J. conceived the study. D.M. M.L., N-S. R. and K.J. carried out the experiments.

M.E., M.A. E., M.J. drafted the manuscript and interpreted the results. All authors contributed equally to the writing, editing and revising the manuscript.

## Declaration of Competing Interest

The authors declare that they have no known competing financial interests or personal relationships that could have appeared to influence the work reported in this paper.

## Data availability

Data will be made available on request.

### *Acknowledgement*

M.A.E and M.J. acknowledge the financial support provided by the Natural Sciences and Engineering Research Council (NSERC) of Canada and by the Region of Haut-De-France (HDF), respectively. DM is grateful to both the Region HDF (France) and INRS (QC, Canada) for his fellowship.

### *Data availability statement*

All data supporting this work are available upon request from the corresponding author M. Jouiad.

## References

[1] R.L. Calderon, The epidemiology of chemical contaminants of drinking water, Food Chem. Toxicol. 38 (2000) 13–20.

[2] G. Bhavya, S.A. Belorkar, R. Mythili, N. Geetha, H.S. Shetty, S.S. Udikeri, S. Jogaiah, Remediation of emerging environmental pollutants: A review based on advances in the uses of eco-friendly biofabricated nanomaterials, Chemosphere 275 (2021), 129975.

[3] M. Moradi, Y. Vasseghian, A. Khataee, M. Harati, H. Arfaeinia, Ultrasound-assisted synthesis of FeTiO3/GO nanocomposite for photocatalytic degradation of phenol under visible light irradiation, Sep. Purif. Technol. 261 (2021), 118274.

[4] N. Han, S. Wang, Z. Yao, W. Zhang, X. Zhang, L. Zeng, R. Chen, Superior three-dimensional perovskite catalyst for catalytic oxidation, EcoMat 2 (2020) 1–10.

[5] N. Han, S. Wang, A.K. Rana, S. Asif, J.J. Klemeš, A. Bokhari, J. Long, V.K. Thakur, X. Zhao, Rational design of boron nitride with different dimensionalities for sustainable applications, Renew. Sustain. Energy Rev. 170 (2022), 112910.

[6] C.R.B. Gama, M.A.G. Pombo, C.P. Nunes, G.F. Gama, S.G.E. Mezitis, M.S. Neto, O. R. Guimarães, M. Geller, L. Oliveira, A de S. da, Fonseca, A. Sitnoveter, G. Goldwasser, K.S. Cunha, L.G. Darrigo Junior, Treatment of recurrent urinary tract infection symptoms with urinary antiseptics containing methenamine and methylene blue: Analysis of etiology and treatment outcomes, Res. Reports Urol. 12 (2020) 639–649.

[7] I. Michael, L. Rizzo, C.S. McArdell, C.M. Manaia, C. Merlin, T. Schwartz, C. Dagot, D. Fatta-Kassinos, Urban wastewater treatment plants as hotspots for the release of antibiotics in the environment: A review, Water Res. 47 (2013) 957–995.

[8] Z. Ansarian, A. Khataee, S. Arefi-Oskoui, Y. Orooji, H. Lin, Ultrasound-assisted catalytic activation of peroxydisulfate on Ti3GeC2 MAX phase for efficient removal of hazardous pollutants, Mater. Today Chem. 24 (2022), 100818.

[9] T. Luo, R. Wang, F. Chai, L. Jiang, P. Rao, L. Yan, X. Hu, W. Zhang, L. Wei, A. Khataee, N. Han, Arsenite (III) removal via manganese-decoration on cellulose nanocrystal -grafted polyethyleneimine nanocomposite, Chemosphere 303 (2022), 134925.

[10] M. Zhang, N. Han, Y. Fei, J. Liu, L. Xing, TiO 2/g-C 3 N 4 photocatalyst for the purification of potassium butyl xanthate in mineral processing wastewater, J. Environ. Manage. 297 (2021), 113311.

[11] M. Jiang, M. Zhang, L. Wang, Y. Fei, S. Wang, A. Núñez-Delgado, A. Bokhari, M. Race, A. Khataee, J. Jaromír Klemeš, L. Xing, N. Han, Photocatalytic degradation of xanthate in flotation plant tailings by TiO 2/graphene nanocomposites, Chem. Eng. J. 431 (2022), 134104.

[12] T.S. Rad, Z. Ansarian, R.D.C. Soltani, A. Khataee, Y. Orooji, F. Vafaei, Sonophotocatalytic activities of FeCuMg and CrCuMg LDHs: Influencing factors, antibacterial effects, and intermediate determination, J. Hazard. Mater. 399 (2020), 123062.

[13] I. Khan, K. Saeed, I. Zekker, B. Zhang, A.H. Hendi, A. Ahmad, S. Ahmad, N. Zada, H. Ahmad, L.A. Shah, T. Shah, I. Khan, Review on Methylene Blue: Its Properties, Uses, Toxicity and Photodegradation, Water 14 (2022) 242.

[14] W. Choi, N. Choudhary, G.H. Han, J. Park, D. Akinwande, Y.H. Lee, Recent development of two-dimensional transition metal dichalcogenides and their applications, Mater. Today 20 (2017) 116–130.

[15] J. Sun, X. Li, W. Guo, M. Zhao, X. Fan, Y. Dong, C. Xu, J. Deng, Y. Fu, Synthesis methods of two-dimensional MoS2: A brief review, Crystals 7 (2017) 198.

[16] D. Mouloua, A. Kotbi, G. Deokar, K. Kaja, M. El Marssi, M.A. El Khakani, M. Jouiad, Recent Progress in the Synthesis of MoS2 Thin Films for Sensing, Photovoltaic and Plasmonic Applications : A Review, Materials (Basel) 14 (2021) 3283.

[17] L.L. Long, J.J. Chen, X. Zhang, A.Y. Zhang, Y.X. Huang, Q. Rong, H.Q. Yu, Layer-controlled growth of MoS2 on self-assembled flower-like Bi2S3 for enhanced photocatalysis under visible light irradiation, NPG Asia Mater. 8 (2016) 1–9.

[18] Q. Li, N. Zhang, Y. Yang, G. Wang, D.H.L. Ng, High efficiency photocatalysis for pollutant degradation with MoS 2/C3N4 heterostructures, Langmuir 30 (2014) 8965–8972.

[19] A. Arulraj, M. Ramesh, B. Subramanian, G. Senguttuvan, In-situ temperature and thickness control grown 2D-MoS2 via pulsed laser ablation for photovoltaic devices, Sol. Energy 174 (2018) 286–295.

[20] A. Shokri, N. Salami, Gas sensor based on MoS2 monolayer, Sensors Actuat. B Chem. 236 (2016) 378–385.

[21] L. Du, H. Zhang, Z. Wang, T. Zhuang, Z. Wang, Boosting the electrochemiluminescence of luminol by high-intensity focused ultrasound pretreatment combined with 1T/2H MoS2 catalysis to construct a sensitive sensing platform, Ultrason. Sonochem. 92 (2023), 106264.

[22] Y. Li, F. Xiang, W. Lou, X. Zhang, MoS2 with structure tuned photocatalytic ability for degradation of methylene blue, IOP Conf. Ser. Earth Environ. Sci. 300 (2019), 052021.

[23] H.F. Liu, S.L. Wong, D.Z. Chi, CVD Growth of MoS2-based Two-dimensional Materials, Chem. Vap. Depos. 21 (2015) 241–259.

[24] L. Seravalli, M. Bosi, A review on chemical vapour deposition of two-dimensional mos2 flakes, Materials (Basel). 14 (2021) 7590.

[25] D. Mouloua, N.S. Rajput, S. Saitzek, K. Kaja, K. Hoummada, M. El Marssi, M.A. El Khakani, M. Jouiad, Broadband photodetection using one-step CVD-fabricated MoS2/MoO2 microflower/microfiber heterostructures, Sci. Rep. 12 (2022) 1–13.

[26] D. Mouloua, N.S. Rajput, J.-F. Blach, M. Lejeune, M. El Marssi, M.A. El Khakani, M. Jouiad, Fabrication control of MoS2/MoO2 nanocomposite via chemical vapor deposition for optoelectronic applications, Mater. Sci. Eng. B 286 (2022), 116035.

[27] G. Deokar, N.S. Rajput, P. Vancsó, F. Ravaux, M. Jouiad, D. Vignaud, F. Cecchet, J. F. Colomer, Large area growth of vertically aligned luminescent MoS2 nanosheets, Nanoscale 9 (2017) 277–287.

[28] G. Deokar, P. Vancsó, R. Arenal, F. Ravaux, J. Casanova-Cháfer, E. Llobet, A. Makarova, D. Vyalikh, C. Struzzi, P. Lambin, M. Jouiad, J.F. Colomer, MoS2–Carbon Nanotube Hybrid Material Growth and Gas Sensing, Adv. Mater. Interfaces 4 (2017) 1–10.

[29] Z. Hu, R. Xu, S. Yu, J. Li, Z. Yang, Facile synthesis of a nanorod-like MoS2nanostructure for sensitive electrochemical biosensing application, Analyst 145 (2020) 7864–7869.

[30] J. Singh, R. Singh, P. Duhan, Y. Mann, A.K. Manna, D. Banerjee, R.K. Soni, Morphology dependent effective charge separation process in nanostructured MoS2 thin films for enhanced photodegradation behavior, J. Phys. D Appl. Phys. 54 (2021), 375103.

[31] X. Zheng, L. Zhu, A. Yan, C. Bai, Y. Xie, Ultrasound-assisted cracking process to prepare MoS2 nanorods, Ultrason. Sonochem. 11 (2004) 83–88.

[32] A. Rani, A.S. Patel, A. Chakraborti, K. Singh, P. Sharma, Enhanced photocatalytic activity of plasmonic Au nanoparticles incorporated MoS2 nanosheets for degradation of organic dyes, J. Mater. Sci. Mater. Electron. 32 (2021) 6168–6184.

[33] L. Chen, C.W. Chen, D.C. Di, Hydrothermal synthesis of Se-doped MoS2 quantum dots heterojunction for highly efficient photocatalytic degradation, Mater. Lett. 291 (2021), 129537.

[34] F. Alexander, M. AlMheiri, P. Dahal, J. Abed, N.S. Rajput, C. Aubry, J. Viegas, M. Jouiad, Water splitting TiO2 composite material based on black silicon as an efficient photocatalyst, Sol. Energy Mater. Sol. Cells 180 (2018) 236–242.

[35] M. Dastborhan, A. Khataee, S. Arefi-Oskoui, Y. Yoon, Synthesis of flower-like MoS2/CNTs nanocomposite as an efficient catalyst for the sonocatalytic degradation of hydroxychloroquine, Ultrason. Sonochem. 87 (2022), 106058.

[36] T. Favet, V. Keller, T. Cottineau, M.A. El Khakani, Enhanced visible-light-photoconversion efficiency of TiO2 nanotubes decorated by pulsed laser deposited CoNi nanoparticles, Int. J. Hydrogen Energy 44 (2019) 28656–28667.

[37] T. Favet, T. Cottineau, V. Keller, M.A. El Khakani, Comparative study of the photocatalytic effects of pulsed laser deposited CoO and NiO nanoparticles onto TiO2 nanotubes for the photoelectrochemical water splitting, Sol. Energy Mater. Sol. Cells 217 (2020), 110703.

[38] N.S. Rajput, Y. Shao-Horn, X.H. Li, S.G. Kim, M. Jouiad, Investigation of plasmon resonance in metal/dielectric nanocavities for high-efficiency photocatalytic device, Phys. Chem. Chem. Phys. 19 (2017) 16989–16999.

[39] M.R. Saber, G. Khabiri, A.A. Maarouf, M. Ulbricht, A.S.G. Khalil, A comparative study on the photocatalytic degradation of organic dyes using hybridized 1T/2H, 1T/3R and 2H MoS2 nano-sheets, RSC Adv. 8 (2018) 26364–26370.

[40] G. Pradhan, A.K. Sharma, Anomalous Raman and photoluminescence blue shift in mono- and a few layered pulsed laser deposited MoS2 thin films, Mater. Res. Bull. 102 (2018) 406–411.

[41] Y. Yao, K. Ao, P. Lv, Q. Wei, MoS2 coexisting in 1T and 2H phases synthesized by common hydrothermal method for hydrogen evolution reaction, Nanomaterials 9 (2019) 1–12.

[42] J. Jeon, S.K. Jang, S.M. Jeon, G. Yoo, Y.H. Jang, J.H. Park, S. Lee, Layer-controlled CVD growth of large-area two-dimensional MoS2 films, Nanoscale 7 (2015) 1688–1695.

[43] T. Han, H. Liu, S. Wang, S. Chen, W. Li, X. Yang, M. Cai, K. Yang, Probing the optical properties of MoS2 on SiO2/Si and sapphire substrates, Nanomaterials 9 (2019) 740.

[44] A. Splendiani, L. Sun, Y. Zhang, T. Li, J. Kim, C.Y. Chim, G. Galli, F. Wang, Emerging photoluminescence in monolayer MoS2, Nano Lett. 10 (2010) 1271–1275.

[45] J. Shi, P. Yu, F. Liu, P. He, R. Wang, L. Qin, J. Zhou, X. Li, J. Zhou, X. Sui, S. Zhang, Y. Zhang, Q. Zhang, T.C. Sum, X. Qiu, Z. Liu, X. Liu, 3R MoS2 with Broken Inversion Symmetry: A Promising Ultrathin Nonlinear Optical Device, Adv. Mater. 29 (2017) 1701486.

[46] Y. Liu, T. Shen, S. Linghu, R. Zhu, F. Gu, Electrostatic control of photoluminescence from A and B excitons in monolayer molybdenum disulfide, Nanoscale Adv. 4 (2022) 2484–2493.

[47] X. Fan, P. Xu, D. Zhou, Y. Sun, Y.C. Li, M.A.T. Nguyen, M. Terrones, T.E. Mallouk, Fast and Efficient Preparation of Exfoliated 2H MoS2 Nanosheets by Sonication-Assisted Lithium Intercalation and Infrared Laser-Induced 1T to 2H Phase Reversion, Nano Lett. 15 (2015) 5956–5960.

[48] X. Xin, Y. Song, S. Guo, Y. Zhang, B. Wang, Y. Wang, X. Li, One-step synthesis of P-doped MoS2 for efficient photocatalytic hydrogen production, J. Alloy. Compd. 829 (2020), 154635.

[49] S. Funke, B. Miller, E. Parzinger, P. Thiesen, A.W. Holleitner, U. Wurstbauer, Imaging spectroscopic ellipsometry of MoS2, J. Phys. Condens. Matter 28 (2016), 385301.

[50] Zhang C, Wang Z, Bhoyate S, Morey T, Neria B, Vasiraju V, Gupta G, Palchoudhury S, Kahol P, Mishra S, Perez F and Gupta R 2017 MoS2 Decorated Carbon Nanofibers as Efficient and Durable Electrocatalyst for Hydrogen Evolution Reaction *C* **3** 33.

[51] R. Sha, S. Badhulika, Few layered MoS2 grown on pencil graphite: A unique single-step approach to fabricate economical, binder-free electrode for supercapacitor applications, Nanotechnology 30 (2019), 035402.

[52] S. Kim, W. Park, D. Kim, J. Kang, J. Lee, H.Y. Jang, S.H. Song, B. Cho, D. Lee, Novel exfoliation of high-quality 2H-MoS2 nanoflakes for solution-processed photodetector, Nanomaterials 10 (2020) 1045.

[53] J. Huang, M. Chen, X. Li, X. Zhang, L. Lin, W. Liu, Y. Liu, A facile layer-by-layer fabrication of three dimensional MoS 2 -rGO-CNTs with high performance for hydrogen evolution reaction, Electrochim. Acta 300 (2019) 235–241.

[54] C.H. Sharma, A.P. Surendran, A. Varghese, M. Thalakulam, Stable and scalable 1T MoS2 with low temperature-coefficient of resistance, Sci. Rep. 8 (2018) 1–9.

[55] H. Fan, R. Wu, H. Liu, X. Yang, Y. Sun, C. Chen, Synthesis of metal-phase-assisted 1T@2H-MoS2 nanosheet-coated black TiO2 spheres with visible light photocatalytic activities, J. Mater. Sci. 53 (2018) 10302–10312.

[56] L. Tian, R. Wu, H.Y. Liu, Synthesis of Au-nanoparticle-loaded 1T@2H-MoS 2 nanosheets with high photocatalytic performance, J. Mater. Sci. 54 (2019) 9656–9665.

[57] J.P.M. Alido, F.N.I. Sari, J.M. Ting, Synthesis of Ag/hybridized 1T–2H MoS2/TiO2 heterostructure for enhanced visible-light photocatalytic activity, Ceram. Int. 45 (2019) 23651–23657.

[58] M.T.L. Lai, K.M. Lee, T.C.K. Yang, G.T. Pan, C.W. Lai, C.Y. Chen, M.R. Johan, J. C. Juan, The improved photocatalytic activity of highly expanded MoS2under visible light emitting diodes, Nanoscale Adv. 3 (2021) 1106–1120.

[59] K. Dou, Y. Lu, R. Wang, H. Cao, C. Yao, J. Liu, N. Tsidaeva, W. Wang, (1T/2H)-MoS2/CoFe2O4 heterojunctions with a unique grape bunch structure for photocatalysis of organic dyes driven by visible light, Appl. Surf. Sci. 605 (2022), 154751.

**Article 6: D. Mouloua, M. El Marssi, M. A. El Khakani, M. Jouiad, in IEEE EUROCON 2023 - 20th Int. Conf. Smart Technol., 2023, pp. 138–141.**

# Enhanced photodetection properties of CVD-grown $MoS_2$ nanosheets onto Ag-nanoparticles decorated substrates

Driss Mouloua
Laboratory of Physics of Condensed Matter, University of Picardie Jules Verne, Scientific Pole, 33 rue Saint-Leu, 80039 Amiens Cedex 1, France
Institut National de la Recherche Scientifique (INRS), Centre-Énergie, Matériaux et Télécommunications, 1650, Blvd, Lionel–Boulet, Varennes, QC J3X-1P7, Canada
driss.mouloua@etud.u-picardie.fr
driss.mouloua@inrs.ca

Mimoun El Marssi
Laboratory of Physics of Condensed Matter, University of Picardie Jules Verne, Scientific Pole, 33 rue Saint-Leu, 80039 Amiens Cedex 1, France
mimoun.elmarssi@u-picardie.fr

My Ali El Khakani
Institut National de la Recherche Scientifique (INRS), Centre-Énergie, Matériaux et Télécommunications, 1650, Blvd, Lionel–Boulet, Varennes, QC J3X-1P7, Canada
*Correspondance: m.a.elkhakani@inrs.ca

Mustapha Jouiad
Laboratory of Physics of Condensed Matter, University of Picardie Jules Verne, Scientific Pole, 33 rue Saint-Leu, 80039 Amiens Cedex 1, France
*Correspondance: mustapha.jouiad@u-picardie.fr

***Abstract*— Coupling two-dimensional (2D)-$MoS_2$ nanostructures with metal nanoparticles (NPs) can lead to unprecedented behaviors because of the coupling between the excitons in $MoS_2$ and the plasmons of the metal NPs. Here, we report the chemical vapor deposition (CVD) growth of vertical 2D-$MoS_2$ nanosheets onto quartz substrates pre-decorated by Ag-NPs. The Ag-NPs were first deposited by pulsed laser deposition (PLD) and used as a catalyst in order to gain more control on the morphology of $MoS_2$. By depositing $MoS_2$ on the PLD-deposited Ag-NPs, we found that the morphology of the CVD grown $MoS_2$ changes from planar to vertical 2D-nanosheets. Moreover, the Ag-NPs were also shown to favor the growth of high-quality 2H-$MoS_2$ phase. Our preliminary results show that the light absorption of these novel Ag-NPs/$MoS_2$ composite films can be enhanced over the entire visible spectrum, leading thereby to an improvement of their specific detectivity (D*) by as high as 516%. This work paves the way towards to design and develop highly responsive optoelectronic devices based on the optimized combination of metal-NPs and 2D-$MoS_2$ nanostructures.**

***Keywords—2D-$MoS_2$, Silver nanoparticles, PLD, CVD, Plasmonics, Photoresponse.***

## I. INTRODUCTION

In the last decade, two dimensional (2D) materials have clearly proven an immense potential for the next generation of photonics and optoelectronics[1]. Unlike bulk materials, 2D materials provide significant sites of light-matter interactions because of the quantum confinement effect[2]. Among the most popular 2D materials are transition metal dichalcogenides (TDMs) which have attracted tremendous interest for plasmonic applications because of their profound coupling effects between excitons and plasmons[3,4]. TMDs have the chemical formula of $MX_2$, where M refers to a transition metal atom (Mo, W, etc.) and X is a chalcogen atom (Se, S, etc.)[5]. Molybdenum disulfide ($MoS_2$) is the most widely studied TMD material because of its abundance in nature[6]. $MoS_2$ exhibits an indirect band-gap for the "bulk form" while it exhibits a direct bandgap for the "mono-to few-layers" ultrathin film form"[7]. This band-gap's transition make 2D-$MoS_2$ a suitable candidate for various applications, for instance as light emitters[8], photodetectors[9], and absorbents in a wide spectrum, etc[10].

A variety of synthesis methods have been proposed for the fabrication of single-to-few layers $MoS_2$[11]. Similar to other 2D materials, mechanical exfoliation was the first technique used for the isolation of mono to few layers of $MoS_2$[12,13]. This technique, however, does not permit precise control of the thickness and uniformity of the exfoliated flakes. Alternatively, chemical methods have been used to produce $MoS_2$ with good crystallinity and a variety of morphologies[14,15]. Meanwhile, the chemical vapor deposition (CVD) method was found to be cost-effective, and facile route to fabricate high-crystalline $MoS_2$[16–18].

Many strategies have been developed to improve the optoelectronic properties of $MoS_2$ by increasing its absorption and charge carrier mobility[19]. Among this approaches, enhancing absorption via the plasmonic effect is considered as one of the most accessible way to enhance the responsivity[20]. In this context, previous studies have shown the impact of decorating mono to few layer of $MoS_2$ with metallic nanoparticles (NPs) in enhancing the performance[20–22]. But so far, the impact of $MoS_2$ synthesis via CVD on Ag NPs is still needed.

In this work, we present a facile processing route to fabricate vertical 2H-$MoS_2$ possessing enhanced optical absorption. In this sense, $MoS_2$ is grown using CVD technique on top of quartz substrate containing Ag-NPs, deposited by pulsed laser deposition (PLD). The aim of this study is to determine the influence of Ag NPs on the nucleation process of $MoS_2$ and examine its impact on optical absorption and the photodetection improvement.

## II. EXPERIMENTAL SECTION

### A. *Materials processing*

Ag-NPs were fabricated by PLD at room temperature. In this process, a KrF laser beam (248 nm, 20 ns, 120 mJ/pulse) was focalized onto an Ag target placed in a chamber with a 0.3 Torr He background pressure. The frequency and the distance between the target and the substrate were fixed to 20Hz and 7cm, respectively. A number of pulse equal to 1000 was used.

Molybdenum trioxide ($MoO_3$, 99.99%) and sulfur (S, 99.5%) were used to synthesize $MoS_2$ films on quartz substrates containing Ag-NPs using CVD technique. 300 mg of sulfur was placed upstream in ceramic boat in a low-temperature zone (400°C). The substrate was placed in the high-temperature zone (850°C). The furnace was heated from room temperature to 400°C at 20°C/min heating rate, then to 850°C at 6°C/min heating rate and a dwell time of 30 min was used during the growth process. The fabrication process was performed at atmospheric pressure under Ar gas flow of 70 sccm. Finally, the furnace was allowed to cool down naturally to room temperature. The preparation sequence and the protocol highlighting different steps are summarized in Fig 1.

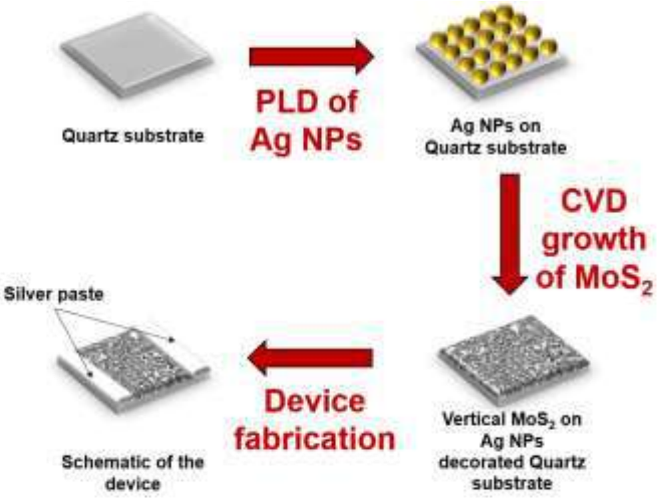

Fig. 1. Schematic of the fabrication of $MoS_2$/Ag NPs device.

### B. *Characterization tools*

The $MoS_2$ microstructure was analyzed by optical microscopy Olympus BX51M, scanning electron microscopy (SEM) Quanta 200 FEG, Thermofisher Scientific and energy dispersive X-ray spectroscopy (EDX) Oxford instruments. The vibrational modes and the photoluminescence (PL) respnses were obtained by a micro-Raman spectrometer, Renishaw, using a 532 nm laser excitation. The optical proprieties were investigated by means of UV-Vis-near IR spectrometer JASCO V-670 and the photo-electrical measurements were performed using Palmsens-4 electrochemical workstation in ambient conditions.

## III. RESULTS AND DISCUSSION

### A. *Growth of $MoS_2$*

The bright field optical images of $MoS_2$ with and without Ag-NPs are shown in Fig 2. The $MoS_2$ on quartz without Ag NPs (Fig 2a) caused in the production of mono to few layers of $MoS_2$ with the most widely known triangular morphology[23]. The average size of these triangles is 6 µm. However, These structures are not evenly distributed on the substrate surface. Fig 2b depicts an optical image of $MoS_2$ grown on Ag NPs, showing high density with no overabundance of the triangular morphology, Moreover, the optical color of the image changed from the green-blue to a yellow-brown tone which could be attributed to a change in morphology. To verify this hypothesis, SEM with EDX mapping was used to better understand the nucleation process of $MoS_2$ with better resolution (Fig 3). The nucleation of $MoS_2$ on Ag NPs shows a larger area of vertical high-density $MoS_2$ and thus prove our hypothesis of morphology transformation. In other words, Ag NPs decorated the Quartz substrate promoted the growth of $MoS_2$ as nucleation assemblies, which will change the morphology of $MoS_2$ from planar to vertical alignment.

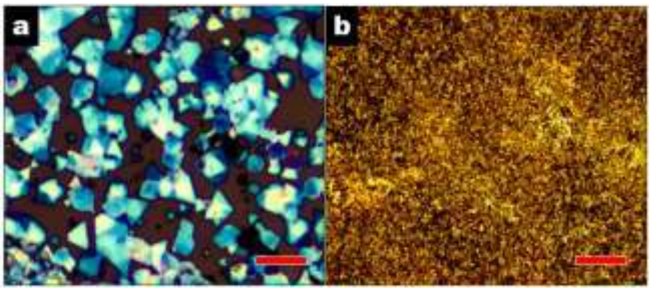

Fig. 2. Optical images of (a) planar $MoS_2$ on Quartz substrate; and (b) vertical $MoS_2$ on Ag NPs (scale bar =10 µm).

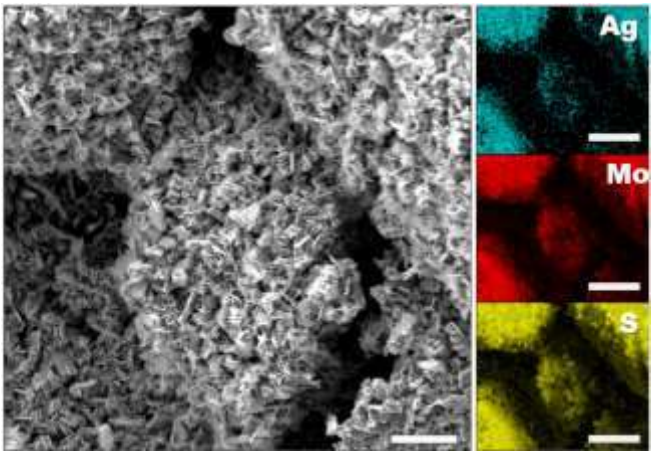

Fig. 3. EDX mapping of $MoS_2$ on Ag NPs decorated Quartz substrate, (scale bar =5 µm).

### B. *Exciton-plasmon coupling of $MoS_2$ with Ag NPs*

The next step in our investigation was to study the impact of fabricating $MoS_2$ on Ag NPs on the physical properties of $MoS_2$. For instance, Raman spectroscopy was used to investigate the vibrational modes of our products under a 532 nm of excitation (Fig 4a). The Raman spectra of the two samples show the Raman fingerprint of pure hexagonal structure of 2H-$MoS_2$ presented by the out-of-plane ($A_{1g}$) and the in-plane ($E^1_{2g}$) modes[24]. Moreover, the Raman spectrum of $MoS_2$ deposited on Ag-NPs shows a high intensity comparing to the sample without Ag-NPs, which could be explained by the strong coupling of plasmonic resonance between Ag NPs and $MoS_2$ due to the electromagnetic field originated from localized surface plasmons of Ag NPs[25]. Moreover, PL measurements was performed for the two samples using the same laser excitation in order to investigate the bandgap of $MoS_2$. The PL spectra of the two samples show the excitonic state (A and B) of $MoS_2$ (Fig 4b), with a blue shift of the two peaks due to the exciton-plasmon coupling between $MoS_2$ and Ag NPs as already reported[26]. Besides that, the intensity of A exciton increased because of the morphology transformation of $MoS_2$ from planar to vertical alignment [16]. Finally, the optical absorption of Ag NPs, planar $MoS_2$, and as-prepared hybrid nanostructures was measured to investigate the exciton-plasmon coupling as presented in Fig 4c. A strong absorption peak at 450 nm was observed for Ag NPs. It is obvious that fabricating $MoS_2$ on Ag NPs increases absorption across the entire visible spectrum. Fig 4d shows illustration of the charge transfer mechanism between Ag NPs and $MoS_2$. Under excitation, the electrons are excited to the surface plasmon of Ag NPs by local surface plasmon resonance (LSPR) followed by the electron transfer to $MoS_2$ which can be used in many photocatalytic applications[25,27,28].

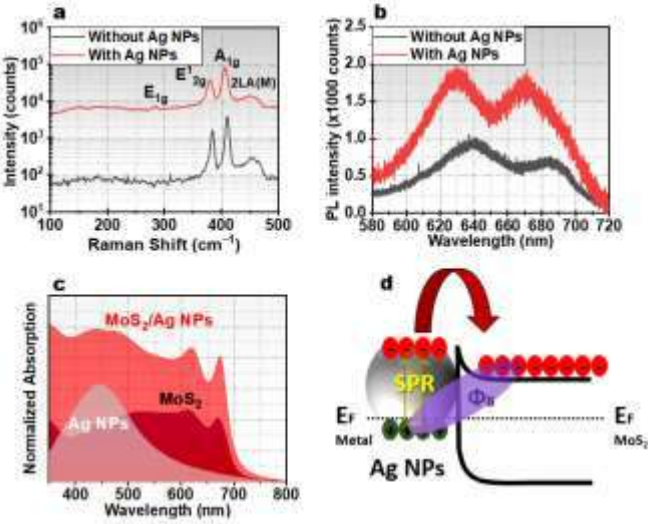

Fig. 4. Physical properties of $MoS_2$ with and without Ag NPs: (a) Raman, and (b) PL spectra of $MoS_2$ with and without Ag NPs. (c) Normalized absorption of Ag NPs, $MoS_2$, and $MoS_2$/Ag NPs. (d) Schematic illustration of charge transfer process in $MoS_2$/Ag NPs.

### C. *Improved photodetection via plasmonic effect*

According to the normalized absorption spectrum obtained (see Fig 4c) the $MoS_2$/Ag NPs heterostructure exhibits high absorption capacity in the entire visible region. To better explore this optical behavior, we conducted photoelectrical measurements for the two $MoS_2$ samples (with and without Ag NPs) to see how the plasmonic effect increase the phoresesponse. The photodetection properties of $MoS_2$ with and without Ag NPs were evaluated using silver past electrodes on their surfaces. Our samples' effective detection area was estimed to be (4 mm$^2$). The current versus bias voltage (I-V) curves of our samples were measured at room temperature, in the dark, and with a halogen lamp (70 mW/cm$^2$). At 1V bias, the current in dark and under illumination is plotted for the two samples and illustrated in Fig 5a. The photocurrent ($I_{Ph}$) defined by ($I_{light}$ - $I_{dark}$) of $MoS_2$ without Ag NPs was equal to 1µA. However, $I_{Ph}$ of the hybrid material found to be equal to 6 µA showing an improvement of 600% in termes of $I_{Ph}$. In addition, the photoresponse ($P_{hr}$) at a biasing voltage of 1V was calculated for the two samples using the following equation:

$$P_{hr}\ (\%) = 100\,\frac{I_{Ph}}{I_{dark}} \qquad (1)$$

We found that the $P_{hr}$ increase from 223% for $MoS_2$ without Ag NPs to 922% for the hybrid material. This can be attributed to the effect of the LSPR in increasing $I_{Ph}$. Furthermore, the responsivity (R) and the specific detectivity (D*) of two sample were calculated using the two following equations respectively.

$$R = \frac{I_{Ph}}{PS} \qquad (1)$$

$$D^* = \frac{R}{\sqrt{2qI_{dark}}} \qquad (2)$$

Where P is the incident power density, S is the active surface of detection, and q is the absolute value of an electron charge (1.6 $10^{19}$ Coulombs). R and D* were found to be equal to 0.42 mA/W and 2.05 $10^{11}$ Jones for $MoS_2$ without Ag NPs, respectively. However, the fabrication $MoS_2$ on Ag NPs lead to achieve high responsivity of 2.2 mA/W and 9.5 $10^{11}$ Jones of detectivity. Finally, transient $I_{Ph}$ was measured in order to get an idea about the time response of ours samples. Fig 5b depicts the transient $I_{Ph}$ response of $MoS_2$ with and without Ag NPs at 1V bias. The device also has a reasonably fast response time, with typical rise and decay times - described as the time required to raise the photocurrent from 10% to 90% of its maximum value and vice versa. The rise and the decay time of our hybrid material were found to be equal to 2.75 and 6.05 s, respectively; Such response times are comparable to the best $MoS_2$ values reported in the literature[9,19].

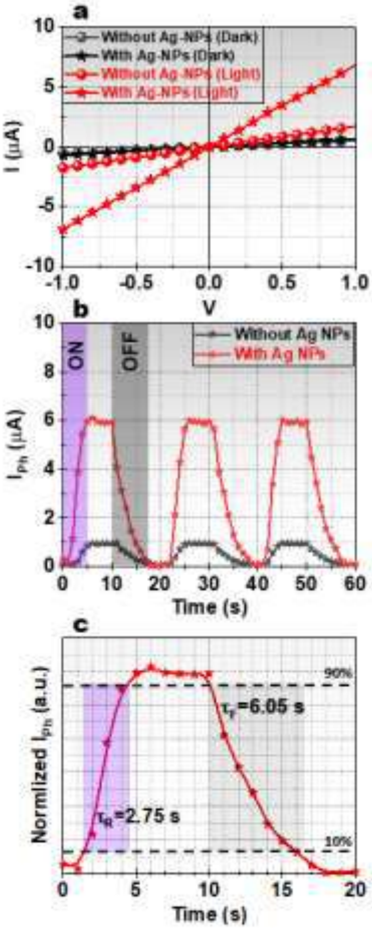

Fig. 5. (a) $I_{Ph}$ measurements of $MoS_2$ with and without Ag NPs; (b) Transient $I_{Ph}$ response of $MoS_2$ with and without Ag NPs registered for three cycles ON/OFF every 10 s, under a constant halogen lamp illumination 70 mW.cm$^{-2}$ and at applied bias of 1V; (c) Rise and decay times of $MoS_2$ with Ag NPs.

## IV. CONCLUSION

In conclusion, a hybrid material composed of MoS$_2$ and Ag NPs was successfully prepared using the CVD method. We reported for the first time that Ag NPs deposited by PLD could be a promising method for morphology transformation from planar to vertical MoS$_2$. Moreover, the resulting hybrid has a high crystalline quality and superior light absorption in the entire visible range. Furthermore, our products have been used photodetection testing. The photoresponse is increased by 414%, while the detectivity was amplified by 516%. This was attributed to the morphology transformation from planar to vertical MoS$_2$ alignment and plasmonic effects. This work demonstrates a new design and development strategy for new plasmonic devices based on 2D-MoS$_2$/Ag NPs.

## ACKNOWLEDGMENT

This work was done in the context of a scientific collaboration between INRS and UPJV. Authors acknowledge the financial support provided by the Region of Haut-De-France (HDF) and the Natural Sciences and Engineering Research Council (NSERC) of Canada, respectively.

## REFERENCES

[1] Mouloua D, Kotbi A, Deokar G, Kaja K, EL Marssi M, El Khakani M A and Jouiad M 2021 Recent Progress in the Synthesis of MoS2 Thin Films for Sensing , Photovoltaic and Plasmonic Applications : A Review *Materials (Basel).* **14** 3283

[2] Mak K F, Lee C, Hone J, Shan J and Heinz T F 2010 Atomically thin MoS2: A new direct-gap semiconductor *Phys. Rev. Lett.* **105** 2–5

[3] Miao P, Ma Y, Sun M, Li J and Xu P 2019 Tuning the SERS activity and plasmon-driven reduction of p-nitrothiophenol on a Ag@MoS2 film *Faraday Discuss.* **214** 297–307

[4] Mukherjee B, Kaushik N, Tripathi R P N, Joseph A M, Mohapatra P K, Dhar S, Singh B P, Kumar G V P, Simsek E and Lodha S 2017 Exciton Emission Intensity Modulation of Monolayer MoS2 via Au Plasmon Coupling *Sci. Rep.* **7** 1–11

[5] Choi W, Choudhary N, Han G H, Park J, Akinwande D and Lee Y H 2017 Recent development of two-dimensional transition metal dichalcogenides and their applications *Mater. Today* **20** 116–30

[6] Yazyev O V and Kis A 2015 MoS2 and semiconductors in the flatland *Mater. Today* **18** 20–30

[7] Gupta D, Chauhan V and Kumar R 2020 A comprehensive review on synthesis and applications of molybdenum disulfide (MoS2) material: Past and recent developments *Inorg. Chem. Commun.* **121** 108200

[8] Late D J, Shaikh P A, Khare R, Kashid R V., Chaudhary M, More M A and Ogale S B 2014 Pulsed laser-deposited MoS2 thin films on W and Si: Field emission and photoresponse studies *ACS Appl. Mater. Interfaces* **6** 15881–8

[9] Taffelli A, Dirè S, Quaranta A and Pancheri L 2021 Mos2 based photodetectors: A review *Sensors* **21** 2758

[10] Chen W, Wang L, Jiang Y and Wang J 2018 A Perfect Absorber Based on Monolayer MoS2 and Nano-Silver in the Visible Regime *2018 Int. Conf. Microw. Millim. Wave Technol. (ICMMT). IEEE* 1–3

[11] Sun J, Li X, Guo W, Zhao M, Fan X, Dong Y, Xu C, Deng J and Fu Y 2017 Synthesis methods of two-dimensional MoS2: A brief review *Crystals* **7** 198

[12] Huang Y, Pan Y H, Yang R, Bao L H, Meng L, Luo H L, Cai Y Q, Liu G D, Zhao W J, Zhou Z, Wu L M, Zhu Z L, Huang M, Liu L W, Liu L, Cheng P, Wu K H, Tian S B, Gu C Z, Shi Y G, Guo Y F, Cheng Z G, Hu J P, Zhao L, Yang G H, Sutter E, Sutter P, Wang Y L, Ji W, Zhou X J and Gao H J 2020 Universal mechanical exfoliation of large-area 2D crystals *Nat. Commun.* **11** 1–9

[13] Jiang J W 2015 Graphene versus MoS2: A short review *Front. Phys.* **10** 287–302

[14] Xin X, Song Y, Guo S, Zhang Y, Wang B, Wang Y and Li X 2020 One-step synthesis of P-doped MoS2 for efficient photocatalytic hydrogen production *J. Alloys Compd.* **829** 154635

[15] Li N, Liu Z, Liu M, Xue C, Chang Q, Wang H, Li Y, Song Z and Hu S 2019 Facile Synthesis of Carbon Dots@2D MoS 2 Heterostructure with Enhanced Photocatalytic Properties *Inorg. Chem.* **58** 5746–52

[16] Deokar G, Rajput N S, Vancsó P, Ravaux F, Jouiad M, Vignaud D, Cecchet F and Colomer J F 2017 Large area growth of vertically aligned luminescent MoS2 nanosheets *Nanoscale* **9** 277–87

[17] Mouloua D, Rajput N S, Blach J-F, Lejeune M, El Marssi M, El Khakani M A and Jouiad M 2022 Fabrication control of MoS2/MoO2 nanocomposite via chemical vapor deposition for optoelectronic applications *Mater. Sci. Eng. B* **286** 116035

[18] Mouloua D, Rajput N S, Saitzek S, Kaja K, Hoummada K, El Marssi M, El Khakani M A and Jouiad M 2022 Broadband photodetection using one-step CVD-fabricated MoS2/MoO2 microflower/microfiber heterostructures *Sci. Rep.* **12** 1–13

[19] Nalwa H S 2020 A review of molybdenum disulfide (MoS2) based photodetectors: From ultra-broadband, self-powered to flexible devices *RSC Adv.* **10** 30529–602

[20] Selamneni V, Raghavan H, Hazra A and Sahatiya P 2021 MoS2/Paper Decorated with Metal Nanoparticles (Au, Pt, and Pd) Based Plasmonic-Enhanced Broadband (Visible-NIR) Flexible Photodetectors *Adv. Mater. Interfaces* **8** 1–12

[21] Rahmati B, Hajzadeh I, Taheri M, Karimzadeh R, Mohajerzadeh S and Mohseni S M 2019 Plasmonic improvement photoresponse of vertical-MoS2 nanostructure photodetector by Au nanoparticles *Appl. Surf. Sci.* **490** 165–71

[22] Guo J, Lin L, Li S, Chen J, Wang S, Wu W, Cai J, Liu Y, Ye J and Huang W 2022 WSe2/MoS2 van der Waals Heterostructures Decorated with Au Nanoparticles for Broadband Plasmonic Photodetectors *ACS Appl. Nano Mater.* **5** 587–96

[23] Zhu D, Shu H, Jiang F, Lv D, Asokan V, Omar O, Yuan J, Zhang Z and Jin C 2017 Capture the growth kinetics of CVD growth of two-dimensional MoS2 *npj 2D Mater. Appl.* **1** 1–7

[24] Lee C, Yan H, Brus L E, Heinz T F, Hone J and Ryu S 2010 Anomalous lattice vibrations of single- and few-layer MoS2 *ACS Nano* **4** 2695–700

[25] Mukherjee S, Chowdhury R K, Karmakar D, Wan M, Jacob C, Das S and Ray S K 2021 Plasmon Triggered, Enhanced Light-Matter Interactions in Au-MoS2Coupled System with Superior Photosensitivity *J. Phys. Chem. C* **125** 11023–34

[26] Mawlong L P L, Paul K K and Giri P K 2021 Exciton-plasmon coupling and giant photoluminescence enhancement in monolayer MoS2 through hierarchically designed TiO2/Au/MoS2 ternary core − Shell heterostructure *Nanotechnology* **32** 215201

[27] Tian L, Wu R and Liu H Y 2019 Synthesis of Au-nanoparticle-loaded 1T@2H-MoS 2 nanosheets with high photocatalytic performance *J. Mater. Sci.* **54** 9656–65

[28] Sun B, Wang Z, Liu Z, Tan X, Liu X, Shi T, Zhou J and Liao G 2019 Tailoring of Silver Nanocubes with Optimized Localized Surface Plasmon in a Gap Mode for a Flexible MoS2 Photodetector *Adv. Funct. Mater.* **29** 1–8